

GEORG-AUGUST-UNIVERSITÄT-GÖTTINGEN

DISSERTATION

**Activation and transformation of small
molecules at a bimetallic β -diketiminato
nickel platform**

*zur Erlangung des mathematisch-naturwissenschaftlichen Doktorgrades
„Doctor rerum naturalium“
der Georg-August-Universität Göttingen*

*im Promotionsprogramm Chemie der Georg-August University School of Science
(GAUSS)*

*vorgelegt von
Roland Alexander Schulz
aus Bremen*

Göttingen 2021

Betreuungsausschuss

PROF. DR. FRANC MEYER
Institut für Anorganische Chemie, Georg-August-Universität Göttingen

PROF. DR. INKE SIEWERT
Institut für Anorganische Chemie, Georg-August-Universität Göttingen

PROF. DR. RICARDO MATA
Institut für Physikalische Chemie, Georg-August-Universität Göttingen

Mitglieder der Prüfungskommission

Referent: PROF. DR. FRANC MEYER
Institut für Anorganische Chemie, Georg-August-Universität Göttingen

Co-Referent: PROF. DR. INKE SIEWERT
Institut für Anorganische Chemie, Georg-August-Universität Göttingen

Co-Referent: PROF. DR. RICARDO MATA
Institut für Physikalische Chemie, Georg-August-Universität Göttingen

Weitere Mitglieder der Prüfungskommission

PROF. DR. DIETMAR STALKE
Institut für Anorganische Chemie, Georg-August-Universität Göttingen

PROF. DR. ANNA KRAWCZUK
Institut für Anorganische Chemie, Georg-August-Universität Göttingen

Acknowledgements

First of all, I am deeply grateful to my supervisor Prof. Dr. Franc Meyer, for giving me the opportunity to work on this research project in your group. I want to thank you for the fruitful discussions, your guidance, and that you always had an open ear for my scientific questions.

Additionally, I want to acknowledge my co-supervisors, Prof. Dr. Inke Siewert and Prof. Dr. Ricardo Mata, for your constructive comments regarding my research and your understanding. I am particularly thankful for the DFT calculations, which were extremely helpful for my work.

Many people have helped me during my Ph.D. thesis. Therefore I want to acknowledge: Dr. Michael John for the NMR measurements and discussion, Dr. Serhiy for the SQUID measurements and data fitting, Prof. Dr. Max Hansmann for the NaPCO, Andreas Schwarz for the starting material for the ligand synthesis, and Dr. Claudia Stückl for performing EPR measurements. I want to thank Britta Müller and Dr. Claudia Stückl for taking care of administrative affairs. I would particularly like to thank Anton Römer for many of the herein presented DFT calculations and our discussion. Thank Dr. Sebastian Dechert, for performing all X-ray diffraction experiments and some of the DFT calculations presented in this work. Even though some of my crystals were probably the most unaesthetic ones you have ever seen, you always did me a favor to measure them.

I thank Wiebke Brunzema, Lena Ratdke, and Niclas Werthmann for their stimulating work and passion during their very successful Bachelor thesis under my supervision. You all did a fantastic job and were an inspiration for my work.

I wish to express my deep gratitude for the splendid cooperation with my lab buddy Manuel Oelschlegel and the superb professional working atmosphere. Notwithstanding, we also had a lot of giggling moments. I sincerely thank Dr. Jerome Spyra, Dr. Thomas Kothe, and Martin Dzemski for the glory nights of "Magic Blue" and the pleasant working atmosphere in this group. Special thanks go to Manuel Oelschlegel and Dr. Jerome Spyra for the proofreading of this thesis.

Last but not least, I want to thank my family and my girlfriend Sarah for always supporting me; I know without you, this all would not be possible.

Contents

Acknowledgements	v
1 Introduction	1
1.1 Nickel and Its Bioinorganic Impact	1
1.2 Ni ^I and its Role in Biological Systems	3
1.2.1 Acetyl-Coenzyme A Synthase (ACS)	4
1.2.2 Methyl-Coenzyme M Reductase (MCR)	6
1.3 β -diketiminato Ligand Systems	8
1.3.1 The β -diketiminato Ligand	8
1.3.2 Metal-Ligand Cooperation (MLC)	9
1.3.3 β -diketiminato Complexes for Small-Molecule Activation . . .	11
1.3.4 Ligand Design for Cooperative Small-Molecule Activation . .	12
1.3.5 Dinickel(II) dihydride complexes	13
1.3.6 Dioxygen activation at Dinickel(II) Complexes	14
1.3.7 A Dinitrogen Radical Complex	15
1.4 Thesis outline	17
2 Binuclear Mono-, and Mixed-valent Dinickel Metalloradicals	19
2.1 State of Knowledge	19
2.1.1 Generation of Double "T"-shaped Dinickel ^I Complexes	20
2.2 Protonation of the nacnac-Backbone	25
2.2.1 Induced Release of Hydrogen	26
2.2.2 Calculated Reaction Mechanism for the Release of H ₂	29
2.2.3 A Mixed-Valent Dinickel Complex	31
2.3 Conclusion and Outlook	36
3 Metal-Metal Cooperative Oxidative Addition of Water Supported by LEWIS Acid Interaction and Dihydrogen Bonding	39
3.1 Oxidative Addition of Water	39
3.2 State of Knowledge and Motivation	42
3.2.1 Synthesis and Isolation	44
3.3 An Intramolecular Dihydrogen Bond	47
3.3.1 Spectral Criteria and Expected Distances of Dihydrogen Bonds	47
3.3.2 Investigation by Infrared Spectroscopy	49
3.3.3 Characterization by NMR Spectroscopy	50
3.3.4 OH \cdots H Bonding Distance Determinations	53
3.3.5 Computational Analysis of the Dihydrogen bond	58
3.4 Reaction Mechanism	60
3.5 Decomposition Mechanism	63
3.6 Conclusion and Outlook	68

4	A Dinickel Phosphaketene Complex for the Synthesis of Novel Phosphorous Compounds	71
4.1	The Chemistry of the Phosphaethanolate Anion (PCO ⁻)	71
4.1.1	Transition Metal Chemistry	72
4.1.2	Reactivity	74
4.2	Motivation	75
4.3	Synthesis of a Dinickel(II) Phosphaketene Complex	76
4.4	Replacement of the Carbonyl Unit	84
4.5	Formation of a P–P Bond	84
4.6	A Carbene-Stabilized Phosphido Complex	89
4.7	An Isocyanide-Phosphido Complex	99
4.8	Synthesis of a Diphospha-Urea Derivative	105
4.9	Conclusion and Outlook	112
5	Experimental Section	115
5.1	General Considerations	115
5.1.1	Materials and Methods	115
5.1.2	Instrumentation	115
5.2	OH···H Bonding Distance Determinations	118
5.2.1	Theoretical Background	118
5.2.2	The NMR Inversion-Recovery (IR) Experiment	119
5.2.3	Isolated-Spin-Pair-Approximation (ISPA)	121
5.3	Reaction Overview	125
5.4	Synthesis of Complexes	126
5.4.1	Synthesis of 3^K	126
5.4.2	Synthesis of 3^{Na}	127
5.4.3	Synthesis of 4	128
5.4.4	Synthesis of 5	129
5.4.5	Synthesis of 6	130
5.4.6	Synthesis of 6-K(crypt)	131
5.4.7	Synthesis of 7	132
5.4.8	Synthesis of 8	133
5.4.9	Synthesis of 9	134
5.4.10	Synthesis of 10	135
5.4.11	Synthesis of 11	136
A	Crystallographic Data	137
A.1	Crystallographic Data of the Complexes 3^K , 3^{Na} , 4 and 5	137
A.2	Crystallographic Data of Complex 6-K(crypt)	143
A.3	Crystallographic Data of the Complexes 7 , 8 , 9 , 10 , and 11	145
B	Further Analytics	153
B.1	SQUID Data of 4	153
B.2	IR spectroscopy	154
B.2.1	Simulated IR Spectra of Dinickel Metalloradicals	154
B.2.2	Activation of Nitrogen by a Mixed-Valent Dinickel Complex	155
B.2.3	IR Spectrum of 6-K(crypt) and Calculated IR Spectrum of 6	156
B.2.4	IR Spectra of Phosphaketene Adducts	157
B.3	UV-vis spectroscopy	159
B.3.1	UV-vis Spectra of Phosphaketene Derivatives	161
B.3.2	ESI-MS spectra of Phosphaketene Derivatives	162

B.4	NMR spectroscopy	164
B.4.1	NMR spectra of 6	164
B.4.2	NMR spectra of 6-K(crypt)	167
B.4.3	NMR spectra of [LNi ₂ (μ-PCO)]	170
B.4.4	NMR spectra of [LNi ₂ (μ-P(NHC))]	173
B.4.5	NMR spectra of 10	176
B.4.6	NMR spectra of K[LNi ₂ (PC(O)PPh ₂)]	179
B.4.7	Reaction of 3 ^K with H ₂	181
C	DFT calculations	183
C.1	DFT calculations for the dinickel(I) complexes 3 ^K , 3 ^{Na} and 4	183
C.1.1	LÖWDIN Spin Population	183
C.1.2	Magnetic Orbitals	184
C.1.3	DFT Calculation for the UV-vis spectra of 3 ^K and 4	185
C.1.4	Reaction Pathway Calculations for the Release of Hydrogen . .	194
C.2	DFT calculations for the Oxidative Addition of Water at Dinickel Complexes	195
C.2.1	Structure Optimizations of 6 and 6-K(crypt)	195
C.3	Reaction Pathway Calculations for the Oxidative Addition of Water .	199
C.3.1	Molecular Dynamics (MD) for 6 and 6-K(crypt)	202
C.4	DFT Optimized Molecular Structures of 7 and 9	204
C.4.1	DFT Optimized Molecular Structures of 7	204
C.4.2	DFT Optimized Molecular Structures of 9	205

List of Abbreviations

a.u.	arbitrary units
CAAC	Cyclic alkyl amino carbenes
COSY	Correlated spectroscopy
Cp	Cyclopentadienyl
δ	Chemical shift
DFT	Density functional theory
DIPP	2,6- <i>i</i> Pr ₂ C ₆ H ₃
ESI	Electron spray ionisation
EPR	Electron paramagnetic resonance
E _{1/2}	Half-cell potential
HMBC	Heteronuclear multiple bond correlation
HOMO	Highest occupied molecular orbital
HSQC	Heteronuclear single quantum coherence
<i>i</i> Pr	<i>iso</i> -propyl
LUMO	Lowest unoccupied molecular orbital
μ B	Bohr magneton
μ_{eff}	Effective magnetic moment
Me	Methyl
Mes	2,4,6-Me ₃ C ₆ H ₂
MO	Molecular orbital
MS	Mass spectrometry
NBO	Natural bonding orbital
NHC	<i>N</i> -heterocyclic carbene
NMR	Nuclear magnetic resonance
OTf	Triflate
PCET	Proton coupled electron transfer
Ph	Phenyl
ppm	Parts per million
r.t.	Room temperature
SOMO	Singly occupied molecular orbital
SQUID	Superconducting quantum interference device
THF	Tetrahydrofuran
vs	versus
WBI	Wiberg bond index

Chapter 1

Introduction

1.1 Nickel and Its Bioinorganic Impact

Nickel is a 3d transition metal found in group 10 of the periodic system with an electronic configuration for elemental nickel of (Ar) $3d^84s^2$. Nickel is used extensively for technical applications^[1] but also plays an important role in nature. Nature harnesses transition metals to catalyze many different biological reactions, leading to an estimated third of all enzymes being metalloenzymes. However, nickel-based enzymes are not as common as the omnipresent biological metal iron.^[2] Nonetheless, nickel serves as an essential cofactor in archaea, bacteria, plants, fungi, and primitive eukaryotes.^[3–5] Even though no Ni-based enzymes are known in mammalian species until today, their impact on human health is significant.^[2] On the one hand, nickel is known to cause cancer by an epigenetic mechanism,^[6] which includes substituting Ni^{II} for Fe^{II} in nonheme iron dioxygenases that are involved in DNA and histone demethylation.^[7,8] Furthermore, one of the most common allergies in the modern world, nickel contact dermatitis, is caused by exposure to nickel compounds.^[9] On the other hand, nickel is an essential trace element for bacteria, plants, animals, and humans.^[10,11]

The predominant oxidation state of nickel is +II or 0 for elemental nickel,^[12] while the uncommon oxidation states of +I and +III are comparatively rare to find. Nickel is found in various coordination geometries, which constitutes an advantage of nickel as a catalytic center allowing diverse functions. For instance, in redox enzymes, the metal environment is crucial to adjust its redox potential, and nickel is thus able to switch between different redox states. In metalloproteins, nickel is found in three distinct oxidation states (I, II, III) and can access potentials spanning over a range of 1.4 V.^[13–15] In an aqueous solution, Ni^{II} forms the octahedral $[\text{Ni}(\text{H}_2\text{O})_6]^{2+}$ complex; however, most of the Ni^{II} enzymes exhibit a square planar coordination environment. This versatility explains the multitude of chemical transformations this first-row transition metal can achieve.

The biological role of nickel was ambiguous for a long time, and it has not been identified as a metal of biological relevance until 1975 when ZERNER discovered the first nickel metalloenzyme, urease.^[16] There are ten nickel enzymes in total by the current state of scientific knowledge, covering an extensive bandwidth of reactivity. Which include, among other things, small-molecule activation or two-electron redox processes.^[17] Further, all but glyoxalase I and lactate racemase catalyze reactions that are involved in the regulation of global gas cycles (CO , CO_2 , CH_4 , H_2 , NH_3 , and O_2) and are therefore assumed to play a crucial part in the evolution of life.^[18,19]

In general, nickel enzymes can be divided into two groups. First, redox enzymes, as Ni-superoxide dismutase (Ni-SOD), methyl-coenzyme M reductase (MCR),^[20] NiFe-hydrogenase (H₂ase),^[21] acetyl-coenzyme A synthase (ACS),^[22] carbon monoxide dehydrogenase (CODH)^[23] and, second, nonredox enzymes comprising urease,^[16] lactate racemase (LarA),^[24] glyoxalase I (GlxI),^[25] quercetin 2,4-dioxygenase,^[26] and acireductone dioxygenase (ARD).^[27] All nickel enzymes and their respective reactivities are listed in table 1.1. Especially methyl-coenzyme M reductase (MCR) and Acetyl-coenzyme A synthase (ACS) will be discussed in further detail as they illustrate the mechanistic importance of the unusual oxidation state of Ni^I.^[28]

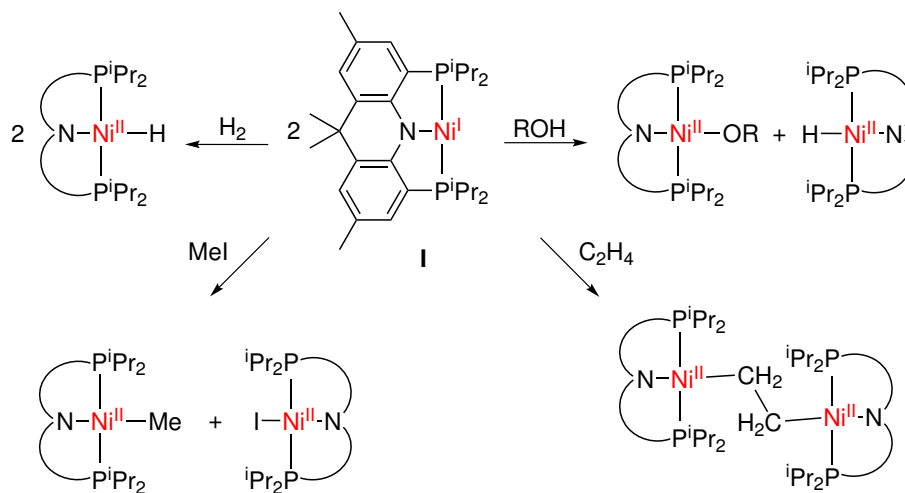
Table 1.1: All known Ni enzymes and compilation of the corresponding catalytic reactions.^[17,28,29]

	Enzyme reaction
Redox enzymes	
[NiFe]-hydrogenase	$2\text{H}^+ + 2\text{e}^- \rightleftharpoons \text{H}_2$
Methyl-coenzyme M reductase	$\text{CoM-S-CH}_3 + \text{H-S-CoB} \rightleftharpoons \text{CH}_4 + \text{CoM-S-S-CoB}$
Nickel CO dehydrogenase	$\text{CO} + \text{H}_2\text{O} \rightleftharpoons \text{CO}_2 + 2\text{H}^+ + 2\text{e}^-$
Acetyl-coenzyme A synthase	$\text{CH}_3\text{-Co}^{\text{II}}\text{-FeSP} + \text{CO} + \text{CoA-SH} \rightleftharpoons \text{Co}^{\text{I}}\text{-FeSP} + \text{CoA-S-CO-CH}_3$
Superoxide dismutase	$2\text{O}_2^{\cdot -} + 2\text{H}^+ \longrightarrow \text{O}_2 + \text{H}_2\text{O}_2$
Nonredox enzymes	
Acireductone dioxygenase	
Quercetin 2,4-dioxygenase	
Urease	$\text{H}_2\text{N-CO-NH}_2 + \text{H}_2\text{O} \longrightarrow \text{H}_2\text{N-CO-O}^- + \text{NH}_4^+$
Glyoxalase I	
Lactate racemase	

1.2 Ni^I and its Role in Biological Systems

As illustrated before, nickel enzymes are involved in processing global gases and in the transformation of small molecules. Thus, elucidating the underlying reaction mechanisms of nickel-dependent enzymes is of critical importance. In this context, Ni^I has proven its potential to mediate the transformations of organic substrates in biological and industrial processes.^[30] Ni^I has a $3d^9$ valence electron configuration and can act as a moderately strong one-electron reducing agent, as oxidation leads to a thermodynamically favored d^8 -configured Ni^{II}.^[31] In biological systems, monovalent nickel intermediates are assumed to play a vital role in acetyl-coenzyme A synthase (ACS) or methyl-coenzyme M reductase (MCR) for developing their function; the underlying mechanisms are presented in the following subsections 1.2.1 and 1.2.2. Besides, the rising use of Ni^I complexes in catalysis, particularly in cross-coupling chemistry, and the reductive activation of small molecules represent a strong driving force for further investigations.^[32–34]

The realization of Ni^I-mediated activation of small molecules depends heavily on the ligand scaffold, which must be capable of stabilizing this uncommon oxidation state while keeping the coordination number low to provide a redox-active metal center with a vacant coordination site. These specific requirements can be fulfilled by pincer-based ligands enforcing a T-shaped geometry.^[35–37] One remarkable example is given by YOO and LEE, who presented a T-shaped Ni^I PNP system that reacts with a diversity of inert substrates.^[38] Notably, the T-shaped metalloradical forms binuclear Ni^{II} species if reacting with double bond containing molecules, such as CO₂ or C₂H₄, see Scheme 1.1.



Scheme 1.1: Reactivity of T-shaped Ni^I PNP complex **I** towards several challenging substrates.^[38]

1.2.1 Acetyl-Coenzyme A Synthase (ACS)

Acetyl-coenzyme A synthase (ACS) is an enzyme that plays a key role in the anaerobic carbon dioxide fixation by the WOOD-LJUNGDAHL pathway metabolism of anaerobic bacteria and archaea.^[39] Along with carbon monoxide dehydrogenase (CODH), a bifunctional protein complex (ACS/CODH) is formed, which catalyzes the reversible synthesis of acetyl-CoA.^[14] This metalloprotein is capable of carbon monoxide fixation and carbon-carbon bond coupling reactions associated with accessing various oxidation states.^[40] A comparable reaction sequence is carried out by the rhodium-based MONSANTO process for the large-scale synthesis of acetic acid by catalytic carbonylation of methanol.^[41] These unique features motivated scientists for decades to develop model complex and to elucidate the ongoing reaction mechanism of ACS.

The interplay of ACS and CODH can be illustrated by briefly describing the present reaction sequence. At the Ni center in CODH, carbon dioxide is reversibly reduced to carbon monoxide, which is subsequently transported through a 70 Å long hydrophobic channel to the nickel-containing ACS active site.^[42] At the so-called proximal nickel center, Ni_p, CO is combined with a methyl group and CoA to form the metabolite and cellular building block, acetyl-CoA. Upon splitting the energy-rich thioester bond, acetyl-CoA serves as a provider of an acetyl group that is oxidized to CO₂. Based on the citric acid cycle (CAC), the released chemical energy is stored in the form of adenosine triphosphate (ATP).^[43] The structure of the active site of the Ni/Fe/S cofactor of acetyl coenzyme A synthase is displayed in Figure 1.1. Both thiolate-bridged nickel centers are in the oxidation state +II and located in a square-planar coordination environment. Lastly, one thiolate links the Ni_p to a [Fe₄S₄] cluster.^[29]

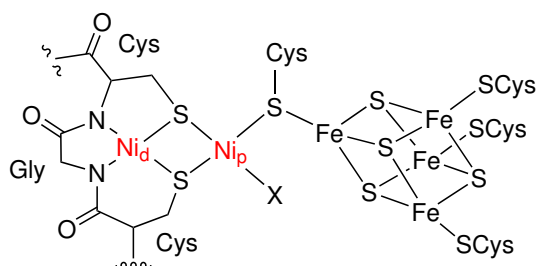


Figure 1.1: Structure of the active site of the Acetyl-coenzyme A synthase (ACS).

Due to its complexity, investigations of the mechanism of this biological system do not provide a definitive result but point to possible competing reaction pathways known as the paramagnetic and diamagnetic mechanisms. The main difference is found in the assignment of the redox states of Ni_p during the reaction. Furthermore, it is unclear in which order the CO and CH₃ groups bind to the enzyme;^[40] however, it is possible as well that the binding is random.^[44] Both reaction mechanisms share the similarity that the distal Ni_d remains in the divalent oxidation state, stabilizing the structure.^[45] In the paramagnetic mechanism, the Ni^{II} ion is activated by reducing it to Ni^I and binding reversibly CO, produced within the CODH subunit. Subsequently, cobalamin transfers CH₃⁺ onto the Ni^I-CO species. The acetyl-CoA is formed after a series of reaction steps while cycling between the Ni_p^I, Ni_p^{II}, and Ni_p^{III} states.^[46] The paramagnetic mechanism is displayed in Scheme 1.2; for simplicity, the intermediate states are abbreviated.

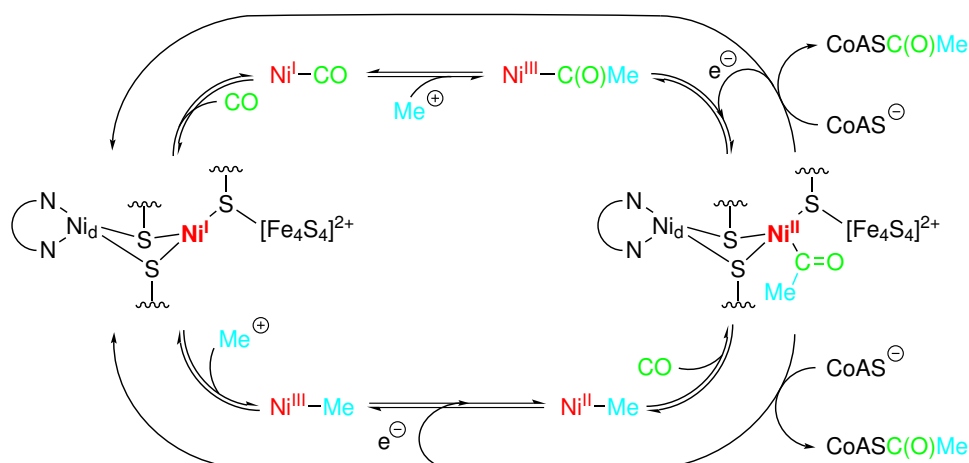


Figure 1.2: Simplified paramagnetic mechanism of the Acetyl-coenzyme A synthase (ACS). Both paths only differ by order of substrate binding.^[31,45] There are strong indications for the coordination of two CO molecules to the Ni_p, but since a molecular structure is lacking, it is omitted for comprehensibility.^[47]

This mechanism relies on rapid reduction of the transient Ni_p^{III} state, generated upon methyl transfer from the methylated corrinoid iron-sulfur protein CH₃-Co^{III}FeSP. However, to balance the electron count, a yet-unidentified redox partner is needed.^[40] However, it has been shown that the rate of electron transfer between the coupled [Fe₄S₄] cluster, and Ni_p is 200-times slower than the rate of observed methyl transfer to Ni_p, which brings the reaction mechanism into question.^[48] Notwithstanding, there is also strong evidence supporting the paramagnetic pathway and the formation of a Ni^I species, while it appears highly probable that two CO molecules are bound to Ni_p.^[47] In this context, it is also worth mentioning that SHAFAT *et al.* presented a nickel-substituted azurin mutant capable of adopting all three relevant oxidation states of nickel and further generating the postulated intermediates (Ni^I-CO and Ni^{III}-Me).^[40,49,50] Further, there is one model complex that supports the idea of oxidative addition of methenium (Me⁺) to a monovalent nickel center. Upon treating the Ni^I bis-amido complex with methyl iodide, an isolable Ni^{III} alkyl species is formed,^[51] see 1.3.

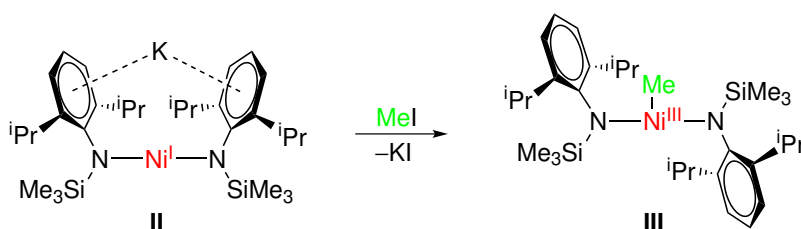


Figure 1.3: Oxidative addition of Me⁺ to the K[Ni[N^I(SiMe₃)DIPP] complex **II** results in a Ni^{III}-Me complex **III**.^[51]

Alternatively, the diamagnetic mechanism proposes a Ni^0 intermediate compound formation instead of a Ni^{I} species.^[52,53] It has been suggested that CO binds to a doubly reduced Ni center that switches between the oxidation states 0 and +II. Although this mechanism is electronically balanced, there is still no solid evidence for the formation of a Ni^0 intermediate, along with the fact that such a zerovalent nickel complex remains unobserved in biological systems.^[54,55] Nonetheless, model complexes could prove oxidative addition of carbon electrophiles to Ni^0 , substantiating the plausibility of this reaction path.^[45]

1.2.2 Methyl-Coenzyme M Reductase (MCR)

The Ni coordinating methyl-coenzyme M reductase (MCR) is the central enzyme in biological methane formation by methanogenic Archaea and consumption by anaerobic methanotrophs.^[56,57] For methane production, the metalloprotein is reversibly catalyzing the conversion of methyl-coenzyme M ($\text{CH}_3\text{-SCoM}$) and coenzyme B CoB-SH to a heterodisulfide (CoM-S-S-CoB) and methane. The enzyme has two active sites containing the nickel cofactor F430, which is displayed in Figure 1.4.^[58] Therefore, MCR carries out the last step of microbial methane formation and the first step of anaerobic methane oxidation.

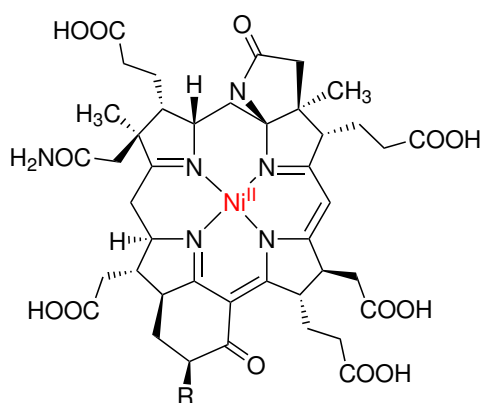
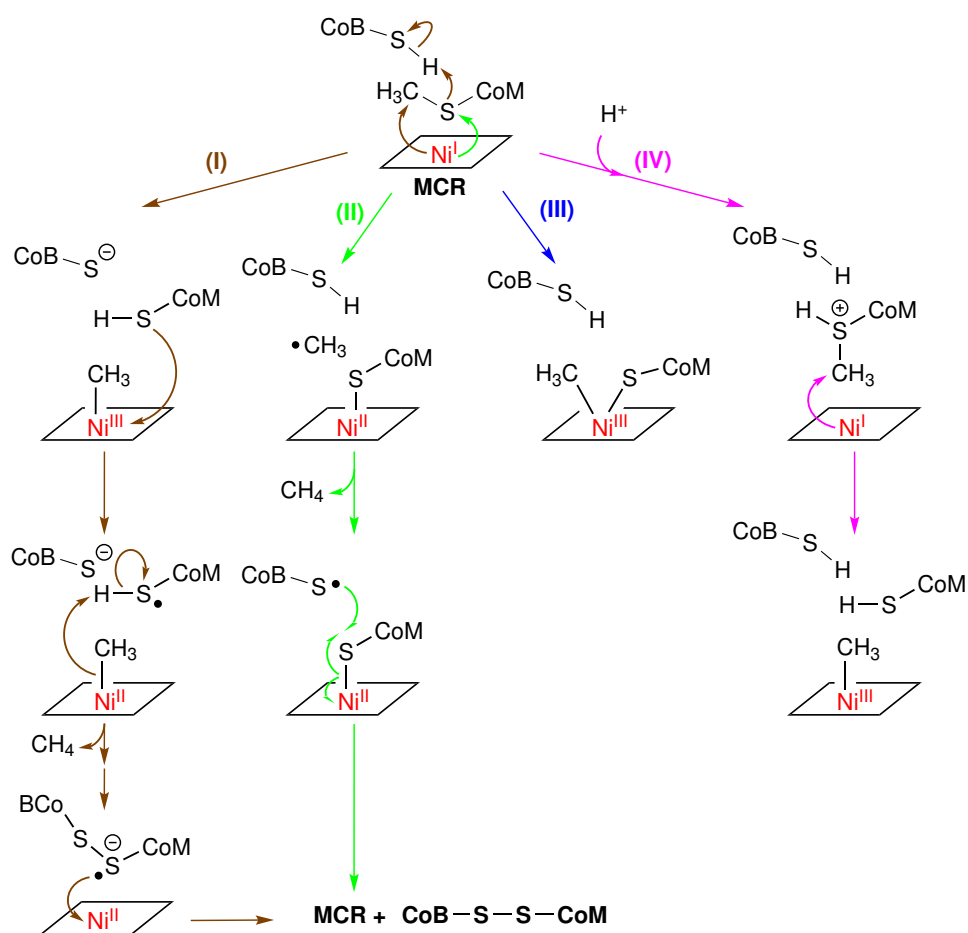


Figure 1.4: Prosthetic group of methyl-coenzyme M reductase (MCR), F430.

Since its discovery 50 years ago,^[59] MCR has been intensively investigated, representing an extraordinary challenge for experimental and computational studies. The hydroporphyrinoid nickel complex coenzyme F430 in its active site must be in the Ni^{I} (MCR-red) oxidation state for the enzyme to be active.^[60] Due to the extreme oxygen sensitivity of the Ni^{I} species, it is necessary to harvest and purify the cells under anaerobic conditions to circumvent the oxidation to Ni^{II} .^[61] Therefore it is not surprising that only the inactive Ni^{II} state has been structurally characterized by X-ray diffraction.^[20] However, the molecular structure could reveal that the substrates are guided to the active site by a long narrow tunnel, which opens into an essentially hydrophobic aromatic environment above the hydrocorphyrinoid plane of F430.^[62] No structural information of the reactive forms of F430 could be obtained until today, and no intermediate could be observed when the active enzyme is incubated with its two natural substrates.^[63] Despite the fact that a definite reaction mechanism is still unclear, some success was achieved by isotopic exchange experiments combined with DFT calculations to illuminate the reaction mechanism partially.^[58,63] Further, EPR and UV-vis spectra have been reported, supported by intensive computational

studies, laying the foundation for in total four proposed reaction mechanisms, presented in Scheme 1.2. To conclude, the best fitting reaction mechanism is the SIEG-BAHN proposal (II), which assumes a methyl radical instead of a Ni^{III} species, resulting in a $CoM-S-Ni^{II}$ F430 intermediate.^[17] However, further investigations are needed as still not all experimental results can be explained.^[58]



Scheme 1.2: Four proposed mechanisms for the MCR reaction. (I) The reaction includes a methyl- Ni^{III} F430 intermediate. (II) The reaction proceeds *via* a methyl radical and a $CoM-S-Ni^{II}$ F430 intermediate. (III) This mechanism assumes an intermediate with a coordinated methyl group and $CoM-S^-$ coordinating to the Ni center. (IV) The last reaction sequence presumes S-protonation of CH_3-SCoM .^[17]

1.3 β -diketiminato Ligand Systems

In 1968, the first documented transition metal complexes based on β -diketiminato ligands were reported by MCGEACHIN,^[64] who isolated complexes of several metal ions, and by PARKS and HOLM,^[65] who focused in particular on bis-(β -diketiminato) Ni^{II} complexes. They set the starting point for the rich organometallic chemistry of this ligand scaffold and were the first who realized their potential tuneability. Even after 50 years, mononuclear β -diketiminato complexes are still of interest today and are intensively investigated, especially in the field of small-molecule activation.

1.3.1 The β -diketiminato Ligand

N-substituted β -diketiminato ligands, also known as “nacnac” or BDI, are well-established and widely used.^[66] By comparing the nacnac ligand with its oxygen analog “acac” (acetylacetonate), it became apparent that new tuneable properties arise upon replacing the oxygen atoms with nitrogen-based moieties NR. As a result, the substitutions at the N-donor function (e.g., alkyl, silyl, or aryl) provide the feasibility to customize the steric protection of the chelated metal ion or the active site.^[66–68] Further, not only the adaptable sterical demand but also the tunable electronic properties enable nacnac ligands to stabilize rare coordination environments and to make it possible to isolate labile intermediates. Nacnac ligand scaffolds are employed to coordinate a large bandwidth of elements, leading to a versatile deployment of this monoanionic ligand. The range of application extends to alkali and alkaline earth,^[69–73] main-group,^[74,75] transition-metal,^[76–80] lanthanide,^[81,82] and actinide^[81,83–85] complexes, which underlines the widespread utility of this versatile ligand.

The electronic structure of the planar, aromatic nacnac ligand is an essential aspect to estimate the ligand interaction with the corresponding coordination center, see Figure 1.5. The molecular orbital diagram is displayed in (a); the residues of the nitrogen moiety are not part of the conjugated π -system and are therefore not considered. The HOMO (2b1) is characterized by out-of-plane p-type orbitals on the two nitrogen donor functionalities. In addition, substantial electron density is located at the γ -C, but none on the two β -carbons. In light of these considerations, it is possible to derive a general reactivity profile of the nacnac ligand scaffold, which will be discussed later. In contrast, the 5b2 and 6a1 orbitals are in-plane and located on the nitrogen atoms. The two last-mentioned orbitals are particularly interesting as they are pointing directly towards the central ion. Consequently, both are expected to take part in ligand-metal bonding. As a result, there is a profound σ -type donation from the 5b2 ligand orbital into the Ni $d_{x^2-y^2}$ orbital (c), as both have the appropriate symmetry to interact (d). As the LUMO (2a2) is very high in energy π backdonation is unlikely; however, this orbital becomes important in terms of UV-vis spectroscopy since it is responsible for a characteristic ligand $\pi \rightarrow \pi^*$ transition around 350 nm. The low-lying orbitals, 1a2 and 1b1, are unlikely to show significant interactions with the metal orbitals.

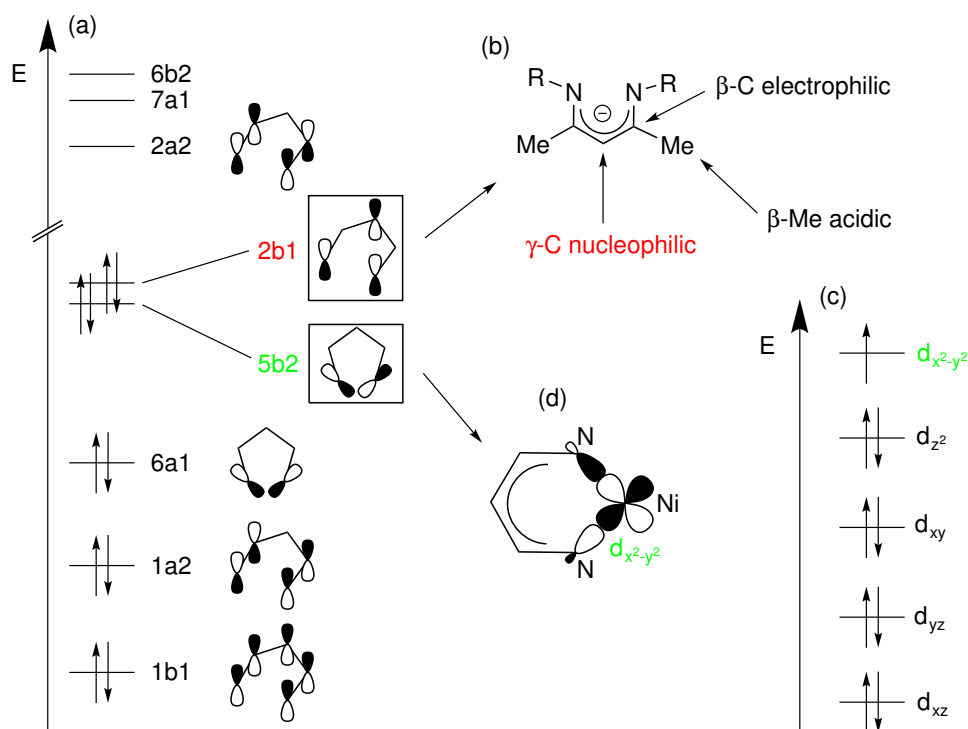
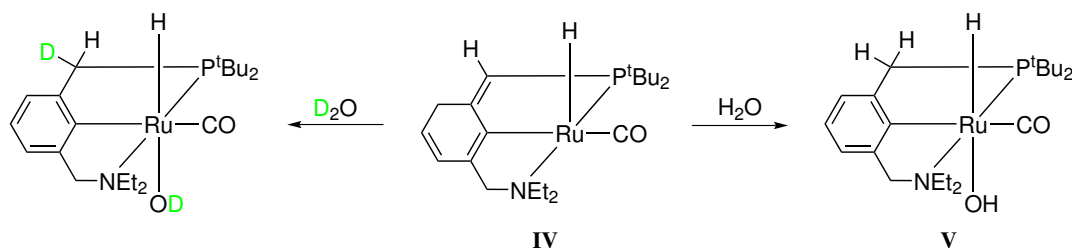


Figure 1.5: Electronic structure of the nacnac ligand ($C_3H_5N_2$) (a) and general reactivity profile of the nacnac ligand (b).^[86] Molecular orbital diagram for a "T"-shaped d^9 system (c) and schematic visualization of the 5b2 orbital interacting with the $d_{x^2-y^2}$ orbital of Ni^I (d).^[38,87]

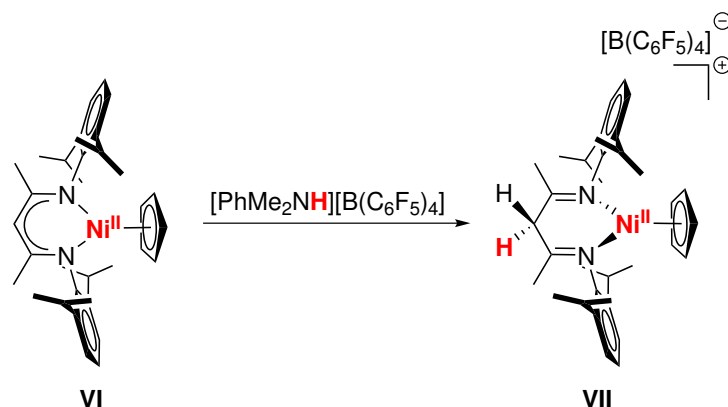
1.3.2 Metal–Ligand Cooperation (MLC)

Metal–ligand cooperation (MLC) has become of general importance in transition metal chemistry exploited by naturally occurring enzymes and synthetic complexes. MLC means that the metal and the coordinated ligand participate in the bond activation processes, by contrast to transition metal catalysis, where the ligand acts as a spectator, while the reactivity happens exclusively at the metal center. The field has rapidly developed, becoming a general strategy for effecting highly efficient molecular transformations. Since there are many examples for reductive transformations of small molecules (such as H_2 , N_2 , and H_2O) involving the synchronized transfer of electrons and protons, metal–ligand cooperativity using proton transfer sites on the ligand has emerged as a powerful concept^[88,89] which is well established for pincer ligand scaffolds bearing N/NH functionalities.^[90] For instance, MILSTEIN *et al.* presented a Ru^{II} complex **IV** consisting of a non-innocent tridentate PNN pincer ligand scaffold, which can donate or accept one proton.^[91] This system is capable of water splitting by oxidative addition *via* a dearomatization–aromatization process in cooperation with the metal center. Upon splitting the O–H bond of H_2O , the proton is accepted by the ligand, and the respective hydroxido is coordinated to the metal center, which remains its initial oxidation state of +II, see Scheme 1.3.^[92]



Scheme 1.3: Reaction of a pincer Ru^{II} complex IV with H₂O/D₂O leads to ligand aromatization and formation of a trans hydrido-hydroxido species V.

The non-innocence of β -diketiminato ligands at the γ -C atom has also been demonstrated, albeit it mainly involves oxygenative ligand modifications or metal-ligand cross additions, while backbone protonation for enhancing the utility of nacnac complexes is relatively rare.^[86] An example is given by STEPHAN *et al.*, who have protonated the Ni^{II} synthon VI with [PhMe₂NH][B(C₆F₅)₄], see Scheme 1.4. As shown in Figure 1.5 (b), the nacnac backbone γ -C is prone to nucleophilic attack. Therefore it is not surprising that protonation yields the corresponding non-planar ligand H₂C(C(Me)NAr)₂ with localized double imine (C=N) bonds.



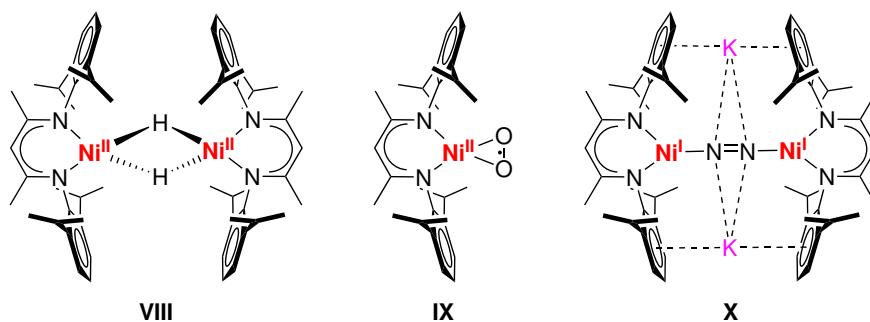
Scheme 1.4: Protonation at the γ -C of the β -diketiminato Ni cyclopentadienyl complex VI yields complex VII.^[86]

Consequently, by protonating the β -diketiminato ligand, the interaction between the metal center and the now neutral ligand is weakened, which can be attributed to the more insufficient donor ability. This was verified by X-ray diffraction (XRD), revealing longer Ni–N distances than for the precursor complex.^[93]

The protonation of the BDI ligand can be unequivocally identified by ¹H NMR spectroscopy since it usually displays two doublets that couple in the ¹H-¹H COSY NMR spectrum, corresponding to the two diastereotopic γ -CH₂ protons in H₂C(C(Me)NAr)₂. In the solid-state, short C=N bond lengths are observed, in agreement with localized double imine functionalities and a non-planar H₂C(C(Me)NAr)₂ ligand core with an sp³ hybridized methylene carbon.^[94]

1.3.3 β -diketiminato Complexes for Small-Molecule Activation

Pincer-type ligands dominate the research field of small-molecule activation. In this context, chelating monoanionic nacnac ligands have been extensively used to stabilize low valent transition metal systems. In addition, several β -diketiminato-nickel^I complexes bearing sterical demanding substituents at the nitrogen atoms have shown their capability of generating highly active Ni^I species. Notably, groups of HOLLAND and LIMBERG have pioneered the development of β -diketiminato ligands for activation of challenging gases such as H₂,^[95,96] O₂,^[97–100] and N₂,^[101,102] some prominent examples are displayed in the following, see Scheme 1.5.

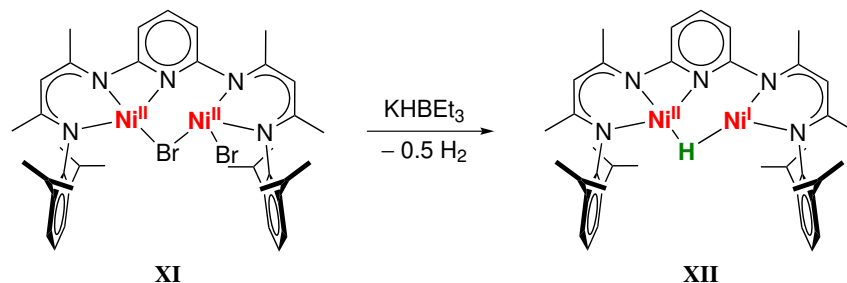


Scheme 1.5: Literature known examples of small-molecule activation by β -diketiminato nickel complexes. Hydrido bridged Ni^{II} complex **VIII**,^[95] side-on superoxo Ni^{II} complex **IX**,^[100] and diazine coordinating Ni^I complex **X**.^[101]

Although this ligand system has been used primarily to synthesize mononuclear complexes, some of them form dimers when reacting with small molecules; however, there is no cooperativity between the coordinated metal ions in these cases. Therefore, dinucleating ligand scaffolds are of great interest due to their capability to provide a preorganized coordination environment while keeping the metal ions at a certain distance.^[103] As presented in Section 1.1, there are several multinuclear biocatalysts that are able to carry out different relevant reactions, such as small-molecule activation or redox processes. Inspired by enzymatic processes, chemists have synthesized novel model complexes that mimic the enzymatic reactivity and further help to elucidate the underlying reaction mechanism.

Since replicating the whole enzyme is not possible, the focus of designing such model complexes is set on the active site. In this regard, the bimetallic system [NiFe] hydrogenase is worth mentioning. This enzyme has received much attention not only because of its biological relevance but also due to its potential industrial application. The central intermediate within the catalytic cycle of the [NiFe]-hydrogenase is assumed to contain a bridging hydrido ligand between the Ni and the Fe centers^[104] and therefore rivals platinum.^[105] As industrial processes for hydrogen production and uptake are dominated by expensive Pt catalysts, the naturally occurring hydrogenase represents a desired replacement since it is based on abundant early transition metals.^[106] Together, this has been a driving force for developing bioinspired catalysts, which mimic enzymatic reactivity.^[107–109] In the context of this work, an example from the LIMBERG group will be presented briefly.^[110] Treatment of the bromide-bridged dinuclear Ni^{II} precursor complex **XI** with KHBET₃ yields into the mixed-valent Ni^{II}-Ni^I complex **XII** featuring a hydrido in the bridging position, see Scheme 1.6. It is important to note that the same reaction procedure for the corresponding mononuclear complex yields to bridging hydrido ligands (see

Scheme 1.5) while the oxidation state of both Ni ions is +II.^[95] Further, this example illustrates that β -diketiminato ligand systems are not only capable of stabilizing different oxidation states but even allow to generate mixed valent complexes, in this case, Ni^{I/II}.



Scheme 1.6: Formation of a mixed-valent Ni^I– μ –H–Ni^{II} complex **XII**.^[110]

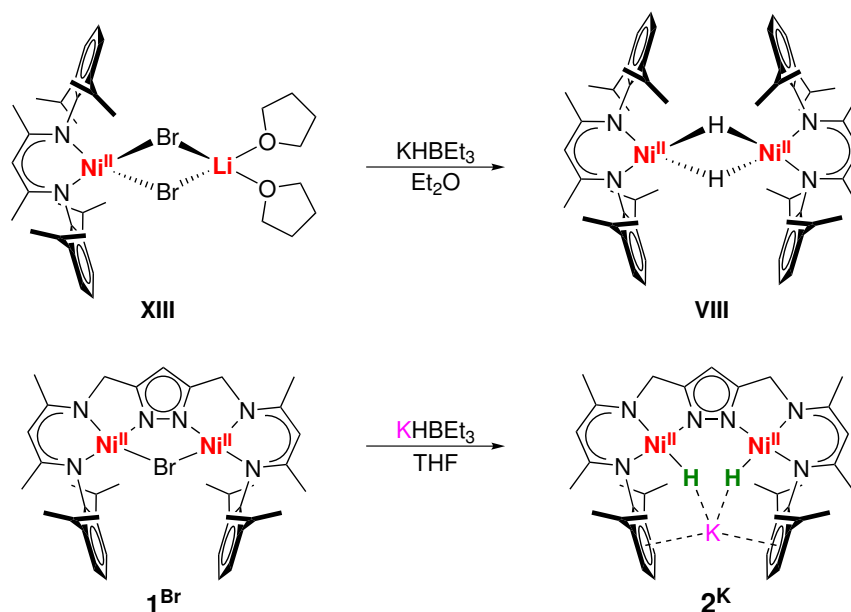
Altogether, nacin based complexes have proven their potential, particularly in the field of small-molecule activation, but also enable the coordinated metal center to switch its oxidation state. Additionally, the possibility to convert mononucleating β -diketiminato ligand scaffolds to binucleating ligand systems has opened up new fields of application and enabled metal-metal cooperativity, which will be discussed in the following.

1.3.4 Ligand Design for Cooperative Small-Molecule Activation

A successful approach to designing such bimetallic ligand scaffolds is by linking already established mononuclear systems. The choice of the bridging unit has a crucial influence not only on the metal-metal distance but also represents an additional adjustment option for fine-tuning the steric demand, electronic properties and potentially offering coordination sites. Lastly, the active site's geometric flexibility and accessibility can be controlled by changing the aliphatic linkers in the ligand backbone. These advantages and the before mentioned characteristics of β -diketiminato ligand systems have led to different approaches to synthesizing bimetallic nacin complexes. Several ligand scaffolds are known to literature composed of nacin compartments but differ from the used bridging unit, for instance, pyridine,^[110] phenylenediamine,^[111] ethylene, and cyclohexyl.^[112] Based on previous work by DENNIS MANZ,^[113] a pyrazolate-bridged compartmental ligand (**H₃L**) with β -diketiminato chelate arms are providing two pincer-type {N₃} binding pockets will be discussed in further detail. The ligand system is similar to the previously reported by LIMBERG, except that the two DIPP-substituted β -diketiminato units were linked by a 3,5-dimethyl-1H-pyrazole bridging unit. The advantage of using a pyrazole-linked ligand scaffold instead is the additional N-donor function, which results in a stronger chelating effect. Overall, the trianionic, hexadentate ligand scaffold with two highly preorganized binding pockets in close proximity facilitates the formation of a bimetallic system harnessing metal-metal cooperativity.

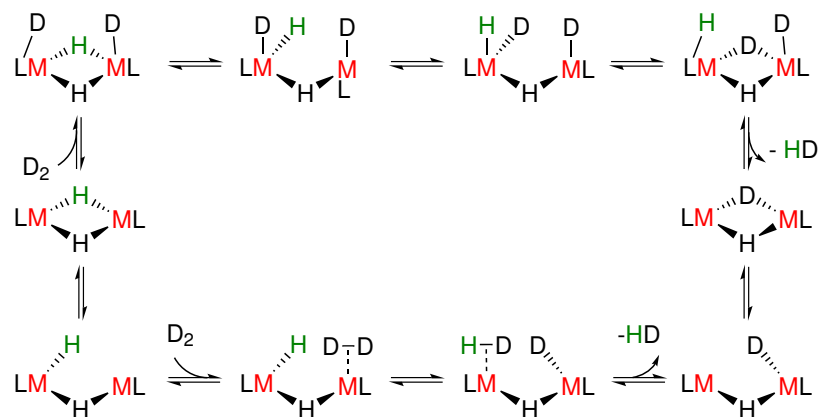
1.3.5 Dinickel(II) dihydride complexes

In contrast to the before shown reaction in Scheme 1.6, the bromido-bridged precursor complex $[\text{LNi}_2(\mu\text{-Br})]$ (1^{Br}) reacts with KHBEt_3 to give the dihydrido nickel complexes $\text{K}[\text{LNi}_2^{\text{II}}(\text{H})_2]$ (2^{K}), see Scheme 1.7:



Scheme 1.7: Synthesis of nickel(II) dihydrido complexes. Note that the upper line's reaction yields the same product **VIII** as in Scheme 1.5 but originates from a different precursor reacting with H_2 .

This system can be described as a masked dinickel(I) synthon bearing two terminal hydrido ligands close to each other, stabilized by the potassium counter ion. This system is capable of cooperative two-electron reductive binding of various small molecules accompanied by H_2 release.^[113–115] The respective substrates within the bimetallic cleft are stabilized by the charge withdrawing potassium counterion, encapsulated by the two flanking aryl groups. Even though the reaction product, dihydrido complex 2^{K} , is comparable to complex **VIII** (Scheme 1.5), the underlying reaction mechanism is different. By treating the corresponding diiron complex of **VIII** with D_2 , results in all hydrido/ deuterido isotopologues. The mechanism is not fully understood, but it is plausible to assume that H_2/D_2 exchange proceeds at the dimeric molecule, leaving two possible reaction pathways,^[116] see Scheme 1.8.



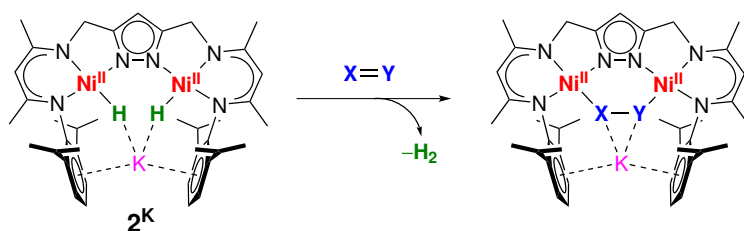
Scheme 1.8: Possible mechanisms of D_2/H_2 exchange for a dihydrido complex which results in the formation of HD.^[116]

During both proposed reaction sequences, one of the bridging hydridos is cleaved to provide a free coordination site to bind dideuterium. The reaction mechanism in the upper line proceeds *via* the oxidative addition of D_2 , while the one in the lower line involves forming a transient side-on D_2 complex. Furthermore, intermolecular hydrido/deuterido ligand exchange between isotopologues of **VIII** has been observed, a phenomenon that does not play a role for $K[Ln_2^{II}(H)_2]$ (**2^K**). This difference in reactivity can be attributed to the divergent ligand binding mode. There are no bridging hydridos, $\mu-H$, for complex **2^K** due to the larger metal-metal separation enforced by the pyrazolate bridging unit (**VIII**: 2.3939(6) Å,^[117] **2^K**: 4.1586(1) Å).^[118]

The significant advantage of using dinickel(II) complex **2^K** compared to low valent Ni^I reductants is that Ni^I species are often extremely sensitive and consequently tricky to isolate. As a result, dinuclear Ni^I systems are relatively seldom.^[30,31] Further, the square-planar coordinated Ni^{II} ions in **2^K** exhibit a singlet spin state ($S = 0$), resulting in a diamagnetic compound that can be unambiguously analyzed by NMR spectroscopy. As mentioned above, the dihydrido complex **2^K** is capable of reductive activation of a wide range of substrates. To illustrate the reactivity of this complex, two examples will be discussed in the following.

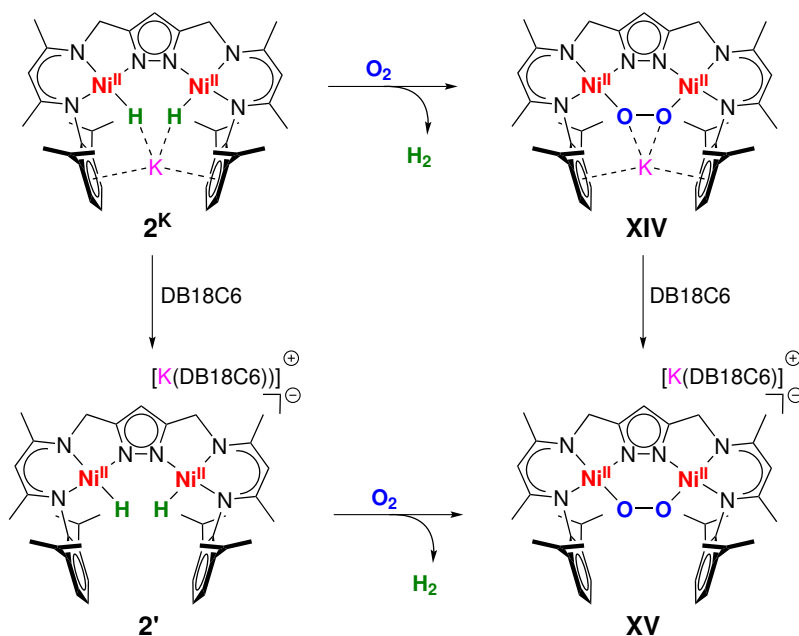
1.3.6 Dioxygen activation at Dinickel(II) Complexes

The dihydrido complex **2^K** has proven its potential in the field of small molecule activation.^[113-115,119,120] The sufficient stability combined with high reactivity of **2^K** can be attributed to the fact that the two hydrido ligands within the pocket of the dinickel(II) core function as reducing equivalents. Therefore, this complex serves as a masked-dinickel(I) complex. Upon the release of H_2 , **2^K** transforms into a transient low-valent dinickel(I) species, which undergoes smoothly reductive substrate activation:



Scheme 1.9: General concept of reductive small molecule ($X=Y$) activation at the dinickel(II) dihydrido complex 2^K accompanied by the release of H_2 .^[114]

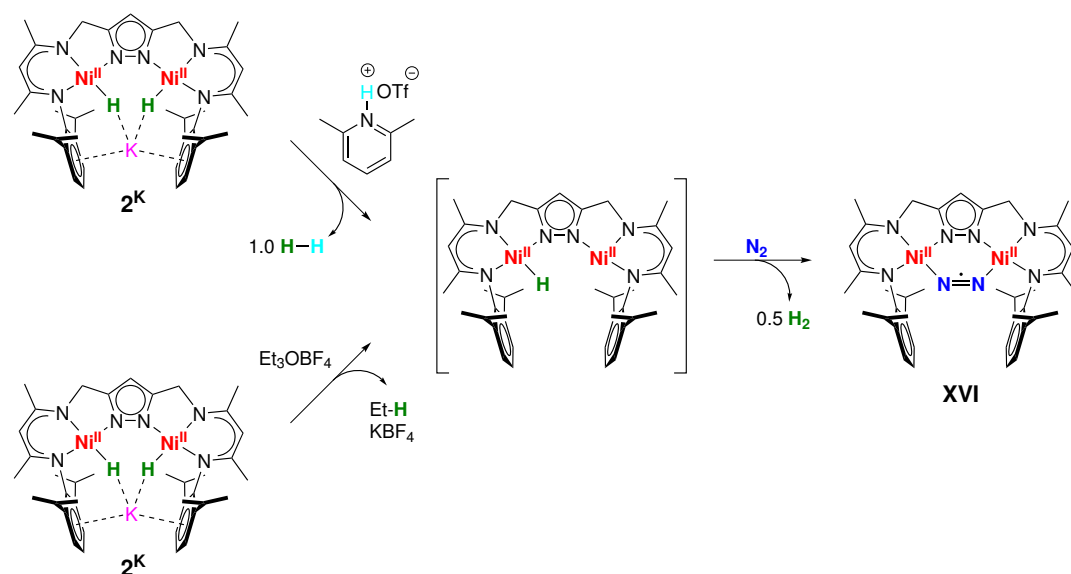
This mechanism was demonstrated by the reaction of 2^K with various small molecules. For example, the reaction of 2^K with one equivalent of O_2 results in the formation of the dinickel(II) peroxido complex **XIV** with concomitant reductive H_2 elimination, see Scheme 1.10. It was also possible to remove the potassium cation with DB18C6 from the peroxy ligand of **XIV**, resulting in the stable complex **XV**.^[114]



Scheme 1.10: Reaction of $2^K/2'$ with O_2 results in the respective peroxido complex **XIV/XV** accompanied by the reductive elimination of H_2 .^[114]

1.3.7 A Dinitrogen Radical Complex

Based on the work of DENNIS MANZ, the dihydrido complex 2^K can be transformed into the dinickel dinitrogen complex **XVI**, see Scheme 1.11.^[118] PENG-CHENG DUAN continued this work and discovered that adding one equivalent of absolute 2,6-lutidinium triflate ($[HLut]OTf$) to 2^K in THF resulted in the release of 1.4 eq. equivalents (eq.) of H_2 (determined by gas chromatography) under N_2 atmosphere. Theoretically, 1.0 eq. of H_2 originates from 2^K and 0.5 eq. of H_2 from the reduced H^+ of the acid. Moreover, alternative synthetic routes were established by THOMAS KOTHE to generate **XVI**. Instead of using BRØNSTED acids, the same complex was isolated when 2^K was treated with hydride abstraction reagents, such as Et_3OBF_4 . This finding supports the hypothesis that one hydrido ligand is removed from the bimetallic cleft in both cases, resulting in a vacant coordination site at the Ni^{II} ion.



Scheme 1.11: Reaction of 2^K with $[HLut][OTf]$ or Et_3OBF_4 under a nitrogen atmosphere leads to the formation of a dinitrogen radical complex $[LNi_2^II(N_2^{\cdot-})]$ (XVI). The postulated hydrido intermediate is placed in square brackets.

It was impossible to trap the assumed intermediate of these reactions; however, XVI was isolated and extensively characterized, including X-ray crystallography.^[118,121] The formation of a dinitrogen radical was confirmed by EPR spectroscopy revealing an $S = 1/2$ system with an g_{iso} value of 2.072. A characteristic band at 1896 cm^{-1} (free N_2 : 2359 cm^{-1})^[122] was detected in the IR spectrum attributed to the $N=N$ stretching vibration. In addition, UV-vis spectroscopy was used to analyze the complex further. Both 2^K and XVI feature absorptions between 300 nm and 500 nm. However, the spectrum of XVI shows a characteristic feature at 698 nm, which was suspected to originate from the electronic transition between the dinitrogen radical ligand and the Ni^{II} ions.^[121]

1.4 Thesis outline

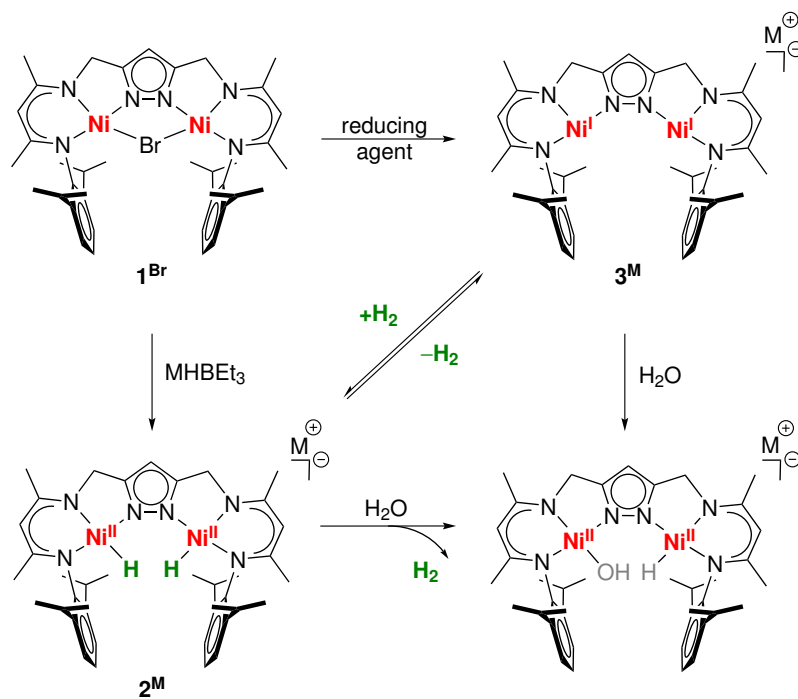
The great potential of the masked dinickel(I) complex **2^K** for the stoichiometric activation of small molecules has been demonstrated by reference to the reductive O₂ binding (Section 1.3.6). This has been achieved by reductive release of H₂, which formally leaves one reducing equivalent for each hydrido ligand on the respective Ni^{III} ion. As a result, the *in situ* generated unmasked Ni^I species is able of reductive substrate binding. Even though this approach is well established, an alternative synthetic route towards an isolable dinickel(I) complex would be desirable. This is due to the fact that the dihydrido complex **2^K** does not exclusively react as masked dinickel(I) complex. An example is given Scheme 1.11. In this case, the addition of an acid to **2^K** under an N₂ atmosphere results in forming a dinitrogen radical complex (**XVI**). Even though the exact mechanism of this reaction is unknown, it is reasonable to assume that one hydrido ligand combines with the incoming proton resulting in a monohydrido intermediate. This transient species is now capable of single reduced substrate binding. To elucidate the underlying reaction mechanism, the reaction should be repeated with a discrete dinickel(I) complex.

In addition, Ni^I complexes are efficient catalysts for the activation of small molecules,^[31] and biologically relevant (compare Section 1.2). Some examples of mononuclear Ni^I complexes are known in the literature. However, these Ni^I complexes are often limited to one-electron transfer or alternatively forming Ni^{II}) dimers.^[95,101] Therefore, a bimetallic version of Ni^I metalloradicals would be highly desirable for enabling two-electron transformations via metal-metal cooperativity (MMC). Consequently, a binucleating ligand scaffold providing two preorganized d⁹ Ni^I ions in an appropriate arrangement for cooperative bimetallic chemistry would be a consistent further development. In this context, β-diketiminato based ligand systems appear to be predestined for providing such a coordination environment to enable reductively binding of inert substrates. Two major prerequisites need to be fulfilled to achieve a relatively stable Ni^I compound with high reactivity towards inert substrates. First, the employed ligand system must be capable of stabilizing such a low valent oxidation state, and second, a vacant coordination site for substrate-binding must be available. In particular, three-coordinate Ni^I complexes with a T-shaped geometry arranged by pincer-type ligands have proven their potential.^[35–38] The coordinated Ni^I metal center is characterized by an unpaired electron located in the accessible σ-antibonding d_{x²-y²} orbital (see Figure 1.5) and therefore eminently suitable for small-molecule activation.

Under consideration of all these factors, the already established binucleating β-diketiminato/pyrazolato hybrid ligand **H₃L** seems to be a suitable ligand system to fulfill these requirements (see subsection 1.3.4). Notwithstanding, Ni^I complexes are considered to be rather unstable, this thesis aims to isolate and structurally characterize such a species. Moreover, the ligand system should be tested towards metal-ligand cooperativity (MLC). In this respect, the before-mentioned γ-C of the nacnac backbone is of interest since its protonation would result in localized double C=N bonds accompanied by a significant change of the electronic structure (Scheme 1.4).

Further efforts should be devoted to small molecule activation. Even though Ni^I compounds are susceptible to moisture, the reactivity with water should be investigated. However, there are no examples of Ni^I compounds, or 3d transition metals in

general, capable of metal-centered oxidative addition of water. DENNIS MANZ carried out initial investigations on this topic by treating 2^{K} with H_2O .^[118] However, it was not possible to fully characterize the postulated hydroxido hydrido species. Therefore further efforts will be dedicated to completing the characterization and isolating this complex.



Scheme 1.12: Overview of reactions towards a dinickel(I) complex and target reaction with H_2O .

Another small molecule that will be investigated in this work is the phosphoethanolate anion PCO^- . This reagent has been utilized in many different reaction types; however, it is rarely found in late transition metal chemistry.^[123] A well-established method to generate phosphoethanolate complex is by salt metathesis reaction. Based on this approach, the bromido precursor 1^{Br} is assumed to react with NaPCO to deliver the desired neutral phosphoethanolate complex. In general, dinuclear phosphaketene complexes are scarcely investigated and are therefore highly interesting. Further, phosphaketenes willingly release CO and are prone to nucleophilic attack at the phosphaketene-C, representing a promising starting point for subsequent investigations. Consequently, this thesis aims to isolate a bimetallic phosphaketene complex and carry out follow-up transformations of the PCO ligand within the bimetallic pocket.

Chapter 2

Binuclear Mono-, and Mixed-valent Dinickel Metalloradicals

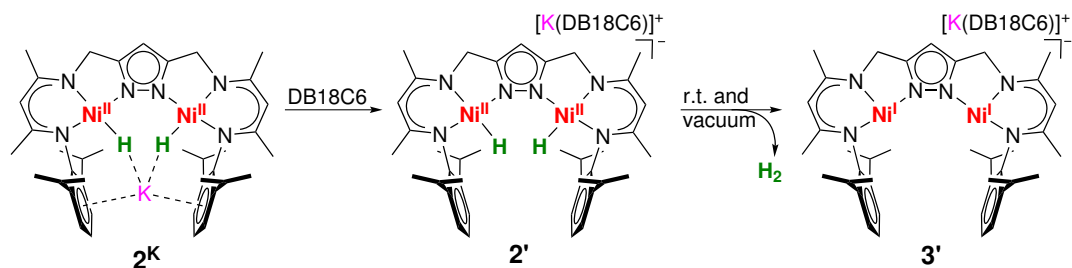
Parts of this chapter were adapted from:

P.-C. Duan, R. A. Schulz, A. Römer, B. E. Van Kuiken, S. Dechert, S. Demeshko, G. E. Cutsail III, S. DeBeer, R. A. Mata, F. Meyer *Angew. Chem. Int. Ed.*, **2021**, *60*, 1891-1896.

2.1 State of Knowledge

In the following, a series of nickel-complexes based on a binucleating bis(tridentate) ligand H_3L that consists of two β -diketiminato compartments linked by a pyrazolate unit will be discussed. The dinickel(II) dihydrido complex $\mathbf{2}^{\text{K}}$ is capable of two-electron reductive binding of small molecules accompanied with the elimination of H_2 while harnessing metal-metal cooperativity (MMC). As described before, this complex can thus serve as a masked dinickel(I) synthon. However, there is a growing interest in Ni metalloradical complexes in catalysis, making it highly desirable to generate a discrete Ni^{I} species, ideally *via* a direct reduction route starting from the bromide-bridged precursor $\mathbf{1}^{\text{Br}}$. In addition, the complexes shall be tested for potential metal-ligand cooperativity (MLC). In this context, the nucleophilic γ -C at the nacnac backbone represents a potential target for manipulating the coordination environment and tuning the electronic properties, see Figure 1.5.

The dinickel(II) dihydrido complex $\mathbf{2}^{\text{K}}$ was already extensively described by MEYER *et al.*, laying the foundation for the herein presented work.^[113] As previously illustrated, complex $\mathbf{2}^{\text{K}}$ is not only capable of behaving as a Ni^{I} synthon but also can be converted into the discrete Ni^{I} species $\mathbf{2}'$ as well, see Scheme 2.1. This has been done by segregating the stabilizing potassium counter ion from the DIPP cleft by [2,2,2]cryptand, yielding $[\text{K}(\text{DB18C6})][\text{LNi}_2(\text{H})_2]$ ($\mathbf{2}'$). During the course of these studies, they were able to isolate and investigate the resulting species, $\mathbf{2}'$, by X-ray diffraction. Even though this data need to be treated with caution, due to the fact that hydrogen atoms are weakly scattering, they revealed a variation of the positions of the hydrido ligands. While the Ni–H distances were elongated, the H \cdots H spacing was shrinking. Accompanied by the absence of the stabilizing counter ion, the former tightly bounded hydrido groups were labilized and consequently prone to elimination. The reductive elimination can be triggered by either increasing the temperature or by applying vacuum on $\mathbf{2}'$, which will finally result in the loss of H_2 , leaving two electrons on the respective nickel core and resulted in the formation of complex $\mathbf{3}'$. This conversion process was monitored by magnetic susceptibility measurements, confirming the predicted presence of two antiferromagnetically coupled $S = 1/2$ sites, in accordance with two $\text{Ni}^{\text{I}}(d^9)$ ions.



Scheme 2.1: Reaction overview towards $[K(DB18C6)][LNi_2(H)_2]$ ($2'$) and subsequent H_2 release under vacuum leading to complex $3'$.

Even though a dinickel(I) complex has been generated, this procedure presents the drawback of lacking potassium ion in the coordination sphere. This is indeed disadvantageous as the counter ion has a profound stabilizing effect on potential substrates within the binding pocket. However, it has been shown that the applied ligand system, H_3L , is capable of stabilizing a low-valent Ni species. Therefore, further efforts will be directed towards an alternative synthetic route to generate an $\{LNi_2^I\}$ compound directly.

2.1.1 Generation of Double "T"-shaped Dinickel^I Complexes

As mentioned above, the dihydrido complex 2^K was utilized to obtain a Ni^I species; another synthetic approach towards generating such a low valent complex involves reducing the bromido-bridged precursor. Since this complex has a reduction potential of -2.1 V *vs.* Fc/Fc^+ , the usage of a strong reducing agent is needed. Additionally, it would be handy if potassium or sodium could be introduced as a counter ion to ensure comparability with the respective hydrido complexes. Finally, since reactivities shall be investigated with the resulting Ni^I complex, the presence of K^+ near the binding pocket for potential stabilization of reduced substrates would be desirable and represent an advantage over $3'$.

Consequently, 1^{Br} was treated with KC_8 in a minimum amount of THF at room temperature. Over a period of two hours, the green suspension turned into a deep red, clear solution, which was filtered afterward. Next, the filtrate was layered with hexane followed by cooling to -38 °C, leading to the formation of polycrystalline material; however, single crystals suitable for X-ray diffraction required several recrystallizations. The molecular structure of 3^K is displayed in Figure 2.1, selected bond lengths, distances, and angles are shown in Table 2.1.

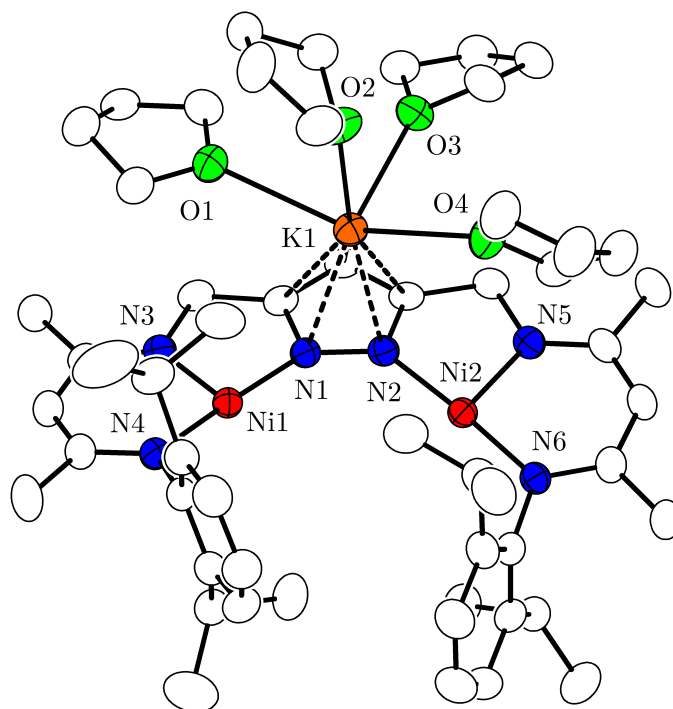


Figure 2.1: Molecular structure of $\text{K}[\text{LNi}_2^{\text{I}}]$ (3^{K}) (30% probability thermal ellipsoids). $\text{K}^+ \cdots \text{C}_{\text{pz}}$ contacts $< 3.5 \text{ \AA}$ are shown as dashed lines.

Table 2.1: Selected bond lengths, distances, and angles of 3^{K} .

Bond length / \AA	Distances / \AA		Angle / $^\circ$		
Ni1–N4	1.890(3)	Ni1 \cdots Ni2	4.1243(7)	N4–Ni1–N1	176.76(13)
Ni1–N1	1.890(3)	Ni1 \cdots K1	3.8554(9)	N4–Ni1–N3	98.75(13)
Ni1–N3	1.917(3)	Ni2 \cdots K1	3.9661(9)	N1–Ni1–N3	84.43(12)
Ni2–N6	1.857(3)	Pz \cdots K1 [†]	2.9036	N6–Ni2–N2	176.21(12)
Ni2–N2	1.892(3)			N6–Ni2–N5	99.22(12)
Ni2–N5	1.917(3)			N2–Ni2–N5	84.49(12)

[†]Measured distance between the pyrazolate centroid and the potassium

The same approach has been followed to synthesize the analogous sodium adduct 3^{Na} . This time, the precursor complex 1^{Br} was treated with a THF solution of freshly prepared sodium naphthalenide. The reaction solution immediately turned red and was worked up in the same way as 3^{K} . Single crystalline material of 3^{Na} was obtained from a THF/hexane solution and subjected to X-ray diffraction; the respective molecular structure is shown in Figure 2.2:

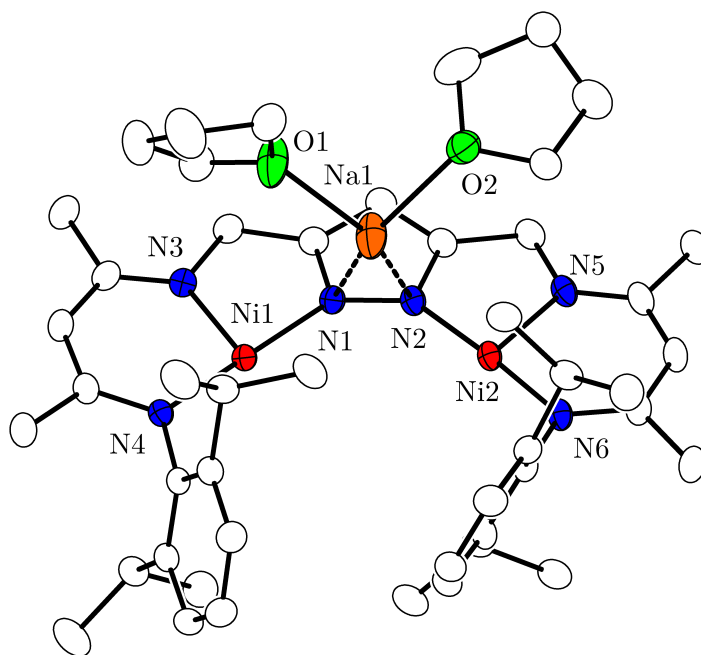


Figure 2.2: Molecular structure of $\text{Na}[\text{LNi}_2^{\text{I}}]$ (3^{Na}) (30% probability thermal ellipsoids). $\text{Na}^+ \cdots \text{N}_{\text{pz}}$ contacts are shown as dashed lines.

Table 2.2: Selected bond lengths, distances, and angles of 3^{Na} .

Bond length / Å	Distances / Å		Angle / °		
Ni1–N4	1.8794(17)	Ni1···Ni2	4.1899(4)	N4–Ni1–N1	175.59(7)
Ni1–N1	1.9118(17)	Ni1···Na1	3.3477(10)	N4–Ni1–N3	98.17(7)
Ni1–N3	1.9212(17)	Ni2···Na1	3.0507(10)	N1–Ni1–N3	84.34(7)
Ni2–N6	1.8624(18)	Pz···Na1 [†]	2.3874	N6–Ni2–N2	176.50(7)
Ni2–N2	1.8944(17)			N6–Ni2–N5	98.36(8)
Ni2–N5	1.9140(17)			N2–Ni2–N5	85.04(7)

[†]Averaged distance between the nitrogen bond (N1–N2) and the sodium anion

Both molecular structures illustrate the nearly ideal „T“-shaped coordination sphere of both nickel centers. The two pincer-type {N3} nickel units are characterized by a metal···metal separation of $d(\text{Ni}\cdots\text{Ni}) = 4.1243(7)$ Å, while the respective bonding angles of the N₁–Ni₁–N₄ and N₂–Ni₂–N₆ fragments are almost reaching 180° (viz. 176.8(1)° and 176.2(1)°). The most apparent difference to the dihydrido complexes 2^{K} and 2^{Na} is the position of the respective counter ion, which is positioned above the pyrazolate and is additionally ligated by a variable number of THF molecules.

Since H-atoms are not unambiguously detectable *via* X-ray diffraction, the distinct position of the alkali metal ion serves as an indicator if a negatively charged ligand is coordinated in the bimetallic pocket. To illustrate this relation, the respective molecular structures of the dihydrido complexes 2^{K} and 2^{Na} are compared with the corresponding Ni^I complexes. In 2^{K} and 2^{Na} , the hydrido ligands are located within the bimetallic pocket, while the coordination environment of the nickel ions can be described as slightly distorted square planar. In both complexes, the alkali metal cation is in close proximity to the negatively charged hydrido groups; though, their position is different. In 2^{K} , the K⁺ ion is sandwiched between the two aryl rings of

the DIPP units *via* cation- π interactions and is placed within the plane spanned by the pyrazolate-bridged dinickel dihydrido core, presumably supported by attractive $K^+ \cdots H^-$ interactions ($d(K^+ \cdots H^-) = 2.45(3) - 2.53(3) \text{ \AA}$). However, the binding situation is different for the smaller Na^+ ion. Due to its smaller size, it is not found in the DIPP cleft but above the pyrazolate-bridged dinickel dihydrido core, associated with the two hydrido ligands, the two pyrazolato-N, and two additional THF molecules. This arrangement is reminiscent of the analogous Ni^I complexes; nonetheless, the Na^+ is not associated with the binding pocket because of the lack of alkali metal-hydride interactions. This finding leads to the conclusion that indeed no hydrido ligand is present in 3^K and 3^{Na} , and therefore the desired binuclear nickel^I metalloradical complex has been formed; however, this is not solid evidence, which makes further analytical investigations necessary.

The NMR spectrum of 3^K revealed paramagnetic behavior, indicating the expected presence of at least one unpaired electron, see Figure 2.3. An assignment of the peaks could not have been achieved, though a minor impurity of 2^K (24.13 ppm) is found, which will be explained in the following chapter. It is also worth mentioning that the observed peak pattern resembles that of the dinickel(I) complex $3'$.^[113]

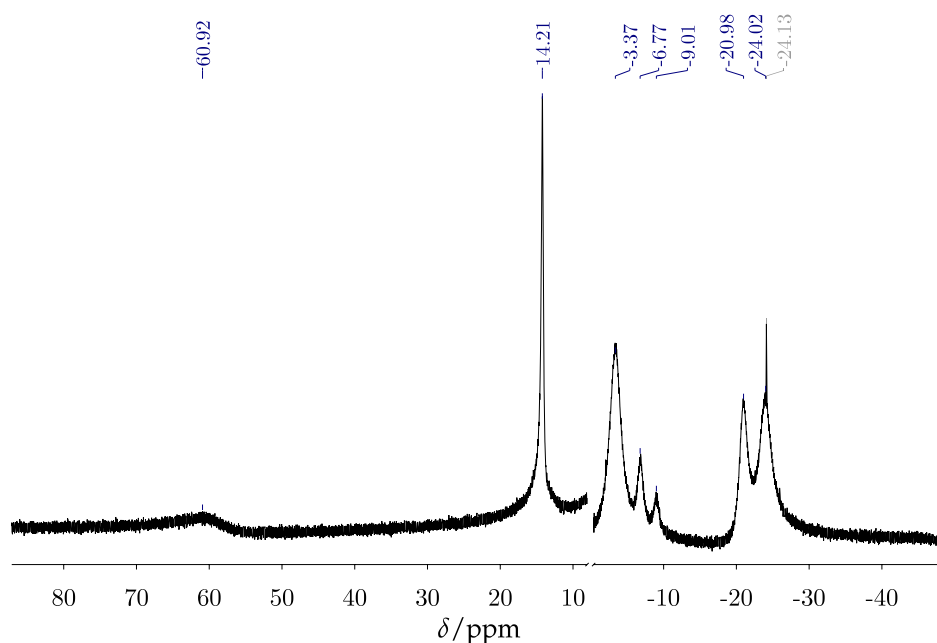


Figure 2.3: 1H NMR spectrum of 3^K in $THF-d_8$ at room temperature. The region of approximately 10-0 ppm is not displayed; the signal at -24.13 ppm can be assigned to complex 2^K .

As stated above, a reliable method to investigate metalloradical complexes is by magnetic susceptibility measurements. First of all, this kind of technique reveals the number of unpaired electrons and, therefore, clearly allows to determine whether the complex is reduced twice. For comparison, complex $3'$ bears two Ni^I centers, which results in a magnetic moment of $0.5 \text{ cm}^3 \cdot \text{mol}^{-1} \cdot \text{K}$ (in cgs-units: $2.0 \mu_B$) at 295 K, close to the estimated value for two $S = 1/2$ ions ($2.45 \mu_B$ for $g = 2.0$). This mismatch can be attributed to diamagnetic impurities, such as unconverted quantities of the dihydrido complex 2^K , which shows diamagnetic behavior. Further,

2' features a coupling constant of $J = -70 \text{ cm}^{-1}$, indicating antiferromagnetic coupling between the two d^9 nickel centers. To validate the hypothesis that the bromido precursor **1^{Br}** was transformed in the desired dinickel(I) complex, superconducting quantum interference device (SQUID) data for a sample of crystalline material of **3^K** has been collected, see Figure 2.4. The measurement shows a $\chi_{\text{M}}T$ value of $0.66 \text{ cm}^3 \text{ mol}^{-1} \text{ K}$ at 270 K, and a decrease of $\chi_{\text{M}}T$ upon decreasing the temperature, approaching zero below 30 K. This indicates considerable antiferromagnetic coupling and an $S_{\text{T}} = 0$ ground state. Analysis of the magnetic data utilizing a dimer model with two coupled $S = 1/2$ spin centers ($\hat{H} = 2J\hat{S}_1\hat{S}_2$ Hamiltonian) revealed a coupling constant of $J = -71 \text{ cm}^{-1}$ ($g = 2.14$), which agrees very well with the J value of **3'**.^[113]

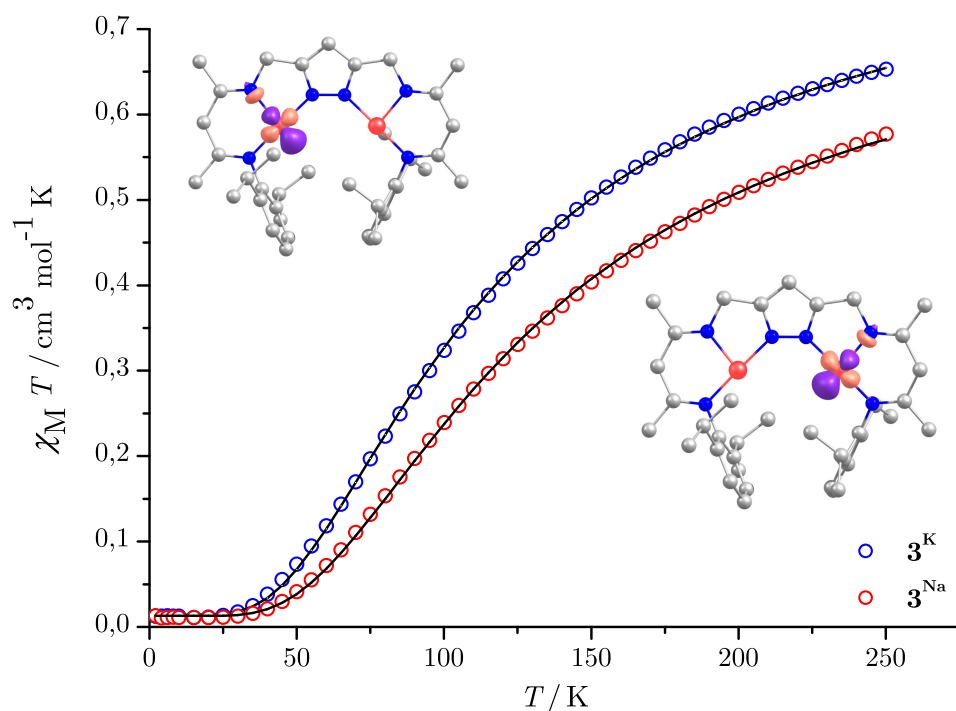


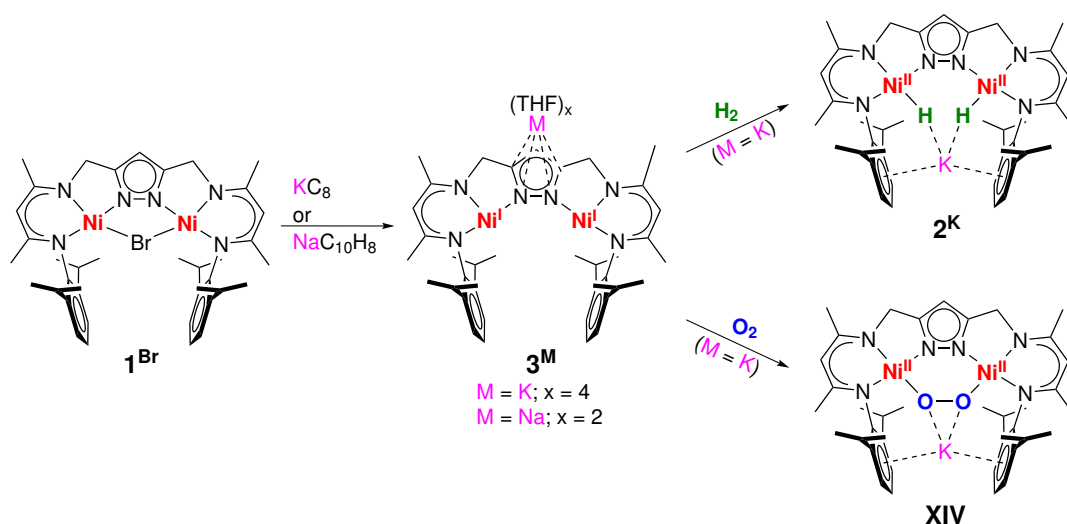
Figure 2.4: $\chi_{\text{M}}T$ vs. T plot for **3^K** and **3^{Na}**; the solid black line represents the calculated curve fit ($\hat{H} = 2J\hat{S}_1\hat{S}_2$ with $J = -71 \text{ cm}^{-1}$ (**3^K**) ($g = 2.14$) and $J = -83 \text{ cm}^{-1}$ (**3^{Na}**) ($g = 2.04$). The insets show the magnetic orbitals derived by DFT calculations, see Section C.1.2 for details.

The antiferromagnetic coupling is slightly stronger in **3^{Na}** with $J = -83 \text{ cm}^{-1}$ ($g = 2.04$), which might be related to the more planar pyrazolato-based dinickel(I) core. The respective torsion angle \sphericalangle are $(\text{Ni}(1)\text{-N}(1)\text{-N}(2)\text{-Ni}(2)) = 4.98^\circ$ for **3^{Na}** versus 18.28° for **3^K**. It is important to notice that the $\text{M-N}_{\text{pz}}\text{-N}_{\text{pz}}\text{-M}$ torsion has previously been shown to substantially affect the magnetic coupling in pyrazolato-bridged bimetallic complexes of $S = 1/2$ metal ions.^[124]

In conclusion, the SQUID results are in agreement with the paramagnetic in solution of the complexes and are in good correlation with the previously described complex **3'**, underlining that in both cases, a dinickel(I) complex has formed. These results were compared with a single-point calculation based on the atomic coordinates derived from the molecular structure of **3^K**, validating an antiferromagnetically coupled ground state of $J \approx -100 \text{ cm}^{-1}$. Corresponding to a LÖWDIN spin population

analysis, 87% of the spin density is centered on the nickel ions, while the magnetic orbitals, derived from unrestricted corresponding orbitals, have mainly (70%) nickel-*d* character, see C.1.1 for details. The small overlap of 0.05 of the associated orbitals is in line with the weak antiferromagnetic coupling of 3^{K} and 3^{Na} .^[125]

The magnetic orbitals of the respective metalloradical subunits can be characterized as the σ -antibonding $d_{x^2-y^2}$ orbitals, compare Figure 1.5. However, the herein presented system utilizes two metal centers, suggesting that metal-metal cooperative $2e^-$ -substrate binding within the cleft should be facile. This was tested by the reaction with H_2 or O_2 , see Scheme 2.2. Indeed, under the exposition of H_2 , 3^{K} forms readily the corresponding dihydrido complex 2^{K} , which was validated by ^1H NMR spectroscopy (Figure B.51). In the same way, 3^{K} reacts with O_2 to **XIV**, which was verified by UV-vis spectroscopy and comparing with the data reported in the literature.^[114] This reaction does not only illustrate the ability of dinickel(I) complexes to activate small molecules but also proves the concept that the hydrido ligands in 2^{K} serve as reducing equivalents.



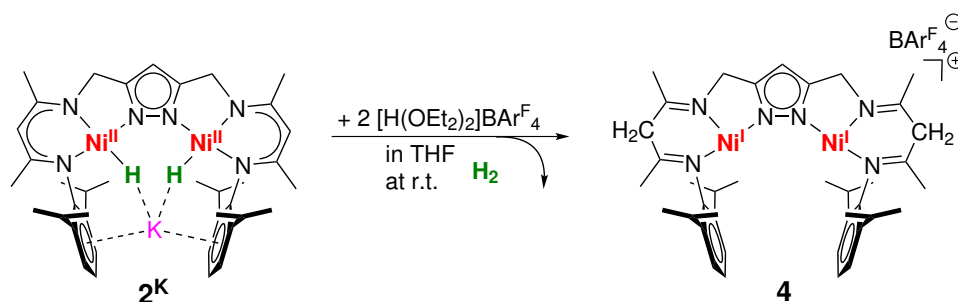
Scheme 2.2: Reduction of the bromido precursor 1^{Br} with a strong reducing agent, depending on the respective counterion, either 3^{K} or 3^{Na} is formed; subsequent oxidative addition of H_2 or O_2 yields 2^{K} or **XIV**, respectively.

2.2 Protonation of the nacnac-Backbone

In subchapter 1.3.2, the principle of metal-ligand cooperation (MLC) has been introduced and briefly described. Even though several examples are known to the literature dealing with this concept, only a few cases have been reported manipulating the properties of nacnac ligands, see Scheme 1.4. Since the γ -C is prone to nucleophilic attack, the herein used ligand scaffold **L** offers the opportunity to investigate the changing electronic properties of the β -diketiminato side arms towards protonation. Therefore, the dihydrido complex 2^{K} and the dinickel(I) complex 3^{K} were treated with different acids in varying ratios.

2.2.1 Induced Release of Hydrogen

The protonation of the γ -C breaks the aromaticity of the β -diketiminato ligand, accompanied by the formation of β -diimine subunits. This ligand transformation reduces the donor ability of the former nacnac sidearms, which consequently weakens the Ni^{II}-ligand interaction.^[86] On the other hand, it can be assumed that the now neutral ligand is more suited to stabilize a Ni^I ion. As explained before, the oxidation state change from Ni^{II} to Ni^I can be observed upon dehydrogenation of the hydrido ligands from complex **2^K**, see Scheme 2.1. Therefore, it was investigated if the protonation of the backbone can trigger the release of H₂. In this context, it is important to note that **2^K** has been treated with the acid 2,6-lutidinium triflate ([HLut]⁺OTf⁻) before, which yields, under a nitrogen atmosphere, in the activation of N₂. To circumvent this reaction, a different acid had to be found. A suitable alternative was found in [H(OEt₂)₂BAR₄^F] (BAR₄^F = tetrakis[3,5-bis(trifluoromethyl)phenyl]borate) since the weakly coordinating counter ion avoids unindented interactions with the nickel centers and facilitates crystalization of the reaction product. Upon adding two equivalents of acid to complex **2^K** results in an immediate color change of the solution from orange to ochre-brown, see Scheme 2.3. In addition, the evolution of gas was observed, which implicates the presumed loss of the hydrido ligands, accompanied by the reduction of both nickel centers.



Scheme 2.3: Peripheral γ -C protonation at the nacnac subunits leads to the loss of H₂ and formation of the dinickel(I) **4**.

Although complex **4** is very sensitive towards even traces of water, single crystals, suitable for X-ray diffraction, were obtained by layering the THF reaction solution with hexane at -38 °C. The molecular structure of the cation of **4** is displayed in Figure 2.5. This complex was previously isolated and described by X-ray crystallography by DUAN;^[126] however, this subject was resumed in this thesis due to the lack of reproducibility.

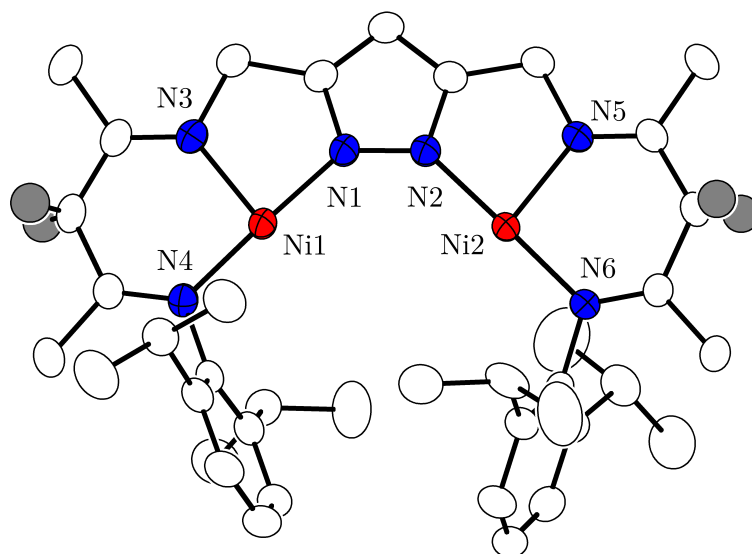


Figure 2.5: Molecular structure of the cation of $[\text{H}_2\text{LNi}_2][\text{BAR}_4^{\text{F}}]$ (**4**) (30% probability thermal ellipsoids). The BAR_4^{F} counterion and all hydrogen atoms except for those at the $\gamma\text{-C}$ of the β -diimine subunits are omitted for clarity.

Table 2.3: Selected bond lengths, distances, and angles of **4**.

Bond length / Å		Distances / Å		Angle / °	
Ni1–N4	1.8881(16)	Ni1⋯Ni2	4.1032(5)	N1–Ni1–N4	177.91(7)
Ni1–N1	1.8807(16)			N1–Ni1–N3	84.73(7)
Ni1–N3	1.9513(16)			N4–Ni1–N3	96.99(7)
Ni2–N6	1.8860(16)			N2–Ni2–N6	178.04(7)
Ni2–N2	1.8785(16)			N2–Ni2–N5	84.62(7)
Ni2–N5	1.9476(15)			N6–Ni2–N5	96.52(7)
N–C [†]	1.285(3)				

[†] Averaged distance between the nitrogen and carbon of the β -diimine subunit

In **4**, the two nickel ions are also found tricoordinate close to an ideal "T"-shaped geometry (N–Ni–N angles of 84.6° , 97.0° , and 177.9° at Ni1 and 84.6° , 96.5° and 178.0° at Ni2), while the Ni ions are separated by a distance of $d(\text{Ni} \cdots \text{Ni}) = 4.1032(5)$ Å. In contrast to the before presented molecular structures of **3^K** and **3^{Na}**, no positively charged counter ion but the anion $\text{BAR}_4^{\text{F}-}$ is found. In addition, the averaged C=N bond of the β -diimine subunits is shortened in comparison with the β -diketiminato sidearms of the beforehand described complexes ($1.285(3)$ Å in **4** vs. $1.330(3)/1.332(5)$ Å in **3^K/3^K**). Due to the high reactivity of **4** and diamagnetic impurities of KBAR_4^{F} , no conclusive SQUID data could be obtained. Nonetheless, it was possible to ascertain antiferromagnetic coupling of the same magnitude as in **3^K** or **3^{Na}**, see Figure B.1.

To substantiate that both nacnac parts are protonated at the $\gamma\text{-C}$ atoms, NMR spectroscopy could not be applied due to the paramagnetic behavior of the compound. Instead, IR spectroscopy was used to identify the newly formed β -diimine units, see Figure 2.6. The characteristic C=N stretch was found at 1670 cm^{-1} in the IR spectrum (Figure 2.6), which is in good agreement with the theoretical calculations, see Figure B.3.

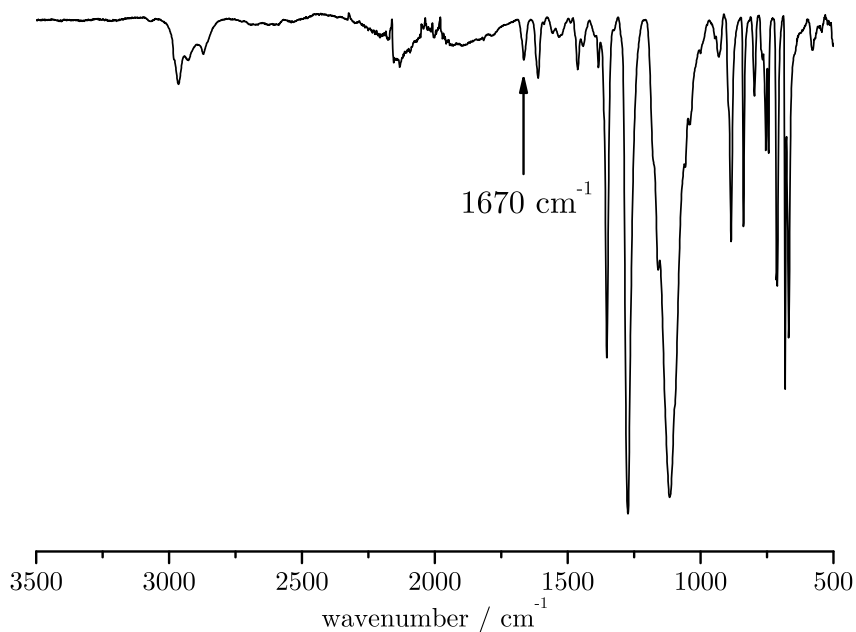


Figure 2.6: IR spectrum of **4**, the C=N stretching vibration is indicated at 1670 cm^{-1} .

The protonation of **2^K** to the twice backbone protonated complex **4** has also been monitored by UV-vis spectroscopy, see Figure 2.7. Subsequent addition of KHMDS (potassium bis(trimethylsilyl)amide) resulted in the formation of **3^K**. Due to the instability of **4**, the titration experiment had to be carried out at $-40\text{ }^{\circ}\text{C}$ and all additions of reagents were done inside a glove box. Since the stepwise addition of $[\text{H}(\text{OEt}_2)_2]\text{BAr}_4^{\text{F}}$ to **2^K** has failed in the past, it was decided to add 2.0 eq. at once. Subsequent addition of 1.0 eq. KHMDS resulted in the formation of **3^K**. In this context, it must be mentioned that the addition of another 1.0 eq. only resulted in a decrease of absorption in the UV-vis spectrum. One explanation for this finding is that the resulted HMDS is capable of deprotonating the backbone of **4**. However, HMDS is a very weak base with a $\text{p}K_{\text{a}}$ value of 25.8,^[127] which makes this theory rather unlikely. Unfortunately, further trials have failed to deprotonate **4**. Even though the spectra are relatively similar, a characteristic shoulder at 380 nm is detectable for complex **4**, which is not present for **2^K** or **3^K** complex. This distinctive feature matches well with the TD-DFT computations, compare Figure B.10 and Figure B.11.

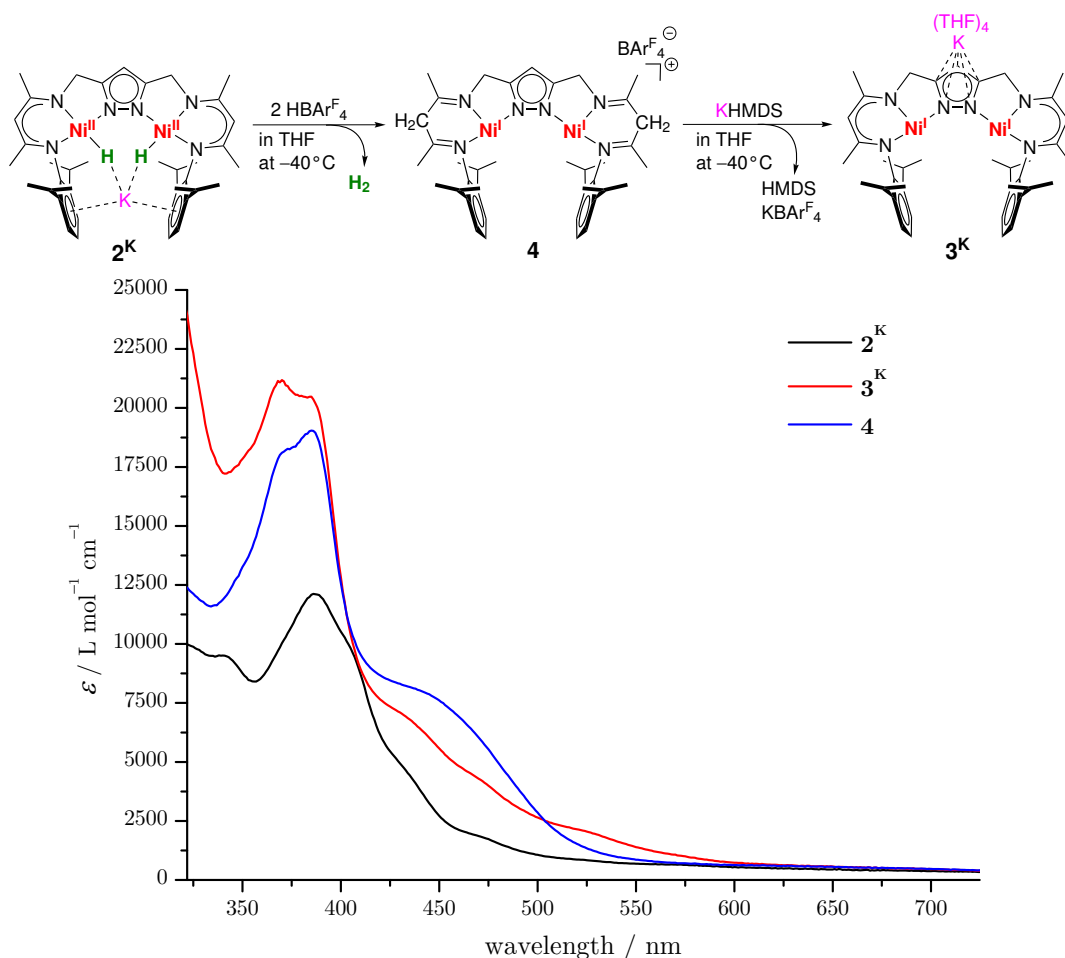


Figure 2.7: UV-vis titration experiment of a 58 μM THF solution of complex 2^{K} at -40°C . First 2^{K} was treated with 2.0 eq. of $[\text{H}(\text{OEt}_2)_2]\text{BAR}_4^{\text{F}}$, which resulted in the formation of **4**. Subsequent addition of 1.0 eq. of KHMDS led to 3^{K} .

2.2.2 Calculated Reaction Mechanism for the Release of H_2

During the complex synthesis of **4**, it was impossible to isolate an intermediate dihydrogen complex; consequently, it can be assumed that the dehydrogenation reaction of 2^{K} is triggered upon the protonation of the β -diketiminato sidearms. Moreover, the release of hydrogen must be even more favored as for complex $2'$ since the dehydrogenation reaction even proceeds at low temperatures and ambient pressure. To verify this assumption, DFT calculations were performed by ANTON RÖMER in cooperation with PROF. MATA, see Section C.1.4 for details. The reaction paths to reductive H_2 release were calculated with and without protonation of the peripheral ligand. As a starting point, the structures of the anion $2'$ and the hypothetical dihydride of **4**, $[\text{H}_2\text{L}(\text{Ni}-\text{H})_2]^+$ (**4'**) were chosen; the calculated reaction pathways are depicted in Figure 2.8.

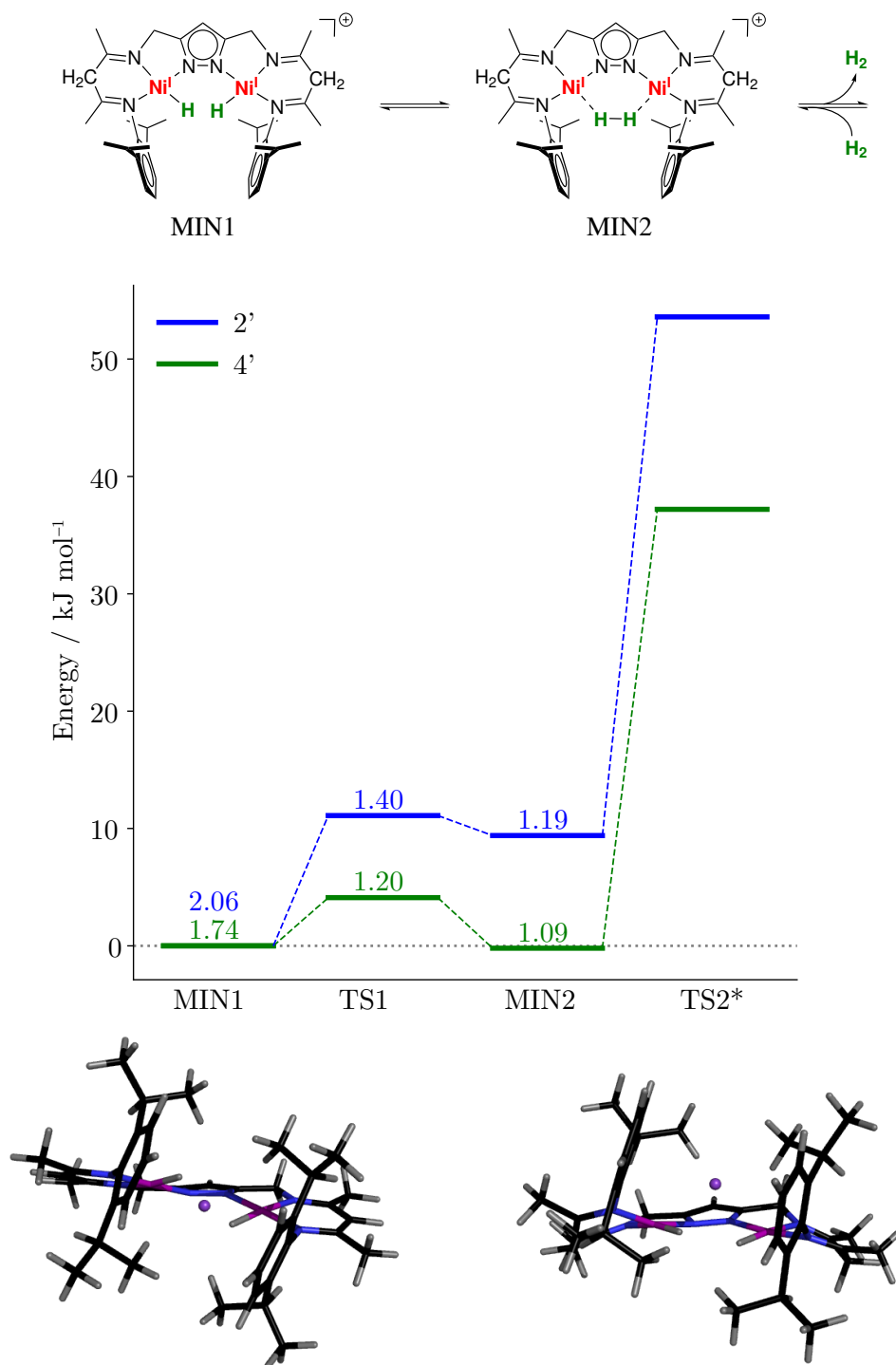


Figure 2.8: **Top:** Theoretical reaction mechanism for the release of dihydrogen from the hypothetical dihydride complex 4'. **Middle:** Calculated reaction pathways for the release of H₂. The distance between the hydrides is indicated by the numbers above the bars, respectively. The second transition state (TS2*) has been approximated by constrained optimization at the equilibrium distance of the hydrogen atoms. **Bottom:** Calculated structure of 2^K (left) and 4' (right).

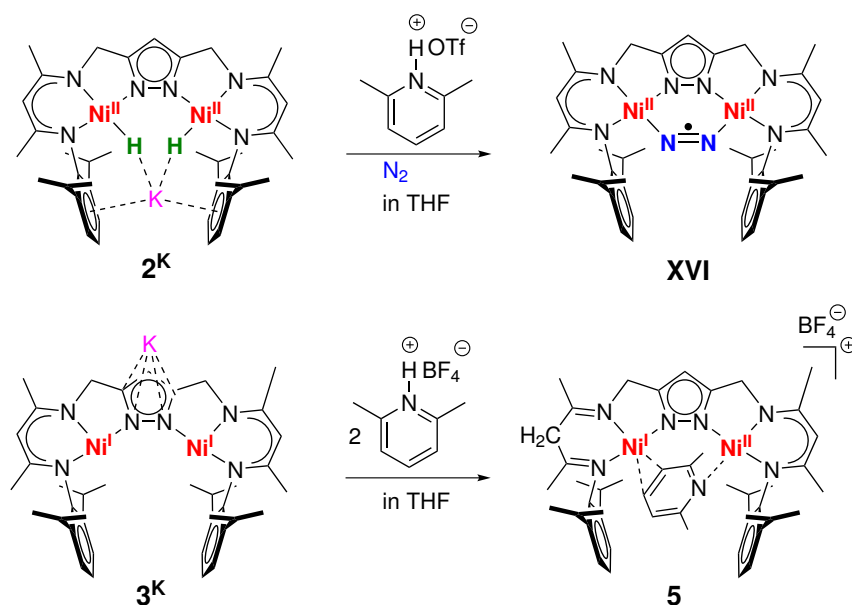
By shortening the distance between the two hydrogen atoms in a predetermined reaction path, the dihydride state (**MIN1**) is transformed into a predissociated station (**MIN2**), separated by a comparatively low barrier (**TS1**). Similar to the previous report on **2^K** and **2'**, the barrier associated with the H₂ release from the bimetallic cleft was derived from the equilibrium dihydrogen H–H distance at the same level of theory (**TS2***). By comparing **2'** with **4'**, it becomes visible that **MIN2** is energetically favored for **4'**, which can be explained by the more profound stabilization of the Ni^I ions by the β-diimine sidearms. Further, the hydrido ligands in the bimetallic cleft of **4^K** are considerably labilized in contrast to **2^K**, resulting in a lower barrier of **TS2*** resulting in a favored release of H₂. To understand this distinction, the different ligand systems of both complexes must be considered. Due to the protonation of the γ-C, the nacnac compartments are transformed into β-diimine subunits accompanied by the loss of conjugation, which leads to increased flexibility. This circumstance allows the sidearms to arrange a configuration where the potassium is no longer closely associated with the H₂, promoting dehydrogenation. Summing up, the peripheral protonation of the ligand not only stabilizes **MIN2** but further significantly facilitates the release of dihydrogen, which is reflected by the reduced **TS2** barrier from 55 to 37 kJ mol⁻¹. At the bottom line of Figure 2.8, both computed minima structures of **2^K** and **4^K** are displayed, respectively, where this difference becomes apparent.

In total, three dinuclear Ni^I complexes have been isolated and structurally characterized. In addition, the metalloradical character could be proved by SQUID measurements unveiling an antiferromagnetic coupling of the respective metal centers. Besides, the non-innocence of the β-diketiminato compartments has been illustrated by protonation of the γ-C, leading to the reductive elimination of H₂. Further, the release of hydrogen was investigated by DFT calculations, which elucidate the significant differences between the β-diketiminato based complex **2^K** and the β-diimine complex **4**.

2.2.3 A Mixed-Valent Dinickel Complex

It has been shown that the protonation of the backbone of the dinickel(II) dihydrido complex facilitates the release of dihydrogen. Moreover, it was found out that the reaction mechanism depends on the choice of acid and how many equivalents were added since complex **4** only forms when **2^K** is treated with two equivalents of [H(OEt₂)₂][BAr₄^F]. Thus, using a sterically less demanding acid, such as [HLut][OTf], results not in protonation of both γ-C but ultimately yields a monoanionic radical species [LNi₂^{II}(N₂⁻)] under a nitrogen atmosphere, see Scheme 2.4 top line. This result is exceptional as the precursor complex **2^K** bears two redox equivalents in the respective metal-hydrido units M–H, which generally lead to double reduced substrate binding. Since the nitrogen is only one time reduced, it can be assumed that only one hydrido group is left after protonation or a mixed-valent dinickel^{I/II} has been formed. All efforts to isolate or analyze the proposed intermediate have been unsuccessful in the past, which can be addressed to its high reactivity. Even carrying out the reaction under an argon atmosphere did not result in an isolable species. However, with the dinickel(I) complex **3^K** in hand, a comparison experiment could be conducted to elucidate the influence of the hydrido groups.

Hence, complex 3^{K} was treated with varying ratios of different acids under an argon atmosphere. As the first attempt, $[\text{H}(\text{OEt}_2)_2][\text{BAR}_4^{\text{F}}]$ was chosen, which did not result in any useful results but yields the hydroxido complex $[\text{LNi}_2(\mu\text{-OH})]$ (1^{OH}) or its one-time protonated analog $[\text{HLNi}_2^{\text{II}}(\mu\text{-OH})][\text{BAR}_4^{\text{F}}]$. The latter complex was identified by X-ray crystallography, see Figure A.4. However, refinement of the molecular structure revealed the co-crystallization of this compound with a chlorido complex $[\text{HLNi}_2^{\text{II}}(\mu\text{-Cl})][\text{BAR}_4^{\text{F}}]$. Details of this side reaction have not been elucidated but can probably be attributed to residues of HCl and H_2O . This result clearly demonstrates that it is crucial to ensure that even the slightest traces of impurities, such as water, must be avoided because of the remarkable reactivity of these Ni^{I} complexes towards water. Consequently, $[\text{HLut}]\text{BF}_4$ was used instead since it can be purified by sublimation, which guarantees the absence of moisture. Consequently, complex 3^{K} was treated with different ratios of acid under argon. However, only the addition of two equivalents results in an isolable species, see Scheme 2.4, bottom line. Even though this complex is very interesting from a coordination chemistry perspective, it is not the intermediate formed in the top line reaction in Scheme 2.4.



Scheme 2.4: Reactions of 2^{K} and 3^{K} with BRØNSTED acids. Upper line: A monoanionic nitrogen complex is formed upon the addition of $[\text{HLut}][\text{OTf}]$ to 2^{K} . Bottom line: Protonation of 3^{K} with $[\text{HLut}][\text{BF}_4]$ yielding complex **5**. Both experiments were conducted under a nitrogen atmosphere.

The dinickel(I) complex 3^{K} was treated with two equivalents of $[\text{HLut}][\text{BF}_4]$ in 2-methyl-THF at $-40\text{ }^\circ\text{C}$. The reaction solution turned dark red immediately and was filtered. Single crystalline material of **5**, suitable for X-ray diffraction, was obtained by layering a 2-methyl-THF reaction mixture with hexane at $-38\text{ }^\circ\text{C}$ within two days in 40% yield. The molecular structure of the cation of **5** is displayed in Figure 2.9, exhibiting two different ligand subunits and a bridging lutidinium ligand.

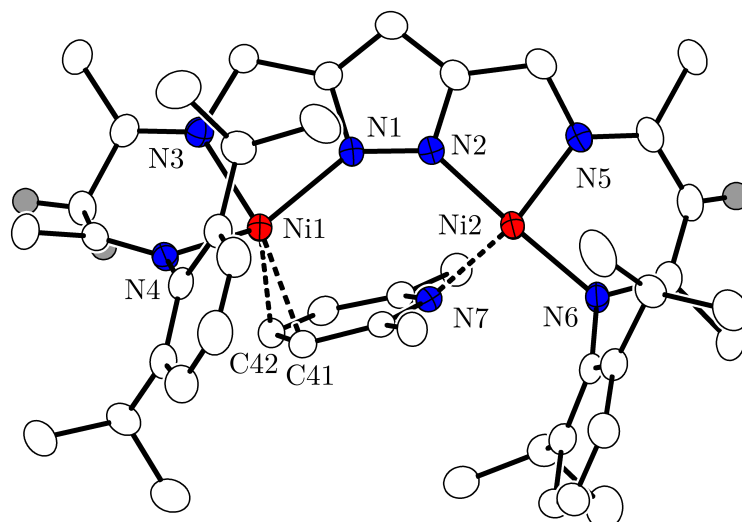


Figure 2.9: Molecular structure of **5** (30% probability thermal ellipsoids). The BF_4 counteranion and hydrogen atoms, except those at the γ -C of the subunits (gray), are omitted for clarity. The lutidinium \cdots Ni contacts are shown as dashed lines.

Table 2.4: Selected bond lengths, distances and angles of the mixed-valent complex **5**.

Bond length / Å	Distances / Å		Angle / °		
Ni1–N4	2.075(2)	Ni1 \cdots Ni2	4.3141(5)	N4–Ni1–N1	144.40(10)
Ni1–N1	2.043(2)			N4–Ni1–N3	88.00(10)
Ni1–N3	2.008(3)			N1–Ni1–N3	81.10(10)
Ni1–C41	2.122(3)			N3–Ni1–C41	162.03(12)
Ni1–C42	2.152(3)			N1–Ni1–C41	109.50(11)
Ni2–N6	1.898(2)			N4–Ni1–C41	90.75(11)
Ni2–N2	1.895(3)			N5–Ni2–N2	84.44(11)
Ni2–N5	1.878(3)			N5–Ni2–N6	93.27(11)
Ni2–N7	1.934(2)			N2–Ni2–N6	176.04(11)
N–C [†]	1.282			N5–Ni2–N7	164.62(11)
N–C*	1.329				

[†]Averaged C–N distance of the β -diimine subunit *Averaged C–N distance of the β -diketiminato subunit

Unlike the twice protonated complex **4**, generating a β -diimine unit did not result in a "T"-shaped nickel center. Moreover, the Ni^{I} ion is not located in the plane spanned by the nitrogen atoms but is additionally coordinated by the nearby carbon atoms C41 and C42, leading to a N1–Ni1–N4 angle of 144.4°. This distorted arrangement can be attributed to the loss of aromaticity of the nacnac sidearm, which increased the flexibility of the coordination environment of Ni1. In contrast, the coordination sphere of Ni2 can be best described as slightly distorted from square planar, with a dihedral angle of 9.9°. The geometry of the unprotonated nacnac unit resembles that of the precursor complex **2^K** and is supported by the rigid β -diketiminato compartment. As a consequence of the high sterical demand of the $\text{Me}_2\text{C}_5\text{H}_3\text{N}$ ligand, the distance of the nickel ions is increased ($d(\text{Ni1} \cdots \text{Ni2}) = 4.3141(5) \text{ \AA}$), and the DIPP substituents are farther apart, as usually observed. This specific coordination environment enables the isolation of the unusual mixed-valent complex **5**. Since Ni1 is better stabilized by the β -diimine, while Ni2 is found in its preferred tetrahedral

coordination geometry. Furthermore, the active site is shielded by the bulky lutidinium ligand.

Another example of a mixed-valent complex **XII** has been presented in Scheme 1.6. Though, there are two striking differences between this compound and the herein presented complex **5**. First of all, complex **5** bears a β -diimine unit, which leads to a more flexible geometry resulting in a more distorted coordination environment for the Ni^I metal center. Additionally, $[\text{HLNi}^{\text{I}}\text{Ni}^{\text{II}}(\mu\text{-Me}_2\text{C}_5\text{H}_3\text{N})][\text{BF}_4]$ (**5**) does not feature a bridging hydrido ligand. Since Ni^I and H⁻ serve as a reducing equivalent, only complex **5** should be capable of carrying out single reducing substrate activation. This has been demonstrated by exposing a THF solution of the complex to a N₂ atmosphere at room temperature. In the IR spectrum, the characteristic N=N stretching vibration arises at 1894 cm⁻¹ (see Figure B.4 and compare Section B.2.2), which is very similar to $[\text{LNi}_2^{\text{II}}(\text{N}_2^-)]$ (**XVI**), compare Section 1.3.7.

Due to the antiferromagnetic coupling of the Ni^I centers, it was not possible to analyze the complexes **3^K**, **3^{Na}**, and **4** by electron paramagnetic resonance (EPR) spectroscopy. However, the situation is different for complex **5** as it only bears one unpaired electron. The resulting EPR spectrum (black line) of the $S = 1/2$ system is displayed in Figure 2.10 together with the simulation (red line).

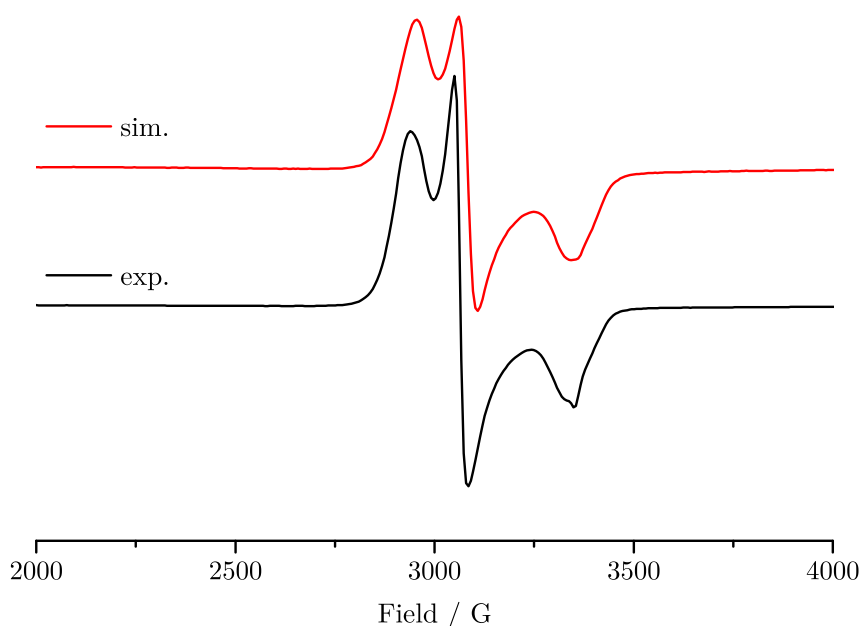


Figure 2.10: Experimental X-band EPR spectrum (9.440 GHz, microwave power 10 mW) (black line) of **5** recorded at 153 K in frozen THF solution. The red line represents the corresponding simulation of the experimental data with $g_{\text{iso}} = 2.121$ ($g_x = 2.031$, $g_y = 2.133$, and $g_z = 2.200$).

The simulation delivers a rhombic signal with an average g value of 2.121 ($g_x = 2.031$, $g_y = 2.133$, and $g_z = 2.200$), while no hyperfine coupling could be resolved. As expected, the large g -anisotropy indicates that the electron density is mainly located on the metal center. The g -values are comparable to the mixed-valent $\text{Ni}^{\text{I}-\mu} - \text{H} - \text{Ni}^{\text{II}}$ complex **XII** in Scheme 1.6, ($g_x = 2.054$, $g_y = 2.159$, and $g_z = 2.454$).^[110] However, the g_z is significantly smaller in **4**. The electronic structure of **5** was additionally examined by SQUID magnetometry. Before the simulation, the experimental data were corrected by a fixed temperature-independent paramagnetism (*TIP*) of $80 \cdot 10^{-6} \text{ cm}^3 \cdot \text{mol}^{-1}$ and modeled according to the formula $\hat{H} = g \cdot \vec{B} \cdot \vec{S}$. The $\chi_{\text{M}}T$ value of $0.31 \text{ cm}^3 \text{ mol}^{-1} \text{ K}$ is constant in almost full temperature range and slightly smaller than the spin-only value expected for an $S = 1/2$ system ($0.375 \text{ cm}^3 \text{ mol}^{-1} \text{ K}$), see Figure 2.11. Analysis of the experimental data reveals the g -value of 1.84 for an $S = 1/2$ spin state of **5**, which is smaller than observed by EPR spectroscopy and may indicate the presence of diamagnetic impurities or partial decomposition of this highly sensitive compound even in the solid-state.

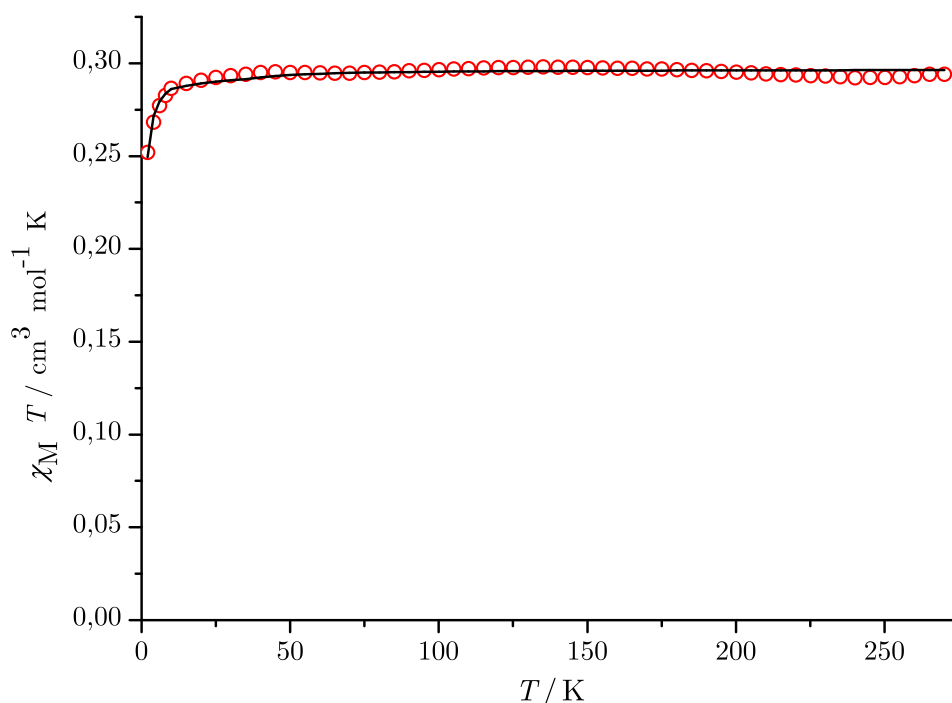


Figure 2.11: $\chi_{\text{M}}T$ vs. T plot for **5**; the solid black line represents the calculated curve fit ($\hat{H} = g \cdot \vec{B} \cdot \vec{S}$). Intermolecular interactions were considered in a mean field approach by using the WEISS temperature Θ .

The mixed-valent nature of **5** could be unambiguously verified by EPR spectroscopy and SQUID magnetometry. Also, the protonation of only one nacnac subunit was indirectly proven by the molecular structure, revealing a shorter C–N distance of 1.282 Å for the β -diimine subunit than for the corresponding β -diketiminato subunit ($d(\text{C} - \text{N}) = 1.329 \text{ \AA}$), see Table 2.4. The hydrogen atoms were placed in positions according to DFT calculations, see Section A.1 for details.

2.3 Conclusion and Outlook

In this chapter, a direct reduction route starting from the bromide-bridged precursor **1^{Br}** to several Ni^I species was established. The resulting dinickel(I) complexes were successfully isolated and structurally characterized. Even though the structural data of **3^K**, **3^{Na}**, **4** and **5** are relatively similar, minor distinctions become visible by comparing the C–N bond lengths of the respective β -diketiminato or β -diimine subunits. For a more convenient overview, the essential metric parameters of all herein discussed complexes are presented in the following table:

Table 2.5: Selected bond lengths, distances, and angles of the herein presented complexes.

Complex	Bond lengths / Å	distances / Å
3^K	N–C* 1.332	Ni1...Ni2 4.1243(7)
3^{Na}	N–C* 1.326	Ni1...Ni2 4.1899(4)
4	N–C [†] 1.285	Ni1...Ni2 4.1032(5)
5	N–C [†] 1.282	Ni1...Ni2 4.3141(5)
	N–C* 1.329	

[†]Averaged C–N distance of the β -diimine subunit

*Averaged C–N distance of the β -diketiminato subunit

Although hydrogen atoms can not be detected unambiguously by X-ray diffraction, the molecular structures of **3^K** and **3^{Na}** indicate the absence of the hydrido ligands since the counterion is not located between the aryl rings but above the pyrazolato unit coordinated by a varying number of THF molecules, see Figures 2.1 and 2.2. An alternative synthetic strategy to obtain mono- and mixed-valent Ni^I complexes was revealed by protonation experiments. Interestingly, the hydrido complex and the nickel complex show different reactivity towards acids. When the dihydrido complex **2^K** complex is treated with [H(OEt₂)₂][BAR₄^F], both nacnac ligands are converted into β -diimine units, resulting in complex **4**. In contrast, the same reaction with **3^K** did not yield an isolable product. On the other hand, the addition of one equivalent of [HLut][OTf] to **2^K** initiates the formation of the nitrogen complex $\text{LNi}_2^{\text{II}}(\text{N}_2^-)$ (**XVI**), whereas the treatment of two equivalents to **3^K** resulted in complex **5** under an Ar atmosphere. By IR spectroscopy, it was possible to observe the transformation of **5** to **XVI**; however, labeling experiments with ¹⁵N₂ would verify this result. By comparing the C–N distances of the β -diketiminato and β -diimine subunits, it was also possible to indirectly identify the backbone's protonation. In particular, this relation was helpful to identify the β -diimine compartment of complex **5**. The slightly shorter C–N bond lengths of the imine functionalities are almost identical to the C–N bonds in twice protonated dinickel(I) complex **4**. For the latter compound, also IR spectroscopy proved the formation of β -diimine subunits, see Figure 2.6.

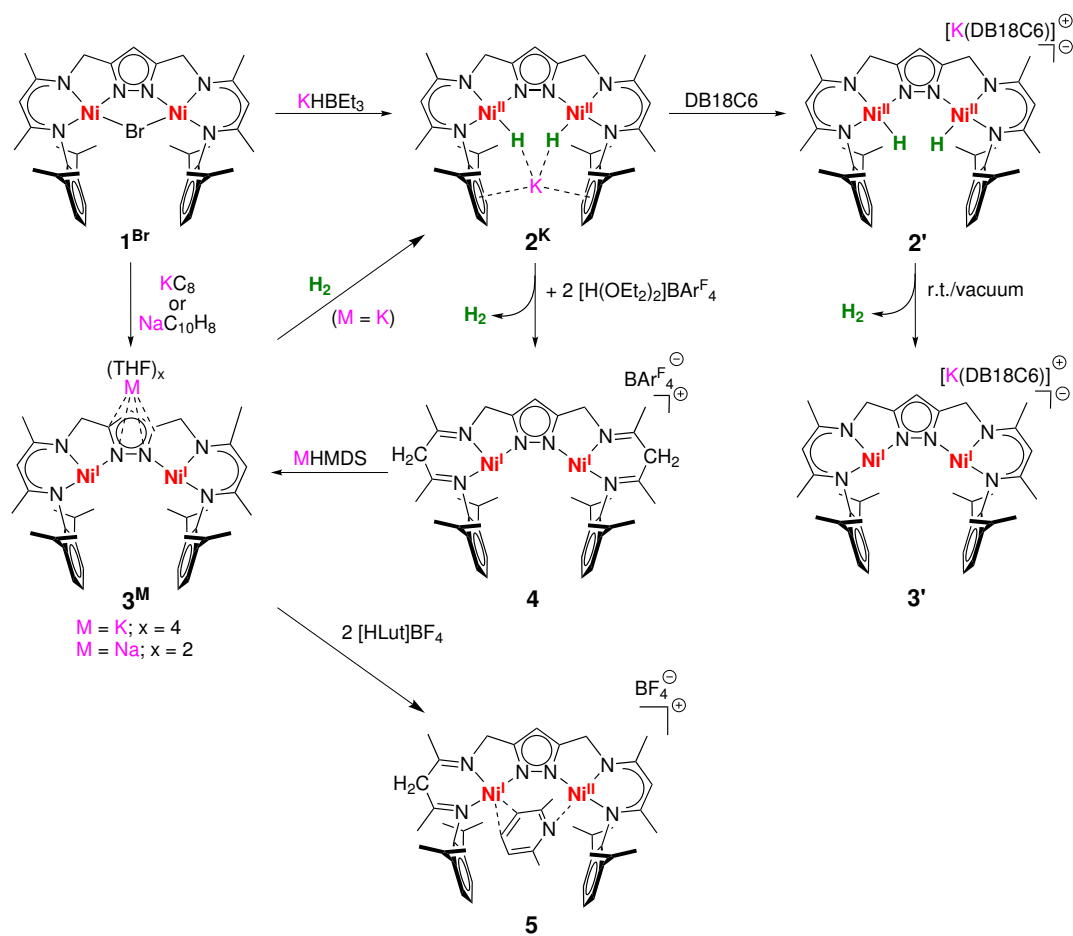
Another clear indication for forming a metalloradical species is found in the ¹H NMR spectrum of **3^K**, which shows a paramagnetic species, see Figure 2.3. Eventually, the oxidation state of the nickel centers was verified by SQUID measurements for all herein presented complexes except for complex **4**. Due to diamagnetic impurities and not further analyzed decomposition products, no undisputed magnetic susceptibility measurement of **4** could be conducted. However, for **3^K** and **3^{Na}**, the SQUID data revealed two S1/2 centers, which are moderately antiferromagnetically coupled ($J = -83 / -71 \text{ cm}^{-1}$), resulting in an $S = 0$ ground state, see Figure 2.4. In contrast, the mixed-valent nickel complex **5** was identified as an $S = 1/2$ system

(Figure 2.11), allowing investigation by EPR spectroscopy, see Figure 2.10.

Further, the mostly unnoted non-innocence of nacnac ligands was investigated, resulting in two different complexes. For complex 2^{K} , it has been demonstrated that the release of hydrogen can be triggered by peripheral ligand protonation, which significantly lowers the barrier for reductive H_2 elimination from the bimetallic cleft and finally yields the dinickel(I) complex, see Section 2.2.2. Formally, this reaction can be interpreted as a proton-coupled electron transfer (PCET) since two protons initiate the transfer of two electrons from the hydrido ligands to the nickel centers. In general, PCET processes are of high interest^[128] and are frequently harnessed by biological systems.^[129,130] Related to this topic are the protonation experiments of 3^{K} resulting in the isolation of complex **5**. Albeit the reaction mechanism stays unclear, this species was fully characterized and represents an interesting example of a mixed-valent dinickel system. For future experiments, complex **4** offers two e^- as a highly reactive dimetallo-diradical and two H^+ stored at the ligand periphery to possibly realize coupled $2e^-/2\text{H}^+$ reactions. The same also applies to complex **5**, which should be probed in terms of $1e^-/1\text{H}^+$ substrate transformations.

In contrast to the masked dinickel(I) complex 2^{K} , the d^9 nickel^I complexes feature two singly occupied $d_{x^2-y^2}$ type orbitals, which are oriented into the bimetallic cleft and easily accessible for incoming substrates. The reactivity of these species was tested by reacting complex 3^{K} with different gases: H_2 and O_2 , see Scheme 2.2. The reaction with H_2 resulted in the formation of the dihydrido complex $\text{K}[\text{LNi}_2(\text{H})_2]$ (2^{K}). Whereas the peroxido complex $\text{K}[\text{LNi}_2(\text{O}_2)]$ (**XIV**) is formed, when 3^{K} reacts with O_2 . While these examples are comparable to the previous reported reactions of 2^{K} , different reactivities of 2^{K} and 3^{K} with acids were noticed.

To conclude, a series of complexes bearing two adjacent "T"-shaped Ni^{I} centers have been isolated and comprehensively characterized by IR and NMR spectroscopy, magnetometry measurement, and X-ray diffraction. Furthermore, the concept of metal-ligand cooperativity (MLC) has been introduced by the protonation of the γ -C of the β -diketiminato subunits. Finally, a mixed-valent complex has been generated, which opens up the possibility of new reactivity, for instance, single reduced substrate binding. All results are summarized by the following overview, including all presented complexes in this chapter:



Scheme 2.5: Overview of reactions towards binuclear mono-, and mixed-valent dinickel(I) metalloradicals and activation of H_2 and N_2 .

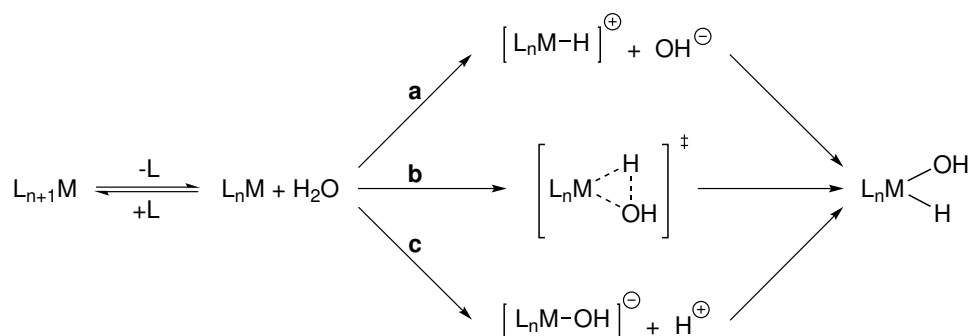
Chapter 3

Metal-Metal Cooperative Oxidative Addition of Water Supported by LEWIS Acid Interaction and Dihydrogen Bonding

3.1 Oxidative Addition of Water

Water is a desired reagent for chemical reactions since it is ubiquitous, cheap, and nontoxic. Therefore, it is not surprising to find several industrial applications utilizing water, such as water-gas shift reaction, hydrocarbonylations of olefins, or the HOECHST-WACKER process.^[131] Further, oxidative addition of water is potentially relevant for solar energy conversion and storage by water photodissociation.^[132] All these processes share the similarity of facing the challenge of cleaving the very stable O–H bond (bond dissociation energy (BDE) = 119 kcal mol⁻¹),^[133] leading to different strategies to overcome this obstacle. That has been done by oxidative addition of water to a transition metal complex, resulting in a splitting of water.^[134] Upon cleaving the O–H-bonds, a metal–hydroxido and a corresponding metal–hydrido bond are formed. From a thermodynamic point of view, it is advantageous for oxidative addition to take place when the newly formed M–O and M–H can energetically compensate the BDE of water. Further, thermodynamic gain from another mode of interaction, e.g., water coordination, must be less beneficial.^[135] A further factor is an entropic contribution which is expected to be unfavorable as an addition decreases the number of free particles.^[136]

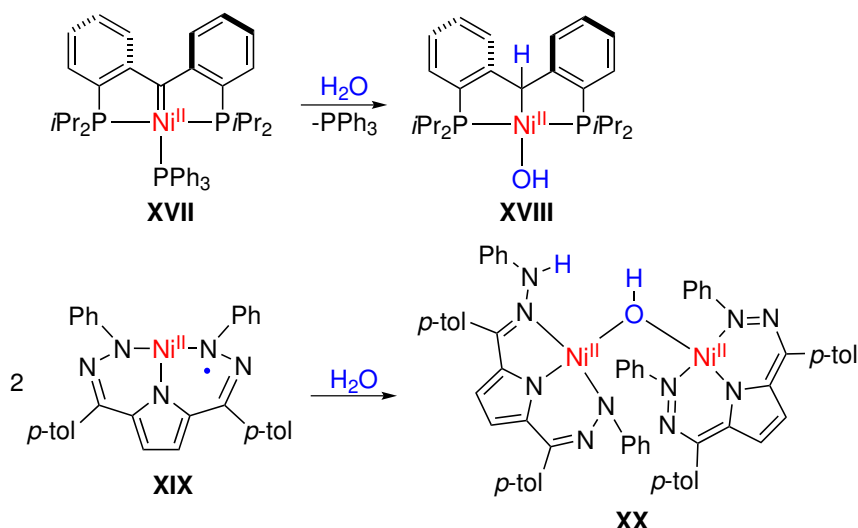
Mechanistic investigations are usually carried out by theoretical calculations since experimental information is often limited. Especially characterization of possible hydrido/hydroxido products, even thermodynamically favorable, can be complicated by possible decomposition reactions. For instance, hydrolysis of M–H with an excess of water yielding into a bis(hydroxido),^[137] dehydration and formation of bridging oxo-ligands, or unintended follow-up reactions of the potentially reactive product.^[138] However, several reasonable proposals suggest how the oxidative addition of water proceeds, see Scheme 3.1



Scheme 3.1: Possible reaction pathways for the oxidative addition of water at a mononuclear complex.^[138]

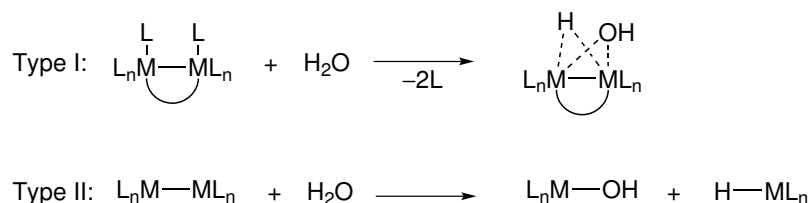
In general, oxidative addition requires both a vacant coordination site at the metal center and the availability of the $\text{Ox}+2/2(\text{Ox}+1)$ oxidation state for a mononuclear/dinuclear system. In order to provide a free binding site, it is necessary in some cases to dissociate a ligand or to cleave a metal-metal bond to initiate dissociation of the respective dimerized complex. The addition of water may proceed either in a concerted way by forming a three-center transition state (**b**) or stepwise. The stepwise addition of water would either lead to protonation of the metal complex (**a**) or the abstraction of hydroxide (**c**).^[138] By thermodynamic considerations, it is possible to exclude the option of direct abstraction of a hydrogen atom from water by late transition metals, since the gained energy for forming the M–H bond cannot compensate for cleaving the O–H bond in water. Although this is different for early transition metals in low oxidation states, especially for an odd electron center, almost every example of oxidative addition of water deals with late transition metal chemistry (*vide infra*). Even though most literature examples present the oxidative addition of water to mononuclear complexes, there are dinuclear complexes as well, yielding to hydrido and hydroxido groups being bound to two different metal centers. There are only a few rare examples of bimetallic ligand-linked complexes capable of oxidative addition of water; more common are dimers bridged by a metal-metal bond which is cleaved upon the addition of water.^[138]

Another approach uses non-innocent ligand scaffolds, which have been employed to split water by storing the H-atom equivalent on the ligand periphery while the respective transition metal coordinates the resulting hydroxido group. One pincer-based Ir complex **IV** exploiting this principle has been presented already in Scheme 1.3, but there are also more recent examples using early transition metals. Both of the following complexes capitalize on metal-ligand cooperation, whereby they contain fundamental disparities. Complex **XIII** in the upper line is a SCHROCK-type carbene which can be assigned a formal charge of +II while compound **XV** in the lower line bears a radical on the nitrogen,^[139,140] see Scheme 3.2. Although the O–H bonds are successfully cleaved, the reaction displayed in the second line cannot be classified as oxidative addition of water. Still, it can be described as homolytic cleavage of water.^[140] This example illustrates that the splitting of water may not only be achieved by oxidative addition, but different reaction mechanisms are conceivable.



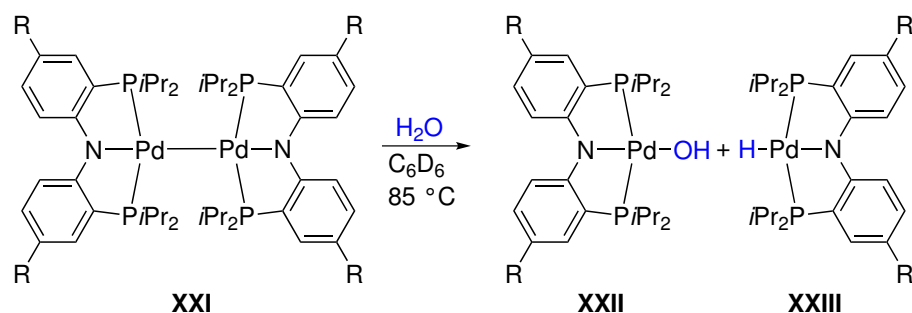
Scheme 3.2: Addition reactions of water by Ni^{II} complexes. Top: PC_{Carbene}P pincer nickel complex **XIII** activating O–H bond.^[139] Bottom: High-spin Ni^{II} complex **XV** splits water upon dimerization **XVI**.^[140]

As indicated above, the oxidative addition of water is not limited to mononuclear complexes but has been shown for binuclear systems as well. Even if the reaction mechanism is uncertain, the known examples can be categorized into two reaction types. Both types have in common that the initial step is generating a free coordination site either by losing a ligand (Type I) or cleaving an M–M bond (Type II). As a consequence, Type I yields into bridging hydroxido and hydrido functionalities^[141] while Type II results in the formation of mononuclear hydrido and hydroxido complexes, see Scheme 3.3.^[138,142]



Scheme 3.3: Possible reaction types for the oxidative addition of water at a dinuclear complex.^[138]

The oxidative addition of water of Type II for binuclear complexes has been reported for a dimeric PNP pincer Pd(I) complex **XVII**. The exact reaction mechanism is unknown, but three feasible options are imaginable. Either, initial attack of water on a metal center or the M–M bond is cleaved, leading to dissociation into monomers. At any rate, the addition of water results in monomeric hydroxido and hydrido Pd(II) complexes, respectively, see Scheme 3.4:



Scheme 3.4: Oxidative addition of water by a dimeric PNP pincer Pd^I complex **XVI**, resulting in monomeric hydroxido (**XXII**) and hydrido complexes (**XXIII**), respectively.^[142]

In summary, oxidative water addition has been shown for a diversity of transition metal complex, whereby the literature is dominated by electron-rich systems coordinating 4d or 5d transition metal as Pt⁰,^[143] Ru⁰,^[144] Pd^I,^[142] Rh^I,^[145] and Ir^I.^[146,147] Even if it is not the focus of this work, it should be noted, for the sake of completeness, that there are also examples of main group element compounds capable of oxidative addition of water.^[148,149] Nevertheless, there are no proven examples for oxidative addition of water with an early transition metal. This circumstance can be attributed to the earlier mentioned preference of alternative reaction pathways, e. g. homolytic cleavage of water or inadvertent side/follow-up reactions are less likely for late transition metals.^[138]

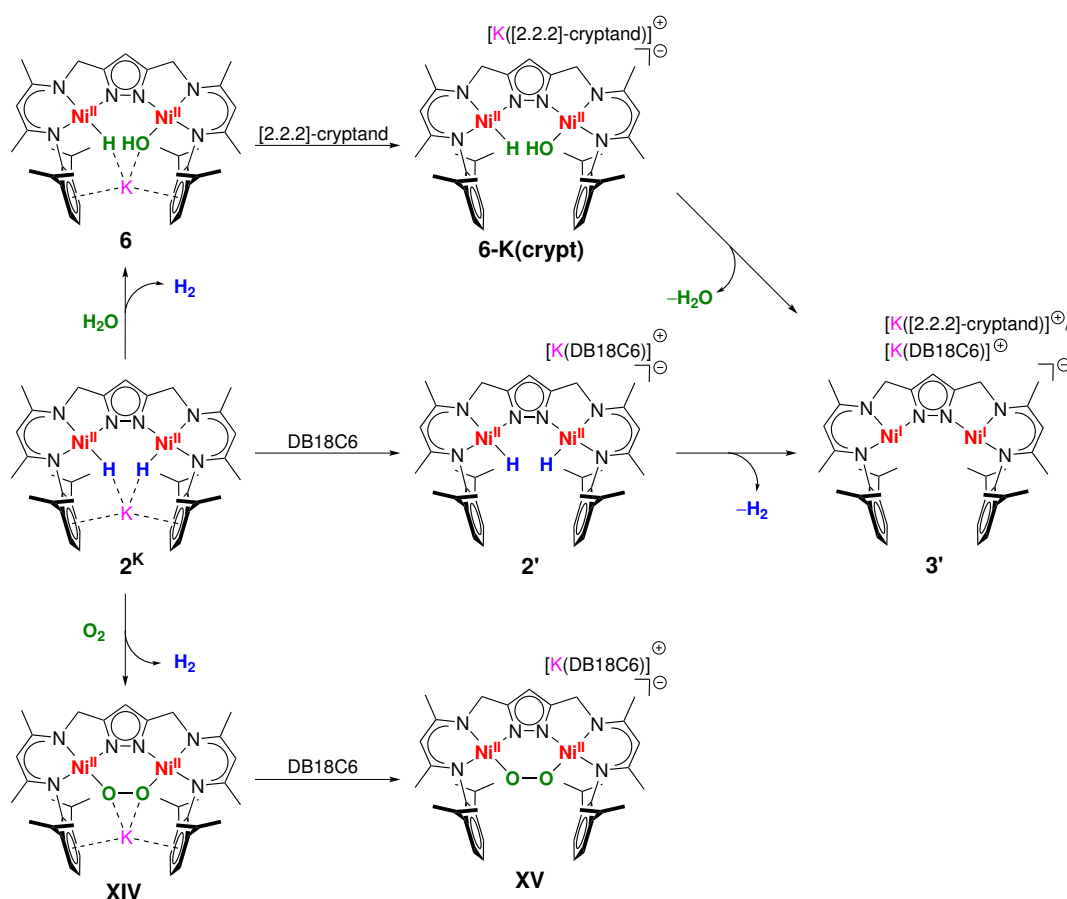
3.2 State of Knowledge and Motivation

The oxidative addition of water is a challenging reaction, which has not been achieved by 3d transition metal based complexes.^[138] Nevertheless, the splitting of water was carried out by different nickel complexes; admittedly, these reactions proceed *via* homolytic activation and are exploiting metal-ligand cooperativity, see Scheme 3.2. An alternative strategy to activate small molecules is based on metal-metal cooperativity (MMC). In this context, the previously described bimetallic nickel complexes **2^K** and **3^K** are worth mentioning as they have proven their potential to activate various small molecules.^[113–115,119,120] For the dinuclear Ni^{II} dihydrido complex (**2^K**), the oxidative addition is accompanied by the reductive release of H₂, which best describes **2^K** as a masked dinickel(I) synthon. Due to its ability to combine high reactivity with the capability to stabilize substrates within the bimetallic pocket, the oxidative addition of water will be investigated. Also, the reactivity of the corresponding dinickel(I) complex **3^K** with water will be tested, offering the possibility to carry out comparative experiments.

All nickel complexes based on the herein used ligand system **L**, including **2^K** and **3^K**, are both highly reactive towards moisture, which eventually results in the undesired [LNi^{II}(μ-OH)] (**1^{OH}**) complex. However, it is evident that this reaction cannot proceed in one step, but an intermediate must be formed beforehand, most likely by splitting water into the respective hydroxido and hydrido units. This conclusion was already made by MANZ,^[118] who has partially characterized the presumed hydrido hydroxido complex **K**[LNi^{II}₂(H)(OH)] (**6**). Even though the target complex could be generated *in situ* by adding one equivalent of water at room temperature, the isolation of this sensitive species was not achieved. Further, large quantities of **1^{OH}**

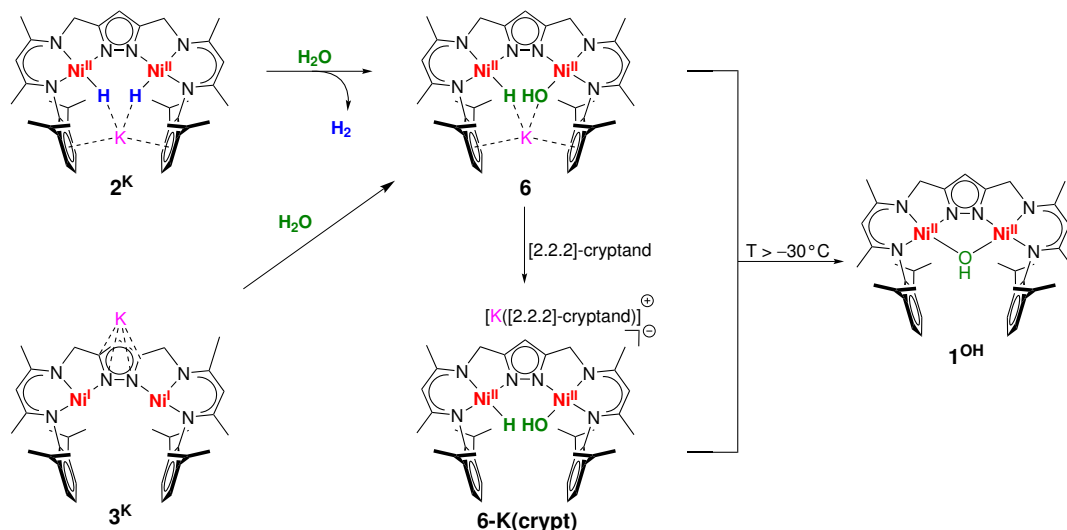
and starting material were detected, which reduces the informative value. Therefore, the reaction procedure must be optimized to avoid the formation of interfering side products.

As illustrated in the preceding chapter, the potassium counterion has a profound stabilizing effect on the hydrido ligands within the pocket of complex 2^{K} . This was illustrated by removing the alkali metal cation from the dihydride cleft by using dibenzo-18-crown-6, which triggers the release of hydrogen, see Scheme 3.5, second line.^[113] For that reason, the postulated species **6** will be treated with [2.2.2]-cryptand to elucidate the influence of the K^+ cation on the H^- and OH^- ligands within the bimetallic pocket. In this context, it is of interest if the substrate binding is reversible when the stabilizing counterion is removed from the $[\text{LNi}_2^{\text{II}}(\text{H})(\text{OH})]^-$ core, see the upper line in Scheme 3.5. If that is the case, the role of the potassium cation would be comparable to what was found for the dihydrido complex 2^{K} . Consequently, it could be assumed that **6** can be converted into a dinickel(I) species upon reductive elimination of H_2O . However, also an alternative scenario is conceivable. For example, the peroxido complex was treated with dibenzo-18-crown-6 as well, which did not lead to reductive O_2 release,^[114] see the third line in Scheme 3.5.



Scheme 3.5: **First line:** Treatment of **6** with [2.2.2]-cryptand and assumed reductive elimination of H_2O . **Second line:** Addition of dibenzo-18-crown-6 to 2^{K} and subsequent reductive release of H_2 . **Third line:** Reaction of with dibenzo-18-crown-6 resulting into **XV**.

Thus, the herein presented work aimed to isolate and characterize the hydrido hydroxido complexes **6** and **6-K(crypt)**. In cooperation with the MATA group, the experimental results will be supported by theoretical calculations. Further, the underlying reaction mechanism and the decomposition pathway will be investigated by experimental and computational methods. An overview of the planned reactions is given in Scheme 3.6, including the decomposition to $[\text{LNi}^{\text{II}}(\mu\text{-OH})]$ (**1^{OH}**).



Scheme 3.6: Reaction overview towards $\text{K}[\text{LNi}_2^{\text{II}}(\text{H})(\text{OH})]$ and subsequent abstraction of the potassium counterion by [2.2.2]-cryptand.

3.2.1 Synthesis and Isolation

In the past, **2^K** to **6** was converted on the NMR scale by adding water at room temperature.^[118] This attempt suffers from some disadvantages. First of all, the target complex is not stable at this temperature, which yields decomposition. Second, at these conditions, a local high concentration of water results in the formation of the hydroxido complex (**1^{OH}**), while still unreacted hydride complex is left over. To circumvent these obstacles, a different approach was chosen. Two flasks were linked *via* a three-way-cock, which was connected to a Schlenk line. One flask was filled with approximately 5 mL of water under an argon atmosphere and freeze-pump-thaw-degassed three times. Afterward, the flask was filled with argon again and the valve was closed, then the solution was slightly heated to ensure that the gas phase is saturated with water. In the other flask, a solution of **2^K** in THF was frozen and set under vacuum; after the gas phase was removed, the valve was closed. The solution was slightly warmed up to -60°C , and the connection to the Schlenk line was closed. Subsequently, the valves of both flasks were opened, which results in the transfer of water *via* the gas phase. This process led to a color change of the reaction solution from orange to yellow, completed within a few minutes. Under vigorous stirring, solvent and unreacted water were removed *in vacuo*. Then, the flask was warmed up to 10°C to ensure that even traces of moisture were eliminated. The same experimental procedure was also carried out with the dinickel(I) complex **3^K** instead of the dihydrido complex **2^K** to identify potential differences in reactivity. However, both reactions resulted in the formation of **6**.

Polycrystalline material of **6** could be obtained by redissolving the crude product in 2-Me-THF and layering the solution with hexane at $-38\text{ }^{\circ}\text{C}$ over two days. Several attempts were made to isolate the target product as single crystalline material, including the use of different solvent combinations and crystallization methods. Albeit any impurities could be removed, only weakly scattering crystals could be obtained, leading to a low-resolution structure:

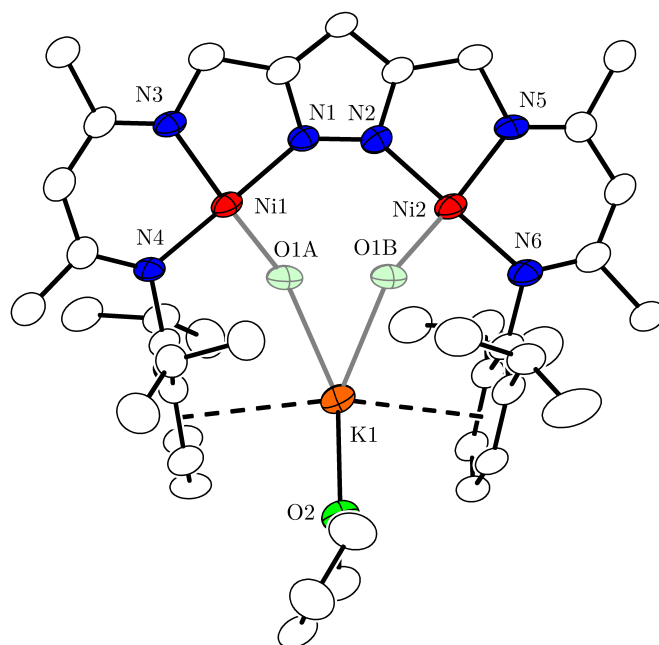


Figure 3.1: Low-resolution molecular structure of **6**. Non-coordinating solvent molecules and hydrogen atoms are omitted for clarity.

The low-resolution structure of **6** supports the assumed formation of the hydrido hydroxido binding motif. In addition, the potassium ion is located between the flanking aryl groups of the DIPP subunits, which indicates the presence of a negatively charged ligand between the bimetallic cleft. Even though the ligands hosted in the bimetallic pocket could not be definitely assigned, one oxygen atom could be detected. However, due to the disorder of the hydroxido and hydrido groups between the two nickel centers, the position of the oxygen atom could not be ascertained.

To investigate the potential interaction of the counterion with the hydrido and hydroxido ligands, the potassium ion was sequestered with a cryptand. Adding [2.2.2]-cryptand to a solution of **6** in 2-Me-THF results in an immediate color change from yellow to red. Vapor diffusion of pentane to the reaction solution at $-38\text{ }^{\circ}\text{C}$ led to the formation of single crystals of **6-K(crypt)** suitable for X-ray diffraction, see Figure 3.2.

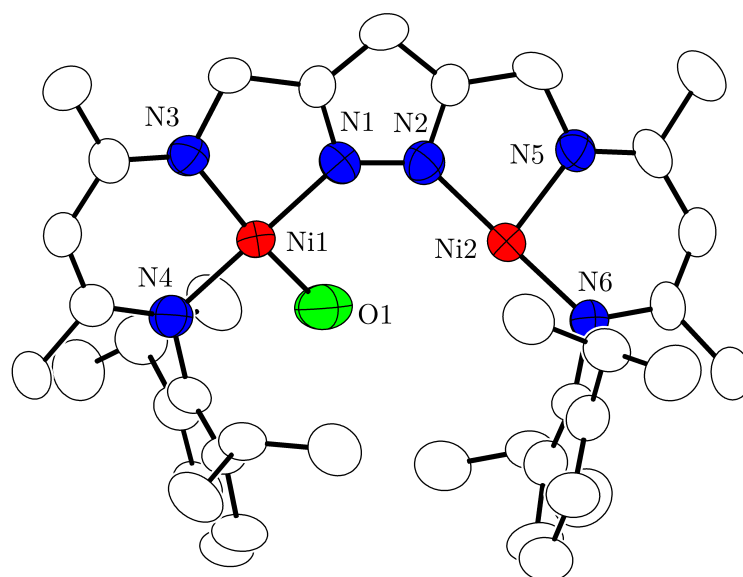


Figure 3.2: Molecular structure (30% probability thermal ellipsoids) of the anionic part of **6-K(crypt)** (first crystallographically independent anion). Solvent molecules and hydrogen atoms are omitted for clarity.

Table 3.1: Selected bond lengths, distances, and angles of **6-K(crypt)**.

Bond length / Å	Distances / Å		Angle / °		
Ni1-N4	1.880(7)	Ni1...Ni2	4.0803(13)	N1-Ni1-N4	177.3(3)
Ni1-N1	1.870(6)			N1-Ni1-N3	83.4(3)
Ni1-N3	1.892(7)			N4-Ni1-N3	95.6(3)
Ni2-N6	1.849(7)			N2-Ni2-N6	178.8(3)
Ni2-N2	1.865(7)			N2-Ni2-N5	83.2(3)
Ni2-N5	1.904(7)			N6-Ni2-N5	96.3(3)
Ni1-O1	1.859(8)			O1-Ni1-N1	92.9(3)
N-C [†]	1.33825(10)			O1-Ni1-N3	168.1(3)
				O1-Ni1-N4	88.5(3)

The molecular structure reveals the expected bimetallic core with the two Ni^{II} ions hosted in the ligand's tridentate {N₃} compartments and bridged by the pyrazolato unit, with a Ni...Ni separation of 4.0803(13) Å. In addition, an oxygen atom is found within the bimetallic cleft coordinated by solely one nickel ion. However, the structure determination's quality was not sufficient to localize hydrogen atom positions within the pocket. Further details are found in Section A.2.

3.3 An Intramolecular Dihydrogen Bond

The hydrogen bond is an intermediate-range force of attraction between electron-deficient hydrogen and a region of high electron density in the same or a separate molecule, and its spectral criteria are well defined.^[150] Hydrogen bonding is omnipresent in nature; multitudinous examples demonstrate the importance of hydrogen bonding in enzymatic catalysis^[151] or its crucial role in the structure and stability of the DNA.^[152] The dihydrogen bond (DHB) represents a particular case involving a transition metal hydride or main-group hydride (M–H) and a protic hydrogen moiety (H–X). Since its discovery, this specific kind of hydrogen bond was a matter of intensive research, especially in organometallic chemistry.^[153] The first evidence for such kind of interaction was found by investigating the reactivity of boron hydrides LBH₃ (L = Py, Et₃P, ...) and Me₃NBH₂X (X = halogen).^[154,155] Another system that is potentially able to form a dihydrogen bond is complex **6**. The positively polarized hydrogen of the hydroxido group and the negatively charged hydride functionality within the pocket should both be at a suited distance for interaction. If there is such attractive bond formation, it should be possible to detect them by different spectroscopically methods such as IR or NMR spectroscopy.

3.3.1 Spectral Criteria and Expected Distances of Dihydrogen Bonds

Numerous examples of dihydrogen bonded systems have been analyzed in the past, making it possible to derive spectral criteria for this form of bonding in solution and the solid state.^[153,156,157] IR spectroscopy is highly suitable for detecting potential interactions between the hydrogen atoms of interest since the minor changes can be resolved. In general, the presence of a dihydrogen bond results in an elongation of the proton-donating HX bond; consequently, the respective stretching vibration appears at a lower wavelength. Mostly, this new band is wider, more intense, and shifted $\Delta\nu_{\text{XH}} = \nu_{\text{XH}}^{\text{bonded}} - \nu_{\text{XH}}^{\text{free}}$, of up to -450 cm^{-1} .^[153] However, in rare cases a shift to higher frequencies is observed.^[158,159] In that case, the HX bond is strengthened, which results in a contraction of the bond.^[160] Therefore it is imperatively required to consider the associated metal hydride signal as well. If the respective M–H stretching band is located at lower frequencies, the existence of a hydrogen bond is demonstrated. Certainly, these observations only indirectly prove the formation of a dihydrogen bond; direct evidence would be detecting a H...H stretching vibration ν_{HH} , which appears below -600 cm^{-1} .^[153] Unfortunately, investigations in the low-frequency range are often challenging due to the interference of many vibrational modes in this region. Especially for large organometallic complexes, no observations of ν_{HH} have been reported; however, simpler DHB complexes were described in the literature.^[161–163]

Another appropriate method for characterizing the interaction between the hydrogen atoms is NMR spectroscopy. Upon forming a dihydrogen bond, the respective ¹H NMR signal of the HX group is shifted to lower field by 2 – 4 ppm.^[156,164,165] In contrast, the hydride resonance is high-field shifted by 0.1 – 0.8 ppm accompanied by a 1.5 – 3.0 fold decrease of its longitudinal relaxation time $T_{1,\text{min}}$.^[166–168] A further parameter that can be derived directly from the ¹H spectrum is the exchange coupling J_{HH} . Both J -coupling and the hydride chemical shift δ_{H} are serving as an indicator for the strength of interaction. For instance, the ruthenium trihydride complex Cp*₃RuH₃(PCy₃) was treated with several proton donors; in line with the donor strength and concentration, J_{HH} and δ_{H} increased progressively.^[169]

An additional benefit offered by ^1H NMR spectroscopy is the opportunity to determine the $\text{H}\cdots\text{H}$ bonding distance by carrying out NMR Inversion-recovery-experiments, which has been done for inter-^[170,171] and intramolecular^[172,173] dihydrogen bonds. However, due to the insufficient numbers of neutron diffraction structures of dihydrogen-bonded transition-metal complexes, $\text{H}\cdots\text{H}$ distances are either provided by NMR spectroscopy or computational investigations. Generally, a distance less than 2.4 \AA , which corresponds to the sum of van der Waals radii of two hydrogen atoms,^[174] can be taken as an indication for a dihydrogen bond; but there are also exceptions. For instance, systems such as $\text{Li}-\text{H}\cdots\text{H}-\text{C}$ ^[175] and $\text{C}-\text{H}\cdots\text{H}-\text{Al}$ ^[176] are exceeding this threshold but still show features typical for dihydrogen bonding. Furthermore, besides the distance, the bonding geometry of the $\text{H}^{\delta-}\cdots\text{H}^{\delta+}-\text{X}$ unit is expected to be almost linear; large divergences can be ascribed to additional interactions or weak hydrogen bonding.^[177-179] In conclusion, five criteria for evaluating the presence of DHB can be considered in the present system:

- Nuclear Overhauser effect (NOE)
- Upfield/Downfield shift of the hydride/hydroxido ^1H NMR signal
- Redshift of the ν_{OH} and $\nu_{\text{Ni}-\text{H}}$ stretching vibrations
- $\text{H}\cdots\text{H}$ distance below 2.4 \AA
- Linear disposition of the $\text{O}-\text{H}\cdots\text{H}$ unit

The last point, as well as the detection of an $\text{H}\cdots\text{H}$ stretching vibration, would serve as a particularly strong indication for the presence of hydrogen bonding. However, these data are often not experimentally ascertainable.

3.3.2 Investigation by Infrared Spectroscopy

To investigate the assumed dihydrogen bond of complex **6**, IR spectroscopy was used. First, **2^K** was treated with H₂O, resulting in the formation of **6**. The same reaction was repeated with D₂O yielding the corresponding deuterated complex **6-DOD**. The absorption bands at 3409 and 1891 cm⁻¹ could be assigned to the O–H and Ni–H units' stretching vibration, see Figure 3.3. The corresponding OD group was identified in the IR difference spectrum (Figure 3.3, inset) at 2531 cm⁻¹ (calculated *via* the harmonic oscillator approximation: 2481 cm⁻¹), while the Ni–D band is assumed to be in the fingerprint region (calc.: 1348 cm⁻¹). These results substantiate the assumption of reductive water splitting into the corresponding hydroxido and hydrido ligands.

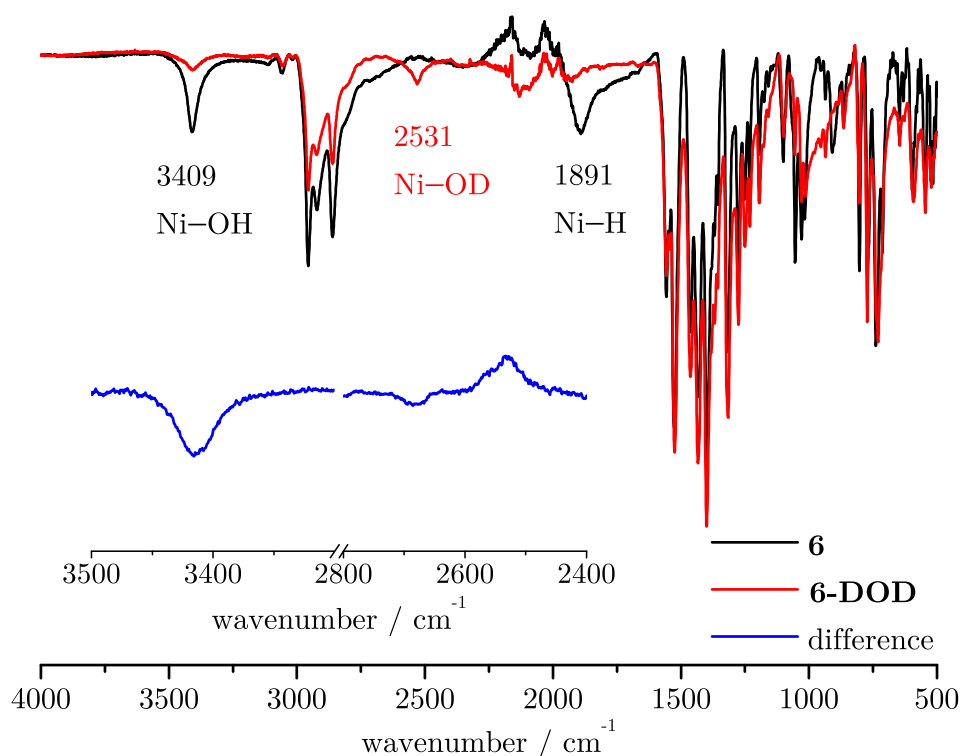


Figure 3.3: ATR-IR spectrum of $\text{K}[\text{LNi}_2^{\text{II}}(\text{H})(\text{OH})]$ (**6**) and $\text{K}[\text{LNi}_2^{\text{I}}](\text{OD})(\text{D})$ **6-DOD**, and difference spectrum of the region of interest (inset).

Additionally, **6-K(crypt)** was investigated by IR spectroscopy, see Figure B.5. This complex offers the advantage that no interaction between the ligands within the pocket and the potassium cation should be present. Since the neutral hydroxido complex $[\text{LNi}_2^{\text{II}}(\mu\text{-OH})]$ (**1^{OH}**) has no counterion, it is reasonable to contrast these two complexes to elucidate the interaction between the two hydrogens within the bimetallic cleft. Therefore, the band positions for the O–H stretch of the respective hydroxido groups of **6-K(crypt)** and the hydroxido complex **1^{OH}** were compared. The formation of a dihydrogen bond results in a band shift of $\Delta\nu_{\text{OH}} = -152 \text{ cm}^{-1}$ (**6-K(crypt)**: $\nu_{\text{O-H}} = 3456 \text{ cm}^{-1}$; **1^{OH}**: $\nu_{\text{O-H}} = 3608 \text{ cm}^{-1}$) caused by an elongated O–H bond. For a better overview, all results are assembled in Table 3.2.

Table 3.2: Compilation of the relevant IR data and comparison with the literature.

Complex	$\nu_{\text{OH}}/\text{cm}^{-1}$	$\nu_{\text{Ni-H}}/\text{cm}^{-1}$	$\Delta\nu_{\text{OH}}/\text{cm}^{-1}$	$\Delta\nu_{\text{Ni-H}}/\text{cm}^{-1}$
1^{OH}	3608			
2^K		1961		
6	3409	1891	-199	-70
6-K(crypt)	3456	1871	-152	-90
Literature ^[153]			< -450	lower

To conclude, the obtained redshifted stretching vibrations of the O–H group indicates the formation of a dihydrogen bond. Accordingly, the respective Ni–H stretches appear at lower frequencies for both complexes (**6** and **6-K(crypt)**). Nevertheless, it remains unclear in which case the hydrogen bond is more pronounced since the stretching vibration of the hydroxido unit is larger for complex **6**, whereas the hydrido group is found at lower wavenumbers for complex **6-K(crypt)**. Also, DFT calculations could not resolve these ambiguities since the dihydrogen bonding stretching frequency could not be identified. Although they matched the experimental spectra reasonably well, the inherent uncertainty is too considerable for a definitive conclusion, see Section B.2.3. However, an alternative approach to determine the strength of the dihydrogen bond is discussed in Section 3.3.5.

3.3.3 Characterization by NMR Spectroscopy

In-depth characterization was carried out by NMR spectroscopy focusing on the hydroxido and hydrido groups within the bimetallic cleft. Following the previously described procedure, **2^K** ($\delta_{\text{Ni-H}} = -24.16$ ppm) was treated with an excess of water to yield complex **6** (compare Section 3.2.1 for details). This approach was successful since no significant amounts of the decomposition product **1^{OH}** ($\delta_{\text{OH}} = -7.26$ ppm) or starting material were detected in the ¹H NMR spectrum, see the bottom line of Figure 3.4. All peaks could be assigned in the ¹H NMR spectrum, see Figure 3.4.

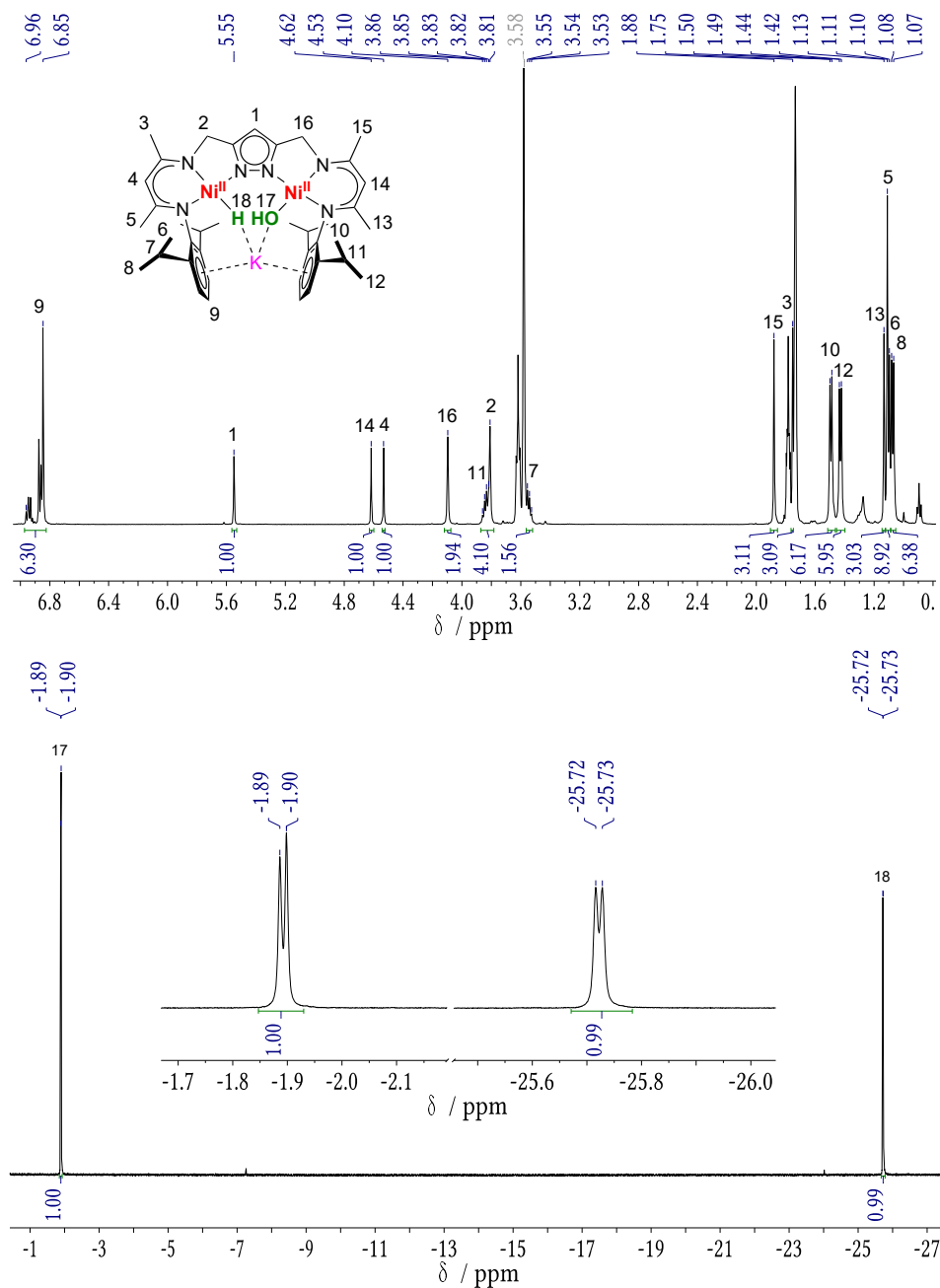


Figure 3.4: ^1H NMR spectrum of **6** at -40°C in $\text{THF-}d_8$ include numbering scheme. **Top:** Assignment of the peaks corresponding to the ligand scaffold (L). **Bottom:** The inset shows the respective signals for the hydroxido and hydrido groups.

The ^1H NMR spectrum of $\text{K}[\text{LNi}_2^{\text{II}}(\text{H})(\text{OH})]$ (**6**) shows two sharp doublet resonances ($J_{\text{HH}} = 6.0$ Hz) at -1.90 and -25.73 ppm, which can be assigned to the O–H and the Ni–H protons, respectively. Comparing hydride resonance of **6** with the corresponding dihydrido complex **2^K** shows a doublet with lower chemical shift ($\Delta\delta_{\text{Ni-H}} = -1.57$ ppm). The observed coupling proves the correlation between the negatively charged hydrido ligand and the positively polarized hydroxido proton. The comparable ^1H NMR spectrum of **6-K(crypt)** reveals two doublets ($\delta_{\text{OH}} = -2.45$ ppm; $\delta_{\text{Ni-H}} = -24.79$ ppm) with a lower coupling constant of $J_{\text{HH}} = 4.5$ Hz as for complex **6**. These results substantiate the hypothesis that the potassium ion is interacting with the ligands within the pocket. Further, it is possible to evaluate the extent of attraction between the hydrogen atoms. As stated above, the strength

of the dihydrogen bonding correlates with the coupling constant J_{HH} , which would mean that the dihydrogen bond is weakened in the absence of the potassium counterion ($\Delta J_{\text{HH}} = 1.5 \text{ Hz}$).

Keeping in mind that the potassium counterion is most probably located between the aryl rings, interacting with negatively charged ligands (Figure 3.1), a comparison between **6-K(crypt)** and the related hydroxido complex (**1^{OH}**) should eliminate interfering side effects. The hydroxido ligand in **6-K(crypt)** is considerably less shielded than the respective hydroxido group in **1^{OH}** ($\Delta\delta_{\text{OH}} = 4.82 \text{ ppm}$). Comparing these findings with the criteria listed above allows evaluating if a dihydrogen bond is present.

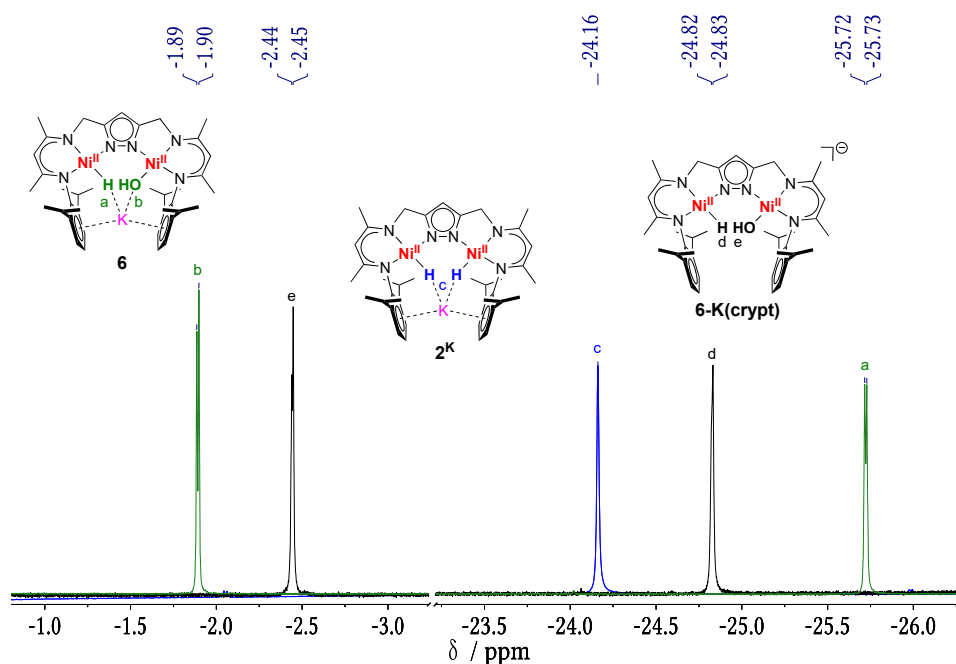


Figure 3.5: Superimposed ^1H NMR spectra of **2^K**, **6** and **6-K(crypt)** at -40°C in $\text{THF-}d_8$. Only the signals of the hydroxido and hydrido ligands are shown and labelled.

Table 3.3: Compilation of the relevant NMR data and comparison with the literature.

Complex	$\delta_{\text{OH}}/\text{ppm}$	$\delta_{\text{H}}/\text{ppm}$	$\Delta\delta_{\text{OH}}/\text{ppm}$	$\Delta\delta_{\text{H}}/\text{ppm}$	J_{HH}/Hz
1^{OH}	-7.27				
2^K		-24.16			
6	-1.90	-25.73	5.37	-1.57	6.0
6-K(crypt)	-2.45	-24.79	4.82	-0.63	4.5
Literature ^[156,164–168]			2 – 4	-(0.1 – 0.8)	2 – 4

In conclusion, the determined upfield shift of the hydride resonance and the accompanying low field shift for the hydroxido ^1H NMR signal (Table 3.3), indicate a dihydrogen bonding (DHB).^[153] However, it is crucial to note that the hydroxido and hydrido groups of complex **6** and the two hydrido groups of **3^K** interact with the

potassium ion, which complicates a simple comparison. Additionally, the hydroxido unit of $[\text{LNi}_2^{\text{II}}(\mu\text{-OH})]$ (1^{OH}) and **6** are exhibiting a divergent binding mode. Despite these circumstances, the signals of interest follow the expected trends. Nevertheless, to figure out whether the two protons of interest are linked by a chemical bond or coupling occurs through space, the usage of 2-D NMR spectroscopy is required.

In agreement with the observed coupling in the ^1H NMR spectrum, ^1H , ^1H COSY spectrum shows the coupling between the two doublets mentioned above. However, the displayed extract of the ^1H , ^1H -NOESY spectrum of **6** (Figure 3.6 (left)) indicates a cross-peak correlation between the hydrido and hydroxido signals providing a through-space correlation and serve as evidence for the presence of dihydrogen bonding.^[180] Chemical exchange peaks must have the same sign as the diagonal peaks; in contrast, opposite signs are predicted for NOE peaks for small molecules.^[181] As expected for the higher molecular mass of **6-K(crypt)**, the cross-peaks share the same sign as the respective diagonal peaks.

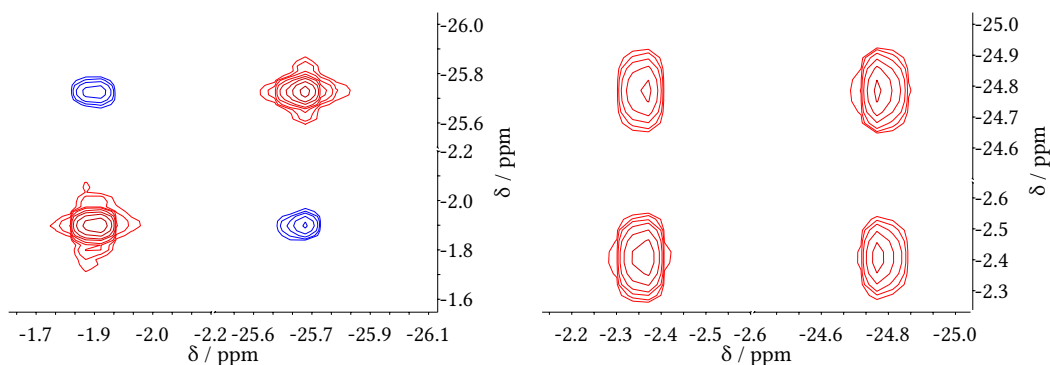


Figure 3.6: ^1H , ^1H NOESY spectra of **6** (left) and **6-K(crypt)** (right). Only the regions of interest are displayed.

3.3.4 OH \cdots H Bonding Distance Determinations

As stated above, the distance between the hydrogen atoms serves as a criterion for hydrogen bonding and gives an indication of its strength. Thus, the intermolecular OH \cdots H distance ($r(\text{H}\cdots\text{H})$) was determined by NMR inversion-recovery (IR) experiments, assuming that the relaxation time T_1 is dominated by proton-proton dipole-dipole interactions, according to the equation:^[182]

$$r(\text{H}\cdots\text{H}) = 5.815 \left(\frac{T_{1,\text{min}}}{\nu} \right)^{\frac{1}{6}} \quad (3.1)$$

As the relaxation time T_1 directly depends on molecular mobility, it is regularly possible to determine minimal relaxation times $T_{1,\text{min}}$ for relatively bulky molecular systems even in non-highly viscous solvents. Furthermore, while the molecular motion correlation time τ_0 depends on the temperature, the desired minimal relaxation time $T_{1,\text{min}}$ can be defined by variable temperature ^1H T_1 experiments.^[183] Therefore, relaxation times T_1 were determined at varying temperatures, locating $T_{1,\text{min}}$ at -30°C .

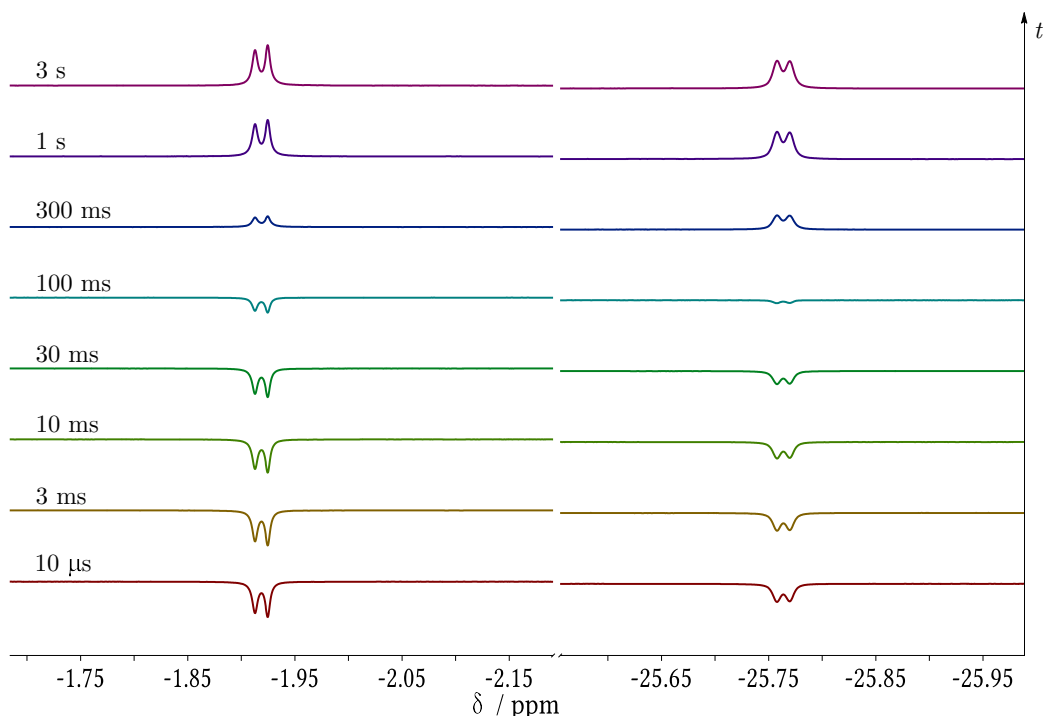
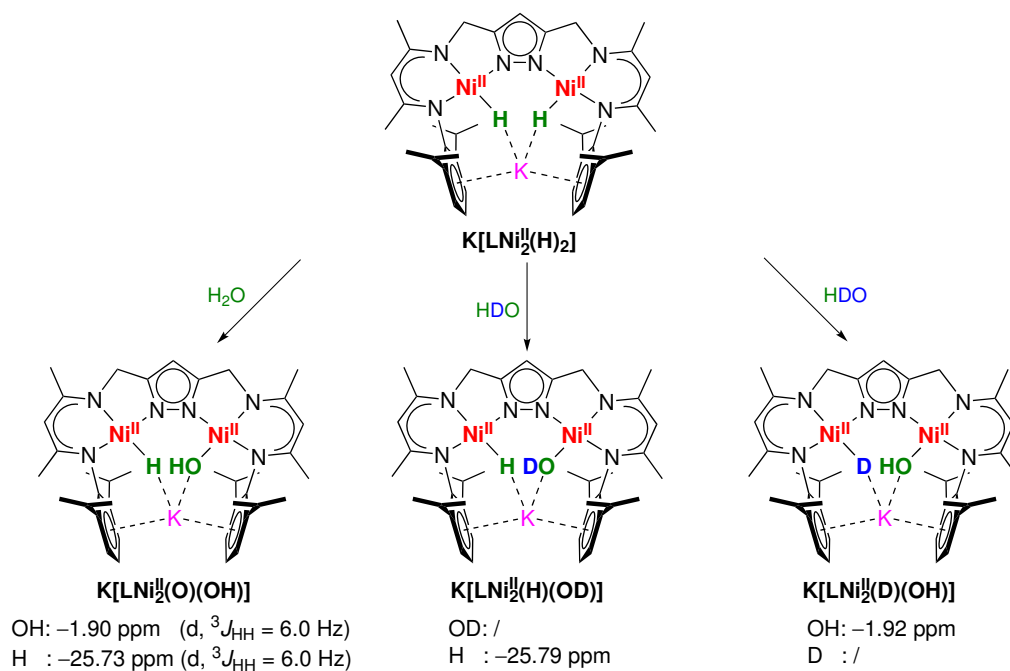


Figure 3.7: NMR inversion-recovery-experiment at $-30\text{ }^{\circ}\text{C}$ in $\text{THF-}d_8$; only the regions around the hydroxido (-1.90 ppm) and hydrido (-25.73 ppm) resonances are shown.

To accurately determine $T_{1,\text{min}}$,^[184] complex **6** was partially deuterated by treating **2^K** with HDO. Therefore the same experimental procedure as previously described was applied. However, this time, a mixture of $\text{H}_2\text{O}/\text{D}_2\text{O}$ in a ratio of 10/90 % was used instead of water. To ensure that most of the H_2O was converted to HDO, the mixture was warmed up and stirred for one day. As a result, three isotopologues are formed, but only the partly deuterated species are of interest, see Scheme 3.7. As a result of the excess of D_2O , mostly the deuterated species $\text{K}[\text{LNi}_2^{\text{II}}(\text{OD})(\text{D})]$ is formed, which did not appear in the ^1H NOE spectrum. Notwithstanding, it was tried to ensure that no unlabelled complex is formed, small signals are visible but still sufficiently displaced to be able to assign all species clearly, see Figure 3.8.



Scheme 3.7: Reaction of $\text{K}[\text{LNi}^{\text{II}}_2(\text{H})_2]$ with a mixture of $\text{H}_2\text{O}/\text{D}_2\text{O}$ in a ratio of 10/90 %, resulting in **6** and its isotopologues. The associated signals in the ^1H NMR spectrum are listed below the respective complex.

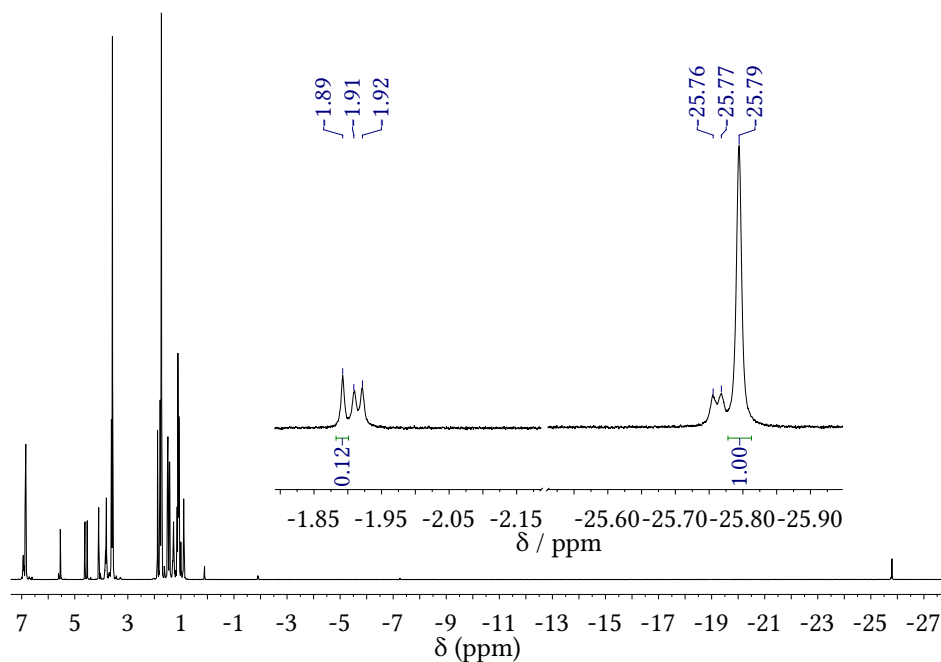


Figure 3.8: ^1H NMR spectrum of the labeling experiment. The inset shows the respective signals for the hydroxido and hydrido groups.

The relaxation time was computed using the following equation, where the factor compensates for the residual dipolar coupling of the deuterium nucleus:^[185]

$$\frac{1}{T_{1,\text{min}}} = \left(\frac{1}{T_1^{\text{HOH}}} - \frac{1}{T_1^{\text{HOD}}} \right) \cdot 0.96 \quad (3.2)$$

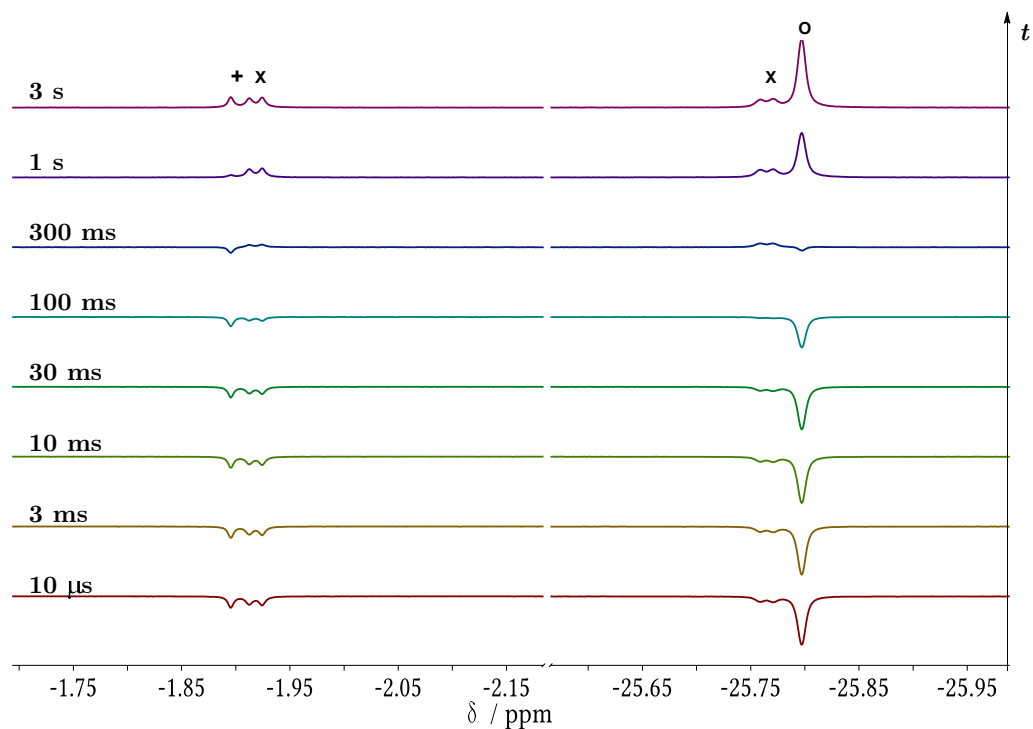


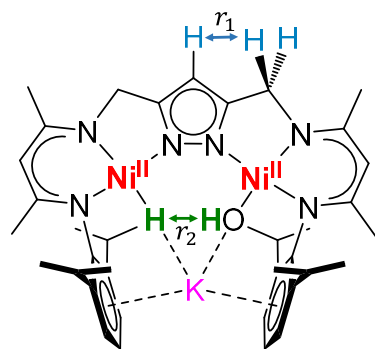
Figure 3.9: NMR Inversion-recovery-experiment at $-30\text{ }^{\circ}\text{C}$ in $\text{THF-}d_8$. The singlets could be assigned to the partly deuterated hydrido hydroxido species **6** (+, o). The small doublets \times are matching with the non-deuterated complex.

Hence $T_{1,\text{min}}$ was determined as 0.44 s. Combining this finding with the given frequency of $\nu = 500.25\text{ MHz}$ according to Equation 3.1, the bonding distance is determined as 1.78 \AA . A detailed overview of all results and theoretical background of the NMR Inversion-Recovery-Experiment is provided in Section 5.2.2.

A different approach to calculate the $\text{OH}\cdots\text{HNi}$ separation is from NOE data using the so-called "Isolated-Spin-Pair-Approximation" (ISPA).^[186] By comparison of the fraction of normalized intensities of a pair of NOE signals I with the associated ratio of their internuclear distances (r). The desired interspace r_1 of the hydroxido and the hydrido protons can be calculated following the equation.^[186,187]

$$\frac{I_1}{I_2} = \frac{r_1^{\frac{1}{6}}}{r_2^{\frac{1}{6}}} \quad (3.3)$$

Since the needed integrals are known from the $^1\text{H}, ^1\text{H}$ -NOESY spectrum, only one distance is required to calculate the unknown $\text{H}\cdots\text{H}$ separation. Thus, a proper reference length r_2 is found between the pyrazolate- H^{δ} proton and the averaged proton positions of the methylene linker unit, see Figure 3.8. This value was either derived by DFT calculations or in the case of **6-K(crypt)** from the molecular structure determined by X-ray diffraction.



Scheme 3.8: Simplified sketch of **6** with indicated H \cdots H separation r_1 (green) and reference distance r_2 (blue) between the pyrazolate–H 4 proton and the averaged proton positions of the methylene linker unit.

With these data in hand, the unknown interatomic H \cdots H distance was derived as 1.63 Å for **6** and 1.68 Å for **6-K(crypt)**. A detailed description of the "Isolated-Spin-Pair-Approximation" (ISPA) is given in Section 5.2.3.

In order to gain a deeper understanding of the experimental results, theoretical calculations were carried out by ANTON RÖMER. Firstly, structures of both complexes **6** and **6-K(crypt)** were optimized by DFT calculations. Particular attention was paid to the H \cdots H distance within the pocket. Therefore, molecular dynamic (MD) simulations were performed, which resulted in greater H \cdots H distances as the values derived by the DFT optimized structures, compare Section C.3.1. In addition, the influence of the solvent on the hydrogen separation within the bimetallic cleft is noticeable. An overview of all distances, including the distances derived by DFT computations, is given in the following table:

Table 3.4: Determined H \cdots H distances of **6** and **6-K(crypt)** by NMR methods and DFT calculations.

methode	DFT opt. struc.	MD	ISPA	NMR IR
complex	H \cdots H distance / Å			
6	1.58	1.93	1.63	1.78
6 + one THF mol.	1.58	1.66		
6-K(crypt)	1.53	1.77	1.68	

By comparing the H \cdots H distances of the optimized structures with each other, almost no differences are observable. However, these results show the same trend as the MD simulations; in both cases the H \cdots H interspace reduces if the potassium ion is removed by [2.2.2]-cryptand. In contrast, the H \cdots H separation derived by the ISPA method, shows the opposite behavior; however, the disparity is marginal. Finally, the H \cdots H distance determined by NMR Inversion-recovery is found in between of the values derived by MD simulations and the ISPA method. To conclude, regardless of the choice of method, all H \cdots H distances are below 2.4 Å, which supports the hypothesis that a dihydrogen bond has formed.

Further computational investigations were carried out to characterize the interaction between the hydroxido and hydrido groups. For instance, the energy of the

hydrogen bond should be approximated, which cannot be directly determined experimentally for the herein presented complexes **6** and **6-K(crypt)**. In addition, the exact reaction mechanism is of interest, with a particular focus on metal-metal cooperativity and the potential mediating role of the potassium ion.

3.3.5 Computational Analysis of the Dihydrogen bond

The calculated and the experimental distances of the O–H···H unit in **6** have been interpreted in the previous section and are listed in Table 3.4. However, the distance is only one important pointer; the other crucial characteristic is the angle of the O–H···HNi fragment. Following the definition of hydrogen bonding, the X–H···Y unit is ideally linear but at least above 110°; further, the closer the bonding angle reaches 180°, the stronger and shorter the hydrogen bond is.^[150] The H···H distance and the corresponding O–H···H angle in **6** can be determined by DFT calculations, however, it is not possible to derive the energy of the dihydrogen bond by this parameters. Therefore, an indirect method was employed to approximate the energy of the hydrogen bond. This was done by comparing two different configurations of **6**. The first one is the DFT optimized structure of **6**, serving as a reference point. The second configuration must include an O–H···H angle where no interactions between the hydrogen atoms of interest are expectable. Provided that all other interactions remain unchanged, the DFT calculated energy difference between these two configurations corresponds to the energy of the hydrogen bond.

First, the optimized structure of **6** (Section C.2.1) was taken as a reference point. The energetic profile of this rotation in steps of 30° is displayed in Figure 3.10. Upon reaching an angle of 180°, the orbital interaction is identical to 0°. Therefore the relative energy value at this point was assumed to indicate the energy of the dihydrogen bond. The ground state is placed at 0°; however, it should be noted that the torsion angle H–O–Ni–N is strictly speaking 177°. The energy profile is antisymmetric due to the initial angle of the O–H···H unit at the starting point of the simulation. Due to the angle of 132° of the O–H···H fragment, the hydrogen of the hydroxido group approaches the hydrido ligand by turning the torsion angle H–O–Ni–N counterclockwise, see Figure 3.11. Furthermore, other factors need to be considered, such as the repulsion energy between the DIPP groups or the influence of the potassium ion.

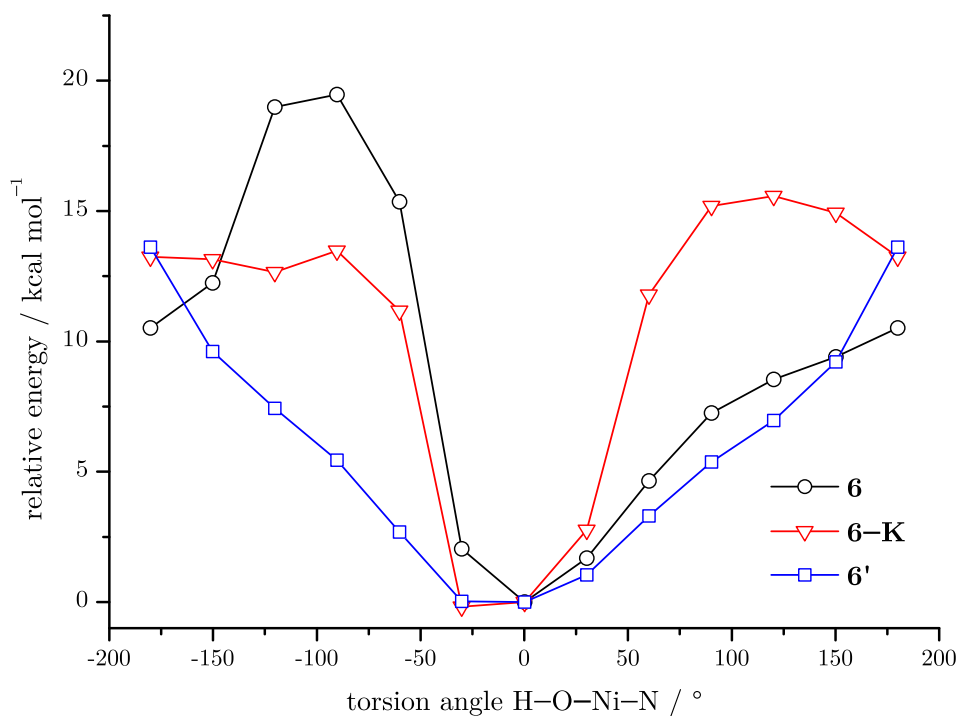


Figure 3.10: Relative energy change depending on the rotation along the Ni–O bond of complex **6** (black line). Modified versions of **6**, where either the potassium ion was removed (**6–K**, redline), or both DIPP groups were replaced by hydrogen atoms (**6'**, blue line) have been simulated to evaluate potential interactions on the rotation.

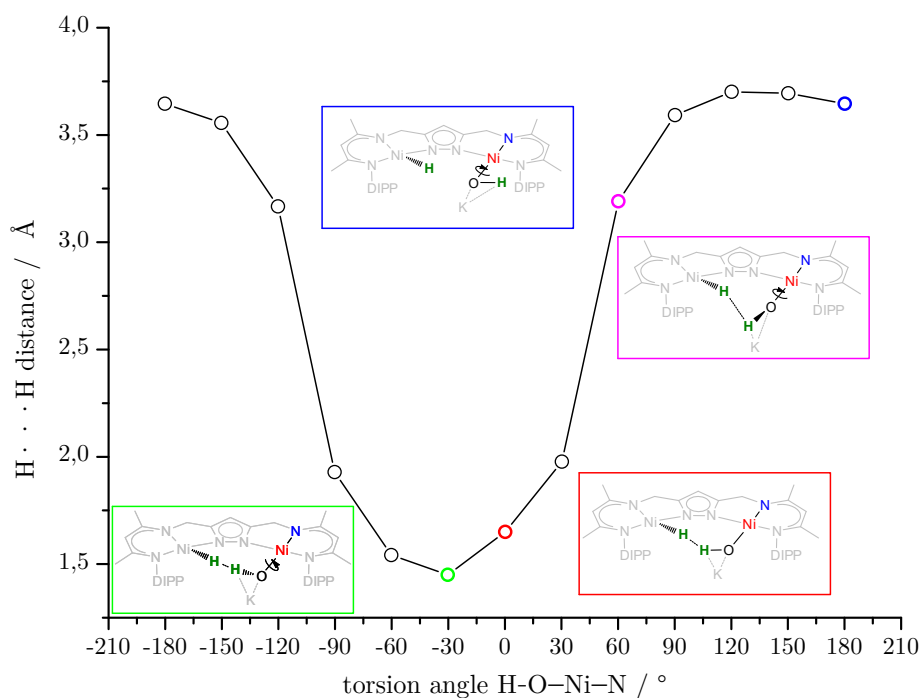


Figure 3.11: Relative H...H distances between the hydroxido and the hydrido groups depending on the rotation along the Ni–O bond of complex **6** (black line). Simplified sketches of the structure at selected H–O–Ni–N torsion angles are provided. The shortest H...H is approximated at -30° (green box).

While turning the O–Ni bond counterclockwise, a $19.0 \text{ kcal mol}^{-1}$ high barrier is found at -120° . The angle of interest is reached at -180° with a relative energy of $10.5 \text{ kcal mol}^{-1}$. However, this value corresponds not exclusively to the strength of the dihydrogen bond, but other contributions must be taken into account as well. First, the influence of the potassium cation was approximated by carrying out the same calculation without the alkali metal, leading to structure **6–K** (red line). By doing so, two differences were identified. First, the torsional barrier is lower and was determined as $15.2 \text{ kcal mol}^{-1}$. Second, the energy profile differs only slightly depending on the rotational direction of the torsion angle and delivers a relative energy of $13.2 \text{ kcal mol}^{-1}$ at -180° . The other factor is the sterical effect of the DIPP groups. To ensure that the rotation was unhindered, each of these units was replaced by a hydrogen atom (**6'**), and the calculation was repeated (blue line). The simulated rotation along the Ni–O axis of **6'** delivered comparable results; however, the slope of the curve is flattened, but the barrier height is not significantly changed ($13.6 \text{ kcal mol}^{-1}$ at 180°). However, this calculation has to be interpreted with caution because the position of the potassium ion has to be fixed to hold it in position. Otherwise, it would have profoundly changed its position in the absence of the stabilizing effect of the aryl rings. To conclude, upon reaching a torsion angle of 180° , an energy difference around 11 kcal mol^{-1} is determined, which would represent a reasonable value for a dihydrogen bond.^[153,188]

3.4 Reaction Mechanism

The possible reaction mechanisms for the oxidative addition of water have been discussed in detail in Section 3.1; further, two examples of nickel complexes capable of splitting water were presented. Though these systems did not split water by an oxidative addition, this reaction type was reported exclusively for late transition metals. However, the herein presented bimetallic nickel precursor complexes **2^K** and **3^K** are incomparable with the systems reported in the literature. The most prominent distinctions are, on the one hand, the two nickel centers in a suited distance to each other, enabling metal-metal cooperativity, and on the other hand, the potassium ion, which is located in close proximity to the active site. The second feature is particularly essential in this context since the reaction does not proceed if the counterion is removed from the DIPP cleft by DB18C6. This was verified by a control reaction. When complex $[\text{K}(\text{DB18C6})][\text{LNi}_2]$ (**3'**) is exposed to H_2O , not the desired target complex **6** is formed but only **1^{OH}**. Thus, even though the role of the LEWIS acid is ambiguous, it must have an essential impact on the reaction mechanism. The suited metal-metal distance and the presence of a LEWIS acid close to the bimetallic cleft are two factors affording a coordination sphere, which enables the splitting of water into the respective hydroxido and hydrido fragments.

In the literature, a few bimetallic complexes are presented, which are categorized into two different classes. Some similarities are revealed by comparing the reaction of **2^K** with water with the reaction mechanism **Type I** or **Type II**, see Scheme 1.11. Both reactions yield in the splitting of H_2O ; however, either the hydroxido is coordinated by both metal centers (**Type I**) or the bimetallic complex disintegrates into mononuclear subunits (**Type II**). In contrast, complex **6** does not feature a bridging OH-unit within the pocket, but both ligands are solely coordinated to one nickel center. Another disparity is found in the absence of an M–M bond, neither for the dinickel(I) complex **3^K** nor for the hydrido hydroxido complex **6**. In addition, for no

system in the literature dealing with the oxidative addition of water at a transition metal complex has been reported the interaction with a LEWIS acid or the subsequent formation of a dihydrogen bond.

To illuminate the reaction mechanism, DFT calculations were carried out, details are found in Section C.3. As a starting point, the dinickel(I) complex 3^{K} and one water molecule placed nearby the pocket was chosen (**MIN1**). Starting from a bimetallic Ni^{I} complex is a valid assumption since it has been proven that the dihydrido complex 3^{K} serves as a masked Ni^{I} synthon. Moreover, it has been shown experimentally that both complexes 2^{K} and 3^{K} react with H_2O to form **6**, see Section 3.2.1. Additionally, the potassium ion was placed between the aryl rings as a starting point for the calculation. This modification was necessary since otherwise, no transition state was found. A DFT optimized structure of **6** was taken as the endpoint of the reaction pathway (**MIN2**). For a first approximation of the reaction pathway, **MIN1** and **MIN2** were taken as starting and endpoint, respectively, of a nudged elastic band (NEB) calculation. After further optimization steps, the transition state **TS** was located; and the final energy levels of **MIN1** and **MIN2** were determined. The proposed reaction mechanism is displayed in Figure 3.13, including all relevant distances and angles, see Table 3.5.

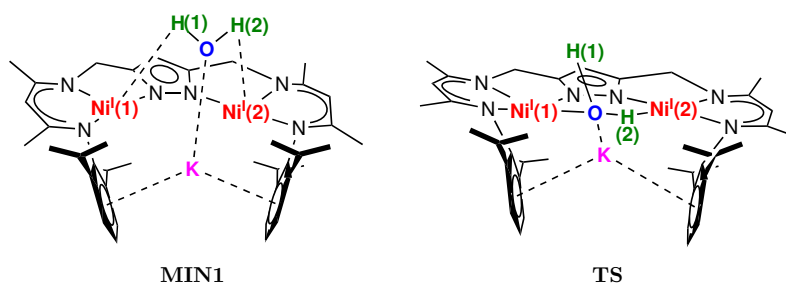


Figure 3.12: Simplified sketch of **MIN1** and **TS**. Relevant interactions are indicated by dashed lines.

Table 3.5: Selected distances and angles of **MIN1**, **MIN2**, and **TS** derived by DFT calculations.

	MIN1	TS	MIN2		MIN1	TS	MIN2
	Distance / Å				Distance / Å		
H(1)···O	1.00	0.98	0.99	Ni(2)···H(1)	3.47	3.36	2.31
H(2)···O	1.00	1.14	2.40	Ni(2)···H(2)	2.26	1.85	1.46
H(1)···H(2)	1.53	1.64	1.63	K···O	2.69	2.59	2.51
Ni(1)···O	3.14	2.10	1.85	K···H(1)	2.97	3.33	2.69
Ni(1)···H(1)	2.27	2.49	2.30	K···H(2)	2.97	2.72	2.66
Ni(1)···H(2)	3.34	2.70	3.46	K···DIPP*	2.87	2.82	2.94
Ni(1)···Ni(2)	4.24	4.08	4.17				
	Angle / °				Angle / °		
Ar–Ar [†]	40.4	19.7	22.1	O–H(1)–H(2)	39.9	42.0	131.9

[†] Angle between the aryl rings

* Averaged distance between the potassium ion and the aryl centroids

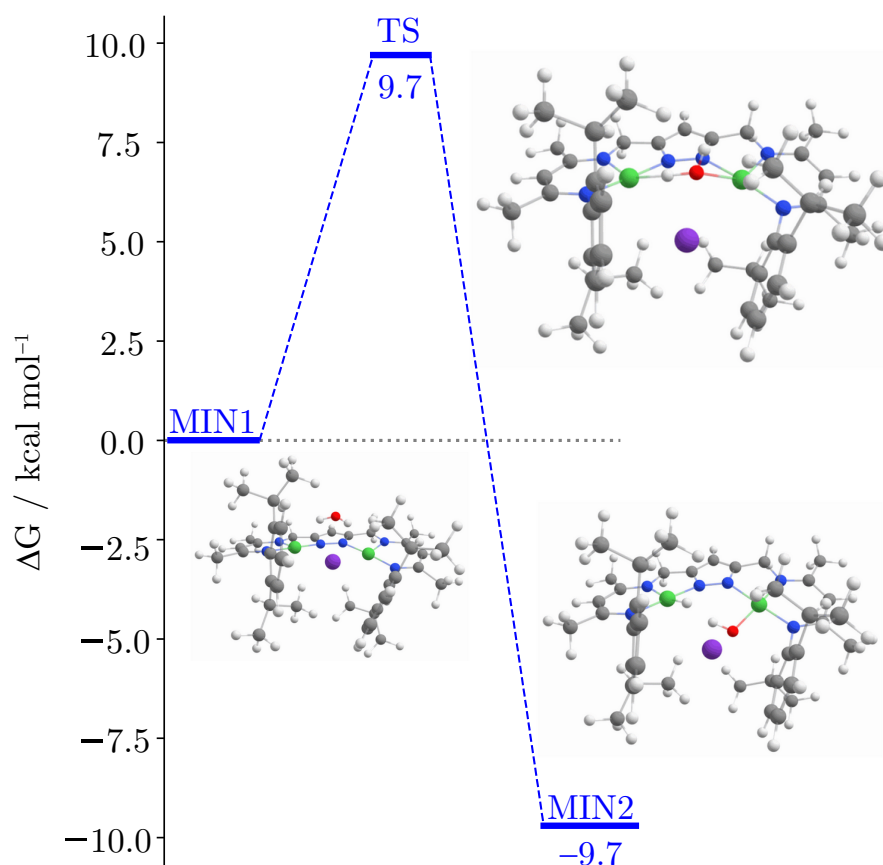


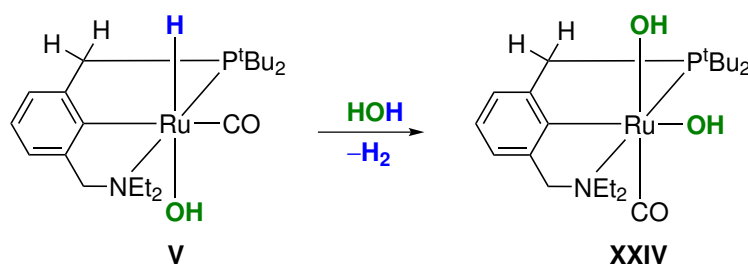
Figure 3.13: Proposed reaction mechanism of the oxidative addition of water towards the hydrido hydroxido complex **6**.

In **MIN1**, each hydrogen atom of the water molecule points towards one Ni^{I} center at approximately the same distance of 2.3 Å, see Figure 3.12 and Table 3.5. This alignment is promoted by the suited $\text{Ni}\cdots\text{Ni}$ distance and the additional interaction of the oxygen atom with the potassium ion. While the water molecule approaches the bimetallic cleft, the oxygen atom approximates Ni(1), whereas the hydrogen atom H(2) reduces its distance to Ni(2). Furthermore, the $\text{K}\cdots\text{O}$ distance decreases, which is followed by a reduced angle of the aryl rings. When the H(2)–O bond is located between the nickel centers, the transition state (**TS**) is reached, which is 9.7 kcal mol^{-1} energetically uphill. Interestingly, the water molecule's bond length and angles did not change significantly between **MIN1** and **TS**. However, this changes along the pathway from the transition state and **MIN2**. The O–H(2) bond breaking is accompanied by an electron density transfer from the Ni^{I} ions to the water molecule. Consequently, a hydroxido and a hydrido ligand have formed accompanied by the formal oxidation of both nickel centers from Ni^{I} to Ni^{II} , leading to the energetically favored minimum (**MIN2**).

To summarize, the oxidative addition of water at the dinickel(I) complex (3^{K}) is facilitated by two circumstances. First, the Ni(1)-Ni(2) distance promotes metal-metal cooperativity, and second, the attractive interaction of the potassium ion with the oxygen of the water molecule. The importance of the alkali metal was also recognized experimentally. In agreement with the experimental observations, the reaction does not proceed if the counterion is separated from the complex anion by cryptand. In contrast, $3'$ decomposes to the hydroxido complex (1^{OH}) in the presence of H_2O at $T > -30^\circ\text{C}$. These findings were also substantiated by single point calculations of **MIN1** and **MIN2** without the potassium ion resulting in significantly higher barriers. Further, no transition state was found in the absence of the cation. It is also worth mentioning that the reaction proceeds exergonic. Even though the stabilizing effect of the formed dihydrogen bond $\text{H}(1)\cdots\text{H}(2)$ could not be evaluated separately within the NEB calculation, the strength of this interaction was determined as roughly 11 kcal mol^{-1} in the previously chapter and contributes to the stability of **MIN2**.

3.5 Decomposition Mechanism

Due to the thermal instability of **6**, the synthesis and the characterization of **6** were performed at -35°C or lower temperatures. At higher temperatures, follow-up reactions were observed. To better understand this decomposition reaction, NMR experiments were carried out. Furthermore, the stabilizing influence of the potassium ion was of interest; thus, comparison experiments using **6** and **6-K(crypt)** were conducted. A few decomposition pathways are discussed in the literature, e.g., hydrolysis of the hydrido ligand $\text{M}-\text{H}$ with excess water accompanied by the loss of H_2 are conceivable.^[138] In this context, an example given by MILSTEIN *et al.* is worth mentioning.^[91] The previously described hydrido hydroxido complex **V** in Scheme 1.3, reacts with an excess of water to the corresponding dihydroxido complex under the release of H_2 :



Scheme 3.9: The hydrido hydroxido Ru^{II} complex (**V**) reacts with H_2O at 100°C to the corresponding cis dihydroxido complex (**XXIV**) under the release of H_2 .

The hydrido hydroxido complex **6** (\times) is stable under inert conditions and at low temperatures; however, decomposition becomes visible from temperatures above -30°C . In contrast, complexes 2^{K} and 2^{M} do not show any transformation even at room temperature. The decomposition of complex **6** was monitored by ^1H NMR spectroscopy over 72 hours at room temperature in $\text{THF}-d_8$. Based on their characteristic signal in the ^1H NMR spectrum, all but the last species could be clearly assigned. Over the entire period, no formation of H_2 ($\delta\{^1\text{H}\} = 4.55 \text{ ppm}$)^[189] was detected. However, it is likely that H_2O has formed. Substantiating this hypothesis is the evolution of a new broad peak at 2.70 ppm, which is assumed to be water ($\delta\{^1\text{H}\} = 2.46 \text{ ppm}$ in THF).^[189]

The resulting decay products are labeled in Figure 3.14. The most dominant species is the hydroxido complex 1^{OH} (★), which has been frequently observed as a decomposition product and is already present in minor amounts in the initial spectrum. For example, at room temperature, 2^{K} and 2^{M} react with traces of water to form the same decomposition product (1^{OH}). However, during this experiment, it is surprising to monitor the evolution of 1^{OH} since the spectrum was recorded in anhydrous THF- d_8 . This finding supports the theory, that the broad at 2.70 ppm is indeed water, which further reacts with the other complexes. The other detected species is the dihydrido complex 2^{K} in very small amounts after 24 hours. Finally, an unknown compound ((+)) arose with a similar chemical shift as 1^{OH} . After 48 hours, this species became visible and was even more dominant after the third day (72 hours). Notably, no paramagnetic species were observed, which could have indicated the formation of a Ni^{I} species. However, the change of the integrals does not provide any indication for a simple decomposition pathway. Therefore investigations were carried out to elucidate the influence of the potassium and the hydrogen bond and will be discussed in the following.

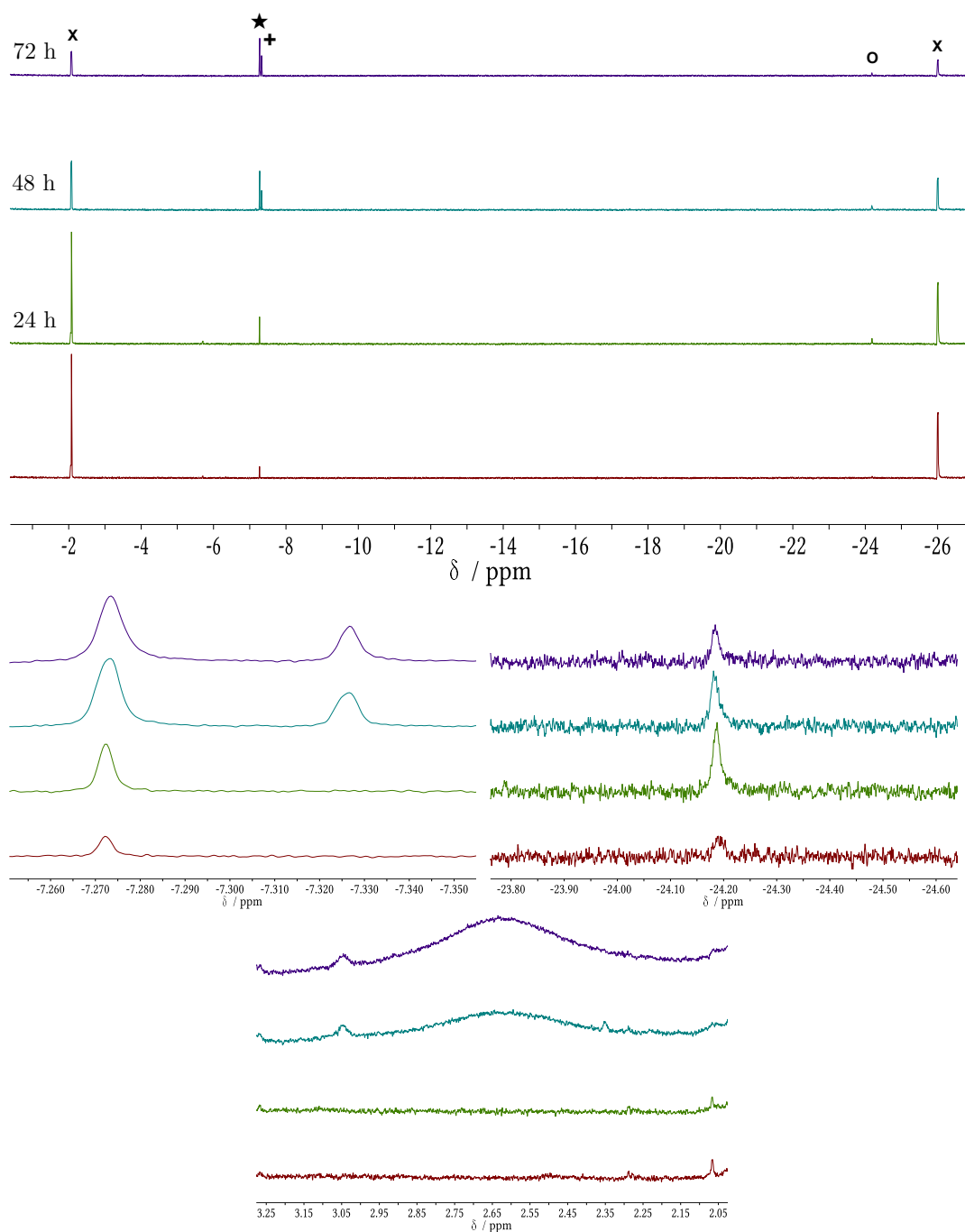


Figure 3.14: ^1H NMR spectra of **6** at room temperature in $\text{THF-}d_8$. The decomposition of the complex was monitored over 72 hours. The first spectrum represents the initial spectrum. The respective species are labeled according to: **6** (\times); 2^{K} (\circ); 1^{OH} (\star); and an unknown species ($+$).

The role of the potassium ion in the reaction mechanism has been discussed in the previous section. Therefore, it can be assumed that it is involved in the decay reaction as well. Thus, the decomposition of complex **6-K(crypt)** was monitored as well by ^1H NMR spectroscopy at room temperature. The same decay products as in the previous experiment were observed, except the unknown species ($+$). Additionally, the reaction was completed much faster. Consequently, the experiment

was repeated at lower temperatures to ensure that possible intermediates were detected. Interestingly, it was found out that **6-K(crypt)** already started to decompose slowly at $-30\text{ }^{\circ}\text{C}$; for that reason, the temperature was held constant at this point. This extraordinary temperature sensitivity was not observed before since **6-K(crypt)** is crystalizing rapidly and is stable in the solid state. While this circumstance facilitated the isolation of this species, it has a detrimental effect on long-time experiments. Throughout the investigation, the compound crystallized in the NMR tube, leading to smaller intensities in the ^1H NMR spectrum, which restricted the observation period to two hours. Nonetheless, the formation of a paramagnetic species was detected at $-30\text{ }^{\circ}\text{C}$, see Figure 3.15.

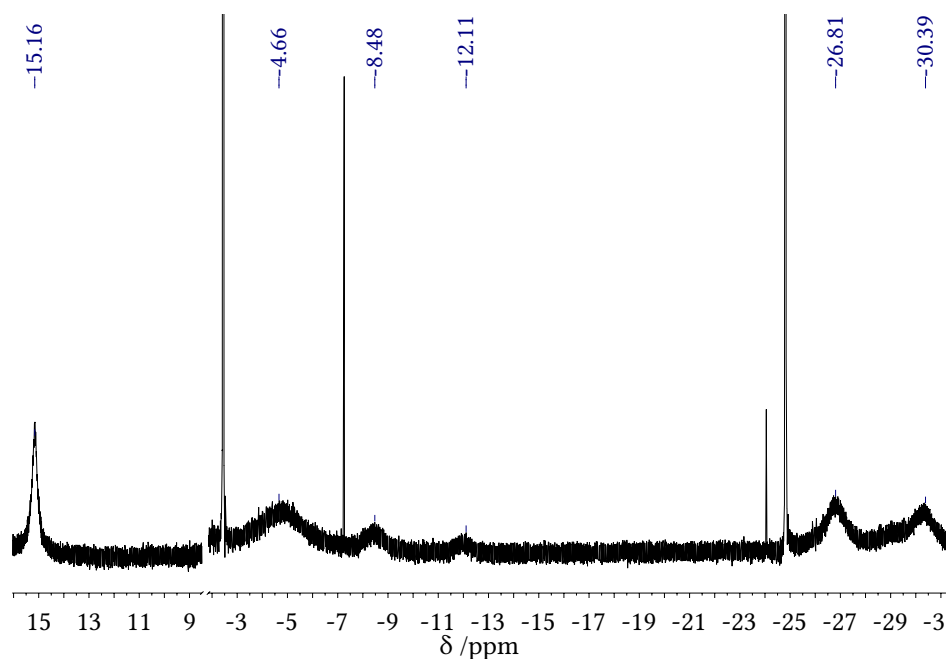
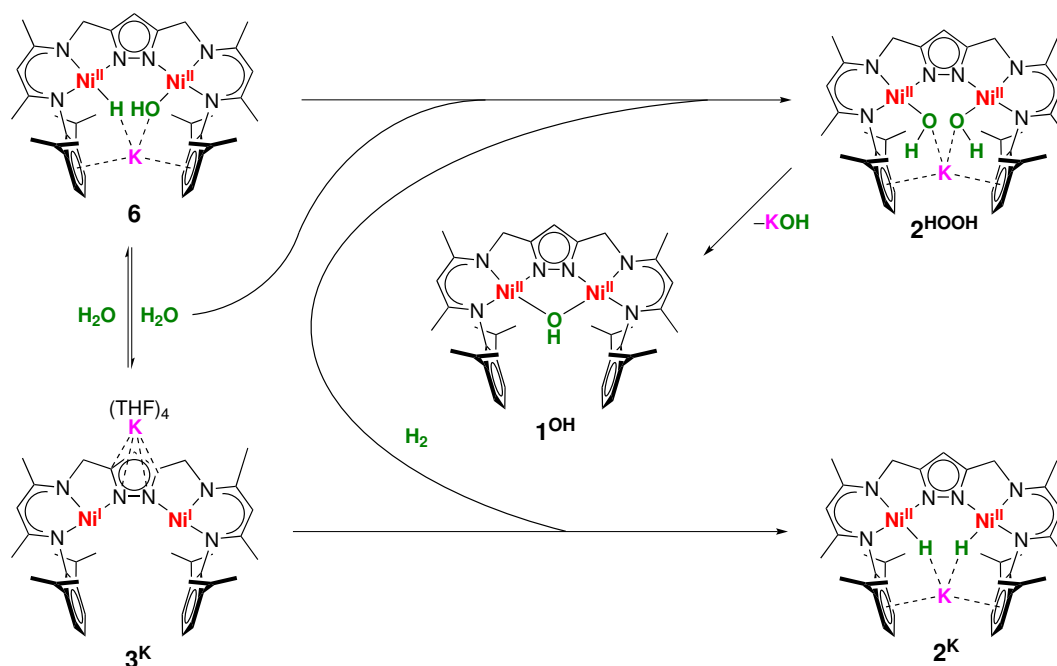


Figure 3.15: ^1H NMR spectrum of the decomposition of **6** at $-30\text{ }^{\circ}\text{C}$ in $\text{THF-}d_8$.

Even though it appears to be reasonable that an analogous dinickel(I) complex like $[\text{K}(\text{DB18C6})][\text{LNi}_2]$ (**3'**), has been formed under dehydration, the NMR signals are not matching exactly. Albeit the peak pattern resembles that of **3^K**, see Figure 2.3. However, in contrast to the previously shown ^1H NMR spectra in Figure 3.14 the characteristic broad band of water could not be detected in Figure 3.15. This could be explained by the interaction of water with the presumed *in situ* formed dinickel(I) species and the different temperatures of this measurement.

To conclude, the decomposition of **6** and **6-K(crypt)** was investigated, revealing significant differences depending on whether the potassium ion is located near the bimetallic pocket (**6**) or chelated by [2.2.2]-cryptand (**6-K(crypt)**). First, the decomposition of complex **6** was observed at higher temperatures as for **6-K(crypt)** ($-10\text{ }^{\circ}\text{C}$ vs $-30\text{ }^{\circ}\text{C}$). Second, during the decomposition of **6** an unknown species and the presumed evolution of water were detected, which were both not observed during the decay of **6-K(crypt)**. Instead, a paramagnetic species has formed, which is most likely a dinickel(I) species. Even though it is not possible to derive a precise reaction mechanism for the decomposition of **6**, one potential pathway will be discussed in the following. A reasonable starting point is the reductive release of H_2O , which would result in the formation of **3^K** and free H_2O , which then can react with **6**.

The hydrido hydroxido complex **6** does not react with H₂O at temperatures below -30 °; however, this is different at r.t. Even though no dihydrogen was detected, it can be assumed that H₂O reacts with the hydrido group of **6** to form a dihydroxido complex (**2^{HOOH}**) under the release H₂. This reactivity would be comparable to the reported example mentioned above, see 3.9. The most reasonable explanation why no H₂ was observed is that it instantaneously reacts with **3^K** to the dihydrido complex **2^K**. The postulated dihydroxido complex (**2^{HOOH}**) would represent a potential intermediate, which might show a comparable resonance for the hydroxido groups in the ¹H NMR spectrum as the hydroxido species (**1^{OH}**) and is therefore assumed to be the unknown species (+) in Figure 3.14. Eventually, this complex decomposes to **1^{OH}**. The proposed decomposition mechanism is displayed below:



Scheme 3.10: Proposed decomposition mechanism of **6**.

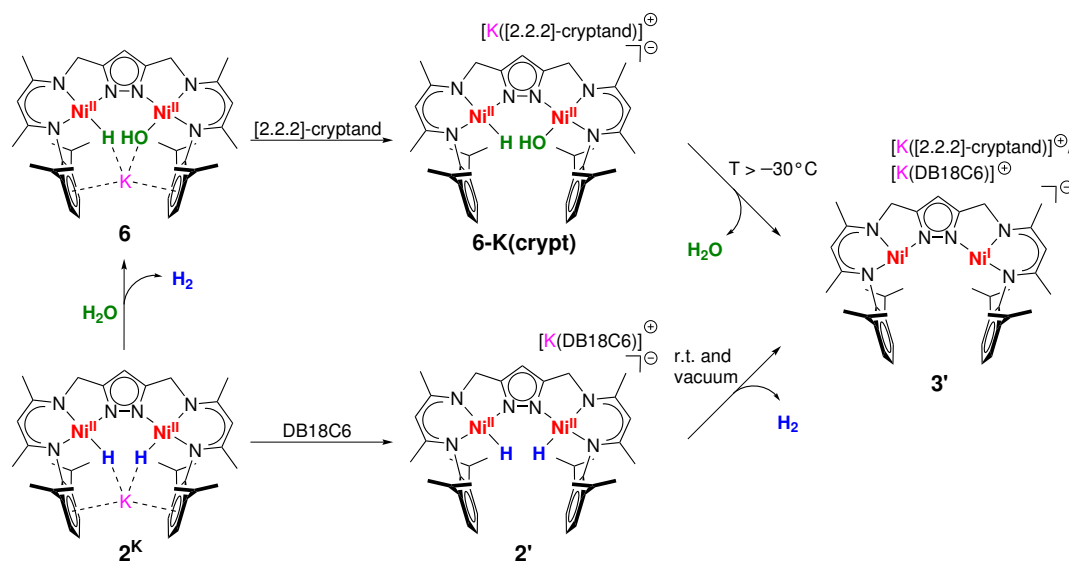
The decomposition for **6-K(crypt)** may proceed comparably. However, since no H₂O nor the assumed **2^{HOOH}** complex were observed during the decay reaction, it is questionable to derive a mechanism. The absence of the stabilising influence of the potassium ion likely results in faster decomposition of all involved dinickel complexes, except for **1^{OH}**. Furthermore, it was impossible to monitor the decomposition reaction over such a long period as for **6**.

3.6 Conclusion and Outlook

Only a few complexes are capable of splitting water *via* oxidative addition; they mainly bear 4d or 5d transition metals^[142–147] or exploit non-innocent ligand scaffolds.^[139,140] In this case, an alternative strategy to overcome the O–H bonds' challenging high bond dissociation energy using a bimetallic system capitalizing on metal–metal cooperativity has been established. Thus the oxidative addition of water at a masked dinickel(I) complex **3^K** or the discrete Ni^I complex **3^K** resulting in a hydrido hydroxido complex **K[LNi₂^{II}(H)(OH)]** was presented. Additionally, the potassium cation of **6** was removed by [2.2.2]-cryptand, yielding **6-K(crypt)**. Even though both complexes are very sensitive to moisture and higher temperatures, they were both successfully isolated and characterized by several spectroscopic methods including, X-ray crystallography.

Characterization by IR and NMR spectroscopy revealed a reductive splitting of H₂O into the respective hydrido (H[−]) and hydroxido (OH[−]) units coordinated by one nickel ion each. Identification of the individual ligands by ¹H NMR spectroscopy revealed two through space coupled doublets (*J*_{HH} = 6.0 Hz) in the expected region for hydroxido ($\delta_{\text{OH}} = -1.90$ ppm) and hydrido ($\delta_{\text{H}} = -25.73$ ppm) groups, respectively. In order to determine the intramolecular hydrogen distances, *T*₁ relaxation times were determined by NMR-inversion-recovery experiments; in addition, NOE spectroscopy was conducted, revealing that both hydrogen atoms are in close proximity to each other, enabling hydrogen bonding interaction. Isotopic labeling experiments with D₂O/HDO and the reaction with previously reported dinickel(I) complex **3^K** provide strong support that indeed water was split. Efforts have been undertaken to elucidate the role of the potassium ion by removing it from the coordination sphere with [2.2.2]-cryptand. The resulting complex **6-K(crypt)** was thoroughly characterized and contrasted with **6**, demonstrating the impact of the counterion on the ligands within the bimetallic cleft. Further, the reaction mechanism is thoroughly investigated by computational studies to provide a more detailed understanding of possible reaction pathways, with a particular focus on the potential mediation by the potassium counterion.

The spectroscopic results can be rationalized by assuming an intermolecular dihydrogen bond between the hydridic Ni–H and the hydroxido proton Ni–OH. Additionally, the strength of the dihydrogen bond was approximate by DFT calculations. Further, the hydroxido and hydrido groups are in suited proximity to interact with the potassium ion. This arrangement and the accompanied stabilizing effect by the electron density withdrawing counterion are known from previous investigations of **3^K**. In this context, the reported reductive release of H₂ from the dihydrido complex **3^K** if a crown ether removes the potassium ion from the DIPP cleft, resulting in **3'**, revealed parallels to the herein presented work, see Scheme 3.11. In both cases, a dinickel(I) complex has formed; however, for complex **3^K** it was necessary to keep the sample at room temperature and to apply vacuum to achieve complete conversion to **3'**.^[113] In contrast, **6-K(crypt)** transforms into a dinickel(I) species in THF at a temperature of −30°C.



Scheme 3.11: **First line:** Treatment of **6** with [2.2.2]-cryptand and reductive elimination of H₂O. **Second line:** Addition of dibenzo-18-crown-6 to **3^K** and subsequent reductive release of H₂.^[113]

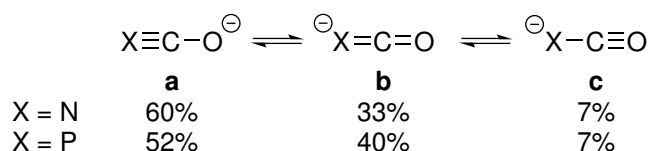
Furthermore, mechanistic investigations by DFT computations elucidate the potassium ion's additional role. The alkali metal stabilizes **6** but further mediates the reaction process, representing a unique example of the oxidative addition of water involving a LEWIS acid. All these factors together enable the metal-centered oxidative addition of water by a *3d* transition metal complex. Further investigations should focus on elucidating the decomposition mechanism. First attempts have already been made by NMR spectroscopy; however, the isolation of the assumed dihydroxido complex (**2^{HOOH}**) or labeling experiments would support the proposed decomposition mechanism. For example, according to Scheme 3.10, the treatment of **6** with D₂O should result in a deuterated version of **2^K** and **2^{HOOH}**. These complexes should be easy to identify by ²H NMR spectroscopy.

Chapter 4

A Dinickel Phosphaketene Complex for the Synthesis of Novel Phosphorous Compounds

4.1 The Chemistry of the Phosphaethanolate Anion (PCO^-)

For approximately one decade, the phosphaethynolate anion (PCO^-) has appeared as a versatile reagent for synthesizing a variety of novel phosphorus-containing compounds. This unique reagent is valence isoelectronic with the cyanate ion (NCO^-); even though a few parallels in terms of reactivity are present, the reactivity of PCO^- is dominated by the relatively fragile P–CO bond. This distinction results in different reaction pathways, for instance, the transfer of phosphorus^[190] or the formation of oligomers.^{[191][192]} These kinds of reactivities illustrate the striking difference between the cyanate anion and its phosphorus-containing analog and represent the primary motivation for exploring the chemistry of PCO^- .



Scheme 4.1: Resonance forms of PCO^- and NCO^- and their weights.^[193]

The different reactivity is explained clearly by the diverging resonance structures. In total, three resonance forms can be considered for PCO^- , exhibiting varying bond orders for the P–C bond, see Figure 4.1. The first and most contributing resonance structure resembles a phosphaethynolate, featuring a triple bond between the phosphorus and carbon atom and a negative charge on oxygen (**a**). The second resonance structure is a phosphaketene species with a double bond between phosphorus and carbon where the negative charge is located on the phosphorus atom (**b**). The last resonance form, which can be described as a carbonyl adduct of a monoanionic phosphide, (**c**), contributes minor to the electronic structure of PCO^- . Nonetheless, it offers a reasonable explanation for the frequently observed decarbonylation.^[193]

In 1992 BECKER *et al.* laid the foundation for today's chemistry of the phosphaethynolate anion by developing an applicable synthesis for the PCO^- anion and subsequent characterization.^[194] Unfortunately, the synthesis yielded an unstable lithium salt, $\text{Li}(\text{DME})_2(\text{PCO})$, which was impractical to use. As a consequence, the phosphaethanolate anion has not gained much attention, and only minor progress was achieved for twenty years. Over the intervening years, attempts have been made to

improve the stability of the phosphoethanolate anion by changing the counterion. For instance, in 2002, WESTERHAUSEN *et al.* were able to synthesize several other salts of PCO^- with different alkaline earth metals as counterion ($\text{Ae}(\text{DME})_3(\text{PCO})_2$ where $\text{Ae}=\text{Mg}, \text{Ca}, \text{Sr}, \text{Ba}$), which show comparable stability as $\text{Li}(\text{DME})_2(\text{PCO})$.^[195] Due to its fragile nature, exploration of its multifunctional chemistry was only possible after more convenient syntheses were published in 2011^[196] and 2012.^[197] Eventually, it was possible to isolate the PCO^- anion as the sodium salt $\text{Na}(\text{DME})_2(\text{PCO})$ on a multi-gram scale, which was indeed the breakthrough for a manifold utilization of the phosphoethanolate anion and represented a substantial driving force for ongoing research.

4.1.1 Transition Metal Chemistry

The phosphoethynolate anion belongs to the class of pseudo-halogen ligands and has been extensively investigated in coordination chemistry resulting in a variety of transition metal and main-group-element complexes. PCO^- binds in an ambiphilic fashion, while a basic assessment to predict whether it binds through the phosphorous or the oxygen can be made based on the HSAB principle, whereby account must be taken that there are exceptions.^[198,199] Hence, soft, polarisable elements favor coordination through the phosphorus atom, while hard, charge-dense Lewis acids favor binding through the oxygen atom. In transition metal chemistry, the dominating bonding mode is through the phosphorus atom, resulting in a so-called phosphaketene complex ($\text{M}-\text{P}=\text{C}=\text{O}$).^[193] Those complexes are, in many cases, readily available by salt metathesis reactions with halide precursors.

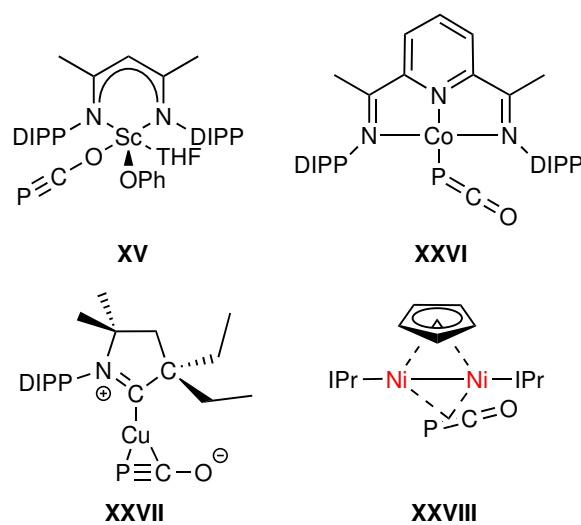


Figure 4.1: Prominent examples for phosphoethynolate coordinating 3d-metal complexes^[200–202] that have been structurally characterized by X-ray diffraction. IPr = 1,3-bis(2,6-diisopropylphenyl)-imidazol-2-ylidene, DIPP = 2,6-diisopropylphenyl.

For instance, the reaction of a β -diketiminato-Scandium complex, $(\text{nacnac})\text{ScCl}(\text{OAr})$ with NaPCO yields complex (XIV).^[200] Since Scandium (III) can be considered redox-inert, no unintended reduction or decarbonylation was observed. In addition, there are numerous examples of phosphaethynolate compounds with main group elements and actinides. As the PCO^- anion can be considered strongly reducing, reactions of the phosphaethynolate anion with transition metals are often accompanied with side reactions leading to decomposition.^[203] Hence, only a few examples of transition-metal-complexes of PCO^- are reported in the literature. The first coordination compound binding PCO^- reported and structurally characterized was a rhenium(I) phosphaethynolate complex $[\text{Re}(\text{PCO})(\text{CO})_2(\text{triphos})]$.^[203] To prevent inadvertent redox chemistry, the supporting ligand system must be redox inert and stabilize the oxidation state of the coordinating metal center. For instance, the halide precursor $[\text{CoCl}(\text{PDIiPr})]$ (PDI = pyridinediimine) reacts with sodium phosphaethynolate *via* salt metathesis reaction to a stable cobalt phosphaketene complex (XXVI).^[201] As the chosen ligand system is known for stabilizing metals in low oxidation states, the obtained molecular structure verifies that no reduction took place, and indeed a terminal phosphaketene transition metal complex has been formed. In addition to these monodentate binding modes, there are also two examples of a bidentate binding mode (side-on) *via* the π -bond. The first of these complexes shows a side-on binding of the PCO^- ion to a Cu^{I} metal center (XXVII).^[201] A related bonding mode has been reported for an intermediary bimetallic Ni^{I} compound (XXVIII), in which the PCO^- ion bridges to metal centers in a unique $\mu_2:\eta_2, \eta_2$ -binding mode.^[202]

Besides the reducing ability of the phosphaethynolate anion, many phosphaethynolate compounds are rather unstable, making full characterization challenging.^[204] Thus, it is not surprising that all of the presented compounds in Figure 4.21 exploit sterically demanding ligand systems to prevent decomposition reaction. As already mentioned above, the PCO^- anion forms willingly oligomers; consequently, in the absence of steric bulk, it has been shown that the corresponding phosphaketene complexes further react by cyclization reaction as well.^[205] From an experimental perspective, there are additional limitations towards forming such complexes. PCO^- is readily oxidized, especially by oxidative tetramerization, resulting in the heterobicyclic dianion $(\text{P}_4\text{C}_4\text{O}_4)^{2-}$.^[206]

The M–P–C bond angles for most phosphaketene compounds are almost rectangular, which can be rationalized by considering the frontier molecular orbitals of PCO^- . The HOMO of this anion has a significant degree of phosphorus p-orbital character. All phosphaketene compounds known to literature show this particular binding geometry which can be related to the corresponding parent acid HPCO.

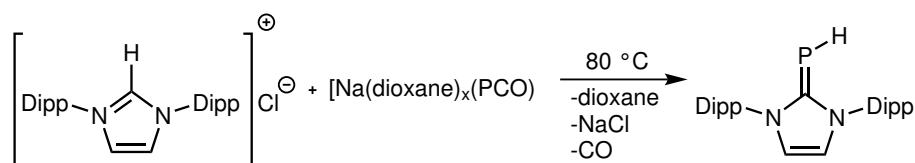
To identify the binding mode, different analytical methods are suited. Besides the most obvious method, single-crystal X-ray diffraction, IR spectroscopy is particularly useful for distinguishing between the E–P=C=O and E–O–C \equiv P coordination modes. The IR spectra of such phosphaketenes often feature bands approximately around 1900 cm^{-1} from the antisymmetric PCO^- vibration, whereas those of the phosphaethynolate-type compounds occur at lower wavenumbers, around 1700 cm^{-1} . Even though ^{31}P NMR spectroscopy is advantageous to monitor *in situ* reactions, it cannot identify the present binding mode since no characteristic chemical shifts are observable.^[193] Nevertheless, for special cases, this might be different. ^{31}P NMR chemical shifts of carbene–phosphinidene adducts have been used as a parameter to quantify the π -accepting properties of carbenes. It was found out that

with increasing π -accepting of the carbene, the signal of the phosphorus nucleus is downfield shifted.^[207,208]

4.1.2 Reactivity

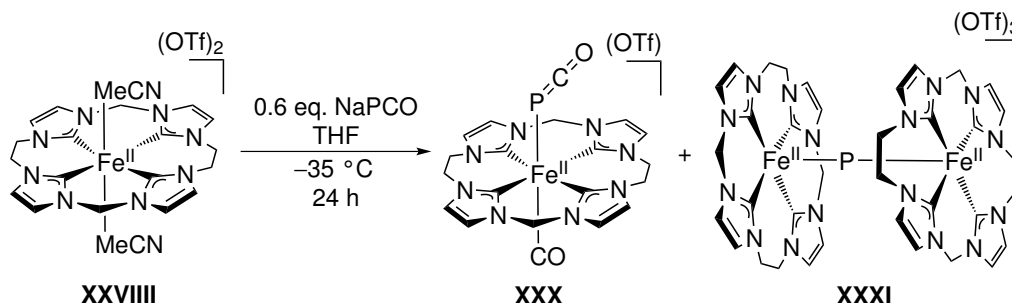
In addition to the aforementioned reaction pathways, the phosphoethynolate anion is suitable for a wide range of applications. Due to the fact that the P–CO bond is relatively easy to break, the PCO^- anion is capable of serving as a phosphorus transfer reagent or of carrying out decarbonylation and deoxygenation reactions. This manifold reactivity profile has enabled PCO^- to be incorporated into many coordination complexes. In addition, it has become a growing field of research to utilize the anion as a synthetic building block for organophosphanes or to synthesize inorganic variants of basic organic molecules in which nitrogen is replaced by phosphorus.

Even though a cation exchange was initially intended, GRÜTZMACHER *et al.* were the first who used PCO^- as a P^- transfer reagent. They synthesized a phosphinidene carbene adduct by reacting NaPCO with an *N*-heterocyclic carbene (NHC), see Scheme 4.2.^[209] Supported by DFT studies, it was assumed that the PCO^- anion is first protonated by the acidic imidazolium cation to form a highly reactive intermediate, H–P=C=O , which under decarbonylation forms the respective *N*-aryl substituted NHC.



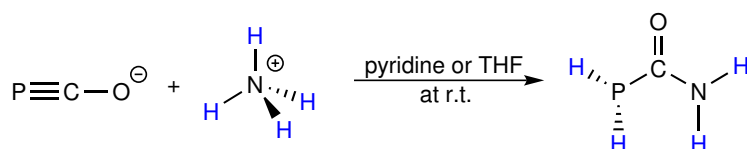
Scheme 4.2: Sodium phosphoethynolate serves as a phosphorus transfer reagent for the synthesis of *N*-heterocyclic carbene-phosphinidene adduct.^[209]

Another interesting example to illustrate the potential of NaPCO to serve as a P^- transfer reagent is given by FRANC MEYER. *et al.* The macrocyclic tetracarbene complex **XXIX** reacts with NaPCO to give a μ -phosphido diiron complex **XXXI** and **XXX**. The latter complex features trans-positioned P-bound PCO^- and CO ligands. This reaction is remarkable because it delivers a (P^-) phosphido bridged dinuclear iron complex, which is an uncommon ligand for late transition metals.^[123]



Scheme 4.3: Reaction of the macrocyclic tetracarbene complex $[\text{LFe}(\text{NCMe})_2](\text{OTf})_2$ **XXIX** with NaPCO results in the formation of a ferrous complex $[\text{LFe}(\text{PCO})(\text{CO})\text{OTf}]$ **XXX** and a μ -phosphido diiron complex $[(\text{LFe})_2\text{P}](\text{OTf})_3$ **XXXI**.^[123]

As mentioned above, interest is growing in synthesizing synthetic building blocks as starting material for a diversity of new phosphorus compounds. In this context, urea represents an interesting example of replacing nitrogen for its heavier congener phosphorous, which will be briefly illustrated by two examples. First, GOICOECHEA *et al.* have reported the reaction of the PCO^- anion with different ammonium salts resulted in a phosphorus-containing analog of urea (phosphinecarboxamide) in which a phosphine replaces an amine group, see Scheme 4.4.^[192] The herein presented example, as well as WÖHLER'S urea synthesis, have been investigated by quantum chemical calculations,^[210] revealing a similar reaction mechanism. In both cases, first, the anion is protonated, yielding the phosphorus-containing analog of cyanuric acid, $\text{H-P}=\text{C}=\text{O}$, as intermediate, which subsequently reacts with ammonia.

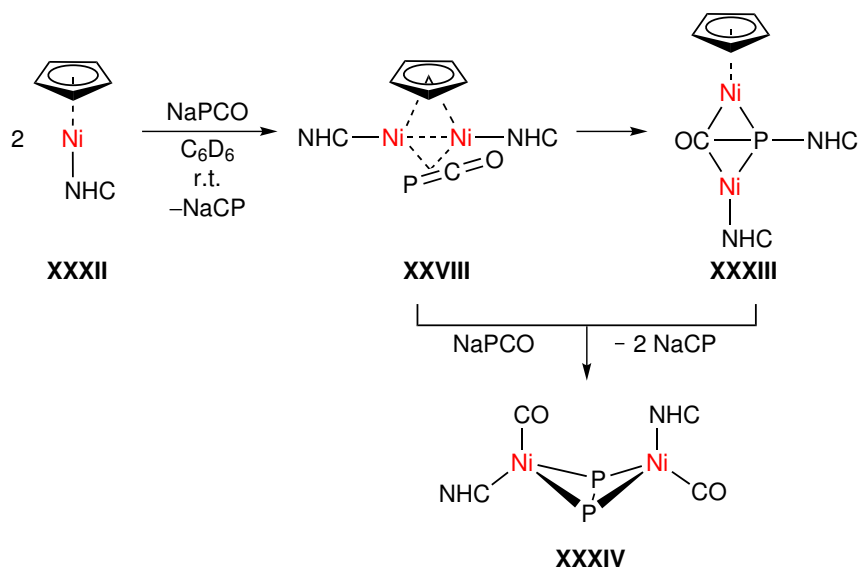


Scheme 4.4: Synthesis of phosphinecarboxamide from reaction of $[\text{K}(18\text{-crown-6})][\text{PCO}]$ with NH_4X salts ($\text{X} = \text{BPh}_4, \text{Cl}$).^[192]

The phosphoethanolate anion has proven itself as a tremendously versatile chemical reagent, which is now, which is now available on a multi-gram scale due to its improved synthesis. Over the last decade, PCO^- has developed into a viable reagent that has been harnessed for many applications, for instance, in transition metal chemistry or synthesizing novel phosphorus-containing building blocks. Therefore it is not surprising that this anion is used by numerous research groups world-wide.^[193]

4.2 Motivation

The PCO^- anion is a unique reagent that has been exploited as a versatile ligand in transition-metal chemistry. However, there are only a few rare examples of dinuclear compounds known to literature utilizing this pseudo-halide; an example is given in Scheme 4.3. The only reported bimetallic nickel complex in which a PCO^- ligand is involved has been reported by GOICOECHEA *et al.*. This complex (**XXVIII**) is remarkable as the ligand is bridging between the two metal centers in an unexpected $\mu_2:\eta^2, \eta^2$ -binding mode, see Scheme 4.5.^[202] Even though **XXVIII** was isolated and its structure elucidated by X-ray crystallography, it is presumably an intermediate, which willingly rearranges upon decarbonylation and carbene migration to the respective phosphinidyne. The addition of a second equivalent of NaPCO leads to the "butterfly-shaped" complex ($\mu_2:\eta^2, \eta^2\text{-P}_2$){Ni(NHC)(CO)}₂ (**XXXIV**).



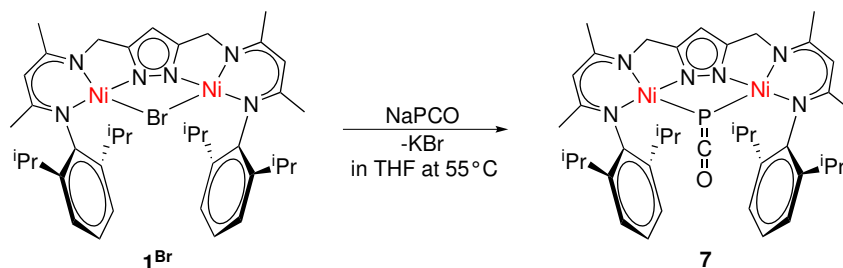
Scheme 4.5: Synthesis of a bimetallic phosphoethynolate Ni^I complex **XXVIII**, which rearranges to (**XXXIII**). Both of these complexes are further reacting with an additional equivalent of NaPCO, affording (**XXXIV**).^[202]

A different approach to generate phosphoethynolate compounds is by a salt metathesis reaction. This synthetic strategy is well established and has been exploited, for instance by pincer-type, and β -diketiminato ligand-based complexes before. In compliance with these reported studies, a similar procedure seems to be a promising starting point. Since the pyrazolato bridged ligand system **L** has proven its ability to stabilize highly reactive nickel species, the bromido complex [LNi₂(μ -Br)] (**1^{Br}**) represents the ideal precursor for synthesizing a phosphaketene complex. With this compound in hand, the next step is to investigate possible follow-up reactivities. Several different strong nucleophiles are known to react with phosphaketene compounds to yield, for instance, phosphorus-based building blocks.^[211,212] In this context, it is worth to be mentioned that particular focus is set on the fragile P–CO bond, which allows versatile conversion of the PCO ligand accompanied with decarbonylation reactions.

4.3 Synthesis of a Dinickel(II) Phosphaketene Complex

Due to the fact that the PCO anion is unstable towards higher temperatures, the first attempts of synthesizing the desired phosphoethynolate complex were carried out at ambient temperatures. However, no reaction was observed on the NMR scale. Therefore the reaction solution was heated until a new signal became visible in the ³¹P NMR spectrum. It is unavoidable under these conditions that the phosphoethynolate partially decomposes accompanied by the formation of an insoluble black precipitate, which was not further analyzed. However, it is also possible that unintended redox reactions with the halide precursor took place.^[203] To compensate for this side reaction, 1.2 equivalents of sodium phosphoethynolate were used, resulting in a complete conversion of the bromido precursor complex **1^{Br}** to the target complex [LNi₂(μ -PCO)] (**7**). The same procedure was applied to obtain the complex **7** on a synthetic scale. To ensure the highest possible yield, the solution was stirred for two days at 55 °C. Carrying out the synthesis at even higher temperatures

was not successful but led to nonisolable decomposition products. After filtration, the concentrated red THF solution was layered with hexane and stored at -35°C .



Scheme 4.6: Salt metathesis reaction of 1^{Br} with NaPCO resulting in the dinickel phosphaketene complex $[\text{LNi}_2(\mu\text{-PCO})]$ (7).

Red block crystals suitable for single-crystal X-ray diffraction (SC-XRD) were isolated in moderate yields (65%) after five days. The molecular structure of 7 is displayed in Figure 4.2, confirming the successful replacement of the bromido anion by a phosphaketene unit. In addition, this has been the only structurally characterized example of so far featuring PCO ligand, which bridges two metal centers in a $\mu_{1,1}$ -binding mode. In cooperation with the group of MAX C. HOLTHAUSEN, theoretical calculations were carried out to support the experimental results. The structural parameters obtained from the molecular structure and the DFT optimized structure are in good agreement, see Chapter C.4.1.

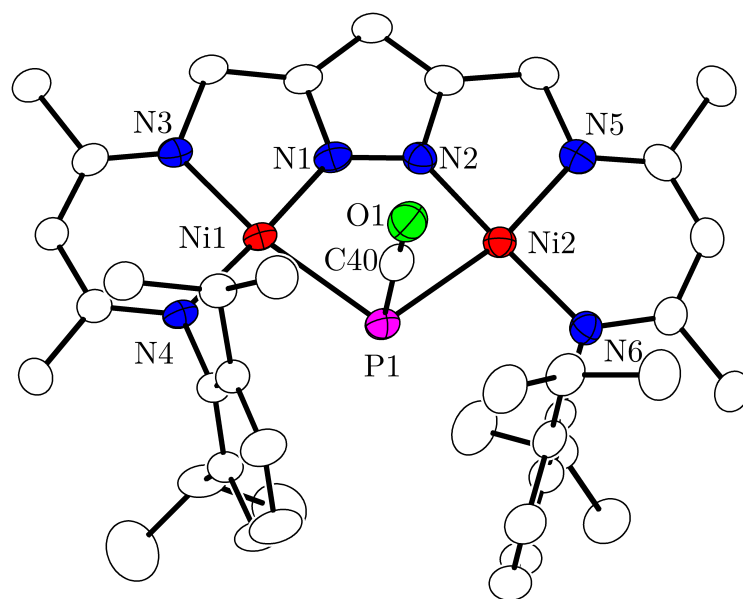


Figure 4.2: Molecular structure of **7** (30% probability thermal ellipsoids). The hydrogen atoms are omitted for clarity.

Table 4.1: Selected bond lengths, distances, and angles of **7**.

Bond length / Å	Distances / Å		Angle / °		
Ni1–N4	1.901(3)	Ni1···Ni2	3.7513(7)	N4–Ni1–N1	177.13(13)
Ni1–N1	1.832(3)			N4–Ni1–N3	94.64(12)
Ni1–N3	1.896(3)			N1–Ni1–N3	82.71(13)
Ni2–N6	1.899(3)			N6–Ni2–N2	176.80(13)
Ni2–N2	1.825(3)			N6–Ni2–N5	95.05(13)
Ni2–N5	1.904(3)			N2–Ni2–N5	85.04(7)
Ni1–P1	2.3354(11)			C40–P1–Ni1	80.85(14)
Ni2–P1	2.3366(11)			C40–P1–Ni2	81.50(14)
P1–C40	1.671(5)			Ni1–P1–Ni2	106.82(4)
C40–O1	1.170(5)			O1–C40–P1	177.8(4)

The coordination sphere of both Ni^{II} centers is only slightly distorted from square planar, and the two metal ions are separated by a distance of 3.7513(7) Å. The PCO ligand within the bimetallic cleft features Ni1–P1–C40/ Ni2–P1–C40 angles of 80.85(14)/81.50(14)°, as expected for a phosphaketene complex.^[193] The obtained interatomic distance for P1–C40 is 1.671(5) Å, which fits very well with the literature known value for P=C double bonds of 1.69 Å, in contrast to triple bonds with a bond length of 1.54 Å.^[193] By taking the C40–O1 distance of 1.170(5) Å and the O1–C40–P1 bonding angle of 177.8(4)° into account, it is possible to assume the most contributing resonance form of the PCO ligand, which is the phosphaketene (P=C=O) type. However, further investigations are needed to validate this presumption.

Topological analysis of the electron densities and energy decomposition analyses computed from PBE0-D3(BJ)/6-311++G(2d,2p)^[213,214] wavefunctions obtained at the PBEh-3c molecular structure of **7** were done to obtain further insight into the bonding and electronic structure of the complex **7**, see Figure 4.3 and Table 4.2.

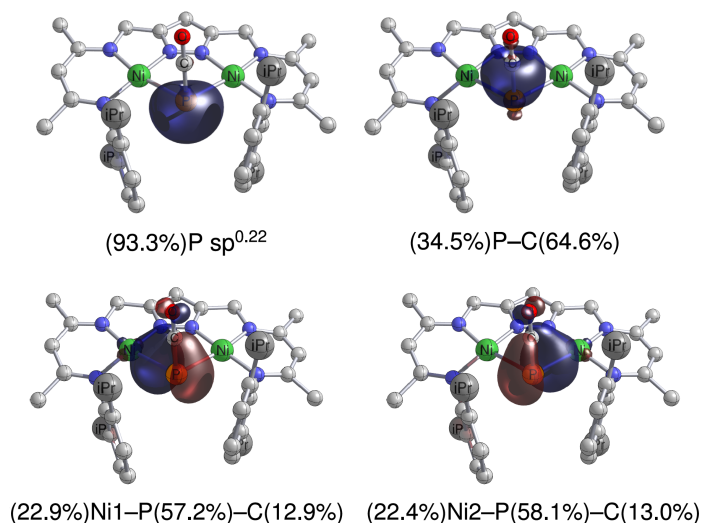


Figure 4.3: Selected NLMOs of **7** resulting from PBE0-D3(BJ)/6-311++G(2d,2p) calculations based on PBEh-3c structures; isovalue $0.05 a_0^{-3/2}$

Table 4.2: Selected properties of the electron density distribution in compounds **7** resulting from PBE0-D3(BJ)/6-311++G(2d,2p) calculations computed at PBEh-3c geometries.

Bond ^[a]	$\rho(r_b)$ ^[b]	$\nabla^2\rho(r_b)$ ^[c]	$H(r_b)/\rho(r_b)$ ^[d]	$G(r_b)/\rho(r_b)$ ^[e]	$\epsilon(r_b)$ ^[f]
Ni1–P1	0.43	1.71	–0.33	0.61	0.09
Ni2–P1	0.44	1.76	–0.33	0.61	0.06
P1–C11	1.11	8.86	–0.86	1.42	0.10
	WBI(A B) ^[g]	$\delta(A B)$ ^[h]	$q(A)/q(B)$ ^[i]		
Ni1–P1	0.35	0.55	0.82 / 0.43		
Ni2–P1	0.36	0.56	0.43 / 0.81		
P1–C11	1.67	1.41	0.43 / 0.44		

^[a]Topological charact. computed at bond critical points (r_b); ^[b]electron den. in $e \text{ \AA}^{-3}$; ^[c]Laplacian of ρ in $e \text{ \AA}^{-5}$; ^[d]rel. total energy den. in Hartree/e; ^[e]rel. kinetic energy den. in Hartree/e; ^[f]ellipticity; ^[g]Wiberg bond index between atoms A and B; ^[h]delocalization index between atoms A and B; ^[i]QTAIM partial charge on atoms A and B in a.u.

Combining these results with the molecular structure, the bonding situation between the phosphaketene unit and the nickel ions can be described in detail. The P–C bond is described by one σ -bonding NLMO, which is polarized by 64.6% towards the carbon. The Ni–P interactions are represented by 2c-2e bonding NLMOs with a P(2p)-Ni(4s) σ -donor character. The dative nature of the P-Ni interaction through a p-bonding orbital results in Ni1–P1–C40/Ni2–P1–C40 angles of 81.6/86.4°. These results are in good agreement with the angles determined by X-ray diffraction, showing Ni1–P1–C40/Ni2–P1–C40 angles of 80.85(14)/81.50(14)°, see Table 4.1. The expected double bond character of the P=C is validated by a natural bond orbital (NBO) analysis and a Wiberg bond index (WBI) of 1.67. To analyze the

bonding scheme, energy decomposition analysis with natural orbitals for chemical valence (EDA-NOCV) were carried out. With these data in hand, the stability of the phosphaketene can be explained, revealing a profound stabilizing $\sigma(\text{CO}) \rightarrow \sigma(\text{P})$ donation associated with less pronounced $\sigma(\text{P}) \rightarrow \pi(\text{CO})$ and $\pi(\text{P}) \rightarrow \pi(\text{CO})$ backdonation from the phosphorous into the carbonyl unit, see Figure 4.14.

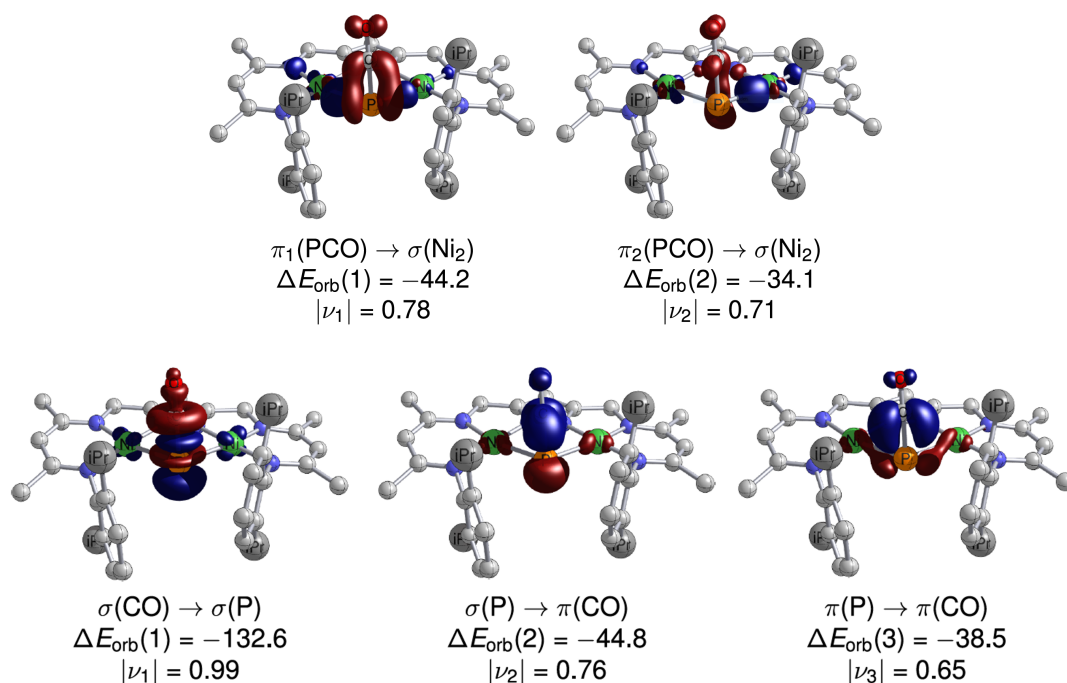


Figure 4.4: Deformation densities $\Delta\rho$ from EDA-NOCV of **7** resulting from PBE0-D3(BJ)/TZ2P//PBEh-3c calculations based on $[\text{LNi}_2(-\text{P})]/[\text{CO}]$ fragmentation (orbital interaction energy contributions ΔE_{orb} in kcal mol⁻¹, charge flow $|\nu_i|$ from red to blue, isovalue $0.005 a_0^{-3/2}$).

The clean conversion to the target complex could be confirmed by ¹H NMR spectroscopy and all peaks assigned, see the numbering scheme for **7** in Figure 4.5. Interestingly, **7** and the respective precursor complex **1^{Br}** do not result in considerably different ¹H NMR spectra. Moreover, both complexes show the same C_{2v} symmetry on the NMR time scale. This result is indeed surprising since the molecular structure of **7** features C_s symmetry. The most reasonable explanation for this disparity is that the PCO ligand can unhindered oscillate through the plane defined by pyrazolato-bridged dinickel core:

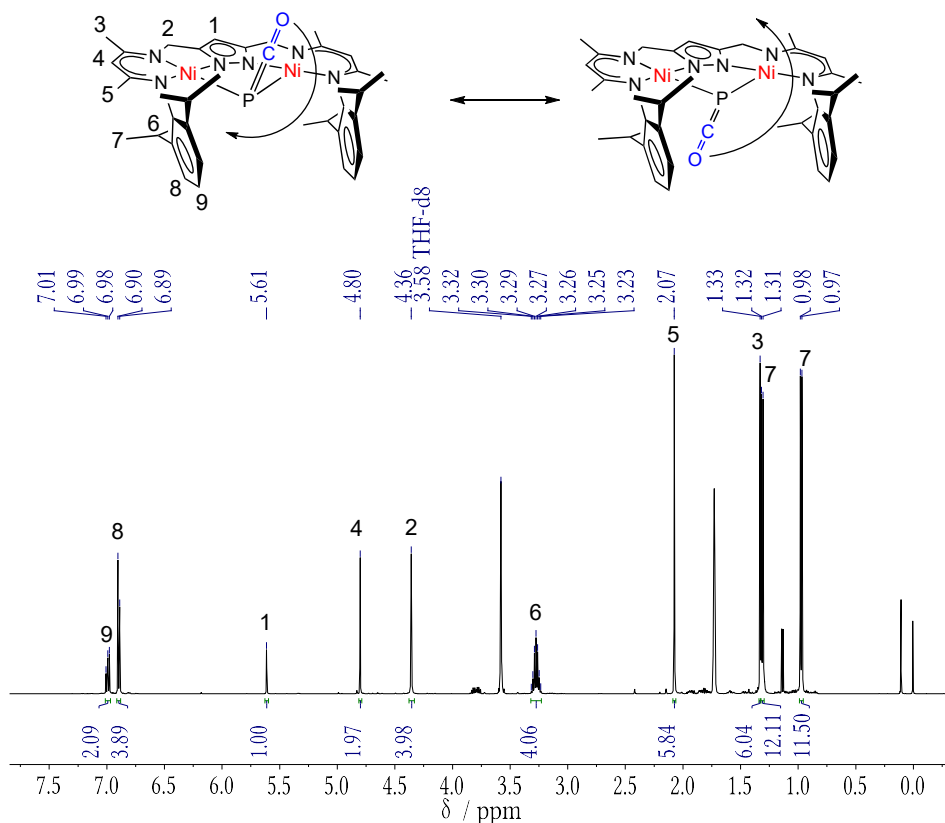


Figure 4.5: Top: Simplified sketch of the suspected oscillation of the PCO ligand, including numbering scheme for 7. Bottom: ^1H NMR spectrum of 7 at -35°C in THF-d_8 .

Further evidence for the replacement of the bromido ligand is given by ^{31}C and ^{31}P NMR spectroscopy. In the phosphorous NMR spectrum, one singlet at 264.5 ppm is detected, which is profoundly displaced in comparison with the sodium phosphoethynolate (392.0 ppm), see Figure B.30. In general, the signals in the ^{31}P NMR spectrum bear a similar shift independently from the coordination mode. Thus it is not possible to differentiate between a $\text{P}\equiv\text{C}-\text{O}$ and a $\text{P}=\text{C}=\text{O}$ species by this method.^[193] A doublet in the $^{13}\text{C}\{^1\text{H}\}$ NMR spectrum at 182.2 ppm can be assigned to the carbon atom (C40), which couples to the phosphorous atom with $^1J_{\text{PC}} = 138$ Hz, see Figure 4.6. In comparison, the starting material (NaPCO) features a doublet at 166.3 ppm with a coupling constant of $^1J_{\text{PC}} = 47$ Hz in THF-d_8 . Primarily, the magnitude of the coupling constant is of interest since it appears to be very informative for identifying the binding mode and which resonance form of the ligand is dominating. More specifically, phosphoethynolate compounds ($\text{P}\equiv\text{C}-\text{O}$) result in smaller $^1J_{\text{PC}}$ coupling constants around 12 Hz than phosphaketene type ions ($\text{P}=\text{C}=\text{O}$), which feature $^1J_{\text{PC}}$ values in the range of 94 Hz.^[193] Therefore, it can be concluded that the latter resonance form best describes the electronic structure of the PCO ligand in complex 7.

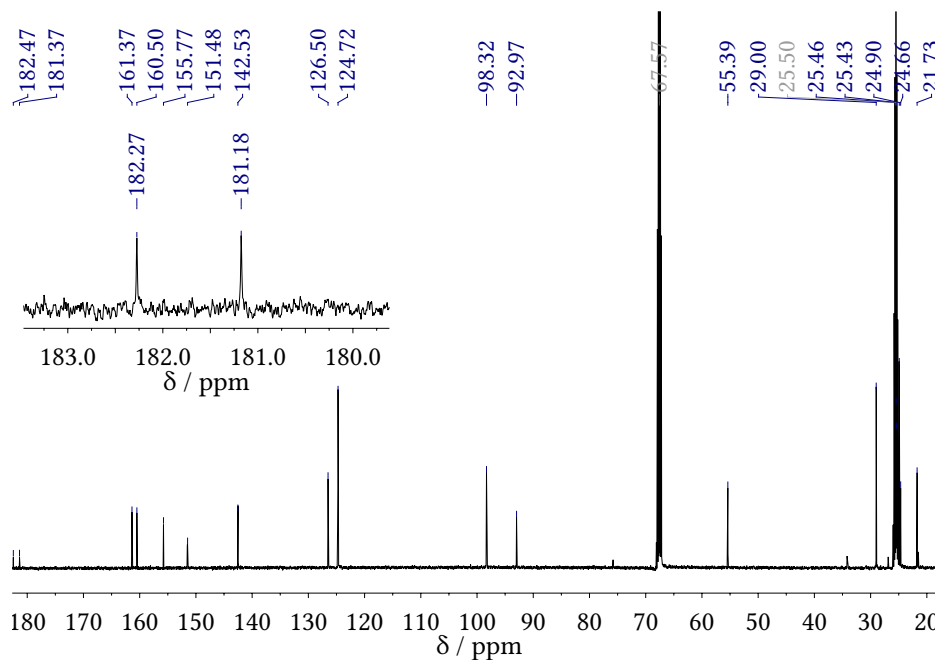


Figure 4.6: $^{13}\text{C}\{^1\text{H}\}$ NMR spectrum of **7** at room temperature in $\text{THF-}d_8$. The inset shows doublet at $\delta_{\text{P-C40}} = 182.2$ ppm, which was assigned to C40 with a coupling constant of $^1J_{\text{PC}} = 138$ Hz.

Even though NMR spectroscopy confirms the clean formation of **7**, it is impossible to determine the PCO ligand's binding mode using this method. For this purpose, infrared spectroscopy is more revealing. For NaPCO, the IR spectrum features two characteristic bands that can be assigned to the antisymmetric (ν_{asym}) and symmetric (ν_{sym}) PCO stretching vibrations. The former of these is located at 1755 cm^{-1} , whereas the latter band is found at 1247 cm^{-1} .^[215] However, these signals are profoundly shifted in the IR spectra of PCO^- , depending on the coordination environment and binding mode. The antisymmetric vibrational mode ν_{asym} of a phosphaketene type compound is usually greater than 1840 cm^{-1} , whereas the respective stretching vibration for a phosphoethynolate-type species is found at lower wavenumbers, with an average value of 1677 cm^{-1} .^[193]

Complex **7** follows this trend and features an intensive peak at 1855 cm^{-1} that can be unambiguously attributed to an antisymmetric stretching vibration, see Figure 4.7. This signal is blue-shifted compared to NaPCO ($\Delta\nu = 100\text{ cm}^{-1}$) and within the characteristic range for a P-bonded compound M-P=C=O .^[201,216,217] Due to overlapping signals in the IR spectrum, the corresponding symmetric stretching vibrations could not be clearly assigned.

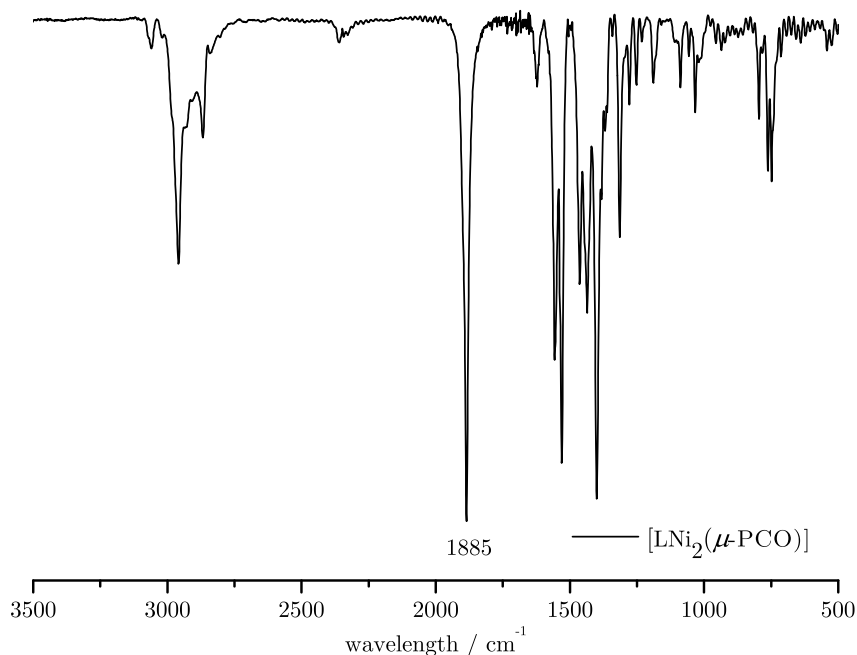


Figure 4.7: IR (KBr) spectrum of **7**. The labeled peak at 1885 cm^{-1} represents the antisymmetric stretching vibration of the phosphaketene unit.

The ESI(+)-MS-spectrum of **7** in THF shows a signal that is consistent with the expected mass to charge ratio calculated for complex **7** at $m/z = 781.4$ [M+H], see Figure 4.8. A further peak is detected at $m/z = 753.4$, which can be attributed to a pnictogen species [M–CO+H]. This highly reactive compound has been formed most likely by decarbonylation and underlines the relative weakness of the P–CO bond.

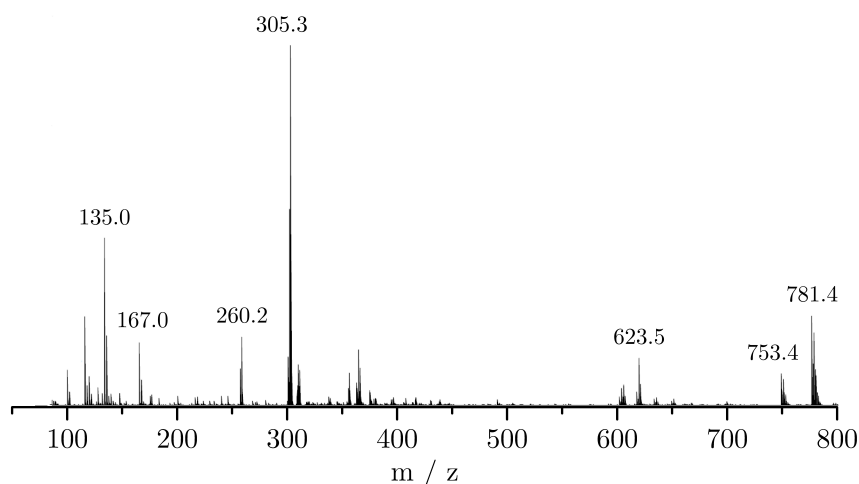


Figure 4.8: ESI(+)-MS-spectrum of **7** in THF. The molecular ion peak is found at $m/z = 781.4$ [M+H].

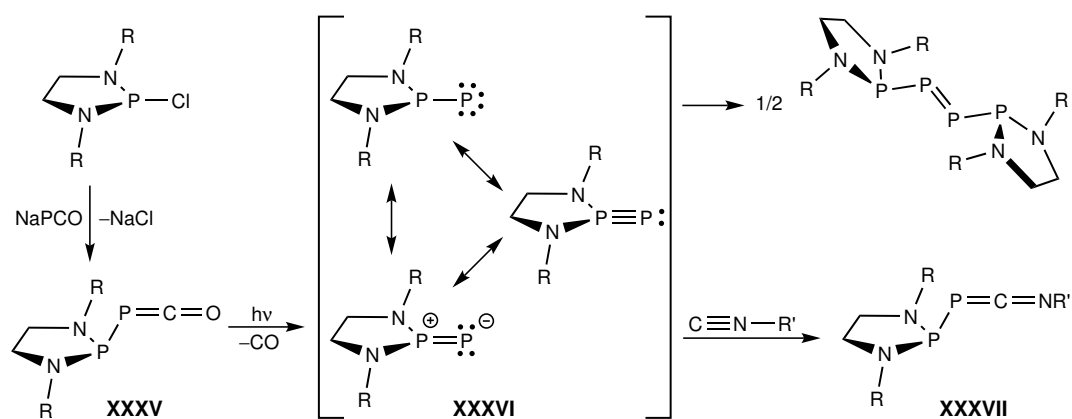
With **7** in hand, the next chapter will deal with its follow-up reactivity. The ESI(+)-MS-spectrum of **7** implies one possible reaction pathway involving the replacement of the carbonyl unit. Consequently, **7** will be treated with varyingly strong nucleophiles to gain a deeper insight into the reactivity of the phosphaketene unit.

4.4 Replacement of the Carbonyl Unit

The obtained complex **7** bears a monoanionic PCO ligand, which can serve as a building block to generate novel phosphorous-based compounds. Based on the extensive characterization of **7**, the most promising approach for follow-up reactivity is a nucleophilic attack on the carbon atom of the P=C=O unit, which will be most likely accompanied by the release of CO. By doing so, the carbonyl group would be replaced by another neutral two-electron donor group. The β -diketiminato based ligand system **L** is very capable of stabilizing reactive substrates, which has been illustrated in the previous chapters. Thus, it is not surprising that this property is also well pronounced in the herein presented phosphaketene complex. Consequently, complex **7** is thermally stable up to 70 °C and is impervious to moisture and oxygen at ambient temperatures. Considering this stability, the isolation of reactive species seems promising and opens up the possibility of carrying out reactions under a wide temperature range.

4.5 Formation of a P–P Bond

In general, phosphaketene compounds R–P=C=O are prone to decarbonylation reactions leading to terminal pnictogenides, which then readily react with a multitude of substrates. This kind of reactivity opens up the possibility of generating novel phosphorus-based compounds, including varying species containing P–P bonds, known as diphosphenes RP=PR'.^[218–220] In order to replace the CO unit of the PCO ligand, different phosphines were added to **7**. A first attempt has been made by treating **7** with an additional equivalent of NaPCO, which should yield a so-called phosphanyl phosphaketene (RP=PCO) functionality. This species would be a desirable target compound as they can be transformed into versatile usable phosphanyl phosphandiyl (RP=P) units, see Scheme 4.7.^[218]

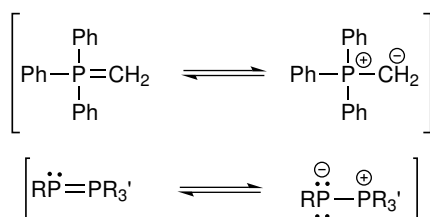


Scheme 4.7: Synthesis of a phosphanyl phosphandiyl species (XXXVI) and subsequent reaction with an isocyanide results in XXXVII.

However, it was not possible to establish a synthetic route starting from **7** to the corresponding phosphanyl phosphaketene complex. All attempts led to impractical results, irrespective of whether the bromido complex **1^{Br}** is reacted with two equivalents of sodium phosphoethynolate or **7** is isolated before. Also, initiating the decarbonylation reaction by irradiation of **7** with a medium-pressure Hg or a LED lamp could not be achieved. A noticeable difference becomes apparent by comparing the literature known examples with the herein presented reaction. In Scheme 4.7,

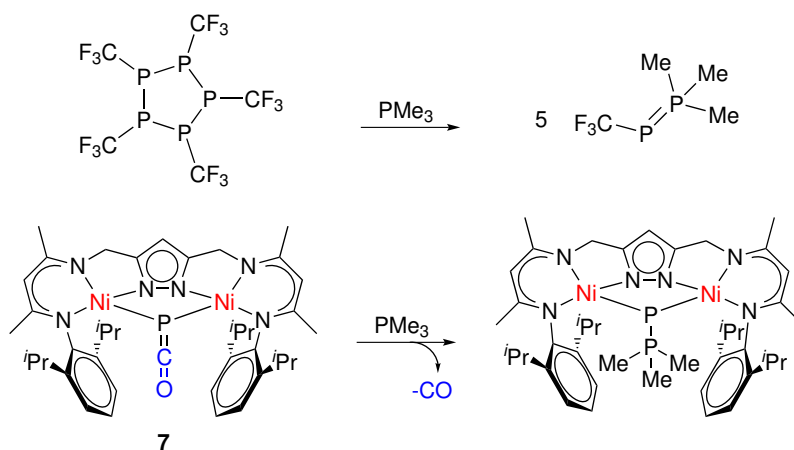
a neutral phosphanyl phosphandiyl compound (XXXVI) is formed. In contrast, the reaction of **7** with PCO^- would have led to a dianionic ligand within the bimetallic pocket. It can be assumed that such a species would be fairly unstable, especially at the here required high temperatures.

Therefore the next attempt should involve a neutral reagent to accomplish the formation of a P–P bond. In this context, phosphines are well suited due to their nucleophilic properties, which makes an attack at the carbon of the phosphaketene ligand most likely resulting in a phosphanylidene phosphorane ($\text{RP}=\text{PR}'_3$) unit. These compounds are particularly interesting since they are considered as phosphorus analogs of phosphonium ylides ($\text{RP}=\text{CR}'_2$).^[221] Both species can be described by similar resonance forms and show comparable reactivity.^[222]



Scheme 4.8: **Top:** Resonance forms of phosphonium ylides. **Bottom:** Resonance forms of phosphanylidene phosphoranes.^[223]

In analogy to WITTIG reagents, phosphanylidene phosphoranes are capable of carrying out "phospha-WITTIG" reactions with C=O functionalities to form phosphalkenes ($\text{RP}=\text{C}(\text{H})\text{R}'$).^[222,224,225] Formally, phosphanylidene phosphoranes are formed upon the transfer of phosphinidenes to phosphines;^[226] therefore, they can be seen as a base-stabilized adduct of phosphinidenes (RP).^[227] The first phosphanylidene phosphorane species was synthesized in 1961 by reacting the cyclopolyphosphine $(\text{PCF}_3)_5$ with trimethylphosphine PMe_3 , yielding the diphosphene $\text{CF}_3\text{P}=\text{PMe}_3$.^[228]

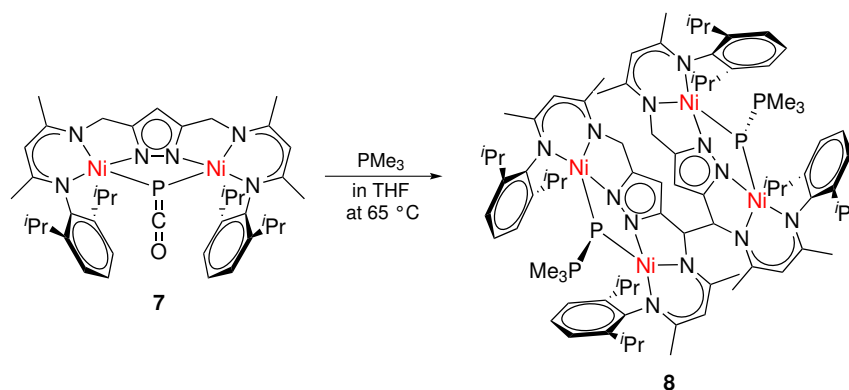


Scheme 4.9: **Top:** Synthesis of a phosphanylidene phosphorane compound.^[228] **Bottom:** Presumed synthesis of a diphosphene complex.

Following this procedure, **7** was treated with two different alkylphosphines, providing that the CO unit of the PCO^- ligand will be released, the desired P– PR_3 unit should be formed, see the bottom line of Scheme 4.9. While **7** did not react with triphenylphosphine PPh_3 , the situation is different with PMe_3 . This distinction in reactivity can likely be attributed to two factors; first, the latter phosphine is a stronger

nucleophile. Second, PMe_3 is sterically less demanding. The reaction of the phosphaketene complex **7** with one equivalent of trimethylphosphine was monitored on the NMR scale in $\text{THF-}d_8$. The reaction took five days to be completed even though the reaction mixture was heated to $T < 70^\circ\text{C}$.

The ^1H NMR spectrum (Figure 4.9) reveals a clean conversion with only one resonance for the pyrazole- H^4 at 5.51 ppm with an unexpected integral of 2H (no. 1); in addition, no intermediates were detected during the reaction. Furthermore, a set of four signals at 4.23 ppm with a total integral of 8H appeared (no. 2 and 3 in Figure 4.9, inset) in the region typical for the methylene linker CH_2 unit. This feature in the ^1H NMR spectrum proved to be characteristic for the dimerization of the complex at the respective methylene bridge:



Scheme 4.10: Reaction of **7** with PMe_3 resulting in **8** accompanied with the dimerization at the CH_2 linker unit.

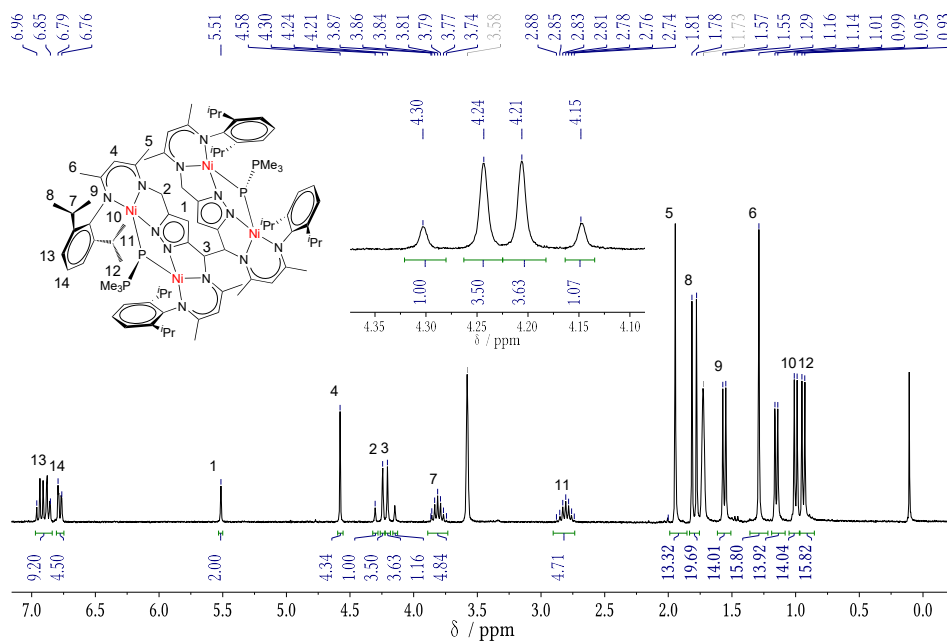


Figure 4.9: ^1H NMR spectrum of **8** at r.t. in $\text{THF-}d_8$. The inset shows the signals for the methylene linker unit.

In the ^{31}P NMR spectrum (Figure 4.10) a doublet at 12.4 ppm (see no.1 in the numbering scheme of Figure 4.10) with a corresponding $^1J_{\text{PP}}$ coupling constants of 516 Hz was detected. Additionally, a multiplet (theoretically: decett) was found at 4.4 ppm (no.2). It was not possible to resolve all peaks originating from the coupling of the phosphorous with the hydrogen of the attached methyl groups. However, a $^2J_{\text{PH}}$ value of 12 Hz was determined.

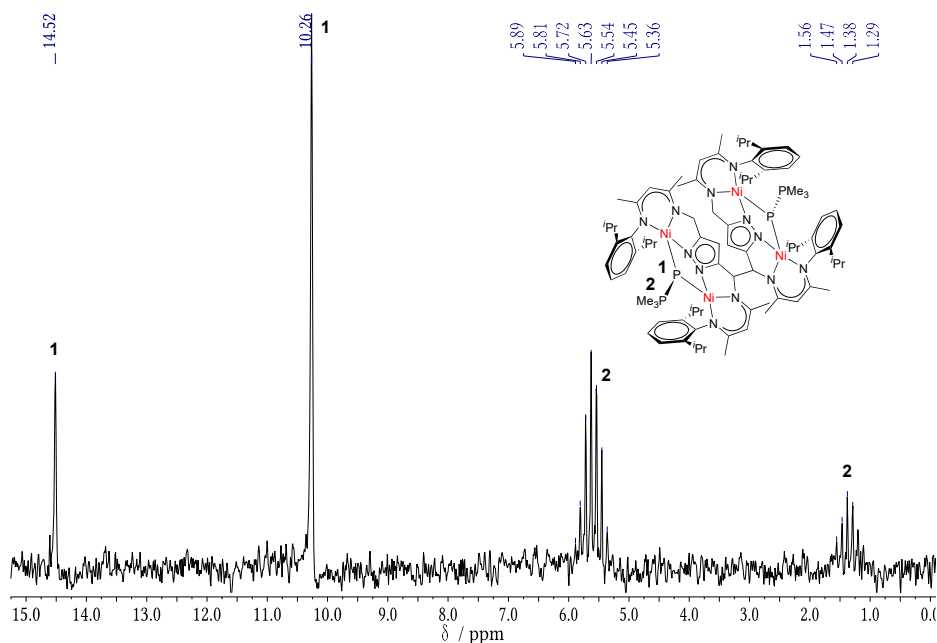


Figure 4.10: ^{31}P NMR spectrum of **8** at r.t. in $\text{THD-}d_8$.

The synthesis was repeated on a larger scale to gain enough material to facilitate crystallization. After work-up and crystallization from a concentrated THF solution, deep red crystals, suitable for X-ray diffraction, were obtained in good yields (80%). The molecular structure of **8** is displayed in Figure 4.11.

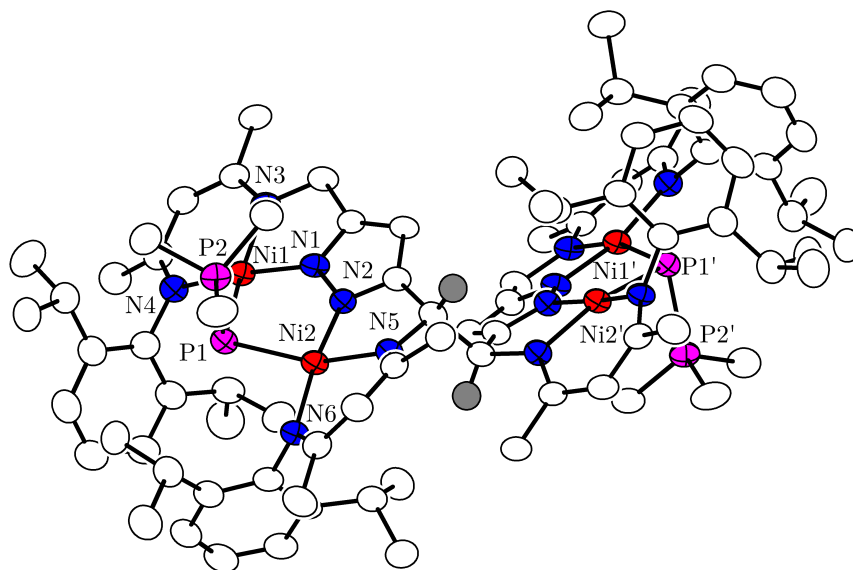


Figure 4.11: Molecular structure of **8** (30% probability thermal ellipsoids). The hydrogen atoms are omitted for clarity.

Table 4.3: Selected bond lengths, distances, and angles of **8**.

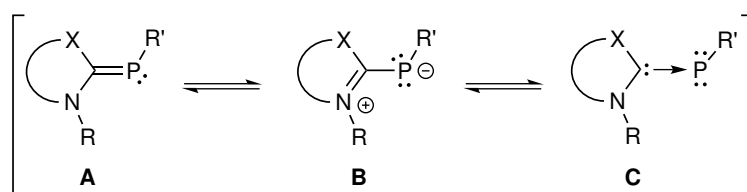
Bond length / Å	Distances / Å		Angle / °		
Ni1–N4	1.894(4)	Ni1...Ni2	3.6669(69)	N4–Ni1–N1	167.11(18)
Ni1–N1	1.823(4)			N4–Ni1–N3	95.62(16)
Ni1–N3	1.926(4)			N1–Ni1–N3	81.38(16)
Ni2–N6	1.909(4)			N6–Ni2–N2	172.31(17)
Ni2–N2	1.935(4)			N6–Ni2–N5	94.40(16)
Ni2–N5	1.942(2)			N2–Ni2–N5	81.21(16)
Ni1–P1	2.2975(13)			P1–P2–Ni1	95.31(6)
Ni2–P1	2.2922(13)			P1–P2–Ni2	86.45(6)
P1–P2	2.1541(18)			Ni1–P1–Ni2	106.05(5)

The molecular structure reveals the formation of two phosphanyl phosphandiyl units and validates the assumed dimerization reaction. However, the dimerization process stays inexplicable. Since X-ray crystallography and NMR spectroscopy agree, the isolation of a side product can be ruled out. The metal centers show a square-planar coordination environment, while the P1–P2–Ni1/P1–P2–Ni2 angles are comparable to the C40–P1–Ni1/C40–P1–Ni2 bonding angles of **7** (**7**: 80.85(14)/81.50(14)° *vs.* **8**: 95.31(6)/86.45(6)°). The P–P bond length was determined as 2.1541 Å, which is between a single and double phosphorus bond.^[229]

Even though it was tried to circumvent the dimerization by tuning the reaction conditions, neither changing the temperature nor varying the educts' ratio led to a different product. Nonetheless, the basic concept of replacing the carbonyl unit by treating complex **7** with a nucleophilic reagent has been demonstrated. In addition, the absent reactivity with triphenylphosphine leads to the conclusion that bulky substituents are unsuited to react with the PCO moiety in **7**.

4.6 A Carbene-Stabilized Phosphido Complex

Motivated by the previous results, various reagents were tested to replace the carbonyl fragment of the PCO ligand within the pocket of **7** by different donor functionalities. In this context, *N*-heterocyclic carbenes represent an appealing option since they have already proven their potential to stabilize highly reactive phosphorous species.^[227,230–233] In 1997, ARDUENGO *et al.* reported the first synthesis of an *N*-heterocyclic carbene-phosphinidene adduct (NHC=PR) by reacting *N*-heterocyclic carbenes with cyclo-polyphosphines.^[231] This class of molecules exhibits P–C bond lengths ranging from 1.69^[232] to 1.80 Å^[234], exceeding the respective P–C bonding distance for nonconjugated phosphalkenes, which are found between 1.65 and 1.68 Å.^[235,236] Moreover, the N–C–P–R dihedral angle between the imidazole ring and the P–R_{ph} bond is informative because it is associated with the P_{pπ}-C_{pπ} interaction. In general, *N*-heterocyclic carbene stabilized phosphinidenes adducts can be characterized as polarized phosphalkenes,^[237] which is visualized by the following resonance structures:^[238]



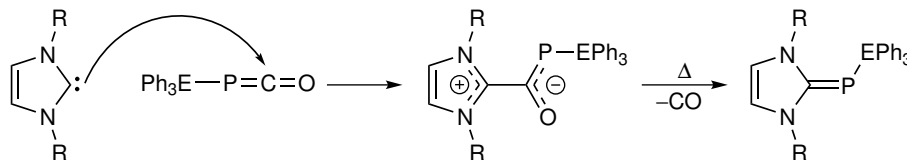
Scheme 4.11: Resonance forms of *N*-heterocyclic carbene-phosphinidene adduct, based on the studies of ARDUENGO^[231] and SCHMIDPETER.^[239]

As a result of the inverse polarization of the P–C bond, the phosphorus atom is electron-rich^[240] (in agreement with resonance forms **B** and **C**). This finding leads to an upfield shifted phosphorus resonance signal, in contrast to phosphalkenes, which are usually found in the region of 230–420 ppm in the ³¹P spectrum.^[226] To conclude, three characteristics to describe the properties of *N*-heterocyclic carbene-phosphinidene adducts were identified. First, the P–C bond length, implying the bonding order.^[230] Second, the N–C–P–R dihedral angle, reaching a value close to zero if the orbital overlap becomes maximal.^[238] And finally, the position of the phosphorous signal in the NMR spectrum, indicating electron density at the phosphorous atom.^[240]

Surprisingly, it took almost 20 years until the first *N*-heterocyclic carbene-phosphinidyne transition metal complex became synthetically accessible.^[241] Even today, this compound class is rarely encountered in coordination complexes.^[233,242] However, an exceptional example of a bimetallic nickel complex featuring this ligand has already been presented at the beginning of this chapter, see Scheme 4.5.^[202] In this case, the anionic [P(NHC)][−] ligand is formed upon the addition of sodium phosphoethynolate to a nickel^I carbene complex (C_pNi(NHC)) (C_p = cyclopentadienyl; NHC = 1,3-bis(2,4,6-trimethylphenyl)-imidazole-2-ylidene), which demonstrates the possibility of synthesizing *N*-heterocyclic carbene-phosphinidyne adducts by the reaction of NHCs with a PCO[−] source.

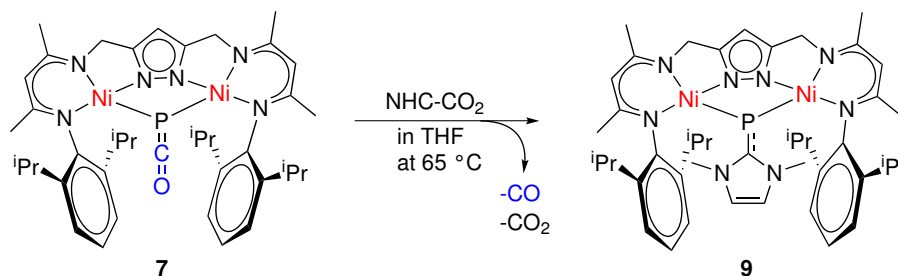
Because the **7** complex is already available, a more convenient synthesis method for generating a carbene-phosphinidyne adduct should involve a phosphaketene metal complex as a precursor. This has been done by GRÜTZMACHER *et al.* by treating the triphenyl tetrel substituted phosphaketenes, such as Ph₃Sn(PCO) and Ph₃Ge(PCO),

with different N-heterocyclic carbenes, see Scheme 4.12.^[243] These phosphaketenes reacted willingly to form the corresponding isolable NHC-phosphaketene adducts (NHC–C(O)PR). Under heating, these complexes decompose under decarbonylation, resulting in the desired NHC-phosphinidene adducts.



Scheme 4.12: Carbene-phosphinidene adduct synthesis from a phosphaketenes complex, where R = DIPP, Mes; E = Sn, Ge.^[243]

Following the same procedure, the phosphaketene complex **7** was reacted with two different carbenes, which only differ in the sterical demand. The first approach was carried out with 1,3-diisopropyl-imidazole-2-ylidene. This attempt was not pursued any further because the ¹H NMR spectrum featured the same characteristic pattern as for the reaction of **7** with PMe₃, clearly indicating dimerization. Therefore a methyl-substituted NHC was used instead. First, the reaction was faster, which means that only two instead of six days were needed for complete conversion. Second, the ¹H NMR spectrum showed the expected signals. The reaction was repeated on a larger scale by treating **7** with 1,3-dimethylimidazolium-2-carboxylate (CO₂–NHC) in THF at 65 °C. At higher temperatures, the carboxylate–NHC releases CO₂ resulting in the free carbene, which then forms, under decarbonylation, the [LNi₂(μ-P(NHC))] complex. Since high temperatures were needed to carry out the reaction, the formation of the hypothetical NHC-phosphaketene intermediate was not observed.



Scheme 4.13: Reaction of **7** with an N-heterocyclic carbene leading to the N-heterocyclic carbene-phosphido nickel complex [LNi₂(μ-P(NHC))] (**8**).

After work-up and crystallization from a 2-Me-THF solution, deep red crystals, suitable for X-ray diffraction, were obtained in moderate yields (55%). The molecular structure of **9** is shown in Figure 4.12 and confirms the molecular constitution of target compound **8**. Moreover, no dimerization reaction like in the synthesis of **8** occurred, which could be correlated with the shorter reaction time of this reaction and the smaller sterical demand of the methyl-substituted carbene.

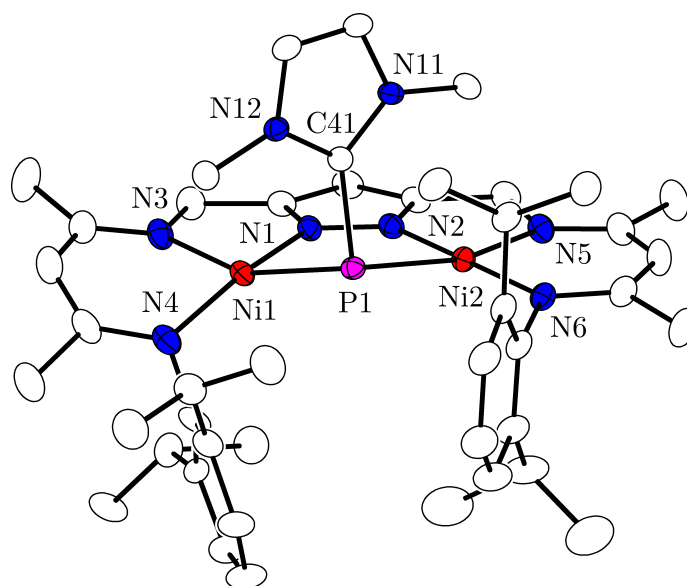


Figure 4.12: Molecular structure of **9** (30% probability thermal ellipsoids). The hydrogen atoms are omitted for clarity.

Table 4.4: Selected bond lengths, distances, and angles of **9**.

Bond length / Å		Distances / Å		Angle / °	
Ni1–N4	1.923(2)	Ni1⋯Ni2	3.6436(6)	N4–Ni1–N1	166.29(9)
Ni1–N1	1.8142(19)	Ni1⋯C41	2.2856(65)	N4–Ni1–N3	93.69(9)
Ni1–N3	1.938(2)	Ni2⋯C41	2.9715(75)	N1–Ni1–N3	81.63(9)
Ni2–N6	1.9044(19)			N6–Ni2–N2	176.25(9)
Ni2–N2	1.8250(19)			N6–Ni2–N5	95.50(8)
Ni2–N5	1.942(2)			N2–Ni2–N5	81.46(8)
Ni1–P1	2.2949(6)			C41–P1–Ni1	93.84(7)
Ni2–P1	2.2714(6)			C41–P1–Ni2	98.58(8)
P1–C41	1.841(2)			Ni1–P1–Ni2	105.87(3)
				N11–C41–N12	103.96(19)

The molecular structure confirmed the expected bimetallic core in which both nickel ions are roughly square-planar coordinated with a Ni⋯Ni separation of 3.6436(6) Å. Interestingly, the binding pocket of Ni1 is slightly twisted, leading to a N4–Ni1–N1 angle of 166.29, which is reminiscent of the coordination environment in the phosphanylidene phosphorane complex **8**, see Table 4.3. The most striking similarity between the complexes **9** and **7** is the related bonding angle between the respective bridging ligand and the nickel centers (averaged bonding angle of the C–P–Ni fragment for **7**: 81.0°, and for **9**: 96.2°). This resemblance points to a comparable bonding situation, which was also shown by theoretical calculations.

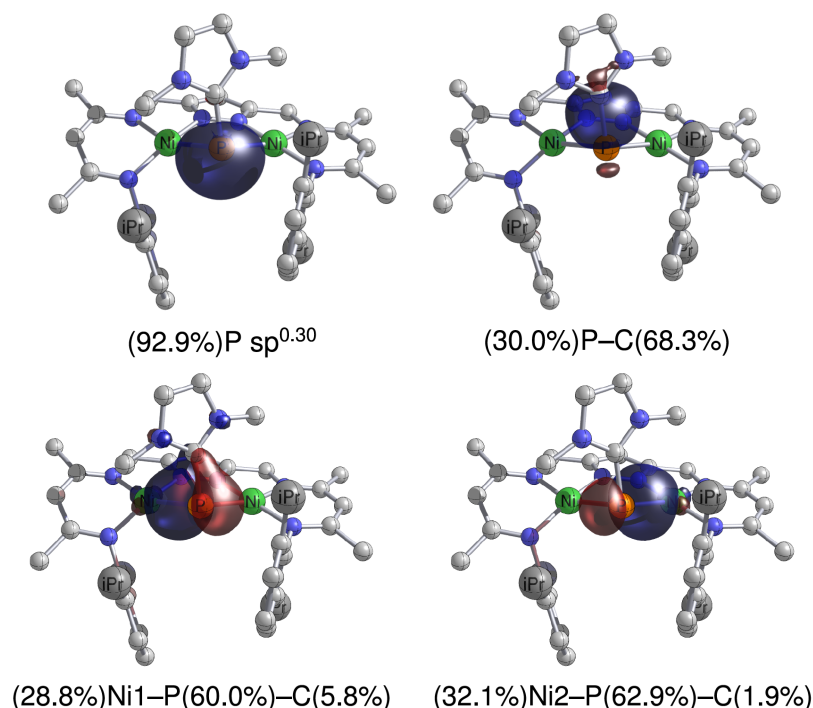


Figure 4.13: Selected NLMOs of **9** resulting from PBE0-D3(BJ)/6-311++G(2d,2p) calculations based on PBEh-3c structures; isovalue $0.05 a_0^{-3/2}$

Table 4.5: Selected properties of the electron density distribution in compounds **9** resulting from PBE0-D3(BJ)/6-311++G(2d,2p) calculations computed at PBEh-3c geometries.

Bond ^[a]	$\rho(r_b)$ ^[b]	$\nabla^2\rho(r_b)$ ^[c]	$H(r_b)/\rho(r_b)$ ^[d]	$G(r_b)/\rho(r_b)$ ^[e]	$\epsilon(r_b)$ ^[f]
Ni1–P1	0.53	1.29	–0.36	0.54	0.03
Ni2–P1	0.55	1.41	–0.37	0.55	0.02
P1–C11	0.96	1.10	–0.87	0.95	0.20
	WBI(A B) ^[g]	$\delta(A B)$ ^[h]	$q(A)/q(B)$ ^[i]		
Ni1–P1	0.49	0.73	0.76 / 0.14		
Ni2–P1	0.55	0.80	0.14 / 0.74		
P1–C11	1.11	1.04	0.14 / 0.37		

^[a]Topological charact. computed at bond critical points (r_b); ^[b]electron den. in $e \text{ \AA}^{-3}$; ^[c]Laplacian of ρ in $e \text{ \AA}^{-5}$; ^[d]rel. total energy den. in Hartree/e; ^[e]rel. kinetic energy den. in Hartree/e; ^[f]ellipticity; ^[g]Wiberg bond index between atoms A and B; ^[h]delocalization index between atoms A and B; ^[i]QTAIM partial charge on atoms A and B in a.u.

In **9**, the P–C interaction is characterized by one pronounced NHC→P donation, accompanied by three weaker P–NHC π backbonding contributions. However, a significant difference is recognized in the more strongly pronounced asymmetry of the P(NHC)–Ni(1/2) binding as for the PCO–Ni(1/2) fragment in complex **7**. The torsion angle of Ni1–P1–C41 is $67.512(190)^\circ$, while the respective Ni2–P1–C41 angle is $-16.105(233)^\circ$, which can be explained by two $\pi(P\rightarrow C)$ backbonding deformation densities $\Delta\rho_3$ and $\Delta\rho_4$. By comparing the Ni(1/2)–P1–C41 angles, this interaction becomes visible as well, as a result, the carbene ligand is tilted by 4.74° towards Ni1. In contrast, the phosphaketene ligand in complex **7** is only slightly tilted by 0.65° due to the presence of only one $\pi(P\rightarrow C)$ backbonding, compare Figure 4.14.

Another variation is found in the P–C bond lengths. The P–C(NHC) bond is significantly elongated in comparison to the P=CO double bond ($d(\text{P}=\text{CO}) = 1.671(5) \text{ \AA}$; $d(\text{P}=\text{C}(\text{NHC})) = 1.841(2) \text{ \AA}$, while the WBI reduces to 1.10 (WBI(P=CO)= 1.67), still surpassing the expected value for a single bond. The P1–C41 bond length in **9** is remarkable as it even exceeds the peak value for a P–C(NHC) distance of $1.8017(18) \text{ \AA}$.^[234]

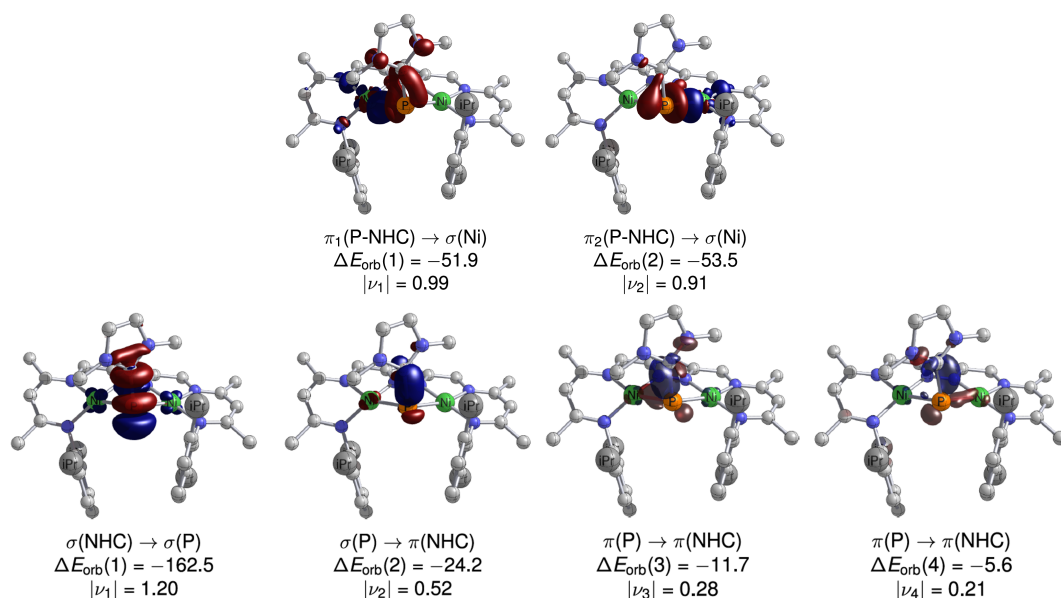


Figure 4.14: Deformation densities $\Delta\rho$ from EDA-NOCV of **9** resulting from PBE0-D3(BJ)/TZ2P//PBEh-3c calculations based on $[\text{LNi}_2(-\text{P})]/[\text{CO}]$ fragmentation (orbital interaction energy contributions ΔE_{orb} in kcal mol^{-1} , charge flow $|\nu_i|$ from red to blue, isovalue $0.005 a_0^{-3/2}$).

Another factor, which must be taken into account, is the P–C interaction. According to a natural bond orbital (NBO) analysis, the associated σ -bonding NLMO is polarized towards the carbene carbon (68.3 %). The $\pi(\text{P} \rightarrow \text{C})$ backbonding contributions are localized mainly on the phosphorous atom (60%), but are weaker as for PCO^- ligand in **7**. To conclude, the donating nature of the P–Ni interaction and the polarized P1–C41 bond lead to a comparative electron-poor phosphorous, which was quantified by BADER'S quantum theory of atoms in molecules (QTAIM), leading to QTAIM partial charges/a.u. of: ($q(\text{P1}: 0.14) / (\text{C41}: 0.37)$).

NMR spectra were recorded with a particular focus on the carbene-phosphido moiety. All peaks in the ^1H and $^{13}\text{C}\{^1\text{H}\}$ NMR spectrum could be assigned, see the numbering scheme in Figure 4.15 and Figure 4.16. As suggested by the molecular structure and theoretical calculations, the P1–C41 bond only shows partial double bond character, allowing relatively free rotation of the carbene fragment. Consequently, a more pronounced double bond would increase the rotational barrier around the PC bond, leading to inequivalent N-substituents of the NHC on the NMR time scale. However, this is not the case. At -35°C , one sharp singlet corresponding to equivalent methyl groups of the carbene is found at 4.06 ppm in the ^1H NMR spectrum, compare no. 2 in the numbering scheme. The same applies to the hydrogen resonance of the carbene (no. 3). In contrast, two septets for the isopropyl groups (no. 9 and 12) are found.

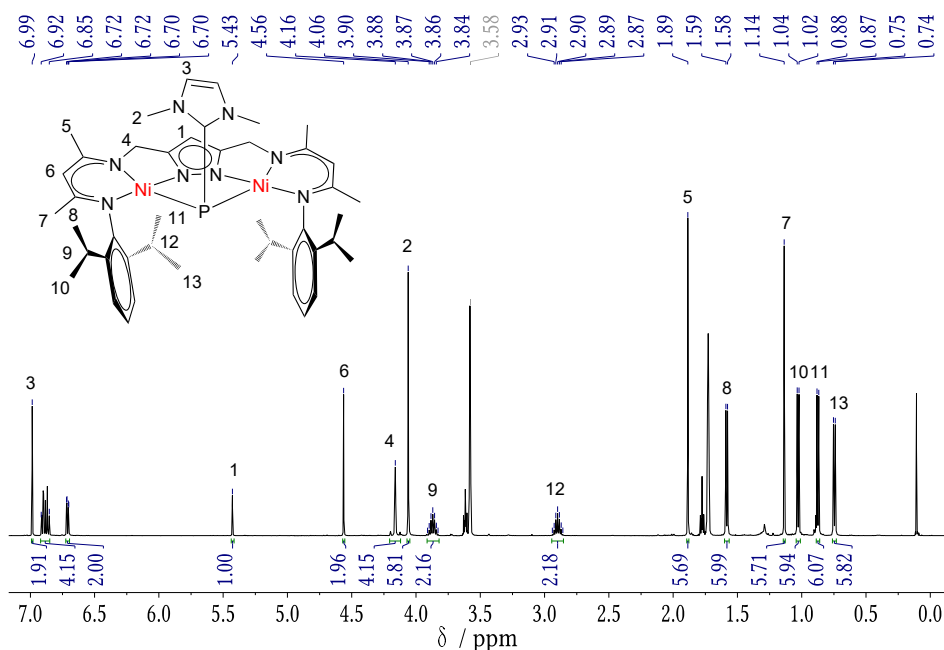


Figure 4.15: ^1H NMR spectrum of **8** at -35°C in $\text{THF-}d_8$, including numbering scheme.

The $^{13}\text{C}\{^1\text{H}\}$ NMR spectrum shows the same symmetry as the ^1H NMR spectrum. However, a doublet can be assigned to the methyl groups of the carbene at 38.5 ppm, which originates from coupling with the phosphorous atom $^3J_{\text{PC}(2)} = 4\text{ Hz}$. These results indicate an unhampered rotation of the ligand. Albeit the carbene fragment does not oscillate as the PCO^- ligand in **7**, compare Figure 4.5. Therefore, **9** only features a σ_h mirror plane, which result in a C_s symmetry on the NMR time scale. Consequently, the DIPP groups only show one set of signals (no. 12-19) in the $^{13}\text{C}\{^1\text{H}\}$ NMR spectrum.

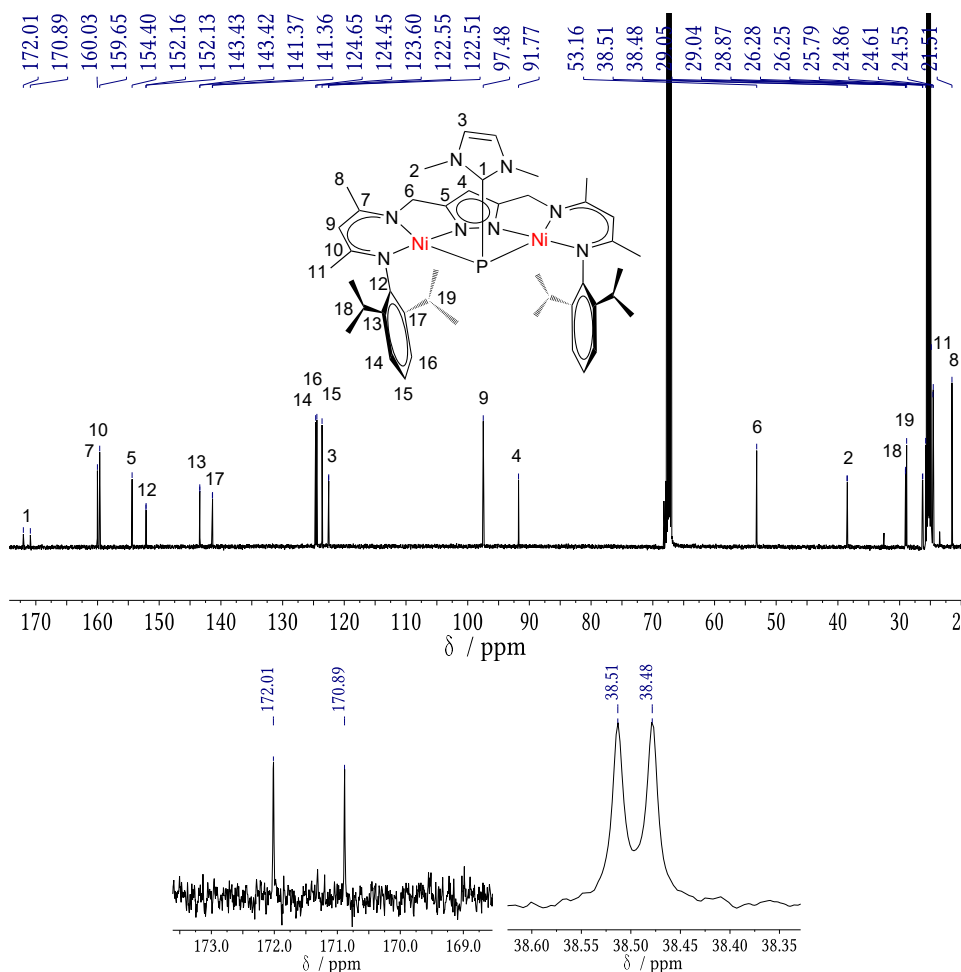
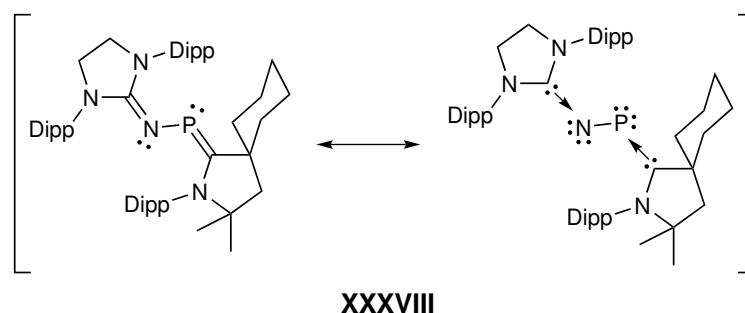


Figure 4.16: $^{13}\text{C}\{^1\text{H}\}$ NMR spectrum of **8** at -35°C in $\text{THF-}d_8$, including numbering scheme. The magnifications below show two doublets. The first one at 171.5 ppm was assigned to C1 with a coupling constant of $^1J_{\text{PC}(1)} = 142$ Hz. The second doublet at 38.5 ppm was assigned to C2 with a coupling constant of $^3J_{\text{PC}(2)} = 4$ Hz.

At the beginning of this chapter, the resonance forms of *N*-heterocyclic carbene-phosphinidene adduct were presented, see Scheme 4.11. To define the most contributing structure, ^{31}P NMR spectroscopy can be used since it provides a rough estimate of the electron density at the phosphorous atom. In general, it can be presumed that an electron-rich phosphorus atom is upfield shifted (resonance form **B** and **C** in Scheme 4.11) and *vice versa*. This method was exploited in numerous cases by organic chemists to gain insight into the bonding situation.^[238] A simple example is given by comparing the ^{31}P signals of the carbene-phosphinidene adducts 1,3-dimethyl-2-phosphanylidene-2,3-dihydro-1*H*-imidazole (NHC=PH) with 1,3-dimethyl-2-(phenylphosphanylidene)-2,3-dihydro-1*H*-imidazole (NHC=PPh). While the parent carbene-phosphinidene NHC=PH features a phosphorous resonance at -149.3 ppm,^[244] the corresponding NHC=PPh species features a downfield shifted signal at -49.1 ppm^[245] in the ^{31}P spectrum upon replacement of the hydrogen atom for an electron-withdrawing phenyl group. The herein discussed complex (**9**) bears the same carbene-phosphinidene ligand resulting in a signal at 44.78 ppm in the ^{31}P spectrum, see Figure B.36. Following the previously described argumentation, the phosphorous atom must be electron-deficient, which would indicate a profound charge flow to the bonded Ni^{II} metal centers. Additionally, the doublet at 171.45 ppm in the $^{13}\text{C}\{^1\text{H}\}$ spectrum (inset, Figure 4.16) follows the same trend. However, this

effect is much weaker^[245] (for comparison, NHC=PH $\delta^{13}\text{C} = 176.0$ ppm).^[244] This hypothesis was again underpinned by computational chemistry, unambiguously identifying the dative ligand-to-metal bonding interactions for both the P1→Ni1 and P1→Ni2 bonds.

Further information to characterize the bonding situation can be derived by electrochemistry. This was done by ARDUNEGO *et al.*, who examined the redox properties of NHC=PPh (NHC = 1,3-bis(2,4,6-trimethylphenyl)imidazole-2-ylidene (IMes)) by cyclic voltammetry (CV), revealing an irreversible one-electron oxidation at -0.08 V (vs SCE).^[230] This relatively low oxidation potential indicates a high electron density at the phosphorus center, corresponding to resonance form C (Scheme 4.11).^[230] For comparison, the one-electron oxidation potentials of phosphalkenes are found in the range of 1.07-2.94 V (vs SCE).^[246] The one-electron oxidation of a carbene-phosphinidanyl would result in the corresponding radical cation. Such a species was isolated by treating a CAAC-phosphinidene-PN adduct (CAAC = cyclic alkyl amino carbene) with $[\text{Ph}_3\text{C}][\text{B}(\text{C}_6\text{F}_5)]$, the bis(carbene)-PN compound is displayed in Figure 4.14.^[247] The cyclic voltammogram of the neutral compound shows two redox events, one reversible one-electron oxidation at $E_{1/2} = -0.51$ V vs Fc^+/Fc , and a second irreversible oxidation at 0.6 V. The reversibility of the first oxidation was experimentally verified by the addition of the strong reductant (KC_8) to the oxidized species, regaining the neutral compound. DFT calculations of a slightly simplified model complex were performed to obtain information about the spin distribution of the oxidized carbene-phosphinidanyl adduct, pointing out that the highest spin density is located on the phosphorous atom.



Scheme 4.14: Resonance forms of the bis(carbene)-PN adduct XXXVIII.^[247]

Driven by these reports, the electrochemical properties of **9** were investigated by cyclic voltammetry as well, see Figure 4.17. The experiment was performed under inert conditions at ambient temperature in THF with Bu_4NPF_6 (0.2 M) as electrolyte. The data was referenced to the Fc/Fc^+ redox couple. The cyclic voltammogram of **8** shows two redox events. The reductive regime shows one irreversible reduction wave centered at -2.86 V vs Fc/Fc^+ , which is most likely associated with the reduction of the metal centers. In contrast, the oxidative region of the cyclic voltammogram shows one reversible oxidation, appearing at -0.58 V that fulfills the criteria for a reversible process, see Figure 4.18.

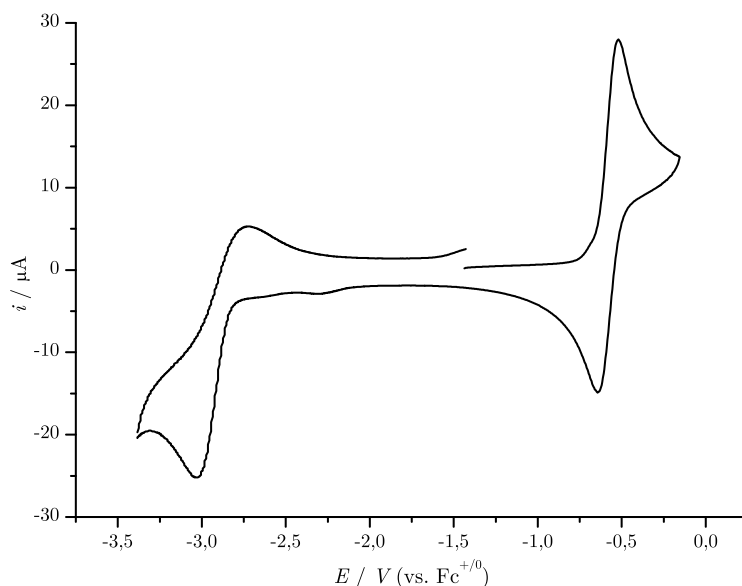


Figure 4.17: Cyclic voltammogram (vs Fc/Fc⁺) of **8** (THF, 0.1 M Bu₄NPF₆) at a scan rate of 100 mV · s⁻¹.

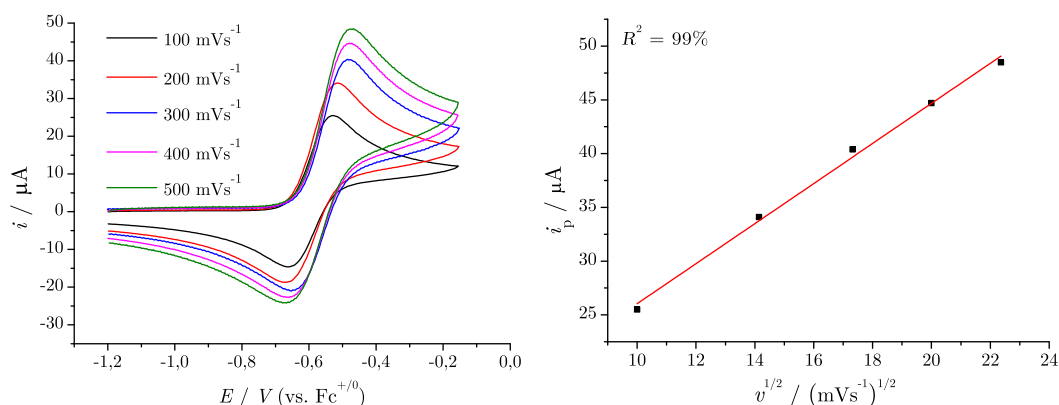


Figure 4.18: **Left:** Fully reversible oxidation wave ($E_{1/2} = -0.58$ V) at 100 mV · s⁻¹ (black), 200 mV · s⁻¹ (red), 300 mV · s⁻¹ (blue), 400 mV · s⁻¹ (magenta), and 500 mV · s⁻¹ (green). **Right:** Reversible electron transfer indicated by the Randles-Sevcik plot that verifies the linearity between the peak current (anodic) and the square root of the scan rate.

It is reasonable to assume that the carbene-phosphido moiety is involved in the process. Interestingly, the oxidation potential is similar to the system mentioned above ($\Delta E_{1/2} = -0.07$ V), although the example dealt with a neutral carbene-phosphinidene adduct. In contrast, the oxidation of the anionic [P(NHC)]⁻ ligand unit would formally lead to the corresponding neutral [P(NHC)] species. Alternatively, the oxidation of the nickel ions from Ni^{II} to Ni^{III} or the oxidation of the ligand scaffold **L** are conceivable.

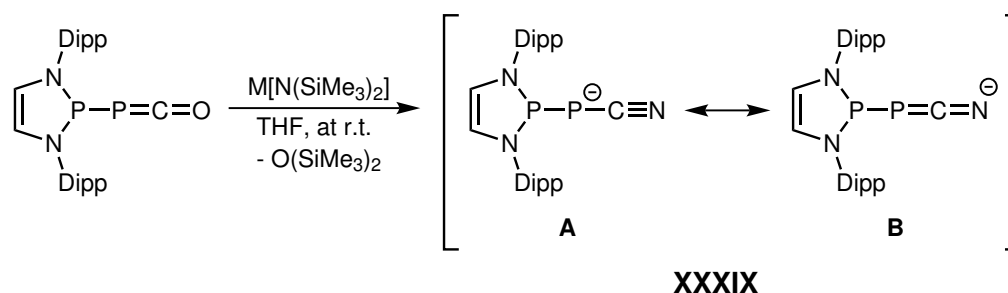
The successful substitution of the carbonyl fragment of the PCO ligand by an *N*-heterocyclic carbene has been demonstrated, yielding a bimetallic *N*-heterocyclic carbene-phosphido nickel complex. In addition, the unintended dimerization of the ligand could be avoided by using a sterically undemanding reagent. Hence, this reaction provides an encouraging outlook for potential follow-up reactions of the phosphaketene complex 7.

4.7 An Isocyanide-Phosphido Complex

In the previous chapters, it was illustrated that the PCO^- ligand of **7** can be transformed into different ligands within the dinickel cleft. Since this kind of reaction triggers the release of CO, complex **7** formally transfers P^- on the respective substrate, which allows the synthesis of phosphorus-based compounds stabilized by the bimetallic pocket. While the interaction of phosphaketenes with LEWIS bases, such as carbenes, has been extensively described, the reactivity with isocyanides ($\text{R}-\text{N}\equiv\text{C}$) has recently gained more attention.^[248] In that sense the conversion of an isocyanide to a cyanophosphide $\text{P}-\text{C}\equiv\text{N}^-$ unit is desirable.

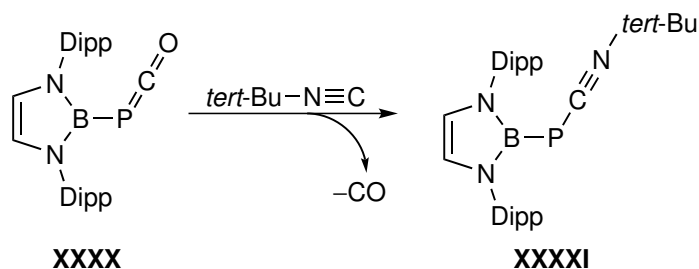
Various synthetic procedures are known in the literature to generate cyanophosphides. However, for the first time, SCHMIDPETER *et al.* reported the isolation of a carbene-cyanophosphinidene unit ($\text{NHC}-\text{PCN}$) by reductive decyanation of di-cyanophosphines ($\text{RP}-(\text{CN})_2$).^[239] Another possibility to generate PCN functionalities involves the deoxygenation of isocyanates (RNCO) using silylphosphines ($\text{R}_2-\text{P}-\text{Si}(\text{Me})_3$)^[249,250] Alternatively, coupling reactions of isocyanides with phosphinidene fragments offers a further synthetic route to disubstituted cyanophosphide compounds.^[251-255] In this matter, it is worth noting that a synthesis following this approach has been presented earlier in this work, see Scheme 4.7.

However, only a few examples deal with the reactivity of the phosphoethanolate anion or the related phosphaketene ligand towards isocyanides. An unusual example, including a PCO unit, for synthesizing monosubstituted cyanophosphide has been presented by GRÜTZMACHER *et al.* They have established a synthetic route for converting phosphaketenes *via* metathesis into PCN building blocks. By treating $\text{NHP}-\text{PCO}$ ($\text{NHP} = \text{N}$ -heterocyclic phosphonium) with $\text{M}[\text{N}(\text{SiMe}_3)_2]$ ($\text{M} = \text{Na}, \text{K}$), the O is isoelectronic replaced for $[\text{N}]^-$, leading to the previously unknown phosphanyl cyanophosphide $[\text{NHP}-\text{PCN}]^-$ compound, see Scheme 4.15.^[212]



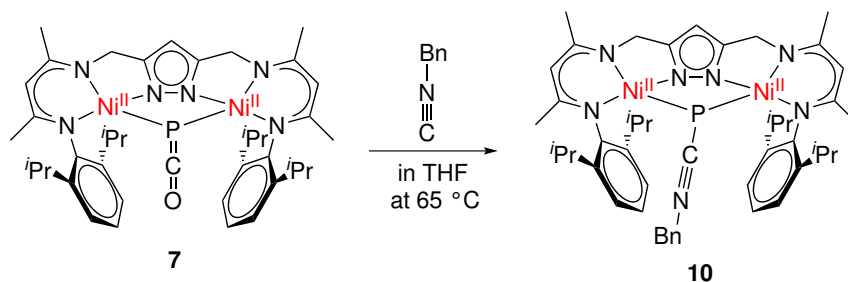
Scheme 4.15: Synthesis of phosphanyl cyanophosphide salts (XXXIX).^[212]

Consequently, complex **7** was treated with KHMDS as well, which did not afford any useful results. An alternative synthetic protocol, which involves an isocyanide and a phosphaketene species, was reported by GOICOECHEA *et al.*^[248] They described the conversion of a phosphoethynolato-borane $[\text{B}]\text{PCO}$ with four equivalents of (*tert*-butyl)isocyanide into the respective $[\text{B}]\text{PCN-tert-Bu}$ compound upon decarbonylation, see Scheme 4.16:



Scheme 4.16: Synthesis of a isocyanide-stabilized phosphinidene (XXXXI).^[248]

Inspired by these studies, **7** was treated with stoichiometric amounts of isocyanides, starting with *tert*-Bu isocyanide. Since no conversion was monitored by ¹H NMR spectroscopy, the temperature was increased, resulting in the same reaction conditions as for the beforehand presented synthesis of complex **8**. Unfortunately, this reaction was accompanied again by the dimerization of the ligand system, which could be clearly identified by the typical peak pattern for the methylene-linker unit. Based on the experience acquired with the [LNi₂(μ-P(NHC))] (**9**) complex, this reaction can be avoided using a less demanding reagent. Therefore, benzyl isocyanide was used instead. Upon decarbonylation, the desired complex [LNi₂(μ-PCNBn)] (**10**) was obtained, see Scheme 4.17:



Scheme 4.17: Reaction of **7** with benzyl isocyanide leading to the cyanophosphide nickel complex [LNi₂(μ-PCNBn)] (**10**).

After work-up and crystallization from a 2-Me-THF solution, deep red crystals suitable for XRD were obtained. The obtained molecular structure confirmed the formation of a PCN-Bn unit, see Figure 4.19. In agreement with the ¹H NMR spectrum, no dimerization reaction of the ligand took place.

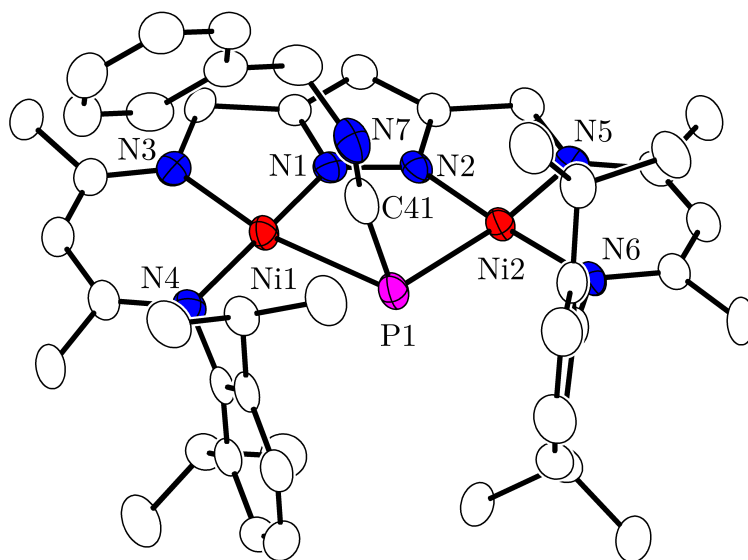


Figure 4.19: Molecular structure of **10** (30% probability thermal ellipsoids). The hydrogen atoms are omitted for clarity..

Table 4.6: Selected bond lengths, distances, and angles of **10**.

Bond length / Å		Distances / Å		Angle / °	
Ni1–N4	1.899(5)	Ni1···Ni2	3.7083(12)	N4–Ni1–N1	173.0(2)
Ni1–N1	1.824(5)	Ni1···C41	2.286(6)	N4–Ni1–N3	95.0(2)
Ni1–N3	1.919(5)	Ni2···C41	2.9715(75)	N1–Ni1–N3	81.8(2)
Ni2–N6	1.893(5)			N6–Ni2–N2	176.9(2)
Ni2–N2	1.825(5)			N6–Ni2–N5	95.3(2)
Ni2–N5	1.911(5)			N2–Ni2–N5	81.9(2)
Ni1–P1	2.2801(17)			C41–P1–Ni1	66.2(2)
Ni2–P1	2.2801(17)			C41–P1–Ni2	95.0(2)
P1–C41	1.719(8)			P1–C41–N7	168.5(6)
C41–N7	1.197(9)			Ni1–P1–Ni2	106.41(7)

Both nickel^{II} centers show an almost perfect square planar coordination environment, and they are separated by a distance of 3.7083(12) Å. The ligand within the pocket is profoundly inclined towards the Ni1 center, resulting in a Ni1–P1–C41/Ni2–P1–C41 angle of 66.2(2)/95.0(2)°. The obtained interatomic distance for P1–C41 is 1.719(8) Å, which only slightly exceeds the literature known value for P=C double bonds of 1.69 Å (ref.: P–C single bonds: 1.86 Å).^[256,257] To describe the C–N binding situation, the molecular structure and IR spectroscopy were taken into account. The C–N bond distance is 1.197(9) Å and the corresponding stretching frequency is found at 1808 cm⁻¹ (calc. : 1816 cm⁻¹) in the IR spectrum, see Figure 4.20. These results lie between the reference numbers for imines ($d(\text{C}=\text{N}) = 1.27 \text{ Å}$; $\nu_{\text{CN}} = 1640 \text{ cm}^{-1}$) and nitriles ($d(\text{C}\equiv\text{N}) = 1.16 \text{ Å}$; $\nu_{\text{CN}} = 2250 \text{ cm}^{-1}$),^[256,257] indicating no clear preference for one of the two possible canonical forms (P=C=N/P–C≡N).

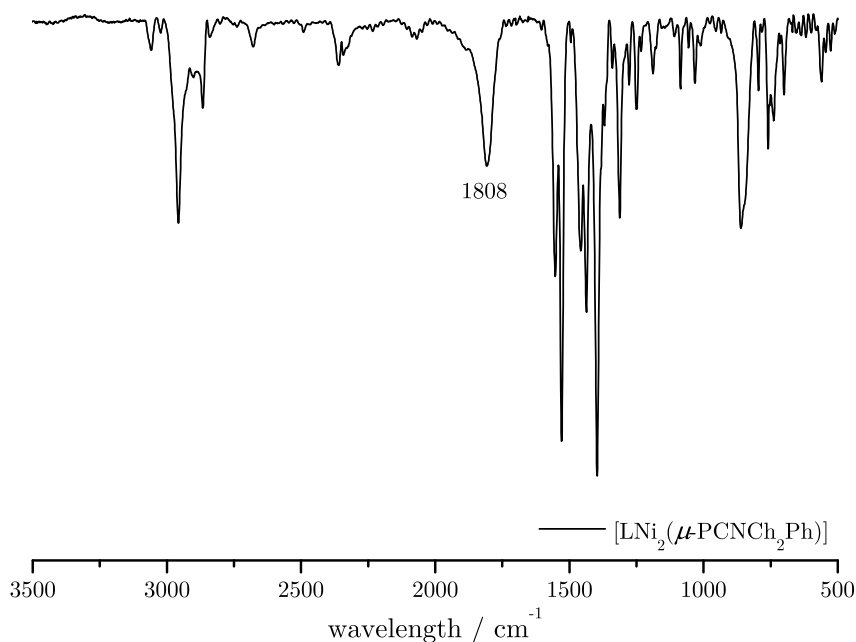


Figure 4.20: IR (KBr) spectrum of **10**. The labeled peak at 1808 cm^{-1} represents the antisymmetric C–N stretching vibration of the isocyanide-phosphido ligand.

Since identifying the most contributing resonance form is valuable information for possible follow-up reactivities, literature known compounds were compared with complex **10**. The cyanophosphide species (**XXXIX**), presented in Scheme 4.15, exhibits similar bond lengths and spectroscopical features. In comparison to the PCN unit in complex **10**, the corresponding PCN unit shows a slightly elongated P–C bond of 1.75 \AA as well as shortened C–N bond of 1.16 \AA . Based on the comparable bond length, it is noticeable that the (C–N) stretching vibration of **XXXIX** appears at higher frequencies of around 2067 cm^{-1} ($\Delta\nu_{\text{CN}} = 259\text{ cm}^{-1}$). This finding might be linked with the different bonding angles of the PCN moieties, while complex **10** features a P1–C41–N7 angle of $168.5(6)^\circ$, the respective PCN unit of the phosphanyl cyanophosphide is nearly linear ($177.0(2)^\circ$). Additionally, in complex **10**, the Ni1 ion is located at a distance of $2.286(6)\text{ \AA}$ from the C41 atom, which could influence the stretching vibration as well. However, GRÜTZMACHER *et al.* concluded that the phosphanyl cyanophosphide compound is best described as [NHP]P–C≡N species, see Scheme 4.15 (A). In contrast, the PCN fragment in **10** shows a larger contribution of the resonance form **B** (P=C=N). This assumption is supported by recently published studies by JUNGHANS and FISCHER addressing 1,3-phosphaazalenes (RP=C=NR).^[258] These compounds share several characteristic properties with the presented PCN unit of **10**, such as a slightly bent P–C–N angle around 170° and a similar bonding length. Moreover, these compounds exhibit an asymmetric stretching vibration (ν_{CN}) between 1830 and 1915 cm^{-1} .^[259]

Further characterization was carried out by NMR spectroscopy while special attention was paid to the isocyanide-phosphido ligand. In the ^1H NMR spectrum, all peaks could be assigned, see Figure 4.21. Thereby it was found that the ligand in the bimetallic pocket of **10** oscillates in a comparable way as the PCO ligand in **7**, compare Figure 4.5. At -35°C , the ^1H NMR spectrum (Figure 4.5 (top)) of **10** shows equivalent resonances for the nacnac sidearms (no. 5 to 7) but two resonances for the CH_2 linker units (no.4 and 14). The latter finding can be explained by the strongly

inclined binding of the ligand within the pocket. In line with the presumed dynamic, the ^1H NMR spectrum features C_{2v} symmetry at higher temperatures. As a result, the resonances associated with the CH_2 linker unit (no. 4) and the isopropyl units of the DIPP groups (no. 9-13) are merging together at r.t. This indicates that the barrier for the oscillation of the ligand is significantly higher in **10** as for **7**.

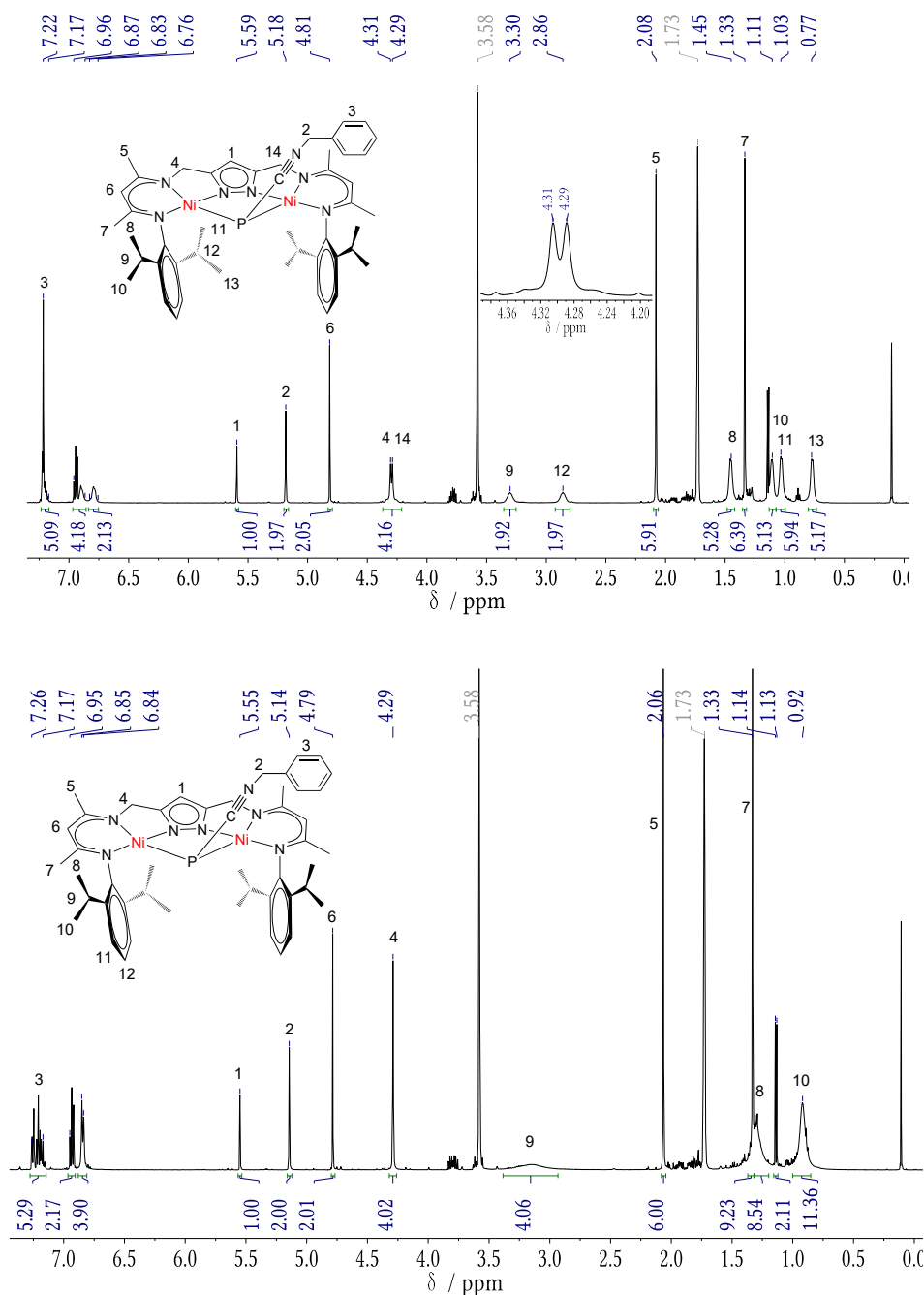


Figure 4.21: ^1H NMR spectrum of **10** at different temperatures in $\text{THF-}d_8$. **Top:** -35°C and **Bottom:** r.t.

In the ^{31}P NMR spectrum (Figure B.42), one singlet with a chemical shift of $\delta = -84$ ppm was detected, which is a comparable value to the phosphanyl cyanophosphide **XXXIX**, displayed in Scheme 4.15 ($\delta = -104$ ppm).^[212] Further, the nitrogen of

the PCN fragment was identified by ^1H - ^{15}N -HMBC NMR spectroscopy, showing a coupling with the methylene unit of the benzene at -159 ppm. In addition, the carbon of the PCN unit was identified in the $^{13}\text{C}\{^1\text{H}\}$ spectrum, displaying a doublet at $\delta_{\text{C}} = 172.7$ ppm with a coupling constant of $^1J_{\text{PC}} = 131$ Hz (Figure 4.22). For comparison, 1,3-phospha-azaallenes are usually found between 170-210 ppm,^[259] whereas cyanophosphides appear at higher field around 140 ppm.^[212] In agreement with the identified stretching vibration of the CN unit, the diagnostic chemical shift of C41 in the $^{13}\text{C}\{^1\text{H}\}$ NMR spectrum indicates a phosphazaallene resonance form.

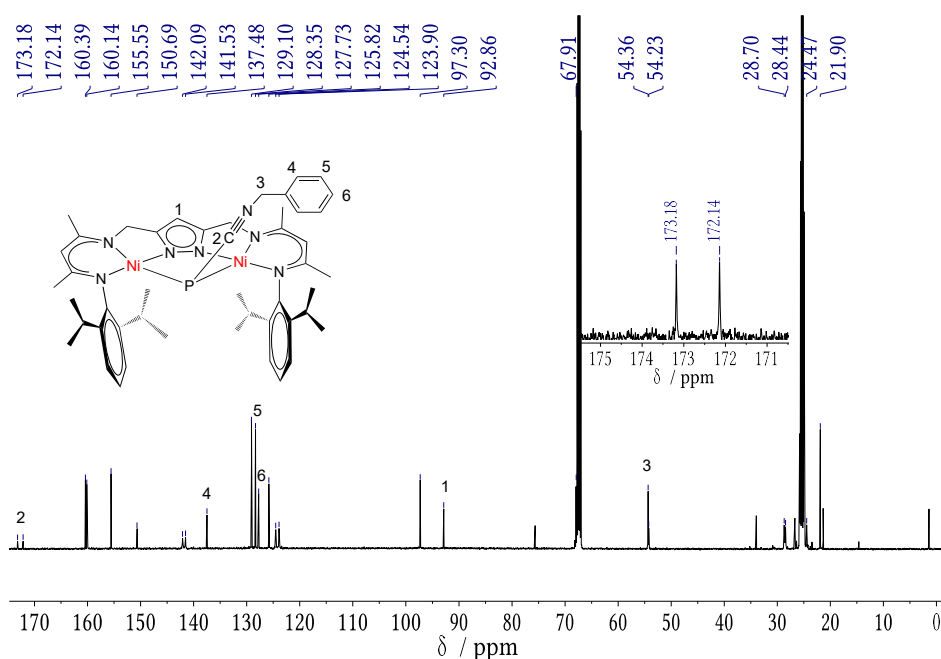


Figure 4.22: $^{13}\text{C}\{^1\text{H}\}$ NMR spectrum of **10** at -35°C in $\text{THF-}d_8$. The inset shows doublet at $\delta_{\text{C}} = 172.7$ ppm, which was assigned to C41 with a coupling constant of $^1J_{\text{PC}} = 130$ Hz.

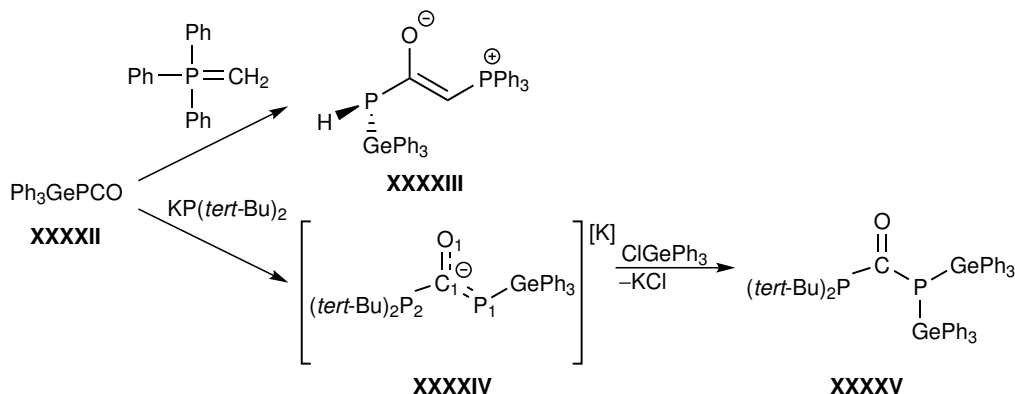
The previously established synthetic strategy for the synthesis of **9** has been successfully applied to generate an isocyanide-phosphido complex **10**. It can be assumed that both syntheses share a comparable reaction mechanism, including the attack of the carbon atom of the phosphaketene unit by an uncharged nucleophile. This initiates the decarbonylation reaction and eventually results in the formation of a phosphorous-based ligand. Additionally, the dimerization reaction, which was observed for **8**, could be circumvented for **8** and **10** by using sterically undemanding substrates. To fully understand the bonding situation, computational methods would be helpful, though IR and NMR spectroscopy delivered valuable information to characterize the most contributing resonance forms. To summarise, the structural data is very similar to the literature reported examples of cyanophosphides; in contrast, spectroscopical methods support the presence of cumulated double bonds ($\text{P}=\text{C}=\text{N}$).

During the reaction, it was not possible to identify the formation of an intermediary phosphaketene-adduct. This circumstance can be attributed to the required high reaction temperatures, which facilitate the release of the CO fragment, see Scheme 4.12. In order to isolate such a species, the next logical step would be to find a reagent that reacts under mild reaction conditions. Thus, the next chapter will describe the reaction of **7** with a more potent nucleophile.

4.8 Synthesis of a Diphospha-Urea Derivative

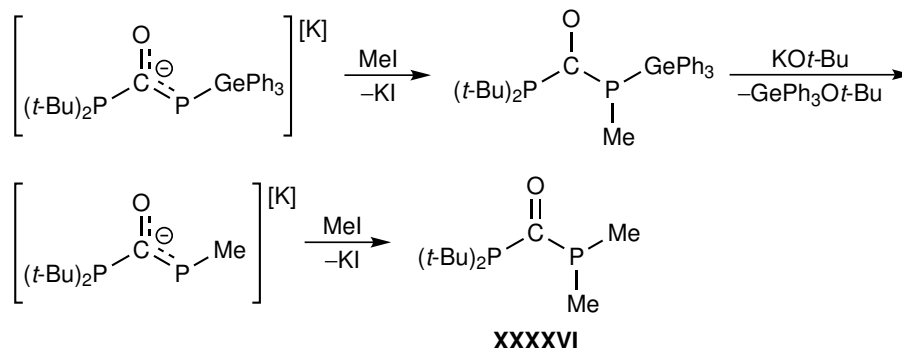
In the previous chapters, the transformation of the phosphaketene ligand of complex **7** was illustrated. However, the reaction mechanism is ambiguous. It can be assumed that the reaction proceeds *via* the nucleophilic attack on the carbon of the PCO ligand, compare Figure 4.12 Unfortunately, no intermediates were detected during the syntheses of **9** or **10**, which can be explained by the applied high temperatures. The previous chapters dealt with the reactivity of **7** with uncharged carbenes and isocyanides. Another potential reactivity includes the usage of an anionic species. However, two factors must be considered beforehand. First, the substrate should not be too bulky to circumvent the dimerization of the ligand. Second, it has been shown in previous studies dealing with the herein used nickel system that two times reduced species in the pocket are best stabilized by potassium ions. Taking these aspects into account, the reactivity of **7** with potassium diphenylphosphide KPPH_2 was tested. In analogy to the reaction of complex **7** with PMe_3 (compare subsection 4.5), the final reaction product should feature a diphosphido unit. Additionally, the isolation of the intermediary phosphaketene adduct is pursued.

As illustrated in the proceeding subsections, the PCO moiety serves as a versatile building block for synthesizing phosphorus-containing compounds. In this regard, STEPHAN *et al.* recently published a synthetic procedure to obtain primary acylphosphines (**XXXXIII**) using a phosphaketene reagent. By treating the triphenylgermanylphosphaketene Ph_3GePCO (**XXXXII**) with the WITTIG reagent methylenetriphenylphosphorane, a ylide stabilized primary acyl phosphine (**XXXXIII**) was isolated, see Scheme 4.18, upper line. More closely related to the reaction of **7** with diphenylphosphide, they also described the reaction of the same germanyl phosphaketene synthon (**XXXXII**) with different alkali phosphides.^[260] Due to the fact that an additional phosphorous moiety instead of an organyl group is introduced, this reaction afforded an acylphosphine phosphide or diphospha-urea derivative (**XXXXVI**). By treating **XXXXII** with the strong nucleophilic reagent, $\text{KP}(\text{tert-Bu})_2$, an asymmetric diphospha-urea derivate (**XXXXIV**) is formed, see scheme 4.18, bottom line. Moreover, the subsequent addition of the halide precursor ClGePh_3 afforded a bimetallic complex(**XXXXV**):



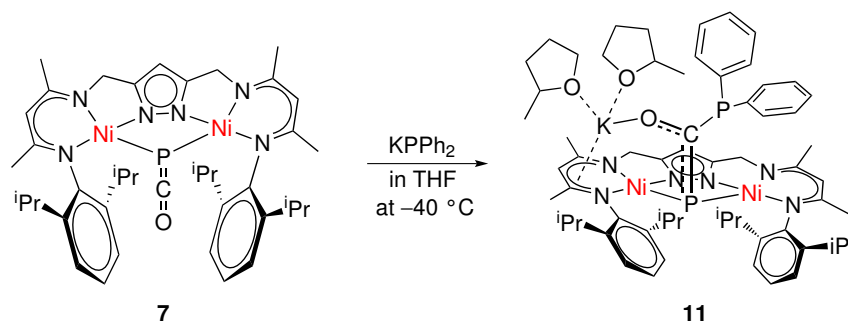
Scheme 4.18: **Top:** Reaction of Ph_3GePCO (**XXXXII**) with a WITTIG reagent resulting in a primary acylphosphine species (**XXXXIII**). **Bottom:** Synthetic route towards a diphospha-urea derivative (**XXXXV**) coordinated by two GePh_3 units.^[260]

Interestingly, the GePh_3 fragments serve as protective groups for the phosphorous moiety. According to a previously established deprotection strategy,^[211] the GePh_3 units can be removed, yielding the asymmetric diphospha-urea derivate (**XXXXVI**) :



Scheme 4.19: P–Ge bond-deprotection strategy resulting into the asymmetric diphospha-urea derivate (**XXXXVI**).^[260]

A similar approach as in Scheme 4.18 (bottom line) was chosen in the present work to synthesize a diphospha-urea complex, see Scheme 4.20. Because of the high thermosensitive, all steps were carried out at cold temperatures. By treating **1^{Br}** with a 0.5 M THF solution of potassium diphenylphosphide, a rapid color change of the solution from red to deep red was observed. Single crystals of the air and moisture-sensitive product $\text{K}[\text{LNi}_2(\text{PC}(\text{O})\text{PPh}_2)]$ (**11**) were obtained in moderate yields (40%) by layering the 2-Me-THF solution with hexane at -38°C . The formation of a diphospha-urea derivate was evidenced by X-ray diffraction.



Scheme 4.20: Reaction of **7** with potassium diphenylphosphide leading to the formation of a diphospha-urea derivate nickel complex $\text{K}[\text{LNi}_2(\text{PC}(\text{O})\text{PPh}_2)]$ (**11**).

The molecular structure of **11** is displayed in Figure 4.23 and reveals an unexpected placement of the potassium counterion. In comparison with the dihydrido complex **2^K** or the corresponding peroxido complex **XIV** (compare Section 1.3.6), it could have been assumed to find the K^+ cation between the aryl rings of the ligand scaffold **L**. However, in this case the potassium ion is located over the nacnac subunit interacting with the electron-rich oxygen of the ligand and two THF molecules. One factor contributing to this different position of the counterion is the Ni–P–C bond angle in **11**, which is similar to the herein presented phosphaketene derivatives. As the bond angle is close to 90° , it is reasonable that the potassium cation is preferably located over the nacnac subunit, stabilizing the electron-rich substrate by withdrawing charge density.

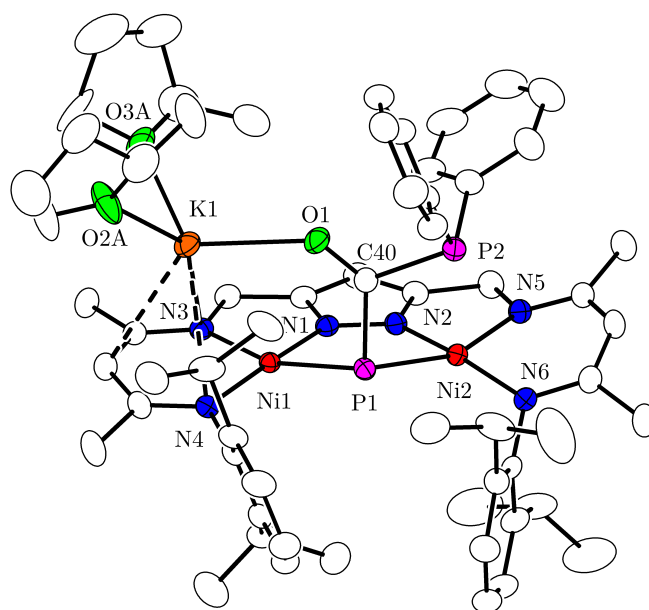


Figure 4.23: Molecular structure of **11** (30% probability thermal ellipsoids). K^+ ...nacnac contacts are shown as dashed lines.

Table 4.7: Selected bond lengths, distances, and angles of **11**.

Bond length / Å		Distances / Å		Angle / °	
Ni1–N4	1.8997(19)	Ni1...Ni2	3.6795(6)	N4–Ni1–N1	174.46(8)
Ni1–N1	1.8250(19)	Ni1...K1	3.1269(6)	N4–Ni1–N3	95.79(8)
Ni1–N3	1.9375(19)	Ni2...P1	3.1250(8)	N1–Ni1–N3	81.69(8)
Ni2–N6	1.901(2)	K1...O1	2.7853	N6–Ni2–N2	169.58(8)
Ni2–N2	1.819(2)	K1...nacnac [†]	2.5905(18)	N6–Ni2–N5	95.21(9)
Ni2–N5	1.921(2)			N2–Ni2–N5	81.9(2)
Ni1–P1	2.2688(6)			C40–P1–Ni1	95.86(8)
Ni2–P1	2.2711(7)			C40–P1–Ni2	91.27(8)
P1–C40	1.806(2)			Ni1–P1–Ni2	108.28(3)
P2–C40	1.908(2)			P1–C40–P2	113.11(12)
O1–C40	1.241(3)			P1–C40–O1	127.63(18)
				P2–C40–O1	119.12(17)

[†]Distance between K1 and the center of the plane spanned by the nacnac subunit

Both Ni^{II} centers exhibit a slightly distorted square-planar coordination environment and are separated by a distance of 3.6795(6) Å. The ligand within the pocket is slightly tilting towards the Ni2 center, resulting in Ni1–P1–C40/ Ni2–P1–C40 angles of 95.86(8)/91.27(8)°. The interatomic distance for P1–C40 is 1.806(2) Å, which corresponds to a shortened P–C single bond, while the bond length P2–C40 of 1.908(2) Å only marginally exceeds the reference value of a P–C single bond of 1.86 Å.^[257] The C40–O1 distance is 1.241(3) Å, which surpasses the reference length of approximately 1.22 Å for a C=O double bond.^[261] This bonding situation resembles that of the anionic diphospha-urea derivate (**XXXXIV**), displayed in Scheme 4.18 ($d(C1–O1) = 1.246(3)$ Å; $d(P1–C1) = 1.901(3)$ Å; and $d(P1–C2) = 1.779(3)$ Å). However, in contrast to **11**, no potassium ion is found in the coordination sphere of **XXXXIV**.

The phosphaketene unit of complex **7** shows a characteristic stretching vibration in the IR spectrum, which is expected to be downshifted upon the transformation into a diphospha-urea species. While comparable species exhibit CO stretching vibrations around 1550 cm^{-1} , such a feature is unidentifiable for complex **11** because of overlapping peaks in this region. However, mass spectrometry was more conclusive.

The ESI(+)-MS-spectrum of **11** in THF did not show a signal consistent with the expected mass to charge ratio calculated for complex **11** (exact mass = 1176.43 u); instead, a nickel species is found at $m/z = 1218.4$, see Figure 4.24, top line. However, the peak with the highest intensity at $m/z = 937.4$ ($[M-(K(2\text{-Me-THF})_2; CO)]$) is more informative since it can be attributed to a decarbonylation reaction, leading to a diphosphene nickel species. This finding is particularly interesting since it correlates with the initially presumed decomposition pathway of the diphospha urea unit. Even though both signals show the expected isotopic pattern (see Figure 4.24, bottom line) and could be detected separately by tandem mass spectrometry (MS/MS), it is noteworthy that this species should be negatively charged since no additional protons were detected. Lastly, at $m/z = 753.4$, the same species as in Figure 4.8 is detected, which is assumed to be a pnictogen species $[M-(K(2\text{-Me-THF}); CO; PPh_2)+H]$.

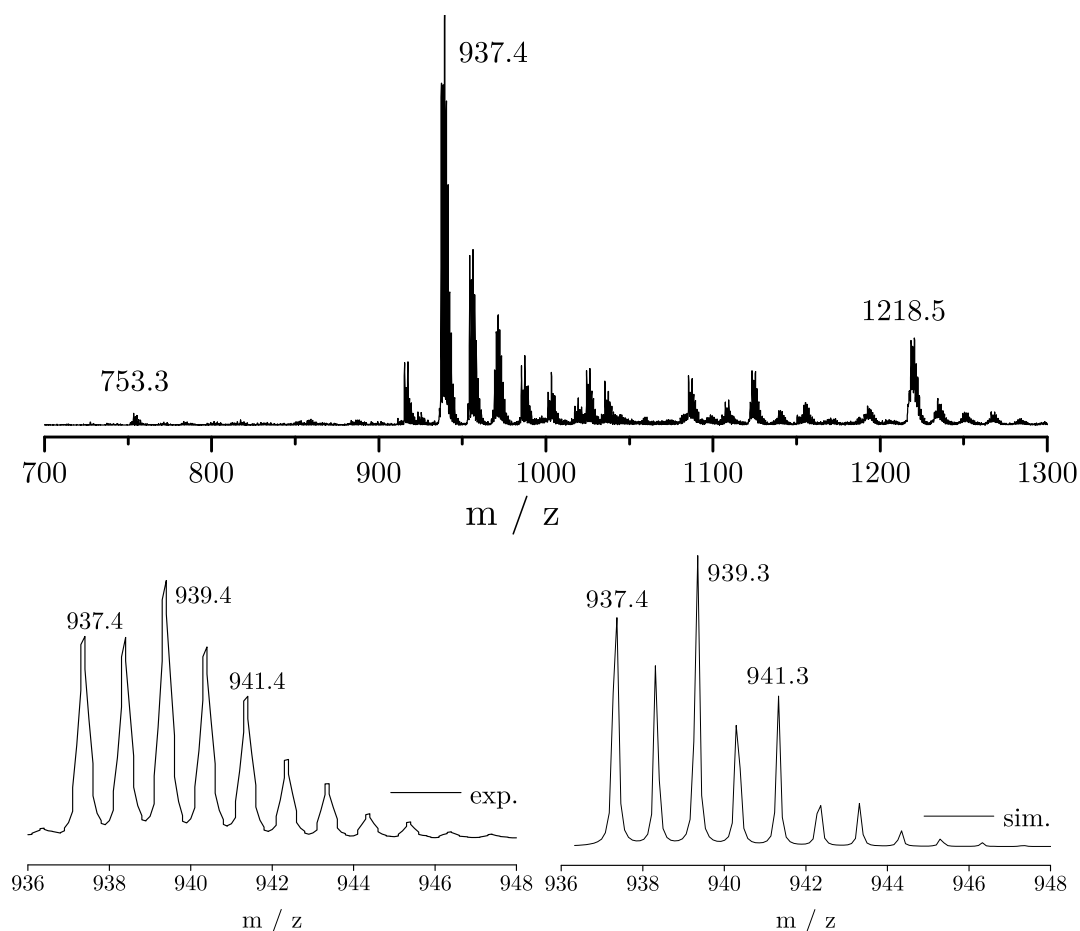


Figure 4.24: Top: ESI(+)-MS-spectrum of **11** in THF. Bottom: Experimental (right) and simulated (left) isotope distribution of the peak at $m/z = 937.4$.

Further analysis has been carried out by NMR spectroscopy. It was possible to identify **11** in the ^1H NMR spectrum with the help of $^1\text{H},^1\text{H}$ -COSY (Figure B.49) and $^1\text{H},^{13}\text{C}$ -HSQC (Figure B.50) NMR spectroscopy. Even though crystalline material was used, the spectrum shows the presence of minor impurities, see Figure 4.25. This finding can be explained by the high temperature-sensitive of complex **11**. Although single-crystalline material was used, and utmost attention was paid to keeping the NMR sample at low temperatures, it is highly probable that the compound partly decomposed. Further, the assignment of all peaks was complicated by the presence of coordinating 2-Me-THF molecules and traces of hexane. Nevertheless, the characteristic pyrazole peak at 5.21 ppm is clearly visible, while the other resonances were assigned with the assistance of 2-D NMR spectroscopy, see Figure B.49 and Figure B.50).

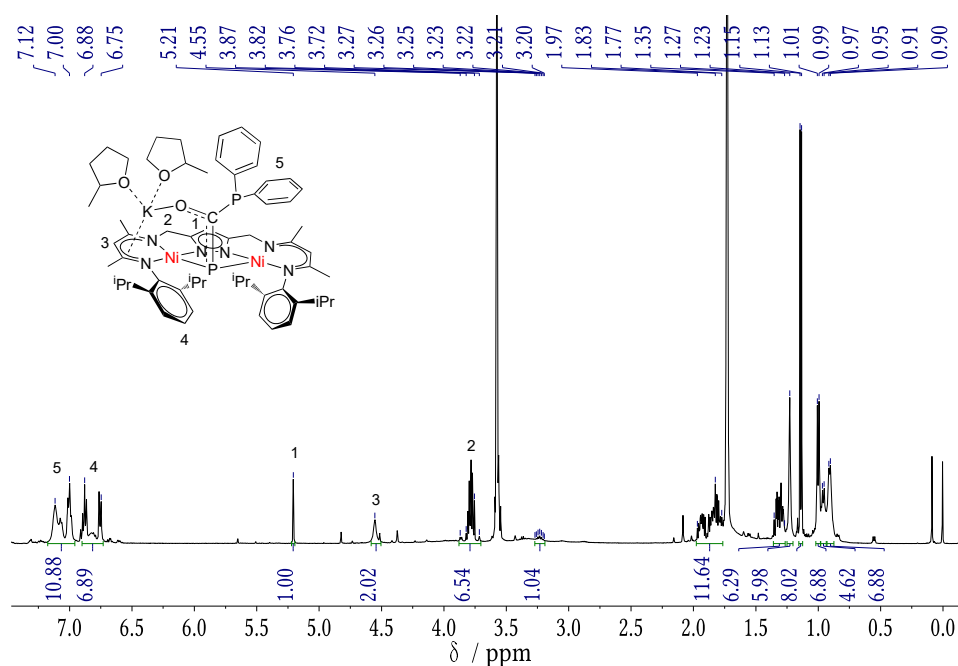


Figure 4.25: ^1H NMR spectrum of **11** at -35°C in $\text{THF}-d_8$.

The ^{31}P NMR spectrum shows two doublets at $\delta = 1.7$ ppm and 203.3 ppm with a relatively small $^2J_{\text{PP}}$ coupling constant of 131 Hz, see Figure 4.26. Even though the doublet resonances could not be assigned to one certain phosphorous atom, the profoundly separated peaks indicate an unequal charge distribution. The $^{13}\text{C}\{^1\text{H}\}$ NMR spectrum shows a characteristic downfield shifted doublet of doublet resonance at 253 ppm with $^1J_{\text{PC}}$ coupling constants of 94 and 57 Hz, see Figure 4.27.

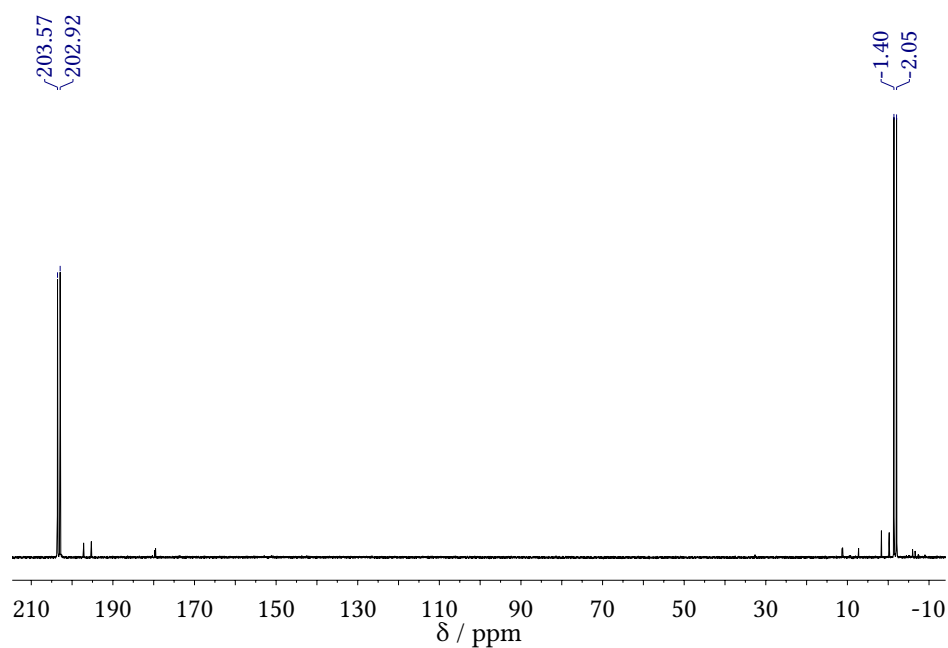


Figure 4.26: ^{31}P NMR spectrum of **11** at -35°C in $\text{THF-}d_8$. The two doublets are featuring a coupling constant of $^2J_{\text{PP}} = 131$ Hz.

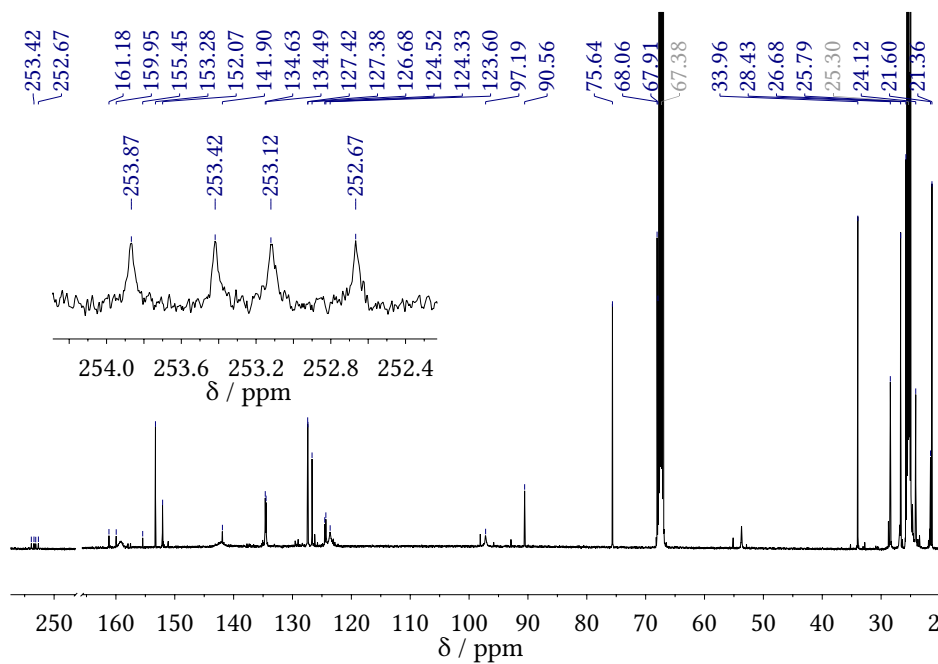
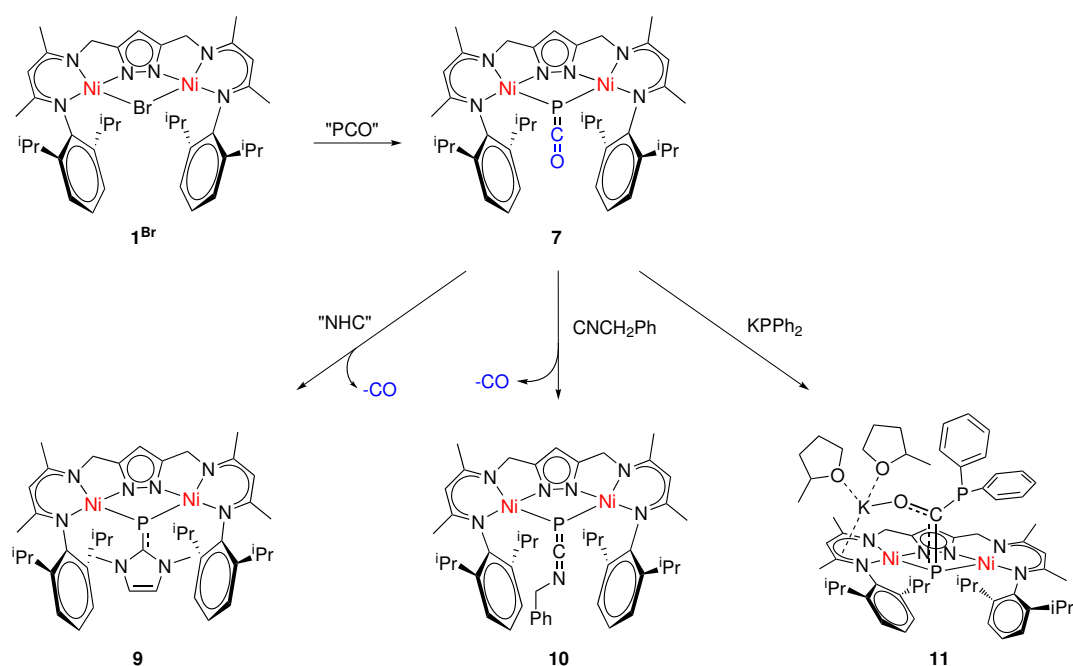


Figure 4.27: $^{13}\text{C}\{^1\text{H}\}$ NMR spectrum of **11** at -35°C in $\text{THF-}d_8$. The inset shows doublet of doublet at $\delta_{\text{PC}} = 253.8$ ppm (dd, $J = 94.3, 56.7$ Hz), that was assigned to the carbon of the PC(O)P part of the ligand.

Both 1,3-dimethylimidazolium and benzyl isocyanide served as neutral nucleophiles, yielding different phosphaketene derivatives. Due to the applied high temperatures, these reactions were accompanied by decarbonylation. A different approach was chosen by reacting **7** with a negatively charged and, thus, even stronger nucleophile at low temperatures. In line with the literature reported examples, the phosphaketene unit of **7** was converted into a diphospha-urea derivative. Due to the enormous sensitivity of **11** it was not possible to isolate the presumed diphosphene species. Even slowly warming up **11** to 0°C resulted in decomposition and no interpretable signals in the ^1H NMR or ^{31}P spectrum.

4.9 Conclusion and Outlook

In summary, the isolation and complete characterization of a dinickel phosphaketene complex **7** and its follow-up reactivity with several nucleophiles are presented. Due to its high stability, **7** represents a handy platform for synthesizing unusual phosphorus-based complexes (Figure 4.21), which were in-depth analyzed. Although these reactions were not mechanistically investigated, the initial step probably includes the nucleophilic attack on the carbon of the PCO-unit resulting in the formation of a phosphaketene-adduct. This hypothesis could be substantiated by the reaction of **7** with potassium diphenylphosphide, yielding a diphospha-urea derivative. It can be assumed that a comparable intermediate is also involved in the reaction of **7** with NHC or isocyanide. However, due to the applied high temperatures, the decarbonylation reaction is considerably facilitated, making the trapping of such an intermediate difficult.



Scheme 4.21: Simplified reaction towards the dinickel phosphaketene complex **7** and follow-up reactivities.

All complexes were characterized by UV-vis (Figure B.14), IR and NMR spectroscopy, and X-ray crystallography, see Table 4.8. Additionally, the electronic structures of **7** and **9** were investigated with the help of DFT calculations, carried out by MAX C. HOLTHAUSEN and coworkers. Combining these results made it possible to identify the most contributing resonance structure and understand the ligand's bent geometry relative to the nickel centers. However, the isocyanide-phosphido complex **10** and the diphospha-urea derivative **11** were not investigated by theoretical calculation, which would be helpful to understand the bonding situation of these complexes entirely.

Table 4.8: Selected bond lengths, distances, angles, and spectroscopic features of the herein presented complexes.

Complex	Bond length / Å		Angle / °	
7	P1–C40	1.671(5)	C40–P1–Ni1	80.85(14)
	C40–O1	1.170(5)	C40–P1–Ni2	81.50(14)
9	P1–C41	1.841(2)	C41–P1–Ni1	93.84(7)
			C41–P1–Ni2	98.58(8)
10	P1–C41	1.719(8)	C41–P1–Ni1	66.2(2)
	C41–N7	1.197(9)	C41–P1–Ni2	95.0(2)
11	P1–C40	1.806(2)	C40–P1–Ni1	95.86(8)
	P2–C40	1.908(2)	C40–P1–Ni2	91.27(8)
	C40–O1	1.241(3)		
Complex	NMR spectroscopy			IR spectroscopy
	³¹ P/ppm	¹³ C/ppm	¹ J _{P–C} /Hz	$\nu_{\text{asym}} / \text{cm}^{-1}$
7	–264.5	181.7	138	1885
9	44.8	171.5	142	
10	–84.2	172.7	130	1808
11	1.7	253.3	94; 57	
	203.24			

The LNi₂ scaffold serves as a suited platform to stabilize reactive phosphorus-based ligands derived from the PCO[–] ligand in the bimetallic pocket. Therefore, the reactivity with potent nucleophiles is worth to be examined in greater detail. In this context, the reaction with potassium diphenylphosphide is interesting since the reaction does not require high temperatures and is not accompanied by the unintended dimerization of the ligand. One example, following this synthetic strategy, would be the reaction of **7** with potassium cyanide to afford a primary cyanophosphide.

Chapter 5

Experimental Section

5.1 General Considerations

5.1.1 Materials and Methods

All experiments were performed under an argon or nitrogen atmosphere using standard Schlenk and glove box techniques. Glasware was dried at 120 °C before use. Solvents were dried over sodium-potassium alloy (2-Me-THF, THF, *n*-hexane, *n*-pentane), CaH₂ or P₄O₁₀ (CHCl₃, Et₃N) and distilled and degassed before use. Deute-rated solvents were dried analogously. Alternatively, toluene, *n*-hexane were dried using a solvent purification system (MB-SPS) and subsequent storage over molecular sieves (3 Å). Hydrogen gas was purchased from Messer and deuterium gas from Linde. Chemicals used were either present in the working group or purchased from commercial sources as Acros, Aldrich, Deutero, Merck, ABCR and used without further purification unless stated otherwise. [HLut]BF₄ was synthesized according to the literatur^[262] but additionally purified by sublimation (100 °C and 1.9 · 10⁻² mbar). The used NaOCP(dioxane)_{2.5} (abbreviated as NaPCO) in this work was gratefully taken from MAX HANSMANN. Gases (O₂ and H₂) were dried by storing them over concentrated H₂SO₄ for at least two days.

5.1.2 Instrumentation

NMR spectra: ¹H NMR and ¹³C NMR spectra were recorded on Bruker Avance spectrometers (300 MHz, and 500 MHz, for ¹H) at room temperature unless otherwise noted. Residual ¹H signals of the deuterated solvent in ¹H NMR were used as internal references (CDCl₃: $\sigma(\text{H}) = 7.26$ ppm, $\sigma(\text{C}) = 77.16$ ppm; THF-*d*₈: $\sigma(\text{H}) = 1.72$ and 3.58 ppm, $\sigma(\text{C}) = 25.31$ and 67.21 ppm).^[189]

Mass spectrometry: Electro ionization (EI) and Electrospray ionization (ESI) mass spectra were collected on a Bruker Daltonics maXis instrument. Moisture or oxygen sensitive samples were prepared in a glovebox (MBRAUN UNILab) under an inert gas atmosphere and injected into the Bruker HCT Ultra spectrometer via a direct Peek[®] tubing connection.

Elemental analyses: (standard CHN) were obtained from the analytical laboratories at the Georg-August-University on an Elementar Vario EL 3.

IR spectroscopy: IR spectra were measured with a Cary 630 FTIR spectrometer equipped with a DialPath and Diamond ATR accessory (Agilent) placed in a glovebox (MBRAUN UNILab, argon atmosphere). IR bands were labeled according to their relative intensities with vs (very strong), s (strong), m (medium), w (weak) and

very weak (vw).

UV-vis spectroscopy: UV-vis experiments in solution were recorded in quartz cuvettes on an AGILENT Cary 60 equipped with a UNISOKU cryostat (CoolSpek) for low-temperature measurements connected with a magnetic stirrer. Temperature-sensitive compounds were recorded at $-40\text{ }^{\circ}\text{C}$ if not otherwise noted. Stock solutions of oxygen or water-sensitive compounds were freshly prepared in a glove box with $<0.1\text{ ppm O}_2$ and H_2O and transferred into glass cuvettes, which were sealed with a J. Young NMR valve.

SQUID: Measurements were performed with a Quantum Design MPMSXL-5 SQUID magnetometer in the temperature range from 295 to 2 K at 0.5 T applied field. The powdered sample was encapsulated in a Teflon bucket and placed in a non-magnetic sample holder. Each raw data point for the measured magnetic moment of the sample was corrected for the diamagnetic contribution by subtraction of the experimentally determined magnetic measurement of the Teflon bucket. Experimental data were modelled with the *julX* program^[263] by applying a fitting procedure to the spin Hamiltonian for isotropic exchange coupling and Zeeman splitting:

$$\hat{H} = 2J\hat{S}_1\hat{S}_2 + g\mu_B\vec{B}(\vec{S}_1 + \vec{S}_2) \quad (5.1)$$

Paramagnetic impurities (PI) and temperature-independent paramagnetism (TIP) were included according to:

$$\chi_{\text{calc}} = (1 - PI)\chi + PI\chi_{\text{mono}} + TIP \quad (5.2)$$

EPR spectroscopy: X-band EPR spectra were recorded on a Bruker ELEXSYS-II E500 CW-EPR equipped with a standard cavity (ER4102ST, 9.45 GHz). The temperature was regulated with an Oxford Instruments Helium flow cryostat (ESP910) and an Oxford temperature controller (ITC-4). The microwave frequency was measured with the built-in frequency counter and the magnetic field was calibrated using an NMR field probe (Bruker ER035M). The spectra were simulated by iteration of the anisotropic *g*-values, and line widths using the MATLAB^[264]-based EPR-simulation program EasySpin.^[265]

Cyclic voltammetry: Cyclic voltammetry measurements of sensitive oxygen complexes were carried out by using a METROHM Autolab potentiostat under inert conditions in a one-compartment gastight cell at $0\text{ }^{\circ}\text{C}$. Stock solutions were prepared freshly in MeCN (0.1 M *n*-Bu₄NPF₆) in a glove box with $<0.1\text{ ppm O}_2$ and H_2O . Cyclic voltammograms were recorded using Ag/Ag⁺ reference-, glassy-carbon working- and Pt-wire counterelectrodes. Ferrocene was added as an internal standard and all spectra were referenced to the ferrocene/ferrocenium redox couple Fc/Fc⁺.^[266]

X-ray structure determination: X-ray data were collected on a STOE IPDS II or a BRUKER D8-QUEST diffractometer (monochromated Mo-K α radiation, $\lambda = 0.71073\text{ \AA}$) by use of ω or ω and ϕ scans at low temperature. The structures were solved with SHELXT and refined on F2 using all reflections with SHELXL.^[267,268] Non-hydrogen atoms were refined anisotropically. Hydrogen atoms were placed in calculated positions and assigned to an isotropic displacement parameter of 1.5/1.2 $U_{\text{eq}}(\text{C})$. Absorption corrections were performed numerically with the program

X-RED^[269] or by the multi-scan method with SADABS.^[270]

5.2 OH...H Bonding Distance Determinations

NMR spectroscopy is a beneficial tool for investigating transition-metal hydrides spectroscopically; moreover, different methods were developed for revealing their structural and dynamic properties. Conveniently, hydride resonances are often found in the characteristic region around -5 to -20 ppm, which allows their distinct identification. Even though these techniques have been designed initially to study η^2 -H₂ complexes,^[182] it is also possible to utilize them to investigate inter-^[170,171] and intramolecular^[172,173] dihydrogen bonds. In this work, the H...H distance of the hydrido hydroxido complex $\mathbf{K}[\text{LNi}_2^{\text{II}}(\text{H})(\text{OH})]$ is of particular interest and was therefore extensively examined. In the following, the applied methods in Chapter 3.3.4 will be further explained, and a more detailed description of the procedure is provided.

5.2.1 Theoretical Background

The distance between two protons $r(\text{H} - \text{H})$ can be ascertained by ¹H T_1 experiments, provided that all portions of the total relaxation rate T_1^{TOT} are known. Alternatively, only the main contribution is considered, while conditions are chosen where the other influences are negligible. Since dipole-dipole (T_1^{DD} interactions often dominate the overall relaxation of hydride resonances, it is crucial to determine its contribution), which is done accordingly:

$$\frac{1}{T_1^{\text{DD}}} = \left(\frac{3}{2}\right) \left(\frac{\mu_0}{4\pi}\right)^2 \gamma_{\text{H}}^4 \hbar^2 \tau_c r(\text{H} - \text{H})^{-6} \left(\frac{1}{1 + \omega_{\text{H}}^2 \tau_c^2} + \frac{4}{1 + 4\omega_{\text{H}}^2 \tau_c^2}\right) \quad (5.3)$$

where μ_0 is the permeability of vacuum, γ_{H} and ω_{H} are the nuclear magnetogyric ratio and resonance frequency of hydrogen respectively, \hbar is the PLANCK'S constant divided by 2π . The molecular motion correlation time τ_c must be determined independently; however, this can be avoided under certain conditions. The molecular correlation time τ_c depends on the temperature according to:

$$\tau_c = \tau_0 \exp(E_A/RT) \quad (5.4)$$

where R is the BOLTZMANN constant and E_A is the activation energy. This formula simplifies if the system of interest features a minimal relaxation time ¹H $T_{1,\text{min}}$ since the influence of τ_c becomes insignificant:

$$\tau_c = \frac{0.6158}{\omega_{\text{H}}} \quad (5.5)$$

Under this conditions, ω_{H} can be replaced by the operating frequency ν , and T_1^{DD} by the minimal relaxation time $T_{1,\text{min}}$. This assumption allows determining the H...H bonding distance accordingly:

$$r(\text{H} \cdots \text{H}) = 5.815 \left(\frac{T_{1,\text{min}}}{\nu}\right)^{\frac{1}{6}} \quad (3.1)$$

This equation only requires the minimal relaxation time $T_{1,\text{min}}$ in seconds and the spectrometer frequency ν in MHz to deliver the distance $r(\text{H} \cdots \text{H})$ in Å. However, to find the desired ¹H $T_{1,\text{min}}$ for the H...H moiety, it is necessary to determine the dipole-dipole contribution T_1^{DD} at variable temperatures. There are two different approaches to examine T_1^{DD} , the first is by measuring the nuclear Overhauser enhancement of the ¹H nuclei.^[271] The second one compares the relaxation rates T_1 for

the non-deuterated (H, H) and partially deuterated (H, D) isotopomers.^[272] More precisely, the latter method requires T_1 measurements of the hydrido (H^-) and the corresponding deuterio (OD^-) resonances or *vice versa* (D^- and OH^-). The individual relaxation times are linked by the following correlation, whereby the factor (0.96) compensates for the residual dipolar coupling of the deuterium nucleus:^[185]

$$\frac{1}{T_1^{\text{DD}}} = \left(\frac{1}{T_1^{\text{HOH}}} - \frac{1}{T_1^{\text{HOD}}} \right) \cdot 0.96 \quad (3.2)$$

5.2.2 The NMR Inversion-Recovery (IR) Experiment

Due to its applicability and convenience, the most popular approach to determine T_1 relaxation times is by NMR inversion-recovery experiments. The pulse sequence of this experiment consists of the following pulse sequence, where RD is the relaxation delay and AT is the acquisition time:

$$\text{RD} - 180^\circ - \tau - 90^\circ - \text{AT}$$

First, a 180° pulse inverts the magnetization vector along the z-direction from $+Z$ to $-Z$. During the time delay τ , relaxation along the longitudinal plane occurs until the equilibrium z-magnetization is reached. Second, the 90° registering pulse creates transverse magnetization, converting the vector from $-Z$ to $-X$. Consequently, the intensity of the NMR signals will show negative intensity at $\tau \ll T_1$. The evolution from negative to positive intensity is observed upon variation of the time delay τ from $\tau \ll T_1$ to $\tau \simeq 3T_1$, yielding so-called inversion recovery curves. These obtained NMR data can be analyzed by a standard nonlinear three-parameter fitting routine. For demonstration, this method is illustrated in the following. First, the complex of interest is measured at a fixed temperature, while τ is varied after each recorded spectrum. Then, after a rough estimation of T_1 , the time delay is adapted accordingly. A common mistake in this context is choosing a too short time delay; to ensure a reliable estimation of the relaxation time, it is advisable to adjust $\tau \simeq 3T_1$. Ideally, the inversion recovery curve becomes linear for long relaxation times, indicating almost complete (approximately 99%) relaxation of magnetization in Z-direction, see Figure 5.2.

The relaxation time T_1 for the hydrido resonance of complex **6** was calculated; accordingly, an example is given below, see Figure 5.1 and Figure 5.2. To determine the H...H distance, it is necessary to ascertain T_1^{DD} at the minimal relaxation time $T_{1,\text{min}}$.

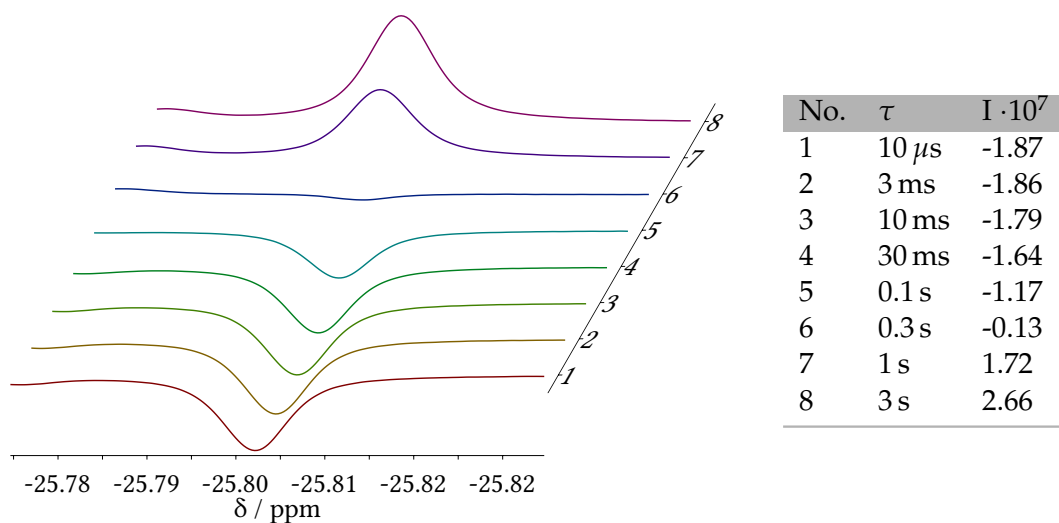


Figure 5.1: NMR inversion-recovery experiment at -30°C in $\text{THF-}d_8$ of $\text{K}[\text{LNi}_2^{\text{II}}(\text{OD})(\text{H})]$. **Left:** Intensity change upon variation of time delay τ . The NMR spectrum only displayed the hydrido region at -25.78 ppm. **Right:** Data points used for the inversion-recovery curve.

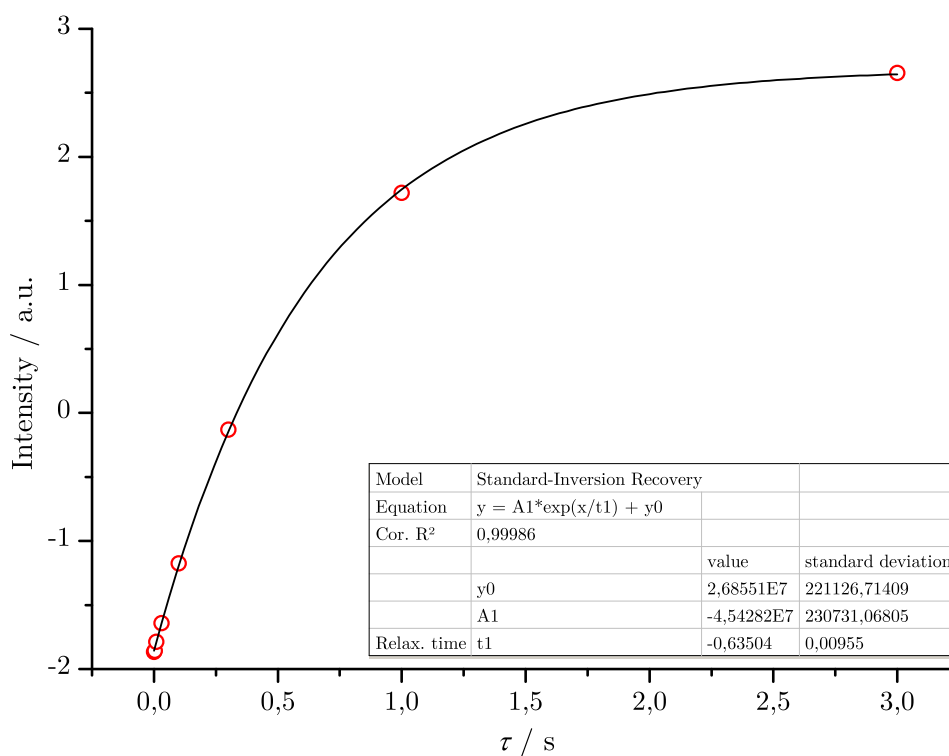


Figure 5.2: Inversion recovery curve for the hydrido peak of $\text{K}[\text{LNi}_2^{\text{II}}(\text{OD})(\text{H})]$ at -25°C in $\text{THF-}d_8$. Experimental values (red circles) and calculated with standard nonlinear three-parameter fitting routine (black line).

Table 5.1: All determined relaxation times T_1 for the respective resonance, T_1^{DD} and H...H distances. The minimal relaxation time $T_{1,\text{min}}$ is located at -30°C , resulting in $r(\text{H}\cdots\text{H})$ of 1.783 Å. To improving the visibility of the resonance of interest, the respective H atom is printed boldly.

Complex	Relaxation time T_1 /s			
	$\text{K}[\text{LNi}_2^{\text{II}}(\text{D})(\text{OH})]$	$\text{K}[\text{LNi}_2^{\text{II}}(\text{H})(\text{OH})]$	$\text{K}[\text{LNi}_2^{\text{II}}(\text{H})(\text{OH})]$	$\text{K}[\text{LNi}_2^{\text{II}}(\text{H})(\text{OD})]$
$T/^\circ\text{C}$	D...HO	H...HO	H...HO	H...DO
-10	1.24	0.33	0.27	0.70
-20	1.09	0.34	0.26	0.66
-25	1.12	0.32	0.27	0.64
-30	1.07	0.33	0.24	0.63
-40	0.98	0.31	0.25	0.59
$T_1^{\text{DD}\dagger}$	$r(\text{H}\cdots\text{H})/\text{Å}$			
0.427	1.791			
0.443	1.802			
0.439	1.799			
0.415 ($T_{1,\text{min}}$)	1.783*			
0.426	1.790			

[†]To minimize measurement errors, T_1^{DD} has been determined for both combinations (OD...H and OH...D) and averaged

*Only this distance was measured at $T_{1,\text{min}}$

5.2.3 Isolated-Spin-Pair-Approximation (ISPA)

An alternative approach to examine proton-proton distances utilizes NOE spectroscopy by the so-called isolated-spin-pair approximation (ISPA). This method has a significant advantage that neither the correlation time nor other independent data must be determined before. Instead, the relative NOE intensities associated with an unknown and a reference distance are required.^[184] In the fast tumbling regime, the normalized NOE intensity I between two resonances is proportional to the cross-relaxation rate σ_{ij} and the experimental mixing time τ_m .^[273]

$$I = \sigma_{ij}\tau_m \quad (5.6)$$

Under these conditions, the cross-relaxation rate is proportional to the distance of the respective protons ($r^{\frac{1}{6}}$) and a prefactor k . Conveniently, this factor can then be regarded as constant, due to the fact that all values defining k are fixed for one experiment.

$$\sigma_{ij} = kr^{\frac{1}{6}} \quad (5.7)$$

$$k = \left(\frac{\mu_0}{4\pi}\right)^2 \frac{\hbar^2\gamma^4}{10} \left(\frac{6\tau_c}{1+4\omega^2\tau_c^2} - \tau_c\right) \quad (5.8)$$

Thus, the ratio of intensities of a pair of NOE signals is equivalent to the ratio of their distances and independent of the mixing time.^[186]

$$\frac{I_1}{I_2} = \frac{r_1^{\frac{1}{6}}}{r_2^{\frac{1}{6}}} \quad (3.3)$$

Since the intensities can be directly derived from the $^1\text{H}, ^1\text{H}$ -NOESY spectrum, the unknown distance can be determined if the reference distance has been obtained previously from DFT calculations or X-ray crystallography. To calculate the intramolecular proton distance, two sets of resonances must be evaluated, whereby one is the interaction of interest, and the other one can be freely chosen. Notwithstanding, the reference must meet the following conditions: First, all signals must be clearly assignable and separated by potentially interfering resonances; second, the associated distance should be fixed. The first prerequisite can be fulfilled by the right choice of NOE diagonal- and cross-peaks. The second requirement is more complicated to accomplish. In general, suitable proton-proton distances are found in rigid molecules or aromatic systems because conformational changes are unlikely to occur.^[187] Theoretically, also more flexible molecules, including structural dynamics, can be analyzed.^[187] However, these kinds of systems should be avoided if possible to keep the procedure more straightforward and less sensitive to errors.

As in the previous chapter, the accurate $\text{H} \cdots \text{HO}$ distance measurement of the hydroxido and hydrido groups within the pocket of the complexes **6** and **6-K(crypt)** is desirable. Therefore, the exemplary procedure is explained in the following. First, a $^1\text{H}, ^1\text{H}$ -NOESY spectrum of **6-K(crypt)** was recorded, revealing overlapping signals in the aromatic regions, see Figure 5.3. Hence, the *meta*- and *para*-H's are inappropriate to serve as a reference point; the distance between the pyrazolato-H and the averaged proton position of the adjacent methylene unit $r(\text{H}^{\text{PYR}} \cdots \text{H}^{\text{CH}_2})$ were taken instead.

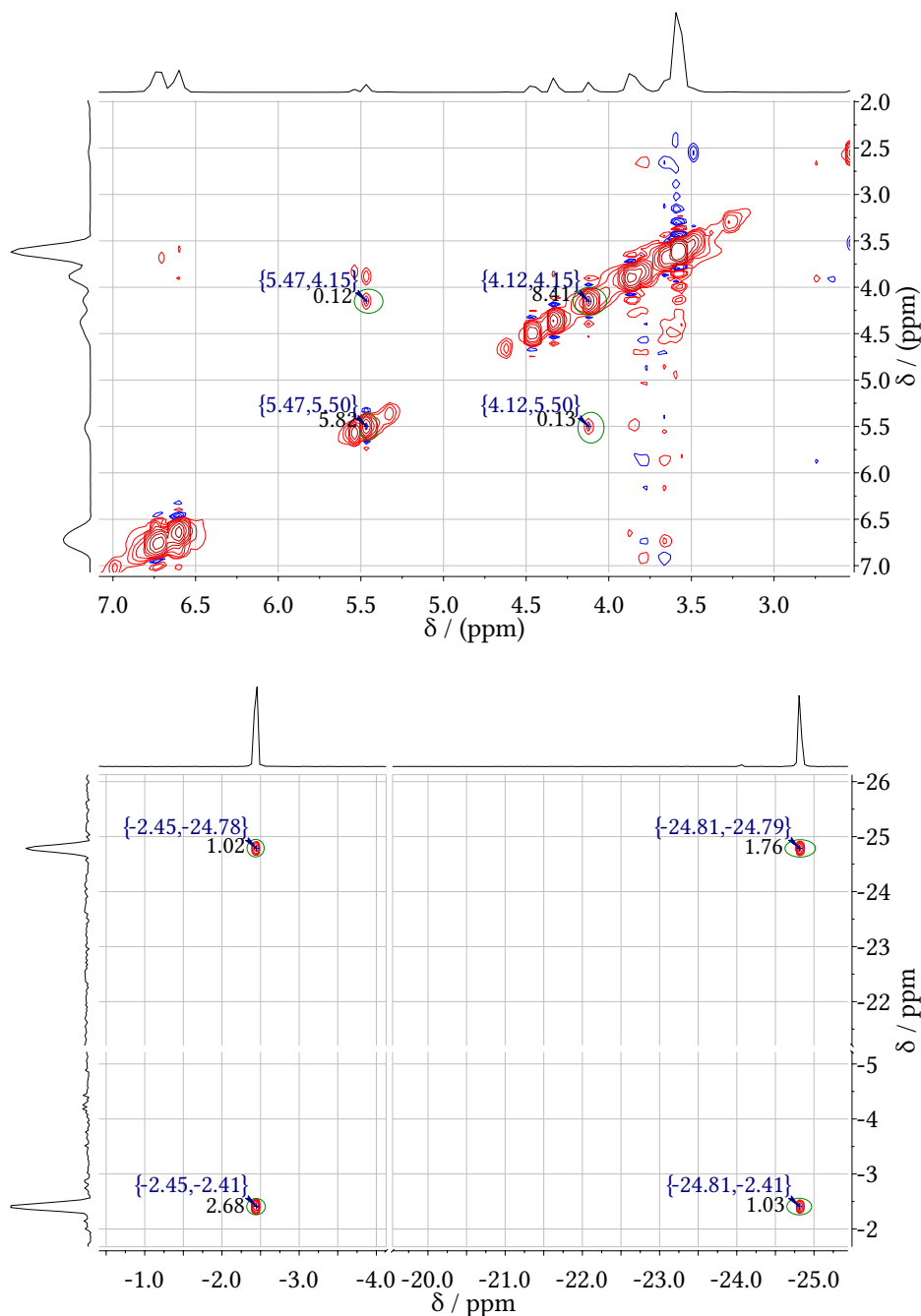


Figure 5.3: $^1\text{H}, ^1\text{H}$ -NOESY spectrum of 6-K(crypt). To provide a better overview, the spectrum is divided into two parts, and the peak position (blue) and the corresponding intensities (black) are listed in Table 5.2.

The $^1\text{H}, ^1\text{H}$ -NOESY spectrum shows a sufficient separation of the respective peaks and consequently allows to determine the diagonal (I_{AA} and I_{BB})- and cross-relaxation terms (I_{AB} and I_{BA}). Ideally, the intensities of the inverted resonances are identical. However, slight deviations are acceptable. The obtained NOE values are summarized in the following table:

Table 5.2: NOE values obtained from the $^1\text{H},^1\text{H}$ -NOESY spectrum at -30°C in $\text{THF-}d_8$ of complex **6-K(crypt)**.

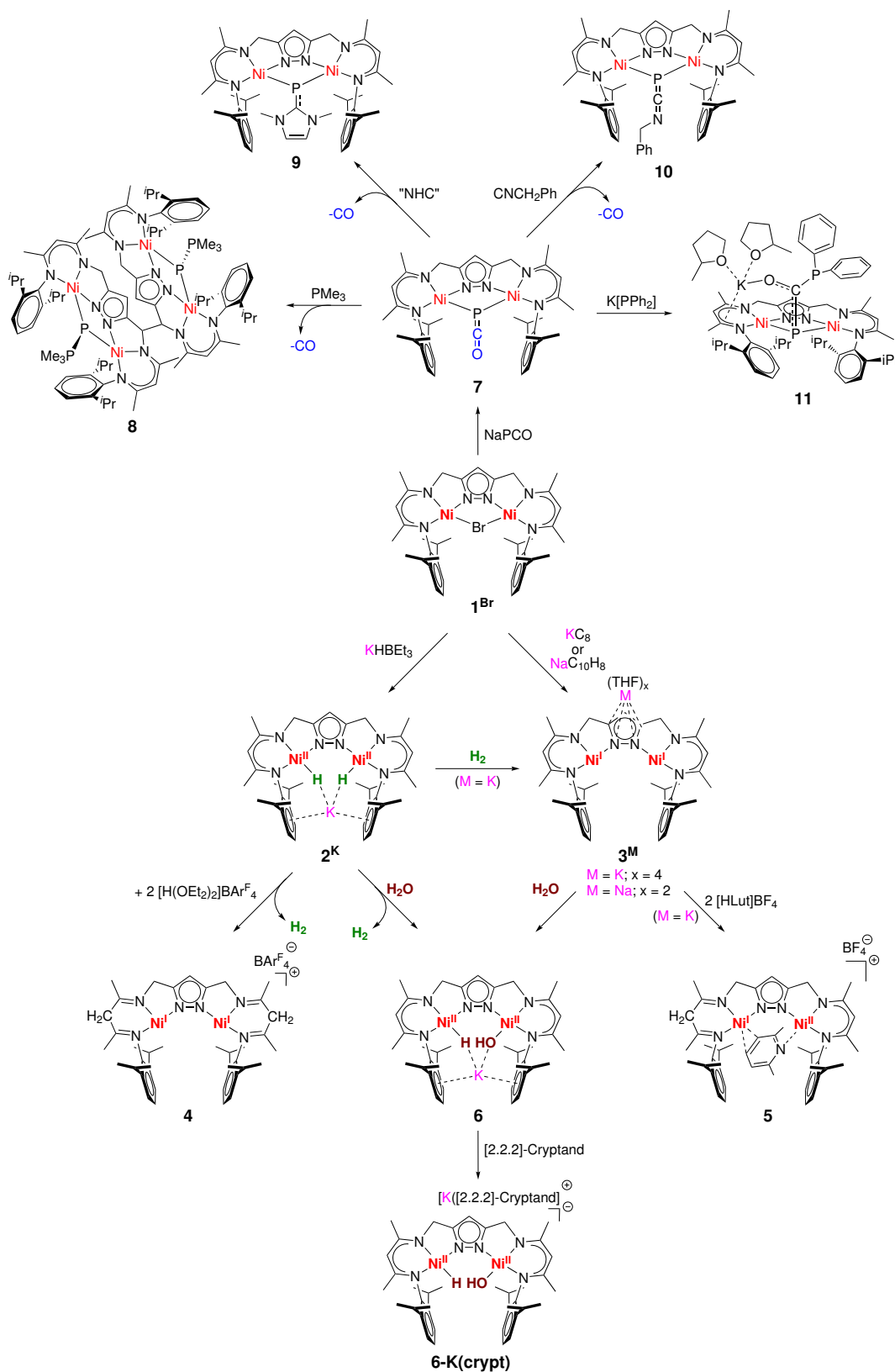
Resonance	Integral / rel	$\delta(F1)/\text{ppm}$	$\delta(F2)/\text{ppm}$	peak type
H...H	1.76	-24.77	-24.78	diagonal
OH...OH	2.68	-2.41	-2.40	diagonal
H...OH	1.02	-24.77	-2.40	cross
OH...H	1.03	-2.41	-24.78	cross
$\text{H}^{\text{CH}_2} \dots \text{H}^{\text{CH}_2}$	8.41	4.15	4,15	diagonal
$\text{H}^{\text{pyr}} \dots \text{H}^{\text{pyr}}$	5.82	5.50	5.49	diagonal
$\text{H}^{\text{pyr}} \dots \text{H}^{\text{CH}_2}$	0.12	4.17	5.49	cross
$\text{H}^{\text{CH}_2} \dots \text{H}^{\text{pyr}}$	0.13	5.50	4.15	cross

First, the cross-peaks I_{AB} and I_{BA} were averaged for a given signal and normalized by the associated diagonal peaks I_{AA} and I_{BB} . Second, the intensities of the measured NOE signals were corrected for the symmetry in each group by dividing the NOE intensity between signals by $\sum_n I_n$, where I_n is the number of chemically equivalent spins of the respective group. This term is 1 for the H...OH spin pair and 2 for the $\text{H}^{\text{pyr}} \dots \text{H}^{\text{CH}_2}$ counterpart.

$$I = \left(\frac{I_{AB} + I_{BA}}{2\sqrt{I_{AA} + I_{BB}}} \right) \frac{1}{\sum_n I_n} \quad (5.9)$$

The reference distance and the normalized intensities I_1 and I_2 are inserted into the formula 3.3 to give the H...HO distance.

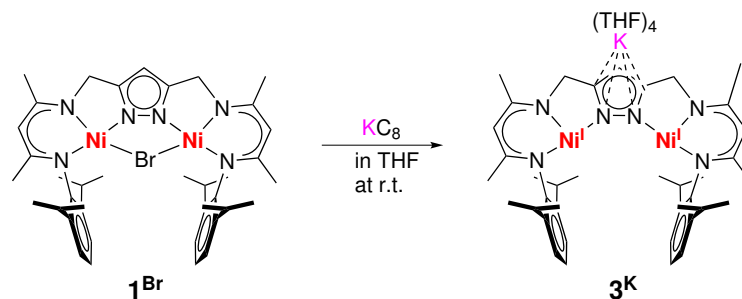
5.3 Reaction Overview



Scheme 5.1: Simplified reaction overview of all reactions presented in this thesis.

5.4 Synthesis of Complexes

5.4.1 Synthesis of 3^{K}



Scheme 5.2: Synthesis of $\text{K}[\text{LNi}_2^{\text{I}}]$ (3^{K}).

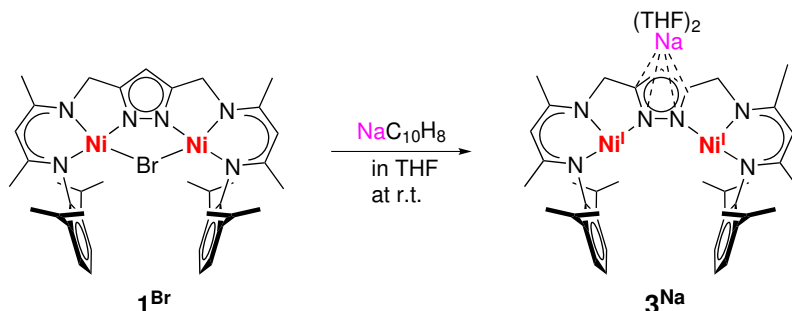
KC_8 (7.4 mg, 55.3 μmol , 2.2 eq.) was added to a brown/green suspension of $[\text{LNi}_2(\mu\text{-Br})]$ (1^{Br}) (20.0 mg, 25.1 μmol , 1.0 eq.) in THF (4 mL). The reaction mixture became dark red within 30 min and was stirred for two hours at room temperature to yield a deep red solution. The solvent was removed under vacuum. The residue was then dissolved in THF, and the KBr and graphite were removed by filtration through a Whatman[®] filter paper. After layering with hexane, the product was obtained as red block crystals after one week (yield: 35%).

$^1\text{H-NMR}$ (500 MHz, 238 K, $\text{THF-}d_8$): δ / ppm = 60.88, 14.18, -3.41 , -6.81 , -9.04 , -21.02 , -24.06 .

UV-Vis (298 K, THF): λ_{max} / nm (ϵ / $\text{M}^{-1}\text{cm}^{-1}$) = 369 (19404), 384 (18752), 449 (5185).

IR (ATR, 298 K): $\tilde{\nu}$ / cm^{-1} = 3056 (w), 2955 (m), 2923 (m), 2863 (m), 1552 (m), 1521 (m), 1458 (m), 1432 (s), 1397 (s), 1319 (m), 1270 (m), 1253 (m), 1231 (m), 1192 (m), 1090 (w), 1056 (m), 1019 (m), 935 (w), 848 (m), 795 (m), 756 (s), 735 (w), 645 (w), 631 (w), 545 (w), 520 (w).

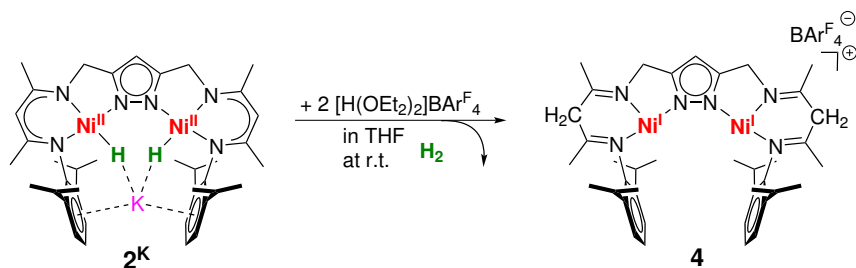
SQUID: $S_1 = S_2 = 1/2$; $g_{1,2} = 2.136$; $J_{1,2} = -71 \text{ cm}^{-1}$.

5.4.2 Synthesis of 3^{Na} Scheme 5.3: Synthesis of $\text{Na}[\text{LNi}_2^{\text{I}}]$ (3^{Na}).

A freshly prepared solution of sodium naphthalide (1 M) in THF (0.53 mL, 53.2 μmol , 2.1 eq.) was added to a brown slurry of $[\text{LNi}_2(\mu\text{-Br})]$ (1^{Br}) (20 mg, 25.1 μmol 1 eq.) in THF. The reaction mixture became dark red immediately and was stirred for 30 min at room temperature to yield a deep red solution. Afterward, the reaction mixture was filtered through a Whatman[®] filter paper. After layering with hexane, the product was obtained as red block crystals after one week (yield: 40%).

SQUID: $S_1 = S_2 = 1/2$; $g_{1,2} = 2.054$; $J_{1,2} = -83 \text{ cm}^{-1}$.

5.4.3 Synthesis of 4

Scheme 5.4: Synthesis of $[\text{H}_2\text{LNi}_2][\text{BARF}_4]$ (**4**).

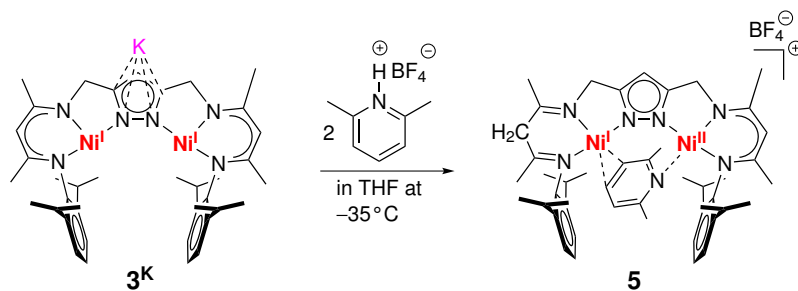
An orange solution of $\text{K}[\text{LNi}_2^{\text{II}}(\text{H})_2]$ (2^{K}) (30.0 mg, 38.7 μmol , 1.0 eq.) in THF (3 mL) was cooled to -38°C . To this solution $[\text{H}(\text{OEt}_2)_2][\text{BARF}_4^{\text{F}}]$ (86.2 mg, 85.1 μmol , 2.2 eq.) was quickly added under vigorous stirring, resulting in a brown-red clear solution. The reaction mixture was filtered through a Whatman[®] filter paper. After one week, the slow diffusion of the solvents yielded the product as yellow, block-shaped crystals suitable for X-ray diffraction (yield: 40%). The crystals were accompanied by inorganic impurities, which were not further analyzed. Manual separation was necessary to collect the pure product.

UV-Vis (298 K, THF): $\lambda_{\text{max}} / \text{nm}$ ($\epsilon / \text{M}^{-1}\text{cm}^{-1}$) = 373 (17012), 385 (17732), 459 (6506).

IR (ATR, 298 K): $\tilde{\nu} / \text{cm}^{-1}$ = 2960 (m), 2926 (m), 2873 (m), 2861 (m), 1670 (m), 1610 (m), 1464 (m), 1442 (m), 1387 (m), 1357 (m), 1271 (m), 1113 (m), 957 (m), 936 (m), 887 (m), 841 (m), 803 (m), 791 (m), 770 (m), 758 (m), 744 (m), 711 (m), 682 (m), 670 (m).

SQUID: $S_1 = S_2 = 1/2$; $g_{1,2} = 1.866$; $J_{1,2} = -78 \text{ cm}^{-1}$.

5.4.4 Synthesis of 5



Scheme 5.5: Synthesis of $[\text{HLNi}^{\text{I}}\text{Ni}^{\text{II}}(\mu\text{-Me}_2\text{C}_5\text{H}_3\text{N})][\text{BF}_4]$ (5).

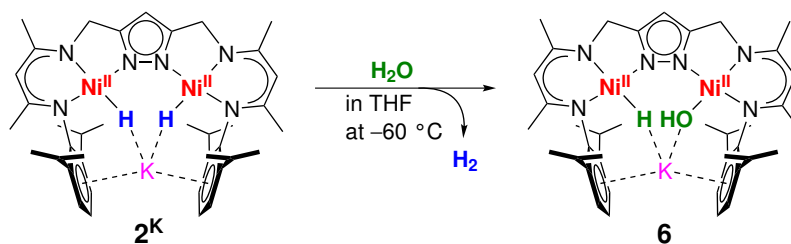
A red solution of $\text{K}[\text{LNi}_2^{\text{I}}]$ (3^{K}) (30.0 mg, 39.6 μmol , 1.0 eq.) in THF (3 mL) was cooled to -38°C . To this solution, $[\text{HLut}][\text{BF}_4]$ (15.4 mg, 79.1 μmol , 2.0 eq.) was quickly added under vigorous stirring, resulting in an intense deep red, clear solution. The reaction mixture was filtered through a Whatman[®] filter paper. Slow diffusion of the solvents yielded the product as yellow, block-shaped crystals suitable for X-ray diffraction (yield: 55%) after three days. Comparable to the synthesis of 4, the crystals were accompanied by inorganic salts; however, the amount of KBF_4 was sufficiently low to be removed manually.

UV-Vis (298 K, THF): $\lambda_{\text{max}} / \text{nm} = 273, 372, 471, 510, 696$.

SQUID: $S_1 = 1/2$; $g_1 = 1.779$.

EPR (THF, 153 K, 9.440469 GHz), 9865 mW) = $g = 2.2955, 2.2007, 2.0211$. Simulation parameters: $g_x = 2.2966$ $g_y = 2.1898$, $g_z = 2.0133$; $s_g(x, y, z) = 0.02$.

5.4.5 Synthesis of 6

Scheme 5.6: Synthesis of $\text{K}[\text{LNi}^{\text{II}}(\text{H})(\text{OH})]$ (6).

A solution of $\text{K}[\text{LNi}^{\text{II}}(\text{H})_2]$ (2^{K}) (20.0 mg, 25.3 μmol , 1.0 eq.) in THF (3 mL) was freeze-pump-thaw degassed once and warmed up to -60°C . In a separate flask, a small amount of water (5 mL) was three-times freeze-pump-thaw degassed and slightly warmed up under an argon atmosphere. The solution was stirred for two hours to ensure that the argon gas phase was saturated with water. Both flasks were connected with the Schlenk line *via* a three-way cock. The tubing and the THF solution were set under a static vacuum. Then, the second flask valve was opened, which allowed the water-saturated argon phase to be transferred to the reaction solution. After a few seconds, the solution turned from orange to yellow until no further color change was visible after approximately one minute. To secure complete conversion, the solution was stirred for 20 min and afterward removed completely *in vacuo*. The yellow crude product was redissolved in THF and filtered through a Whatman[®] filter paper at cold temperatures. For crystallization, the solution was layered with hexane and stored at -38°C . After two days, the product was isolated as yellow polycrystalline material in moderate yields ((15.2 mg, 18.8 μmol , yield: 60%).

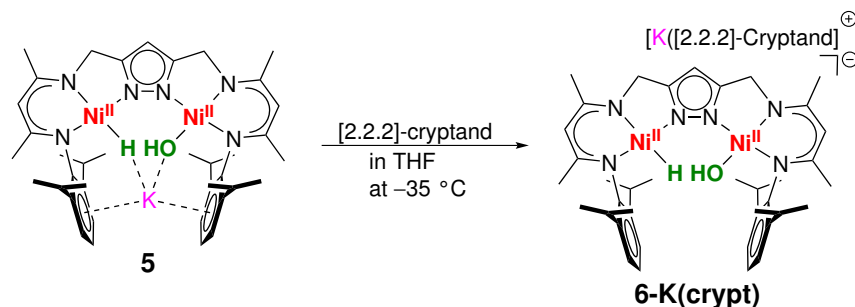
$^1\text{H-NMR}$ (500 MHz, 238 K, THF- d_8): δ / ppm = 6.95-6.85 (m, 6H, H^{Ar}), 5.55 (s, 1H, CH^{Pz}), 4.62 (s, 1H, $\text{CH}^{\text{Nacnac}}$), 4.53 (s, 1H, $\text{CH}^{\text{Nacnac}}$), 4.10 (m, 2H, CH_2), 3.87-3.81 (m, 2H, CH^{iPr}), 3.81 (m, 2H, CH_2), 3.58-3.52 (m, 2H, CH^{iPr}), 1.88 (s, 3H, CH_3), 1.75 (s, 3H, CH_3), 1.49 (d, $^3J_{\text{HH}} = 6.7\text{ Hz}$, 6H, CH_3^{iPr}), 1.43 (d, $^3J_{\text{HH}} = 6.7\text{ Hz}$, 6H, CH_3^{iPr}), 1.13 (s, 3H, CH_3), 1.11 (s, 3H, CH_3), 1.10 (d, $^3J_{\text{HH}} = 7.3\text{ Hz}$, 6H, CH_3^{iPr}), 1.07 (d, $^3J_{\text{HH}} = 7.0\text{ Hz}$, 6H, CH_3^{iPr}), -1.90 (d, $^3J_{\text{HH}} = 6.0\text{ Hz}$, 1H, Ni-OH), -25.73 (d, $^3J_{\text{HH}} = 6.0\text{ Hz}$, 1H, Ni-H).

$^{13}\text{C}\{^1\text{H}\}$ -NMR (125 MHz, 238 K, THF- d_8): δ / ppm = 159.9 (C-Me^{Nacnac}), 159.5 (C-Me^{Nacnac}), 159.1 (C^{Ar}), 158.2 (C^{Pz}), 157.5 (C-Me^{Nacnac}), 156.4 (C-Me^{Nacnac}), 155.2 (C^{Pz}), 150.6 (C^{Ar}), 144.5 (o-C^{Ar}), 141.2 (o-C^{Ar}), 123.9 (m-C^{Ar}), 123.6 (m-C^{Ar}), 123.3 (p-C^{Ar}), 122.7 (p-C^{Ar}), 97.7 (CH^{Nacnac}), 97.6 (CH^{Nacnac}), 91.8 (CH^{Pz}), 51.6 (CH₂), 51.2 (CH₂), 28.8 (CH^{iPr}), 28.4 (CH^{iPr}), 25.5 (CH₃^{iPr}), 24.9 (CH₃), 24.2 (CH₃^{iPr}), 23.7 (CH₃^{iPr}), 23.5 (CH₃^{iPr}), 23.1 (CH₃), 21.9 (CH₃), 21.7 (CH₃).

UV-Vis (298 K, THF): λ_{max} / nm (ϵ / $\text{M}^{-1}\text{cm}^{-1}$) = 385 (14800), 401 (14100), 440 (3900), 510 (600).

IR (ATR, 298 K): $\tilde{\nu}$ / cm^{-1} = 3410 (s), 3057 (w), 2956 (m), 2922 (w), 2861 (m), 1891 (w), 1525 (s), 1463 (m), 1430 (s), 1399 (s), 1316 (m), 1253 (m), 1233 (m), 1195 (w), 1101 (w), 1054 (m), 1029 (m), 1017 (m), 909 (w), 865 (m), 803 (m), 771 (m), 739 (m).

5.4.6 Synthesis of 6-K(crypt)

Scheme 5.7: Synthesis of Crypt(K)[LNi^{II}(OH)(H)] (6-K(crypt)).

To a solution of K[LNi^{II}(H)(OH)] (6) (20.0 mg, 24.8 μmol , 1.0 eq.) in THF (2 mL), [2.2.2]-cryptand (9.4 mg, 24.8 μmol , 1.0 eq.) was added at cold temperatures, which was accompanied by an instantaneous color change from yellow to red. The reaction solution was filtered through a Whatman[®] filter paper, layered with hexane, and stored at $-38\text{ }^\circ\text{C}$. After two days, the product was isolated as red plate-shaped crystals in good yields (yield: 95%).

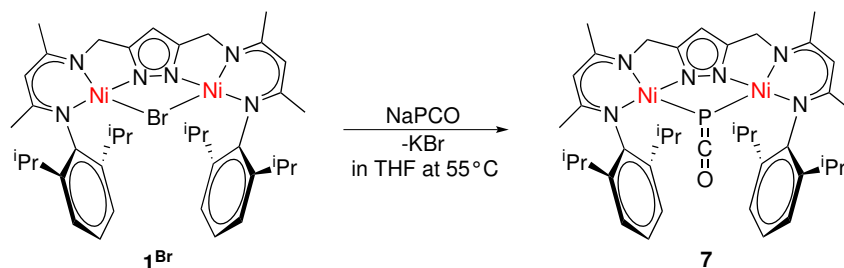
¹H-NMR (500 MHz, 238 K, THF-*d*₈): δ / ppm = 6.78-6.70 (m, 4H, *m*-CH^{Ar}), 6.61-6.58 (m, 2H, *p*-CH^{Ar}), 5.46 (s, 1H, CH^{Pz}), 4.46 (s, 1H, CH^{Nacnac}), 4.32 (s, 1H, CH^{Nacnac}), 4.12 (m, 2H, CH₂), 3.90-3.86 (m, CH^{iPr}), 3.86 (m, 2H, CH₂), 2.67 (s, 12H, [2.2.2]-cryptand), 1.83 (s, 3H, CH₃), 1.67 (s, 3H, CH₃), 1.20 (s, 3H, CH₃), 1.16 (s, 3H, CH₃), 1.10 (d, ³J_{HH} = 7.8 Hz, 6H, CH₃^{iPr}), 1.01 (d, ³J_{HH} = 6.9 Hz, 6H, CH₃^{iPr}), -2.44 (d, ³J_{HH} = 4.2 Hz, 1H, Ni-OH), -24.82 (m, 1H, Ni-H).

¹³C{¹H}-NMR (125 MHz, 238 K, THF-*d*₈): δ / ppm = 157.6 (C-Me^{Nacnac}), 157.5 (C-Me^{Nacnac}), 157.4 (C-Me^{Nacnac}), 157.3 (C-Me^{Nacnac}), 156.6 (C^{Ar}), 156.6 (C^{Ar}), 156.5 (C^{Pz}), 153.8 (C^{Pz}), 142.7 (*o*-C^{Ar}), 140.2 (*o*-C^{Ar}), 123.9 (*m*-C^{Ar}), 123.6 (*m*-C^{Ar}), 123.3 (*p*-C^{Ar}), 122.7 (*p*-C^{Ar}), 96.5 (CH^{Nacnac}), 99.1 (CH^{Nacnac}), 90.7 (CH^{Pz}), 71.0 (CH₂^{[2.2.2]-cryptand}), 68.1 (CH₂^{[2.2.2]-cryptand}), 51.8 (CH₂), 51.6 (CH₂), 33.0 (CH₂^{[2.2.2]-cryptand}), 28.8 (CH^{iPr}), 28.5 (CH^{iPr}), 24.7 (CH₃^{iPr}), 24.6 (CH₃), 24.3 (CH₃^{iPr}), 23.9 (CH₃^{iPr}), 23.2 (CH₃^{iPr}), 22.1 (CH₃), 21.6 (CH₃), 21.4 (CH₃).

UV-Vis (298 K, THF): λ_{max} / nm (ϵ / M⁻¹cm⁻¹) = 389 (11400), 440 (9000), 468 (8600), 522 (3200), 561 (2300).

IR (ATR, 298 K): $\tilde{\nu}$ / cm⁻¹ = 3410 (s), 3057 (w), 2956 (m), 2922 (w), 2861 (m), 1891 (w), 1525 (s), 1463 (m), 1430 (s), 1399 (s), 1316 (m), 1253 (m), 1233 (m), 1195 (w), 1101 (w), 1054 (m), 1029 (m), 1017 (m), 909 (w), 865 (m), 803 (m), 771 (m), 739 (m).

5.4.7 Synthesis of 7

Scheme 5.8: Synthesis of $[\text{LNi}_2(\mu\text{-PCO})]$ (7).

To a brown/greenish suspension of $[\text{LNi}_2(\mu\text{-Br})]$ (1^{Br}) (100 mg, 0.125 mmol, 1.0 eq.) in THF (7 mL), $\text{Na}(\text{dioxane})_{2.5}(\text{PCO})$ (45 mg, 0.163 mmol, 1.3 eq.) was added. The reaction mixture was heated to 55 °C for two days and changed its colour to dark red. The solvent was removed under vacuum. The residue was then again dissolved in a minimum amount of THF, and the NaBr removed by filtration through a Whatman[®] filter paper. After layering with hexane, the product was obtained as red block crystals after five days (yield: 65%) suitable for X-ray structure analysis.

$^1\text{H-NMR}$ (500 MHz, 238 K, $\text{THF-}d_8$): δ / ppm = 7.01-6.69 (m, 4H, $m\text{-C}^{\text{Ar}^{\text{Ar}}}$), 6.91-6.89 (m, 4H, $m\text{-C}^{\text{H}^{\text{Ar}}}$), 5.62 (s, 1H, C^{Pz}), 4.80 (s, 2H, CH), 4.36 (m, 4H, C^{H_2}), 3.30 (m, 2H, $\text{C}^{\text{H}^{\text{iPr}}}$), 3.32-3.24 (sept, $^3J_{\text{HH}} = 6.8$ Hz, 1H, $\text{C}^{\text{H}^{\text{iPr}}}$), 2.08 (s, 6H, C^{H_3}), 1.33 (s, 6H, C^{H_3}), 1.15-1.13 (s, 6H, C^{H_3}), 1.32-1.31 (d, $^3J_{\text{HH}} = 6.1$ Hz, 12H, $\text{C}^{\text{H}_3^{\text{iPr}}}$), 0.98-0.97 (d, $^3J_{\text{HH}} = 6.0$ Hz, 6H, $\text{C}^{\text{H}_3^{\text{iPr}}}$).

$^{13}\text{C}\{^1\text{H}\}\text{-NMR}$ (125 MHz, 238 K, $\text{THF-}d_8$): δ / ppm = 182.2 (d, $^1J_{\text{PC}} = 138$, C-P), 161.2 (C-Me^{Nacnac}), 160.3 (C-Me^{Nacnac}), 155.6 (C^{Pz}), 151.3 (C^{Ar}), 142.2 (o-C^{Ar}), 126.3 (p-C^{Ph}), 124.5 (m-C^{Ar}), 123.9 (p-C^{Ar}), 98.1 (CH), 92.8 (C^{H}Pz), 55.2 (C^{H}_2), 28.8 (C^{H}iPr), 25.3 (C^{H}_3^iPr), 25.2 (C^{H}_3^iPr), 24.9 (C^{H}_3^iPr), 24.7 (C^{H}_3^iPr), 24.5 (C^{H}_3), 21.6 (C^{H}_3).}}}}}}}}}

$^{15}\text{N}\{^1\text{H}\}\text{-NMR}$ (50 MHz, 238 K, $\text{THF-}d_8$): δ / ppm = -164.8 (N^{Pz}), -218.7 (N^{Nacnac}), -239.7 (N^{Nacnac}).

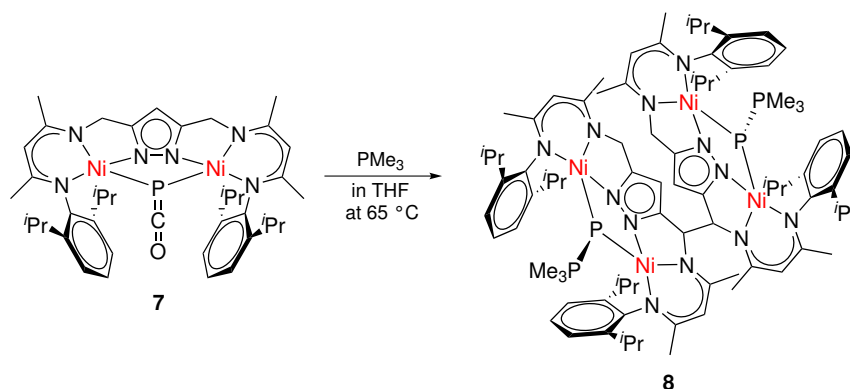
$^{31}\text{P}\{^1\text{H}\}\text{-NMR}$ (202 MHz, 238 K, $\text{THF-}d_8$): δ / ppm = -264.5.

UV-Vis (298 K, THF): λ_{max} / nm (ϵ / $\text{M}^{-1}\text{cm}^{-1}$) = 318 (17337), 365 (18816), 481 (3153).

IR (KBr, 298 K): $\tilde{\nu}$ / cm^{-1} = 3060 (w), 2958 (m), 2868 (w), 1885 (s), 1622 (w), 1557 (s), 1530 (s), 1463 (m), 1435 (m), 1400 (s), 1314 (m), 1278 (w), 1189 (w), 1032 (w), 795 (w), 761 (w), 748 (w).

ESI⁺-MS in THF m/z = 781.4 [$\text{M}+\text{H}$] (100%), 753.4 [$\text{M}-\text{CO}+\text{H}$] (36%).

5.4.8 Synthesis of 8

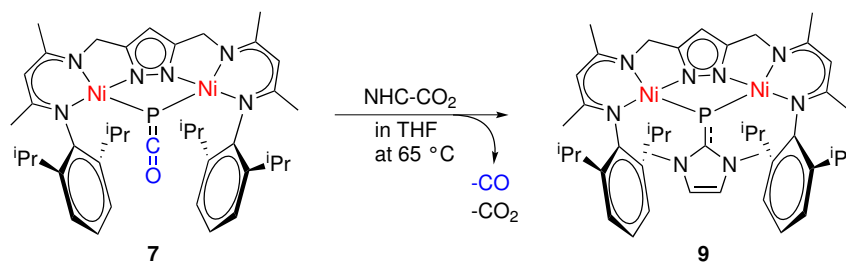
Scheme 5.9: Synthesis of $[L'\{Ni_2P(PMe_3)\}_2]$ (8).

To a dark red solution of $[LNi_2(\mu-PCO)]$ (7) (20 mg, 25.6 μmol , 1.0 eq.) in THF (3 mL) PMe_3 (2.9 μL , 26 μmol , 1.0 eq.) was added. The reaction mixture was heated to 65 $^\circ\text{C}$ for two days. The solvent was removed afterwards under vacuum. The residue was then dissolved in a minimum amount of THF and filtrated through a Whatman[®] filter paper. Afterwards, the solution was layered with hexane and stored at $-35\text{ }^\circ\text{C}$ for one week. The product was isolated as red block crystals (yield: 45%) suitable for X-ray structure analysis.

$^1\text{H-NMR}$ (300 MHz, 238 K, $\text{THF-}d_8$): δ / ppm = 6.99 (s, 2H, CH^{NHC}), 6.92-6.85 (m, 4H, m- CH^{Ar}), 6.72-6.70 (dd, $^3J_{\text{HH}} = 7.4\text{ Hz}, 1.7\text{ Hz}$, 2H, p- CH^{Ar}), 5.43 (s, 1H, CH^{Pz}), 4.57 (s, 2H, CH), 4.16 (m, 2H, CH_2), 4.06 (s, 6H, CH_3^{NHC}), 3.91-3.83 (sept, $^3J_{\text{HH}} = 6.9\text{ Hz}$, 1H, CH^{iPr}), 2.94-2.86 (sept, $^3J_{\text{HH}} = 6.8\text{ Hz}$, 2H, CH^{iPr}), 1.89 (s, 6H, CH_3), 1.59-1.58 (d, $^3J_{\text{HH}} = 6.9\text{ Hz}$, 6H, CH_3^{iPr}), 1.14 (s, 6H, CH_3), 1.04-1.02 (d, $^3J_{\text{HH}} = 6.9\text{ Hz}$, 6H, CH_3^{iPr}), 0.88-0.87 (d, $^3J_{\text{HH}} = 6.9\text{ Hz}$, 6H, CH_3^{iPr}), 0.76-0.74 (d, $^3J_{\text{HH}} = 6.9\text{ Hz}$, 6H, CH_3^{iPr}).

$^{31}\text{P-NMR}$ (202 MHz, 238 K, $\text{THF-}d_8$): δ / ppm = 4.4 (m, $^1J_{\text{PP}} = 516\text{ Hz}, ^2J_{\text{PC}} = 12\text{ Hz}$), 12.4 (d, $^1J_{\text{PP}} = 516\text{ Hz}$).

5.4.9 Synthesis of 9

Scheme 5.10: Synthesis of $[\text{LNi}_2(\mu\text{-P}(\text{NHC}))]$ (9).

To a dark red solution of $[\text{LNi}_2(\mu\text{-PCO})]$ (7) (20 mg, 25.6 μmol , 1.0 eq.) in THF (3 mL) benzyl isocyanide (2.9 μL , 26 μmol , 1.0 eq.) was added. The reaction mixture was heated to 65 °C for two days. The solvent was removed afterwards under vacuum. The residue was then dissolved in a minimum amount of Me-THF and filtrated through a Whatman[®] filter paper. The consequent vapour diffusion with TMS yielded the product as red block crystals after two weeks (yield: 45%) suitable for X-ray structure analysis.

$^1\text{H-NMR}$ (500 MHz, 238 K, THF- d_8): δ / ppm = 6.99 (s, 2H, CH^{NHC}), 6.92-6.85 (m, 4H, $m\text{-CH}^{\text{Ar}}$), 6.72-6.70 (dd, $^3J_{\text{HH}} = 7.4$ Hz, 1.7 Hz, 2H, $p\text{-CH}^{\text{Ar}}$), 5.43 (s, 1H, CH^{Pz}), 4.57 (s, 2H, CH), 4.16 (m, 2H, CH_2), 4.06 (s, 6H, CH_3^{NHC}), 3.91-3.83 (sept, $^3J_{\text{HH}} = 6.9$ Hz, 1H, CH^{iPr}), 2.94-2.86 (sept, $^3J_{\text{HH}} = 6.8$ Hz, 2H, CH^{iPr}), 1.89 (s, 6H, CH_3), 1.59-1.58 (d, $^3J_{\text{HH}} = 6.9$ Hz, 6H, CH_3^{iPr}), 1.14 (s, 6H, CH_3), 1.04-1.02 (d, $^3J_{\text{HH}} = 6.9$ Hz, 6H, CH_3^{iPr}), 0.88-0.87 (d, $^3J_{\text{HH}} = 6.9$ Hz, 6H, CH_3^{iPr}), 0.76-0.74 (d, $^3J_{\text{HH}} = 6.9$ Hz, 6H, CH_3^{iPr}).

$^{13}\text{C}\{^1\text{H}\}\text{-NMR}$ (125 MHz, 238 K, THF- d_8): δ / ppm = 171.5 (P-C^{NHC}), (d, $^1J_{\text{PC}} = 142$ Hz, C^{NHC}), 160.0 ($\text{C-Me}^{\text{Nacnac}}$), 159.7 ($\text{C-Me}^{\text{Nacnac}}$), 154.4 (C^{Pz}), 152.1 (C^{Ar}); 143.4 ($o\text{-C}^{\text{Ar}}$), 141.4 ($o\text{-C}^{\text{Ar}}$), 124.7 ($m\text{-C}^{\text{Ar}}$), 124.5 ($m\text{-C}^{\text{Ar}}$), 123.6 ($p\text{-C}^{\text{Ar}}$), 122.5 (CH^{NHC}), 97.5 ($\text{CH}^{\text{Nacnac}}$), 91.8 (CH^{Pz}), 53.2 (CH_2), 38.5 (d, $^3J_{\text{PC}} = 4$ Hz, CH_3^{NHC}), 29.1 (CH^{iPr}), 28.9 (CH^{iPr}), 26.3 (CH_3^{iPr}), 25.8 (CH_3^{iPr}), 24.9 (CH_3), 24.6 (CH_3^{iPr}), 24.6 (CH_3^{iPr}), 21.2 (CH_3).

$^{15}\text{N}\{^1\text{H}\}\text{-NMR}$ (50 MHz, 238 K, THF- d_8): δ / ppm = -228.8 (N^{Pz}), -209.4 (N^{NHC}), -207.0 (N^{Nacnac}), -151.9 (N^{Nacnac}).

$^{31}\text{P}\{^1\text{H}\}\text{-NMR}$ (202 MHz, 238 K, THF- d_8): δ / ppm = 44.8.

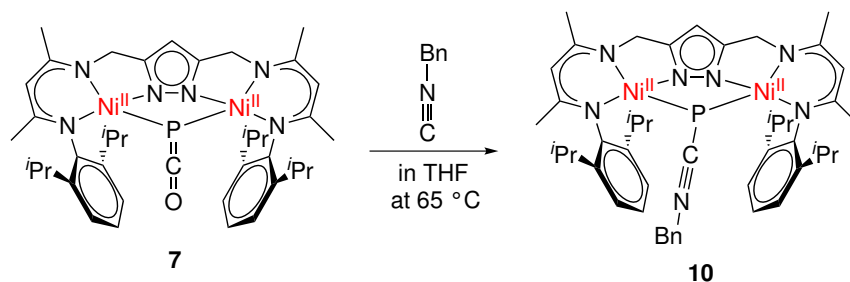
UV-Vis (298 K, THF): λ_{max} / nm (ϵ / $\text{M}^{-1}\text{cm}^{-1}$) = 337 (14612), 377 (11953), 541 (2200).

IR (ATR, 298 K): $\tilde{\nu}$ / cm^{-1} = 3080 (w), 2945 (m), 2851 (w), 1637 (s), 1618 (s), 1555 (w), 1528 (w), 1462 (w), 1433(m), 1401 (m), 1314 (w), 1260 (w), 1088 (m), 1030 (m), 801 (w).

ESI⁺-MS in THF $m/z = 849.4$ [$\text{M}+\text{H}$] (100%).

EA Anal. calcd (%) for $\text{C}_{44}\text{H}_{61}\text{N}_8\text{Ni}_2\text{P}$: C 62.15, H 7.23, N 13.18; Found: C 61.87, H 7.05, N 12.96

5.4.10 Synthesis of 10

Scheme 5.11: Synthesis of $[\text{LNi}_2(\mu\text{-PCNBn})]$ 10.

To a dark red solution of $[\text{LNi}_2(\mu\text{-PCO})]$ (7) (20 mg, 25.6 μmol , 1.0 eq.) in THF (3 mL) 1,3-Dimethylimidazolium-2-carboxylate (3.97 mg, 28.1 μmol , 1.1 eq.) was added. The reaction mixture was heated to 65 °C for three days. The solvent was removed afterwards under vacuum. The residue was then dissolved in a minimum amount of Me-THF and filtrated through a Whatman[®] filter paper and layered with hexane (10 ml). The product was isolated as deep red block crystals after one week (yield: 55%) suitable for X-ray structure analysis.

$^1\text{H-NMR}$ (500 MHz, 238 K, THF- d_8): δ / ppm = 7.22-7.17 (m, 4H, m- CH^{Ar}), 6.96-6.87 (m, 4H, m- CH^{Ar}), 6.83-6.76 (dd, $^3J_{\text{HH}} = 7.4 \text{ Hz}, 1.7 \text{ Hz}, 2\text{H}, \text{p-CH}^{\text{Ar}}$), 5.59 (s, 1H, CH^{Pz}), 5.18 (s, 2H, CH_2^{Bn}), 4.81 (s, 2H, CH), 4.29 (m, 4H, CH_2), 3.30 (m, 2H, CH^{iPr}), 2.86 (m, 2H, CH^{iPr}), 2.08 (s, 6H, CH_3), 1.45 (m, 6H, CH_3^{iPr}), 1.33 (m, 6H, CH_3^{iPr}), 1.11 (m, 6H, CH_3^{iPr}), 1.03 (m, 6H, CH_3^{iPr}), 0.77 (m, 6H, CH_3^{iPr}).

$^{13}\text{C}\{^1\text{H}\}\text{-NMR}$ (125 MHz, 238 K, THF- d_8): δ / ppm = 172.7 (d, $^1J_{\text{PC}} = 130 \text{ Hz}, \text{P-C}$), 160.4 (C-Me $^{\text{Nacnac}}$), 160.1 (C-Me $^{\text{Nacnac}}$), 155.6 (C^{Pz}), 152.1 (C^{Ar}); 150.7 (C^{Ar}), 142.1 (o- C^{Ar}), 141.5 (o- C^{Ar}), 137.5 (C^{Ph}), 129.1 (m- C^{Ar}), 128.4 (m- C^{Ph}), 127.7 (p- C^{Ph}), 125.8 (m- C^{Ar}), 124.5 (m- C^{Ar}), 123.9 (p- C^{Ar}), 97.3 (CH), 92.9 (CH^{Pz}), 54.2 (CH_2^{Bn}), 53.4 (CH_2), 28.7 (CH^{iPr}), 28.4 (CH^{iPr}), 25.8 (CH_3^{iPr}), 25.7 (CH_3), 25.1 (CH_3^{iPr}), 25.0 (CH_3^{iPr}), 24.5 (CH_3), 21.9 (CH_3).

$^{15}\text{N}\{^1\text{H}\}\text{-NMR}$ (50 MHz, 238 K, THF- d_8): δ / ppm = -232.6 (N^{Nacnac}), -200.6 (N^{Nacnac}), -160.0 (N^{Pz}), -159.13 (NC).

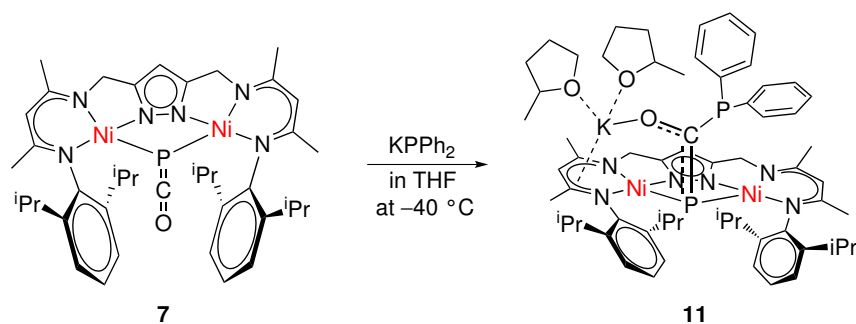
$^{31}\text{P}\{^1\text{H}\}\text{-NMR}$ (202 MHz, 238 K, THF- d_8): δ / ppm = -84.2.

UV-Vis (298 K, THF): λ_{max} / nm (ϵ / $\text{M}^{-1}\text{cm}^{-1}$) = 336 (20739), 361 (16429), 376 (16070), 480 (2444).

IR (KBr, 298 K): $\tilde{\nu}$ / cm^{-1} = 3080 (w), 2945 (m), 2851 (w), 2070 (w), 1809 (m), 1637 (w), 1617 (m), 1553 (m), 1529 (s), 1456 (m), 1436 (s), 1395 (s), 1312 (m), 1030 (w), 795 (w), 758 (w).

ESI⁺-MS in THF, $m/z = 870.3$ [M+H] (100%).

5.4.11 Synthesis of 11

Scheme 5.12: Synthesis of $\text{K}[\text{LNi}_2(\text{PC}(\text{O})\text{PPh}_2)]$ (11).

To a dark red 2-methyl-THF (2 mL) solution of $[\text{LNi}_2(\mu\text{-PCO})]$ (7) (20 mg, 25.6 μmol , 1.0 eq.), a 0.5 M THF solution of potassium diphenylphosphide (51 μL , 25.6 μmol , 1.0 eq.) was added at $-38\text{ }^\circ\text{C}$. The reaction mixture immediately turned darker. Subsequently, the solution was filtered through a Whatman[®] filter paper. The consequent vapour diffusion with TMS yielded the product as black block crystals after two weeks (yield: 65%) suitable for X-ray structure analysis.

$^1\text{H-NMR}$ (500 MHz, 238 K, THF- d_8): δ / ppm = 7.12-6.75 (m, 16H, CH^{Ar}), 5.21 (s, 1H, CH^{Pz}), 4.55 (s, 2H, CH), 3.87-3.72 (m, 4H, CH_2), 3.27-3.20 (sept, $^3J_{\text{HH}} = 6.8\text{ Hz}$, 1H, CH^{iPr}), 1.97-1.77 (m, 6H, CH_3), 1.23 (s, 6H, CH_3), 1.15-1.13 (d, $^3J_{\text{HH}} = 6.1\text{ Hz}$, 6H, CH_3^{iPr}), 1.01-0.99 (d, $^3J_{\text{HH}} = 6.8\text{ Hz}$, 6H, CH_3^{iPr}), 0.97-0.95 (d, $^3J_{\text{HH}} = 6.8\text{ Hz}$, 6H, CH_3^{iPr}), 0.91-0.90 (d, $^3J_{\text{HH}} = 6.0\text{ Hz}$, 6H, CH_3^{iPr}).

$^{13}\text{C}\{^1\text{H}\}$ -NMR (125 MHz, 238 K, THF- d_8): δ / ppm = 253.3 (dd, $J = 94.3, 56.7\text{ Hz}$, P-C-P), 153.3 ($\text{C-Me}^{\text{Nacnac}}$), 152.07 ($\text{C-Me}^{\text{Nacnac}}$), 141.9 ($3,5\text{-C}^{\text{Pz}}$), 134.6, 134.5, 127.4, 127.4, 126.7, 124.5, 124.3, 123.6 (C^{Ar}), 97.2 ($\text{CH}^{\text{Nacnac}}$), 90.6 (CH^{Pz}), 67.9 (CH_2), 28.4 (CH^{iPr}), 25.7 (CH_3^{iPr}), 24.1 (CH_3), 21.6 (CH_3).

$^{31}\text{P}\{^1\text{H}\}$ -NMR (202 MHz, 238 K, THF- d_8): δ / ppm = 203.3 (d, $^2J_{\text{PP}} = 131\text{ Hz}$), 1.7 (d, $^2J_{\text{PP}} = 131\text{ Hz}$).

UV-Vis (298 K, THF): λ_{max} / nm (ϵ / $\text{M}^{-1}\text{cm}^{-1}$) = 377 (29676), 517 (5194), 726 (1270).

IR (ATR, 298 K): $\tilde{\nu}$ / cm^{-1} = 1542 (m), 1516 (m), 1432 (s), 1398 (s), 1303 (s), 1273 (w), 1251 (w), 1184 (w), 1077 (m), 1017 (m), 815 (s), 7378 (s), 693 (s).

Appendix A

Crystallographic Data

A.1 Crystallographic Data of the Complexes 3^{K} , 3^{Na} , **4** and **5**

The crystal data and refinement details of the data collections and the molecular structures are given in the following: 3^{K} : Figure A.1; 3^{Na} : Figure A.2; **4**: Figure A.3; and **5**: Figure A.5. The molecular structure of the side product of the protonation experiment of 3^{K} with $[\text{H}(\text{OEt}_2)_2][\text{BAR}_4^{\text{F}}]$ is displayed in Figure A.4. Selected bond lengths and angles are shown and discussed in the respective section of this work. Non-hydrogen atoms were refined anisotropically. The structures were solved with SHELXT and refined on F^2 using all reflections with SHELXL.^[267,268] Hydrogen atoms were placed in positions with the help of DFT calculations and assigned to an isotropic displacement parameter of 1.5/1.2 $U_{\text{eq}}(\text{C})$.

In 3^{Na} , one *iso*-Pr group (occupancy factors: 0.837(4) / 0.163(4) (C37, C38, C39A/B)) and a THF solvent molecules (occupancy factors: 0.679(9) / 0.321(9) (only C46A/B)) were found to be disordered. SADI restraints ($d_{\text{C46A/B-C45/47}}$) and EADP constraints (for *iso*-Pr carbon atoms) were applied to model the disordered parts.

In **4**, one *iso*-Pr group was found to be disordered about two positions (occupancy factors: 0.602(5) / 0.398(5)). SAME, SADI & RIGU restraints and EADP constraints were applied to model the disorder. Two CF_3 groups of the $[\text{BAR}_4^{\text{F}}]^-$ counterion (occupancy factors: 0.305(4) / 0.695(4) and 0.552(19) / 0.448(19)) and three THF molecules (occupancy factors: 0.226(15) / 0.774(15), 0.569(7) / 0.431(7) and 0.497(8) / 0.503(8)) are disordered as well. SADI, RIGU & ISOR restraints and EADP constraints in case of the CF_3 groups and DFIX $d(\text{C-O}) = 1.44 \text{ \AA}$, $d(\text{C-C}) = 1.44 \text{ \AA}$, SAME, SIMU, DELU & ISOR restraints in case of the THF molecules and a BUMP restraint have been used.

In **5**, one THF solvent molecule was found to be disordered (occupancy factors: 0.580(12) / 0.420(12)). SAME, RIGU and DELU restraints were applied to model the disordered parts.

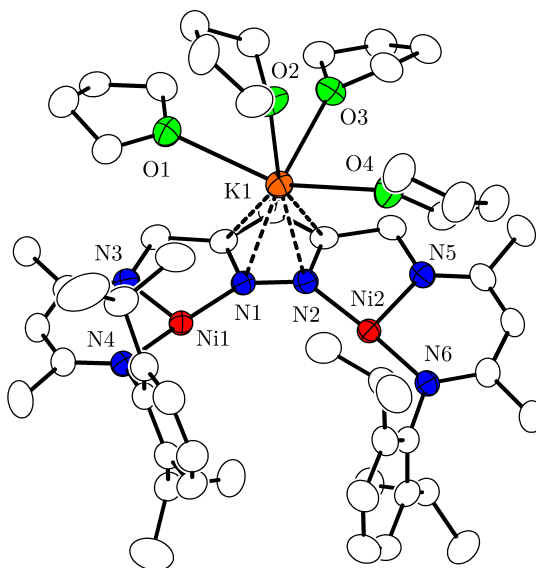


Figure A.1: Top: Molecular structure of $\text{K}[\text{LNi}_2]$ (3^{K}) (30% probability thermal ellipsoids). The hydrogen atoms are omitted for clarity. **Bottom:** Crystal data and refinement details of 3^{K} .

Empirical formula	$\text{C}_{55}\text{H}_{85}\text{KN}_6\text{Ni}_2\text{O}_4$	
Formula weight	1050.80	
T/K	133(2)	
Crystal size / mm^3	0.500 x 0.490 x 0.360	
Crystal system	monoclinic	
Space group	$\text{P2}_1/\text{n}$	
Unit cell dimensions	$a = 13.8033(4) \text{ \AA}$	$\alpha = 90^\circ$
	$b = 14.7683(3) \text{ \AA}$	$\beta = 106.622(2)^\circ$
	$c = 14.2159(4) \text{ \AA}$	$\gamma = 90^\circ$
$V/\text{\AA}^3$	2776.83(13)	
Z	2	
$\rho/\text{g cm}^{-3}$	1.257	
Absorption coefficient	0.801 mm^{-1}	
$F(000)$	1128	
Θ -range / $^\circ$	1.495-25.649	
hkl -range	$-16 \leq h \leq 16$	
	$-17 \leq k \leq 17$	
	$-17 \leq l \leq 17$	
Measured refl.	32019	
Unique refl. / R_{int}	10195 [0.437]	
Data / restr. / param.	10195 / 1 / 625	
Goodness-of-fit (F^2)	1.053	
$R1, wR2 (I > 2\sigma(I))$	0.0302 / 0.0749	
$R1, wR2$ (all data)	0.0344 / 0.0785	
Largest diff. peak and hole	0.481 / $-0.197 e\text{\AA}^3$	

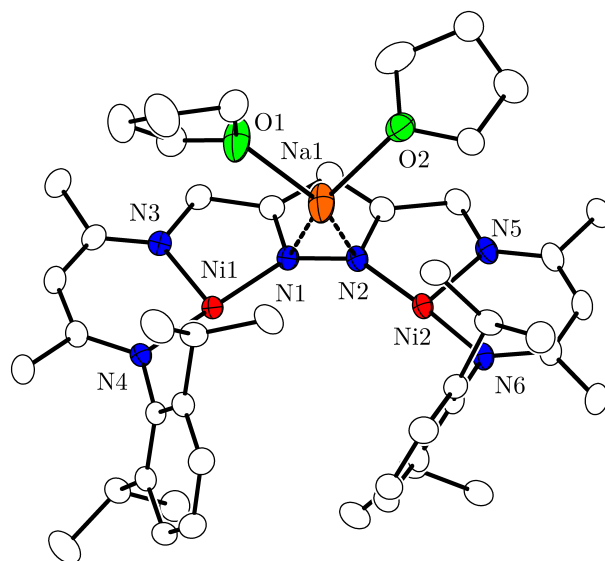


Figure A.2: Top: Molecular structure of $\text{Na}[\text{LNi}_2]$ (3^{Na}) (30% probability thermal ellipsoids). The hydrogen atoms are omitted for clarity. **Bottom:** Crystal data and refinement details of 3^{Na} .

Empirical formula	$\text{C}_{47}\text{H}_{69}\text{NaN}_6\text{Ni}_2\text{O}_2$	
Formula weight	890.49	
T/K	100(2)	
Crystal size / mm^3	0.352 x 0.263 x 0.176	
Crystal system	monoclinic	
Space group	$\text{P}2_1/n$	
Unit cell dimensions	$a = 18.6514(7) \text{ \AA}$	$\alpha = 90^\circ$
	$b = 13.9305(5) \text{ \AA}$	$\beta = 108.8700(10)^\circ$
	$c = 18.7394(7) \text{ \AA}$	$\gamma = 90^\circ$
$V/\text{\AA}^3$	4607.3(3)	
Z	4	
$\rho/\text{g cm}^{-3}$	1.284	
Absorption coefficient	0.870 mm^{-1}	
$F(000)$	1904	
Θ -range / $^\circ$	2.297-28.293	
hkl -range	$-24 \leq h \leq 23$	
	$-18 \leq k \leq 18$	
	$-24 \leq l \leq 24$	
Measured refl.	128356	
Unique refl. / R_{int}	11438 [0.0821]	
Data / restr. / param.	11438 / 6 / 557	
Goodness-of-fit (F^2)	1.062	
$R1, wR2 (I > 2\sigma(I))$	0.0372 / 0.0776	
$R1, wR2$ (all data)	0.0592 / 0.0903	
Largest diff. peak and hole	0.961 / $-0.994 e\text{\AA}^3$	

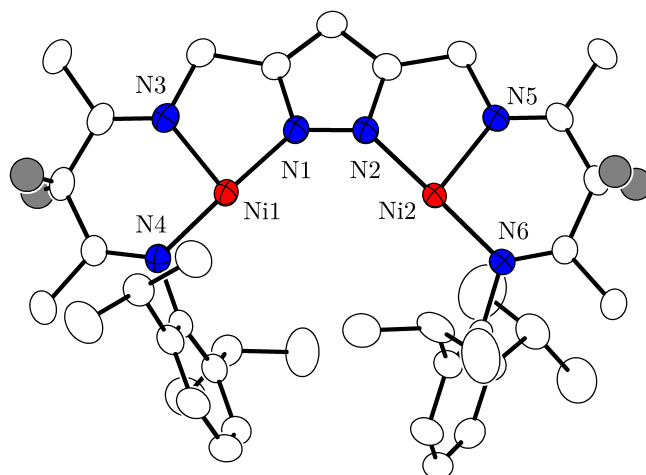


Figure A.3: Top: Molecular structure of the cation of $[\text{H}_2\text{LNi}_2][\text{BAR}_4^{\text{F}}]$ (**4**) (30% probability thermal ellipsoids). The $[\text{BAR}_4^{\text{F}}]^-$ counterion and all hydrogen atoms except for those at the γ -C of the β -diimine subunits (gray), are omitted for clarity. **Bottom:** Crystal data and refinement details of **4**.

Empirical formula	$\text{C}_{87}\text{H}_{99}\text{BF}_{24}\text{N}_6\text{Ni}_2\text{O}_4$	
Formula weight	1876.95	
T/K	133(2)	
Crystal size / mm^3	0.500 x 0.490 x 0.480	
Crystal system	triclinic	
Space group	P-1	
Unit cell dimensions	$a = 12.7703(4) \text{ \AA}$	$\alpha = 72.510(2)^\circ$
	$b = 18.0462(5) \text{ \AA}$	$\beta = 74.014(2)^\circ$
	$c = 20.8906(6) \text{ \AA}$	$\gamma = 80.426(2)^\circ$
$V/\text{\AA}^3$	4395.8(2)	
Z	2	
$\rho/\text{g cm}^{-3}$	1.418	
Absorption coefficient	0.532 mm^{-1}	
$F(000)$	1944	
Θ -range / $^\circ$	1.359-26.968	
hkl -range	$-16 \leq h \leq 14$	
	$-22 \leq k \leq 22$	
	$-26 \leq l \leq 26$	
Measured refl.	59769	
Unique refl. / R_{int}	18539 [0.0198]	
Data / restr. / param.	18539 / 724 / 1335	
Goodness-of-fit (F^2)	1.025	
$R1, wR2 (I > 2\sigma(I))$	0.0399 / 0.1001	
$R1, wR2$ (all data)	0.0504 / 0.1076	
Largest diff. peak and hole	0.636 / $-0.503 e\text{\AA}^{-3}$	

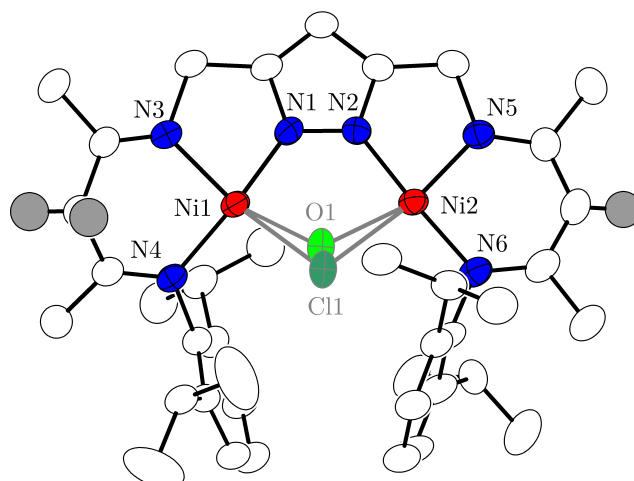


Figure A.4: **Top:** Molecular structure of the cation of $[\text{HLNi}_2^{\text{II}}(\mu\text{-OH})][\text{BAR}_4^{\text{F}}]$ (30% probability thermal ellipsoids). The $[\text{BAR}_4^{\text{F}}]^-$ counterion and all hydrogen atoms, except those at the $\gamma\text{-C}$ of the side arms (gray), are omitted for clarity. **Bottom:** Crystal data and refinement details of $[\text{HLNi}_2^{\text{II}}(\mu\text{-OH})][\text{BAR}_4^{\text{F}}]$.

Empirical formula	$\text{C}_{72}\text{H}_{63}\text{BCl}_{0.59}\text{F}_{20}\text{N}_6\text{Ni}_2\text{O}_{0.415}$	
Formula weight	1548.08	
T/K	133(2)	
Crystal size / mm^3	0.500 x 0.490 x 0.480	
Crystal system	monoclinic	
Space group	$\text{P2}_1/\text{c}$	
Unit cell dimensions	$a = 14.8942(2) \text{ \AA}$	$\alpha = 90^\circ$
	$b = 11.2036(2) \text{ \AA}$	$\beta = 100.0250(10)^\circ$
	$c = 41.0168(5) \text{ \AA}$	$\gamma = 90^\circ$
$V/\text{\AA}^3$	6739.92(2)	
Z	4	
$\rho/\text{g cm}^{-3}$	1.526	
Absorption coefficient	0.687 mm^{-1}	
$F(000)$	3165	
$\Theta\text{-range}/^\circ$	1.388-25.716	
$hkl\text{-range}$	$-18 \leq h \leq 18$	
	$-13 \leq k \leq 13$	
	$-49 \leq l \leq 49$	
Measured refl.	75223	
Unique refl. / R_{int}	12740 [0.0551]	
Data / restr. / param.	18539 / 724 / 1335	
Goodness-of-fit (F^2)	1.034	
$R1, wR2 (I > 2\sigma(I))$	0.0378 / 0.0845	
$R1, wR2 (\text{all data})$	0.0546 / 0.0939	
Largest diff. peak and hole	0.379 / $-0.0442 e\text{\AA}^3$	

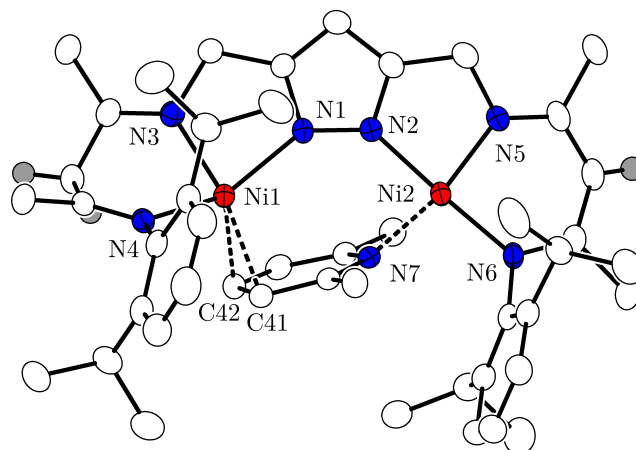


Figure A.5: Top: Molecular structure of $[\text{HLNi}^{\text{I}}\text{Ni}^{\text{II}}(\mu\text{-Me}_2\text{C}_5\text{H}_3\text{N})][\text{BF}_4]$ (**5**) (30% probability thermal ellipsoids). The lutidinium \cdots Ni contacts are shown as dashed lines. The BF_4 counteranion and hydrogen atoms, except those at the γ -C of the side arms (gray), are omitted for clarity. **Bottom:** Crystal data and refinement details of **5**.

Empirical formula	$\text{C}_{58}\text{H}_{87}\text{BF}_4\text{N}_7\text{Ni}_2\text{O}_3$	
Formula weight	1134.57	
T/K	133(2)	
Crystal size / mm^3	0.500 x 0.180 x 0.110	
Crystal system	triclinic	
Space group	P-1	
Unit cell dimensions	$a = 13.3610(4) \text{ \AA}$	$\alpha = 74.184(3)^\circ$
	$b = 13.7556(5) \text{ \AA}$	$\beta = 73.891(3)^\circ$
	$c = 16.8590(6) \text{ \AA}$	$\gamma = 79.539(3)^\circ$
$V/\text{\AA}^3$	2845.26(18)	
Z	2	
$\rho/\text{g cm}^{-3}$	1.324	
Absorption coefficient	0.725 mm^{-1}	
$F(000)$	1210	
Θ -range / $^\circ$	1.293–26.846	
hkl -range	–16 $\leq h \leq$ 15	
	–17 $\leq k \leq$ 17	
	–21 $\leq l \leq$ 21	
Measured refl.	38213	
Unique refl. / R_{int} .	12075 [0.0486]	
Data / restr. / param.	12075 / 110 / 736	
Goodness-of-fit (F^2)	1.068	
$R1, wR2 (I > 2\sigma(I))$	0.0499 / 0.1222	
$R1, wR2$ (all data)	0.0778 / 0.1380	
Largest diff. peak and hole	0.698 / $-0.508 e\text{\AA}^3$	

A.2 Crystallographic Data of Complex **6-K(crypt)**

The crystal data and refinement details of the data collections and the molecular structures of **6-K(crypt)** are given in Figure A.6. Selected bond lengths and angles are shown and discussed in the respective section of this work. Non-hydrogen atoms were refined anisotropically. The structures were solved with SHELXT and refined on F^2 using all reflections with SHELXL.^[267,268] Hydrogen atoms were placed in positions according to DFT calculations and assigned to an isotropic displacement parameter of 1.5/1.2 $U_{eq}(C)$.

During a multitude of crystallization attempts of **6-K(crypt)** with varying solvent combinations and ratios, and several measuring trials, the presented molecular structure in Figure A.6 shows the best data quality in comparison with all previous structures. The otherwise observed disorder of the hydroxido group among the two nickel ions was also not present. The quality of the structure determination, however, was not sufficient to localize hydrogen atom positions. Furthermore, the unit cell contains highly disordered solvent molecules for which no satisfactory model for a disorder could be found. The solvent contribution to the structure factors was calculated with PLATON SQUEEZE^[274] and the resulting .fab file was processed with SHELXL using the ABIN instruction. The empirical formula and derived values are in accordance with the calculated cell content. The crystal was racemically twinned which is expressed in an absolute structure parameter of $x = 0.66(2)$. One *iso*-Pr group (occupancy factors: 0.47(3) / 0.53(3); (C56, C57, C58A/B)) in one of the two crystallographically independent anions was found to be disordered. SAME, RIGU, SIMU, DELU restraints were applied to model the disorder.

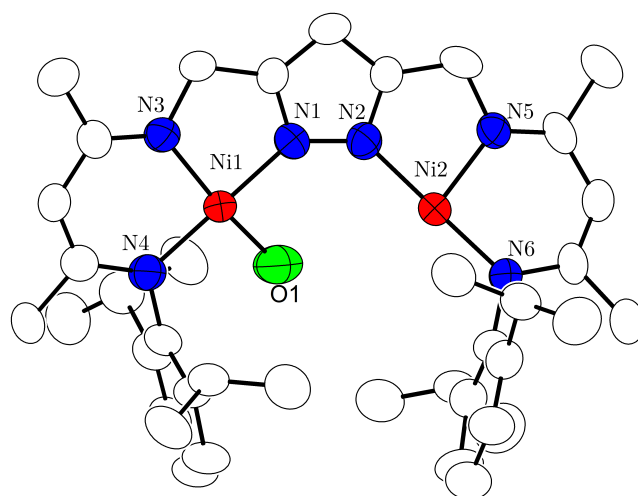


Figure A.6: Top: Molecular structure (30% probability thermal ellipsoids) of the anionic part of **Crypt(K)[LNi₂^{II}(OH)(H)] (6-K(crypt))** (first crystallographically independent anion). Solvent molecules and hydrogen atoms are omitted for clarity. **Bottom:** Crystal data and refinement details of **6-K(crypt)**.

Empirical formula	C ₅₇ H ₈₉ KN ₈ Ni ₂ O ₇	
Formula weight	1154.88	
<i>T</i> /K	133(2)	
Crystal size /mm ³	0.500 x 0.180 x 0.110	
Crystal system	orthorhombic	
Space group	P2 ₁ 2 ₁ 2 ₁	
Unit cell dimensions	<i>a</i> = 18.1769(3) Å	<i>α</i> = 90°
	<i>b</i> = 25.3653(4) Å	<i>β</i> = 90°
	<i>c</i> = 34.2811(7) Å	<i>γ</i> = 90°
<i>V</i> /Å ³	15805.7(5)	
<i>Z</i>	8	
<i>ρ</i> /g cm ⁻³	0.971	
Absorption coefficient	0.571 mm ⁻¹	
<i>F</i> (000)	4944	
Θ-range /°	1.188-25.754	
<i>hkl</i> -range	-20 ≤ <i>h</i> ≤ 22	
	-30 ≤ <i>k</i> ≤ 30	
	-41 ≤ <i>l</i> ≤ 41	
Measured refl.	93704	
Unique refl. / <i>R</i> _{int.}	29700 [0.0589]	
Data / restr. / param.	29700 / 58 / 1406	
Goodness-of-fit (<i>F</i> ²)	1.033	
<i>R</i> ₁ , <i>wR</i> ₂ (<i>I</i> > 2σ(<i>I</i>))	0.0728 / 0.2055	
<i>R</i> ₁ , <i>wR</i> ₂ (all data)	0.0922 / 0.2229	
Largest diff. peak and hole	1.225 / -0.584 eÅ ³	

A.3 Crystallographic Data of the Complexes 7, 8, 9, 10, and 11

The crystal data and refinement details of the data collections and the molecular structures are given in the following: **7**: Figure A.7 and Figure A.8; **8**: Figure A.9; **9**: Figure A.10; **10**: Figure A.11; and **11**: A.12. Selected bond lengths and angles are shown and discussed in the respective section of this work. Non-hydrogen atoms were refined anisotropically. The structures were solved with SHELXT and refined on F^2 using all reflections with SHELXL.^[267,268] Hydrogen atoms were placed in positions according to DFT calculations and assigned to an isotropic displacement parameter of 1.5/1.2 $U_{\text{eq}}(\text{C})$.

Two different conformations of **7** were isolated. Interestingly, the molecular structures show different C–P–Ni(1/2) bond angles (C40–P1–Ni1 80.85(14) and C40–P1–Ni2 81.50(14) (in Figure A.7): *vs* C40–P1–Ni1 69.42(9) and C40–P1–Ni2 96.21(8) (in Figure A.8)), which results either in a symmetric or tilted confirmation of the PCO^- ligand. It was not possible to reproduce the confirmation displayed in Figure A.8, which is also not in agreement with the DFT calculations, see Section C.4.1.

In **9** atoms of one DIPP group (occupancy factors: 0.508(8) / 0.492(8) (C12–C15A/B & C19–C21A/B)) and a 2-methyl-THF solvent molecule were found to be disordered (occupancy factors: 0.441(14) / 0.559(14)) about 2 positions and another 2-methyl-THF solvent molecule about a center of inversion. The latter was refined at 1/2 occupancy. SAME, SADI and RIGU restraints were applied to model the disorder of the side arm and DFIX ($d(\text{C-C}) = 1.44 \text{ \AA}$, $d(\text{C-O}) = 1.44 \text{ \AA}$, $d(\text{C-CH}_3) = 1.52 \text{ \AA}$), SAME, RIGU, SIMU and DELU restraints to model the disorder of the 2-methyl-THF molecules.

In **11** two methyl groups of one *iso*-Pr group are disordered (occupancy factors: 0.60(3) / 0.40(3) (C38 & C39 A/B)). DFIX restraints (for H···H separation) and an EADP constraints were applied. Two 2-methyl-THF solvent molecules coordinating the potassium atom (occupancy factors: 0.693(6) / 0.307(6) & 0.691(6) / 0.309(6)) and two methyl groups of one *iso*-Pr group (occupancy factors: 0.68(2) / 0.32(2) (C20 & C21 A/B)) were found to be disordered in **11**. SAME and RIGU restraints and EADP constraints were used to model the disordered 2-methyl-THF molecules.

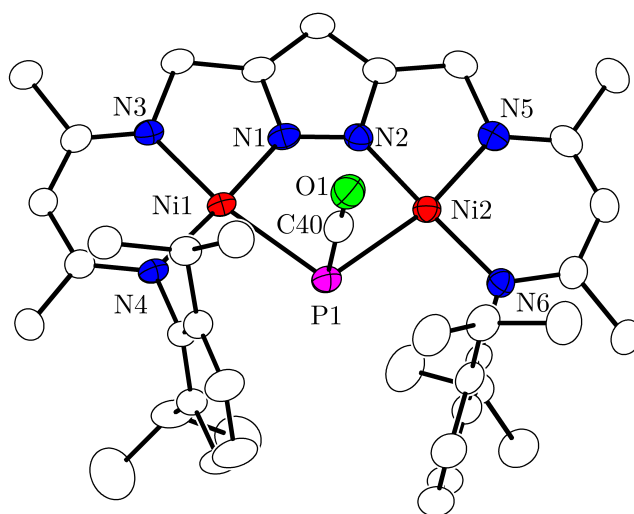


Figure A.7: Top: Molecular structure of $[\text{LNi}_2(\mu\text{-PCO})]$ (**7**) (30% probability thermal ellipsoids). The hydrogen atoms are omitted for clarity. **Bottom:** Crystal data and refinement details of **7**.

Empirical formula	$\text{C}_{43}\text{H}_{59}\text{N}_6\text{Ni}_2\text{OP}$	
Formula weight	824.35	
T/K	133(2)	
Crystal size / mm^3	0.500 x 0.160 x 0.110	
Crystal system	triclinic	
Space group	P1	
Unit cell dimensions	$a = 9.4510(4) \text{ \AA}$	$\alpha = 80.052(3)^\circ$
	$b = 12.4897(5) \text{ \AA}$	$\beta = 76.311(3)^\circ$
	$c = 18.3311(8) \text{ \AA}$	$\gamma = 86.639(3)^\circ$
$V/\text{\AA}^3$	2070.38(15)	
Z	2	
$\rho/\text{g cm}^{-3}$	1.322	
Absorption coefficient	0.988 mm^{-1}	
$F(000)$	876	
Θ -range / $^\circ$	1.656-26.877	
hkl -range	$-11 \leq h \leq 10$	
	$-15 \leq k \leq 15$	
	$-23 \leq l \leq 23$	
Measured refl.	29454	
Unique refl. / R_{int}	8766 [0.0500]	
Data / restr. / param.	8766 / 0 / 490	
Goodness-of-fit (F^2)	1.079	
$R1, wR2 (I > 2\sigma(I))$	0.0494 / 0.1327	
$R1, wR2$ (all data)	0.0721 / 0.1450	
Largest diff. peak and hole	1.032 / $-0.443 e\text{\AA}^{-3}$	

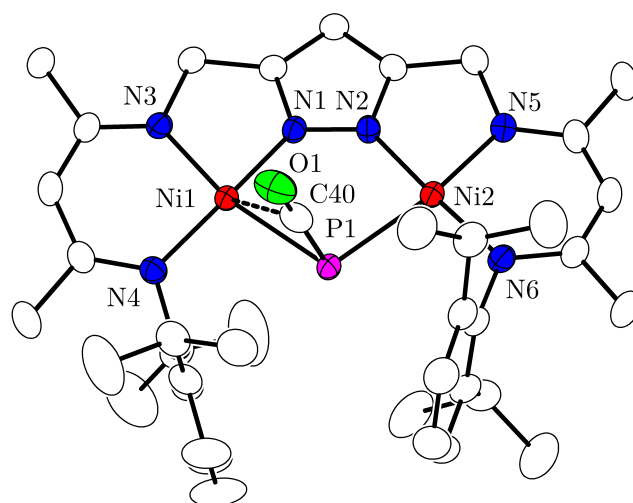


Figure A.8: Top: Molecular structure of a different configuration of $[\text{LNi}_2(\mu\text{-PCO})]$ (30% probability thermal ellipsoids). The hydrogen atoms are omitted for clarity. Selected bond lengths / Å, distances / Å, and angles /°: Ni1–P1 2.3542(6), Ni2–P1 2.3293(6), P1–C40 1.638(2), C40–O1 1.173(3), C40–P1–Ni1 69.42(9), C40–P1–Ni2 96.21(8), Ni1–P1–Ni2 106.64(2), O1–C40–P1 173.5(2). **Bottom:** Crystal data and refinement details.

Empirical formula	$\text{C}_{42.50}\text{H}_{58}\text{N}_6\text{Ni}_2\text{O}_{1.50}\text{P}$	
Formula weight	825.34	
T/K	133(2)	
Crystal size / mm^3	0.500 x 0.380 x 0.320	
Crystal system	monoclinic	
Space group	$\text{P}2_1/\text{c}$	
Unit cell dimensions	$a = 18.1406(4) \text{ \AA}$	$\alpha = 90^\circ$
	$b = 14.7063(3) \text{ \AA}$	$\beta = 116.884(2)^\circ$
	$c = 17.3432(4) \text{ \AA}$	$\gamma = 90^\circ$
$V/\text{\AA}^3$	4126.79(17)	
Z	4	
$\rho/\text{g cm}^{-3}$	1.328	
Absorption coefficient	0.993 mm^{-1}	
$F(000)$	1752	
Θ -range /°	1.871–26.903	
hkl -range	$-21 \leq h \leq 23$	
	$-18 \leq k \leq 18$	
	$-21 \leq l \leq 22$	
Measured refl.	59288	
Unique refl. / R_{int}	8759 [0.0397]	
Data / restr. / param.	8759 / 58 / 529	
Goodness-of-fit (F^2)	1.026	
$R1, wR2 (I > 2\sigma(I))$	0.0328 / 0.0826	
$R1, wR2$ (all data)	0.0456 / 0.0883	
Largest diff. peak and hole	0.760 / $-0.321 e\text{\AA}^3$	

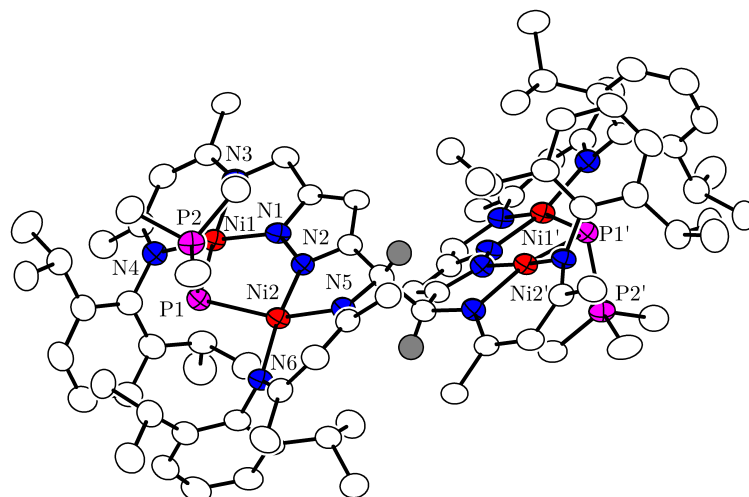


Figure A.9: Top: Molecular structure of $[L'\{Ni_2P(PMe_3)_2\}]_2$ (**8**) (30% probability thermal ellipsoids). The hydrogen atoms are omitted for clarity. **Bottom:** Crystal data and refinement details of **8**.

Empirical formula	$C_{108}H_{146}N_{12}Ni_4P_4$	
Formula weight	1971.08	
T/K	133(2)	
Crystal size / mm^3	0.400 x 0.290 x 0.260	
Crystal system	monoclinic	
Space group	$C2/c$	
Unit cell dimensions	$a = 43.670(2) \text{ \AA}$	$\alpha = 90^\circ$
	$b = 13.8603(8) \text{ \AA}$	$\beta = 108.535(3)^\circ$
	$c = 18.0979(8) \text{ \AA}$	$\gamma = 90^\circ$
$V/\text{\AA}^3$	10386.0(9)	
Z	4	
$\rho/g \text{ cm}^{-3}$	1.261	
Absorption coefficient	0.828 mm^{-1}	
$F(000)$	4200	
Θ -range / $^\circ$	1.549-26.990	
hkl -range	$-53 \leq h \leq 53$	
	$-16 \leq k \leq 16$	
	$-20 \leq l \leq 22$	
Measured refl.	64759	
Unique refl. / R_{int} .	9840 [0.1512]	
Data / restr. / param.	9840 / 0 / 592	
Goodness-of-fit (F^2)	1.079	
$R1, wR2 (I > 2\sigma(I))$	0.0690 / 0.1688	
$R1, wR2$ (all data)	0.1011 / 0.1960	
Largest diff. peak and hole	1.714 / $-0.824 e\text{\AA}^3$	

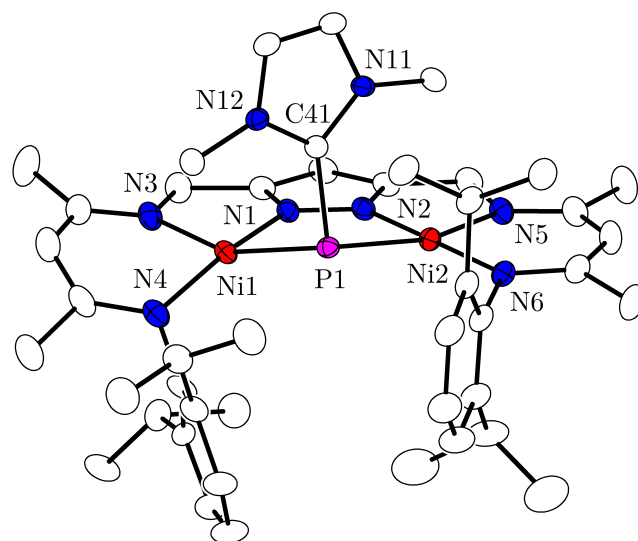


Figure A.10: Top: Molecular structure of $[\text{LNi}_2(\mu\text{-P}(\text{NHC}))]$ (**9**) (30% probability thermal ellipsoids). The hydrogen atoms are omitted for clarity. **Bottom:** Crystal data and refinement details of (**9**).

Empirical formula	$\text{C}_{55.50}\text{H}_{88}\text{N}_8\text{Ni}_2\text{O}_{1.50}\text{PSi}$	
Formula weight	1067.81	
T/K	103(2)	
Crystal size / mm^3	0.500 x 0.081 x 0.071	
Crystal system	monoclinic	
Space group	$\text{P2}_1/\text{n}$	
Unit cell dimensions	$a = 19.1474(9) \text{ \AA}$	$\alpha = 90^\circ$
	$b = 14.5682(7) \text{ \AA}$	$\beta = 107.672(2)^\circ$
	$c = 21.6180(10) \text{ \AA}$	$\gamma = 90^\circ$
$V/\text{\AA}^3$	5745.6(5)	
Z	4	
$\rho/\text{g cm}^{-3}$	1.234	
Absorption coefficient	0.749 mm^{-1}	
$F(000)$	2296	
Θ -range / $^\circ$	2.202-27.907	
hkl -range	$-25 \leq h \leq 25$	
	$-19 \leq k \leq 19$	
	$-28 \leq l \leq 28$	
Measured refl.	196932	
Unique refl. / R_{int}	13717 [0.1018]	
Data / restr. / param.	13717 / 324 / 791	
Goodness-of-fit (F^2)	1.035	
$R1, wR2 (I > 2\sigma(I))$	0.0450 / 0.1016	
$R1, wR2$ (all data)	0.0664 / 0.1130	
Largest diff. peak and hole	1.096 / $-1.307 e\text{\AA}^3$	

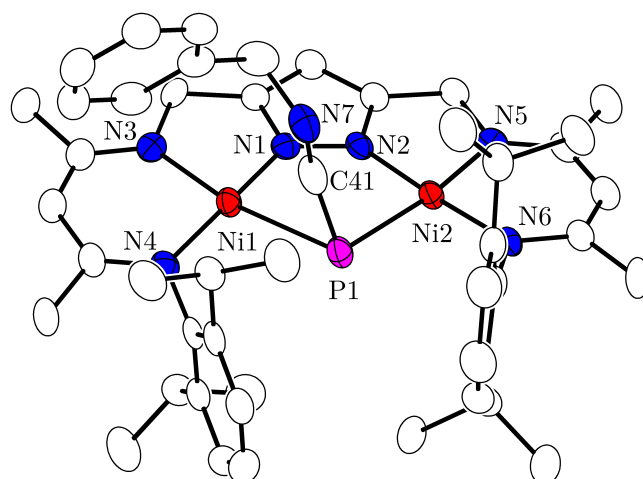


Figure A.11: Top: Molecular structure of $[\text{LNi}_2(\mu\text{-PCNBn})]$ (**10**) (30% probability thermal ellipsoids). The hydrogen atoms are omitted for clarity. **Bottom:** Crystal data and refinement details of **10**.

Empirical formula	$\text{C}_{52}\text{H}_{70}\text{N}_7\text{Ni}_2\text{OP}$
Formula weight	957.54
T/K	120(2)
Crystal size / mm^3	0.445 x 0.118 x 0.070
Crystal system	monoclinic
Space group	$\text{P2}_1/\text{n}$
Unit cell dimensions	$a = 11.9670(13) \text{ \AA}$ $\alpha = 90^\circ$ $b = 29.801(3) \text{ \AA}$ $\beta = 99.649(3)^\circ$ $c = 13.7524(14) \text{ \AA}$ $\gamma = 90^\circ$
$V/\text{\AA}^3$	4835.1(9)
Z	4
$\rho/\text{g cm}^{-3}$	1.315
Absorption coefficient	0.857 mm^{-1}
$F(000)$	2040
Θ -range / $^\circ$	2.090-26.372
hkl -range	$-14 \leq h \leq 14$ $-37 \leq k \leq 37$ $-15 \leq l \leq 17$
Measured refl.	106115
Unique refl. / R_{int}	9879 [0.1277]
Data / restr. / param.	9879 / 1 / 599
Goodness-of-fit (F^2)	1.243
$R1, wR2 (I > 2\sigma(I))$	0.0941 / 0.2125
$R1, wR2$ (all data)	0.1158 / 0.2236
Largest diff. peak and hole	1.426 / $-0.614 e\text{\AA}^{-3}$

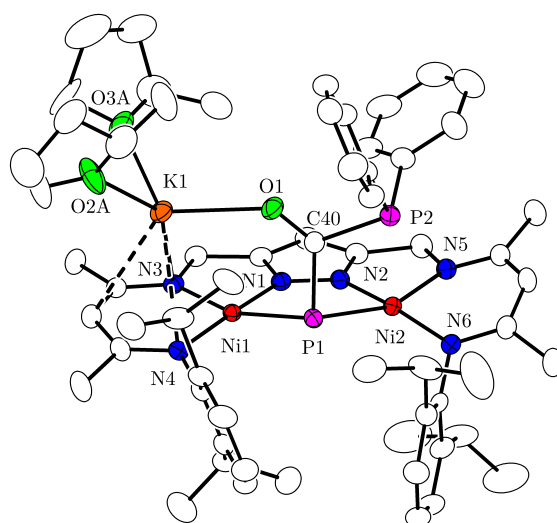


Figure A.12: Top: Molecular structure of $\text{K}[\text{LNi}_2(\text{PC}(\text{O})\text{PPh}_2)]$ (**11**) (30% probability thermal ellipsoids). The hydrogen atoms are omitted for clarity. **Bottom:** Crystal data and refinement details of **11**.

Empirical formula	$\text{C}_{62}\text{H}_{83}\text{KN}_6\text{Ni}_2\text{O}_3\text{P}_2$	
Formula weight	1178.80	
T/K	100(2)	
Crystal size / mm^3	0.474 x 0.169 x 0.154	
Crystal system	monoclinic	
Space group	$\text{P2}_1/\text{n}$	
Unit cell dimensions	$a = 12.4348(6) \text{ \AA}$	$\alpha = 90^\circ$
	$b = 22.2658(9) \text{ \AA}$	$\beta = 93.359(2)^\circ$
	$c = 21.9192(9) \text{ \AA}$	$\gamma = 90^\circ$
$V/\text{\AA}^3$	6058.4(5)	
Z	4	
$\rho/\text{g cm}^{-3}$	1.292	
Absorption coefficient	0.792 mm^{-1}	
$F(000)$	2504	
Θ -range / $^\circ$	2.053-27.904	
hkl -range	$-16 \leq h \leq 16$	
	$-29 \leq k \leq 29$	
	$-28 \leq l \leq 28$	
Measured refl.	162761	
Unique refl. / R_{int}	14469 [0.0868]	
Data / restr. / param.	14469 / 91 / 756	
Goodness-of-fit (F^2)	1.038	
$R1, wR2$ ($I > 2\sigma(I)$)	0.0428 / 0.0960	
$R1, wR2$ (all data)	0.0647 / 0.1078	
Largest diff. peak and hole	1.003 / $-0.459 e\text{\AA}^{-3}$	

Appendix B

Further Analytics

B.1 SQUID Data of 4

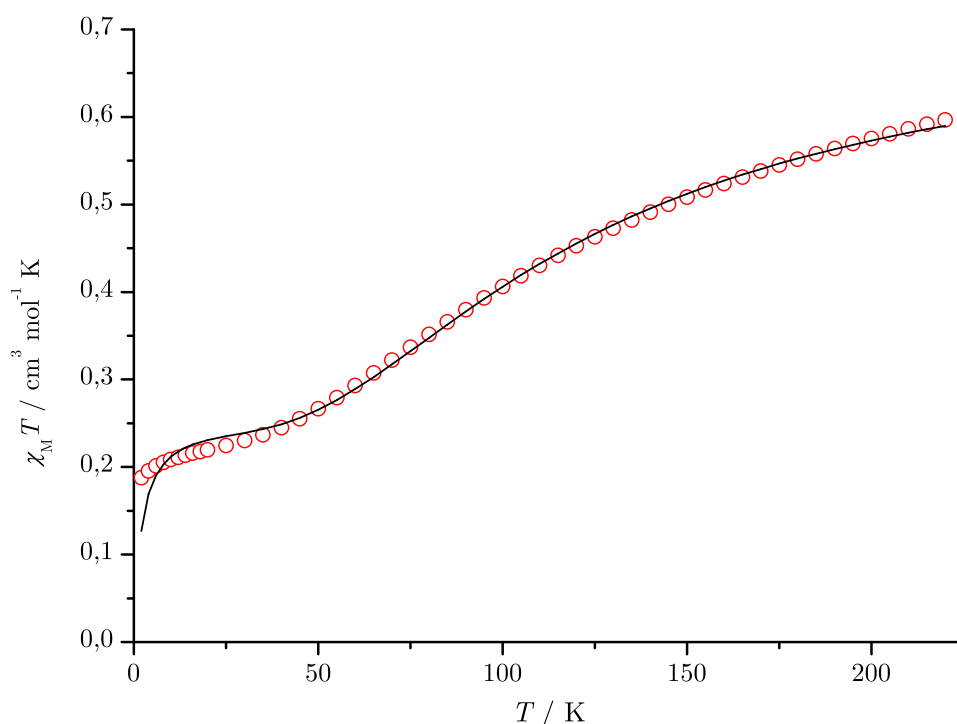


Figure B.1: $\chi_M T$ vs. T plot for **4**; the solid black line represents the calculated curve fit ($\hat{H} = 2J\hat{S}_1\hat{S}_2$ with $J = -78 \text{ cm}^{-1}$).

The SQUID data of $[\text{H}_2\text{LNi}_2^{\text{I}}][\text{BAr}_4^{\text{F}}]$ (**4**) reveals an antiferromagnetically coupling of $J = -78 \text{ cm}^{-1}$ but do not match the expected $\chi_M T$ at low temperatures. The coupling constant is in the same order of magnitude as for the other Ni^{I} complexes. However, the $\chi_M T$ value does not reaches 0 upon lowering the temperature, indicating the presence of a paramagnetic compound. Even though this impurity has not been isolated, it is reasonable to assume that a mixed-valent nickel complex was formed. Further, the amount of diamagnetic impurities were assumed to be 25.3%. It is highly probable that this impurities are KBar_4^{F} and the hydroxido complex $[\text{LNi}_2^{\text{II}}(\mu\text{-OH})]$, which has formed due to traces of moisture.

B.2 IR spectroscopy

B.2.1 Simulated IR Spectra of Dinickel Metalloradicals

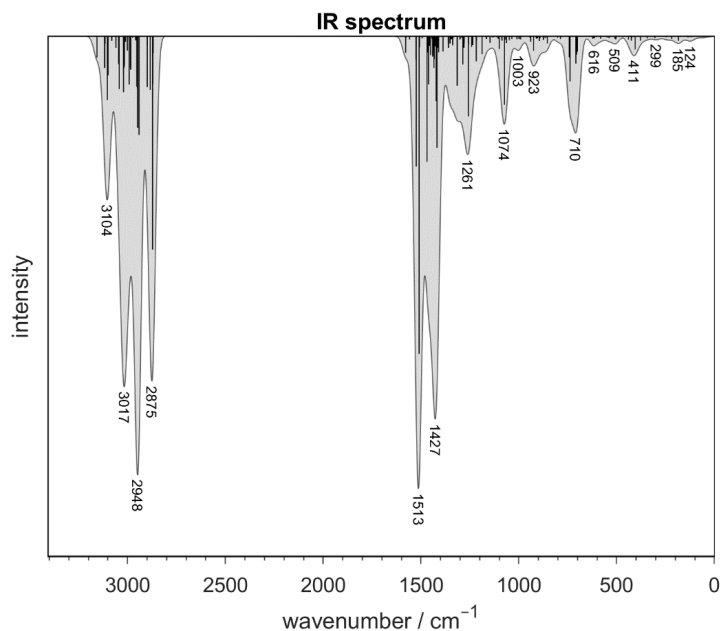


Figure B.2: Calculated IR spectrum of $\text{K}[\text{LNiI}_2]$. The spectrum was convoluted using a Gaussian line shape function with a half-width of 20 cm^{-1} . The spectrum was simulated by TD-DFT calculation, see Section C.1.3 for details.

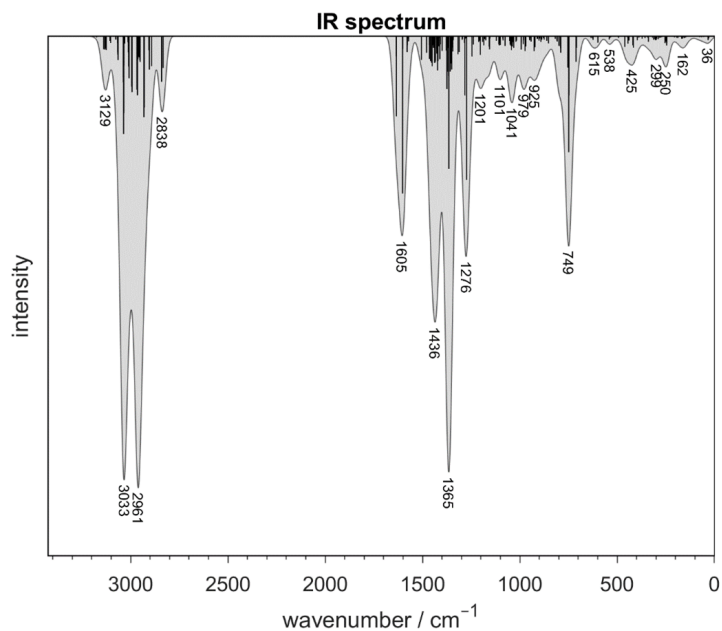


Figure B.3: Calculated IR spectrum of $[\text{H}_2\text{LNiI}_2][\text{BarF}_4]$ (4). The spectrum was convoluted using a Gaussian line shape function with a half-width of 20 cm^{-1} . The CN stretching vibration of the β -diimine subunits is found at 1605 cm^{-1} . The spectrum was simulated by TD-DFT calculation, see Section C.1.3 for details.

B.2.2 Activation of Nitrogen by a Mixed-Valent Dinickel Complex

During the transport from the synthetic glove box to the analytic glove box, it was unavoidable that the sample warmed up to room temperature. It is likely that the $[\text{HLNi}^{\text{I}}\text{Ni}^{\text{II}}(\mu\text{-Me}_2\text{C}_5\text{H}_3\text{N})][\text{BF}_4]$ complex (**5**) reacted with the nitrogen atmosphere and formed the $\text{LNi}_2^{\text{II}}(\text{N}_2^-)$ (**XVI**) ($\nu_{\text{N}=\text{N}} = 1896 \text{ cm}^{-1}$, compare Section 1.3.7) complex. In addition, it was not possible to identify a C=N stretching vibration, which would indicate the presence of a β -diimine unit. However, to verify the formation of **XVI** the further investigations, such as isotopic labelling experiments with $^{15}\text{N}_2$ would be necessary.

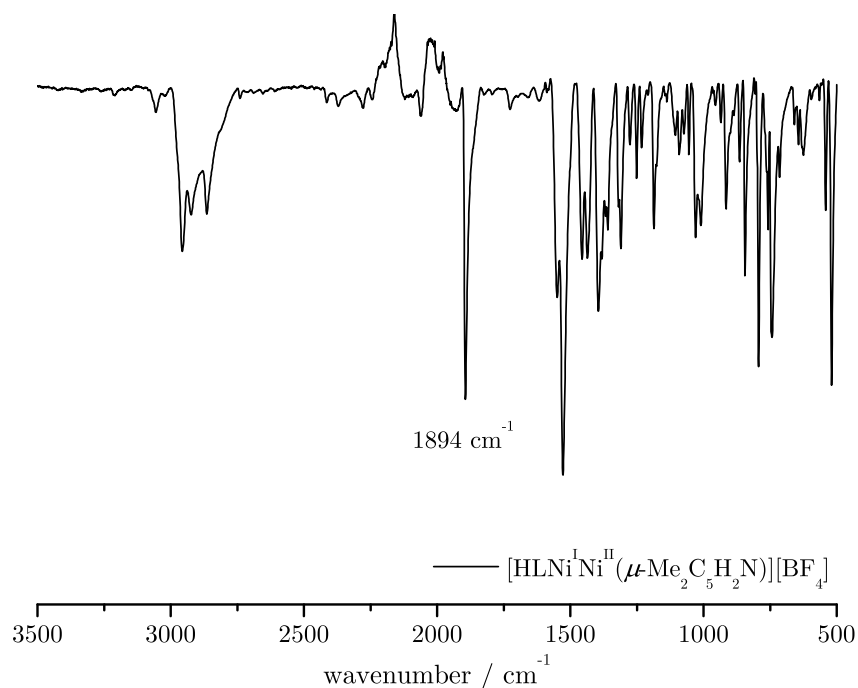


Figure B.4: IR (ATR) spectrum of (**5**) under a nitrogen atmosphere. The presumed N=N stretching vibration is indicated at 1894 cm^{-1} .

B.2.3 IR Spectrum of 6-K(crypt) and Calculated IR Spectrum of 6

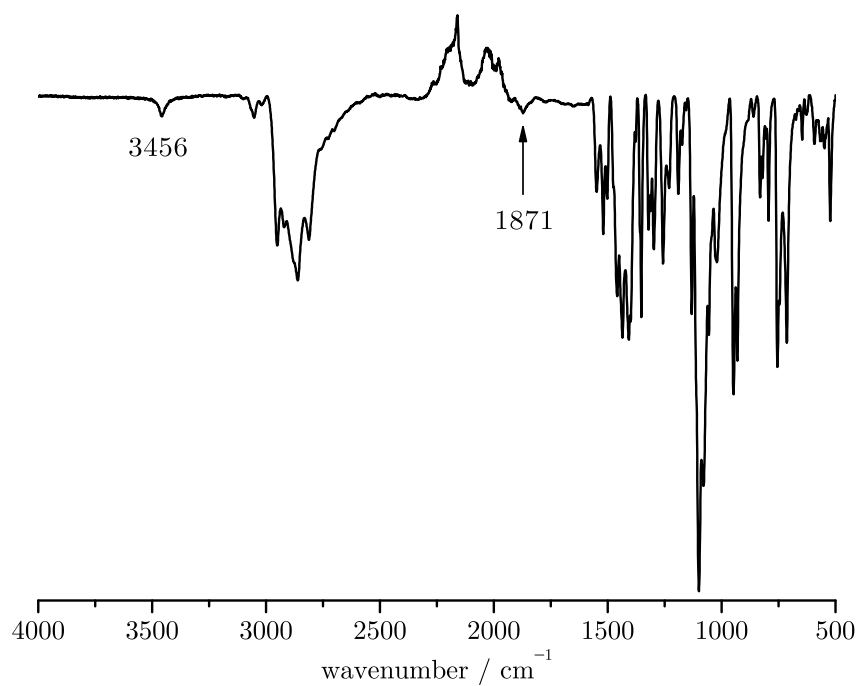


Figure B.5: IR (ATR) of $\text{K}[\text{LNi}_2^{\text{II}}(\text{H})(\text{OH})]$ (**6-K(crypt)**). The O–H and Ni–H stretching vibrations are found at 3456 and 1871 cm^{-1} , respectively.

The calculated IR spectrum of $\text{K}[\text{LNi}_2^{\text{II}}(\text{H})(\text{OH})]$ (**6**) is in good agreement with the experimental result. The Ni–H stretching vibration is shifted by $\Delta\nu_{\text{sim.}-\text{exp.}} = 71 \text{ cm}^{-1}$. This procedure is usually applied to allow an easier comparison of experimental and computed spectra.^[275] However, the simulated feature appears narrower than the experimental one; moreover, the calculated hydroxido resonance is more intense.

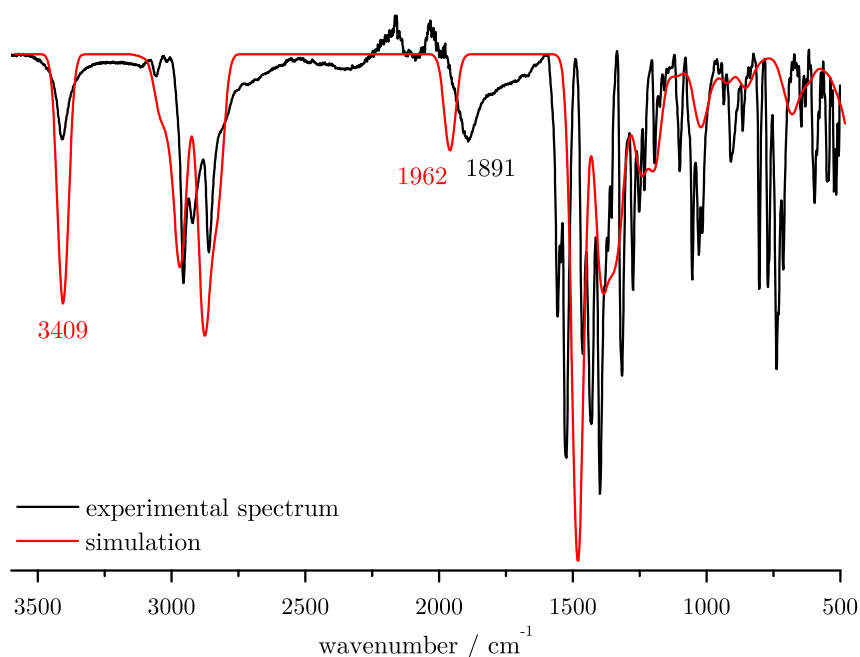


Figure B.6: IR (ATR) and calculated IR spectrum of **6**. The O–H stretching vibration at 3409 cm^{-1} was taken as reference point. The calculated Ni–H stretching vibration is found at 1962 cm^{-1} .

B.2.4 IR Spectra of Phosphaketene Adducts

All phosphaketene adducts were investigated by IR spectroscopy. However, no characteristic P–C stretching vibrations could be detected for **9** (Figure B.7) or **11** (Figure B.8), which can be attributed to the band position close to the resonances of the ligand system. The calculated IR spectrum of $[\text{LNi}_2(\mu\text{-PCNBn})]$ (**10**) is in good agreement with the experimental result. The CN stretching vibration is only minor shifted by $\Delta\nu_{\text{sim.}-\text{exp.}} = 8 \text{ cm}^{-1}$.

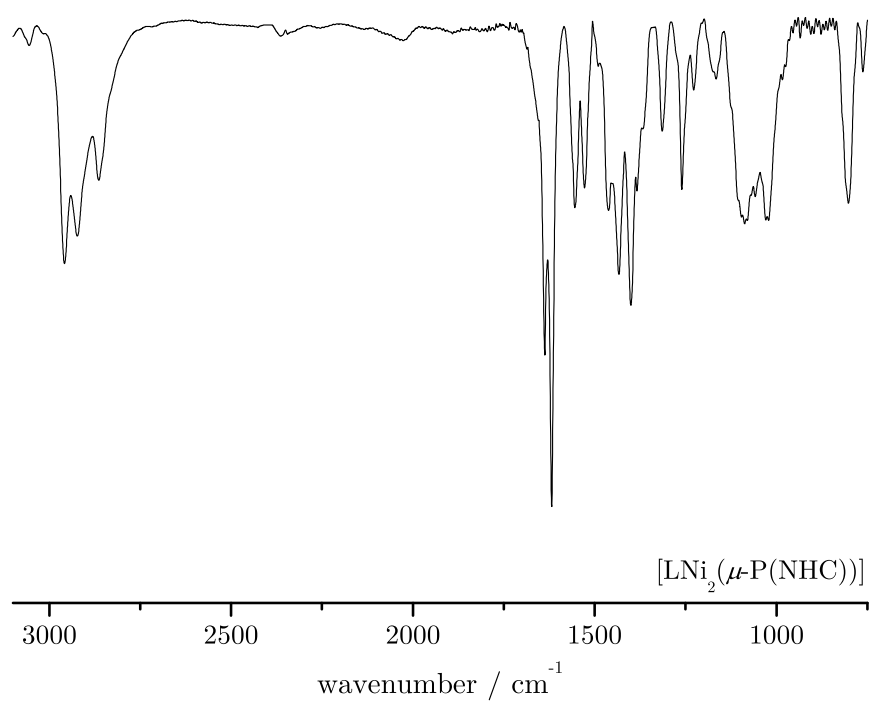


Figure B.7: IR (KBr) spectrum of **9**.

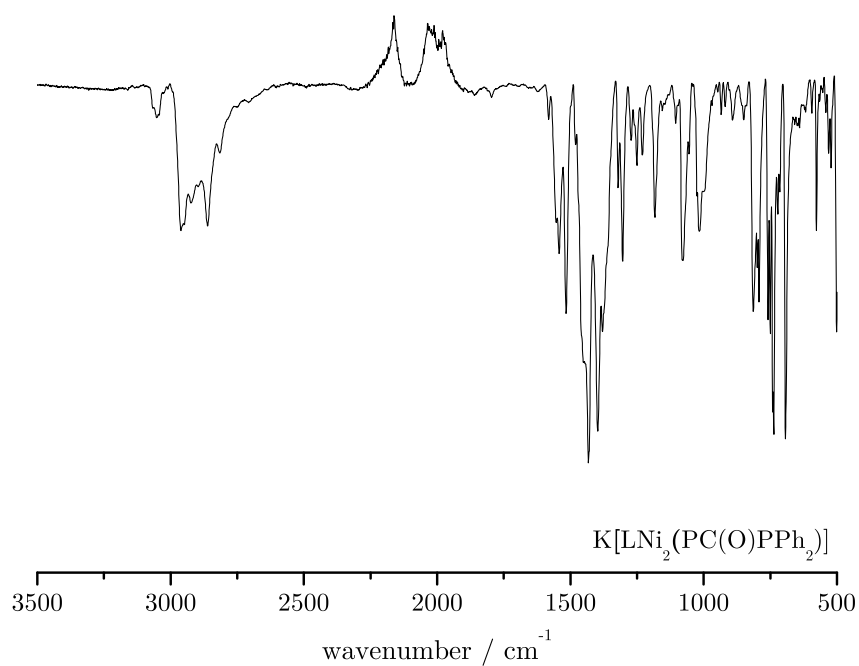


Figure B.8: IR (ATR) spectrum of **11**.

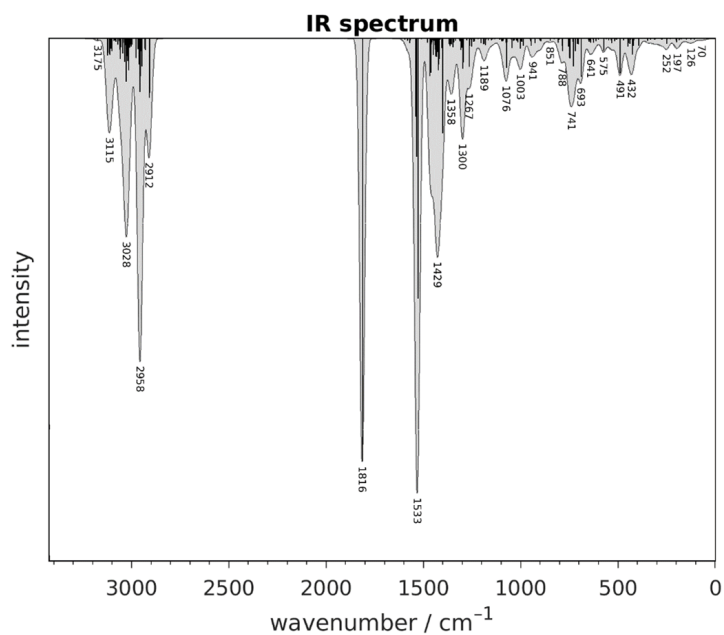


Figure B.9: Calculated IR spectrum of $[\text{LNi}_2(\mu\text{-PCNBn})]$. The spectrum was convoluted using a Gaussian line shape function with a half-width of 20 cm^{-1} . The CN stretching vibration is found at 1816 cm^{-1} .

B.3 UV-vis spectroscopy

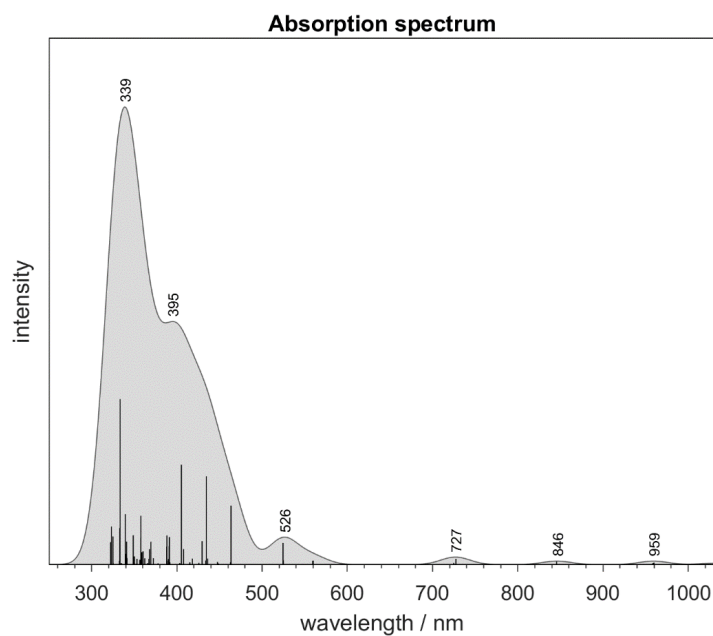


Figure B.10: Calculated absorption spectrum of $\text{K}[\text{LNi}_2]$ (2K) in THF. The spectrum was convoluted using a GAUSSIAN line shape function with a half-width of 20 nm . The spectrum was simulated by TD-DFT calculation, see Section C.1.3 for details.

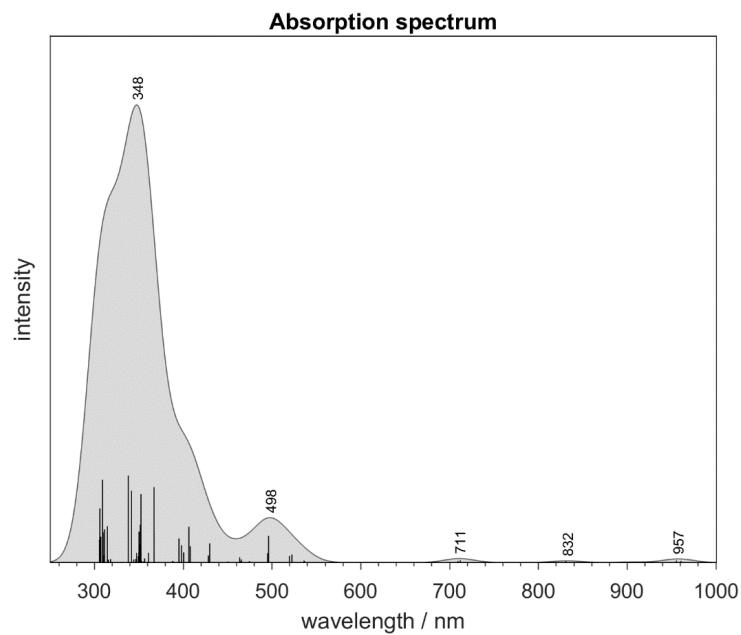


Figure B.11: Calculated absorption spectrum of $[\text{H}_2\text{LNi}_2][\text{BAR}_4^{\text{F}}]$ (**4**) in THF. The spectrum was convoluted using a GAUSSIAN line shape function with a half-width of 20 nm. The spectrum was simulated by TD-DFT calculation, see Section C.1.3 for details.

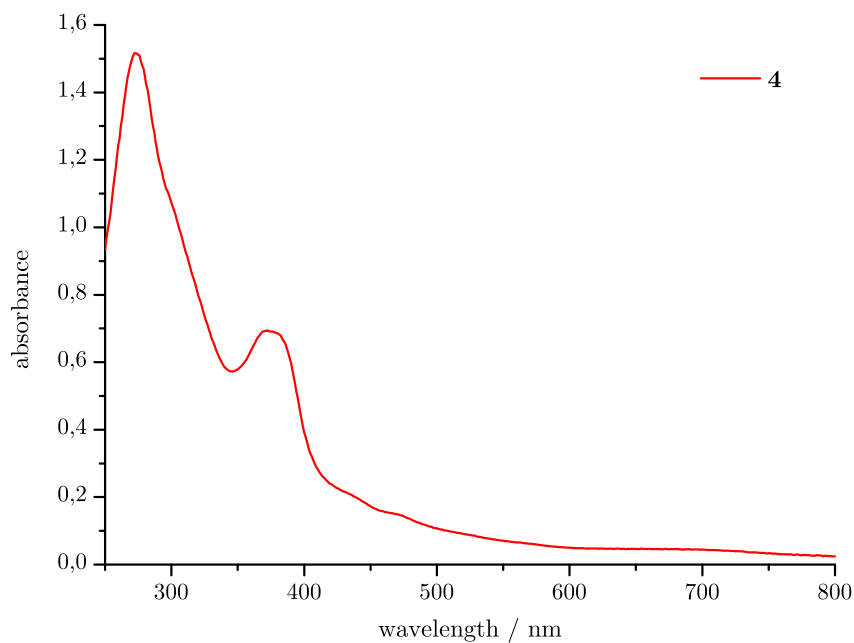


Figure B.12: UV-vis spectrum of $[\text{HLNi}^{\text{I}}\text{Ni}^{\text{II}}(\mu\text{-Me}_2\text{C}_5\text{H}_3\text{N})][\text{BF}_4]$ (**5**) in THF at -40°C .

Uv-vis spectroscopy was used to characterize complex **6** and **6-K(crypt)** in THF at -40°C . Complex **6** shows a relatively strong absorption in the range of 350-400 nm ($\epsilon > 10^4 \text{ L mol}^{-1} \text{ cm}^{-1}$). To investigate the counterion's influence the potassium ion was abstracted with [2.2.2]-cryptand. By doing so, the prior pale yellow solution turned instantly red, which is reflected by additional features at 440 nm and 469 nm and a broad band around 550 nm.

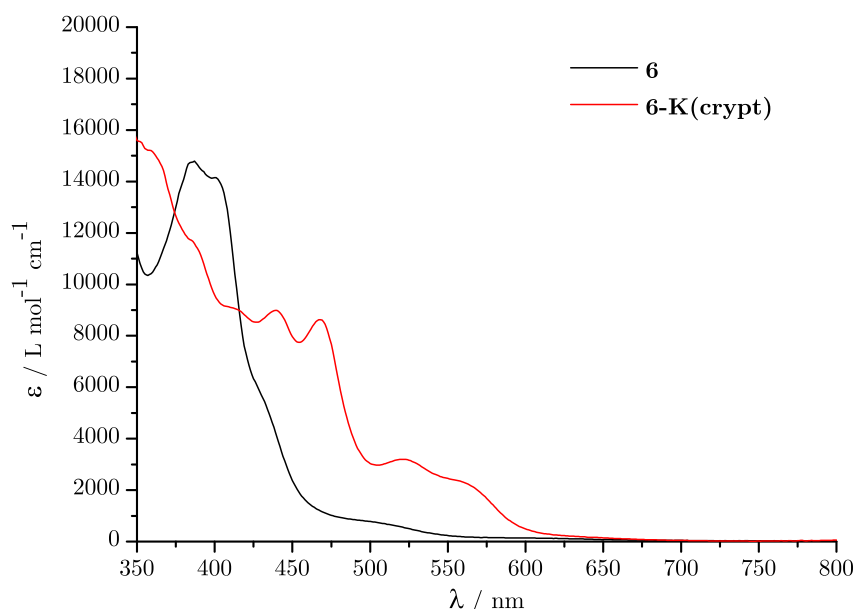


Figure B.13: UV-vis absorption spectra of **6** and **6-K(crypt)** in THF at -40°C .

B.3.1 UV-vis Spectra of Phosphaketene Derivatives

The $[\text{LNi}_2(\mu\text{-PCO})]$ complex and all its derivatives were investigated by UV-vis spectroscopy showing intensive bands in the range of 350 – 400 nm. All complexes, except $[\text{LNi}_2(\mu\text{-P}(\text{NHC}))]$, feature an additional weaker absorption at 480 – 520 nm. In contrast to the other compounds, $\text{K}[\text{LNi}_2(\text{PC}(\text{O})\text{PPh}_2)]$ features a third broad absorption at 720 nm which can be assigned by DFT calculations (Figure B.15, band at 637 nm) to ligand-to-metal charge transfer (LMCT) transitions involving the phosphorous.

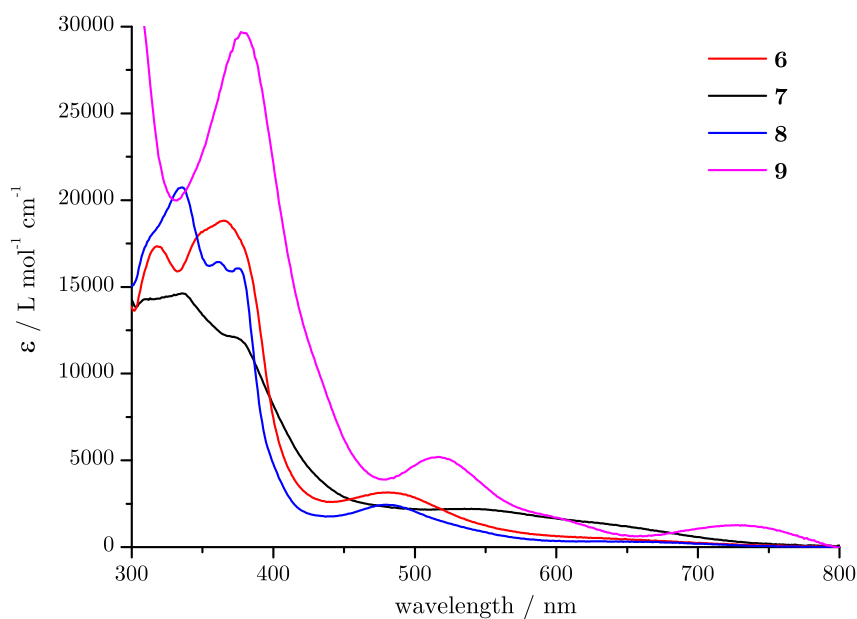


Figure B.14: UV-vis spectra of the presented complexes in Chapter 4, $[\text{LNi}_2(\mu\text{-PCO})]$ (7), $[\text{LNi}_2(\mu\text{-P(NHC)})]$ (9), $[\text{LNi}_2(\mu\text{-PCNBn})]$ (10) and $\text{K}[\text{LNi}_2(\text{PC(O)PPh}_2)]$ (11) in THF at r.t. (11 was measured at -40°C).

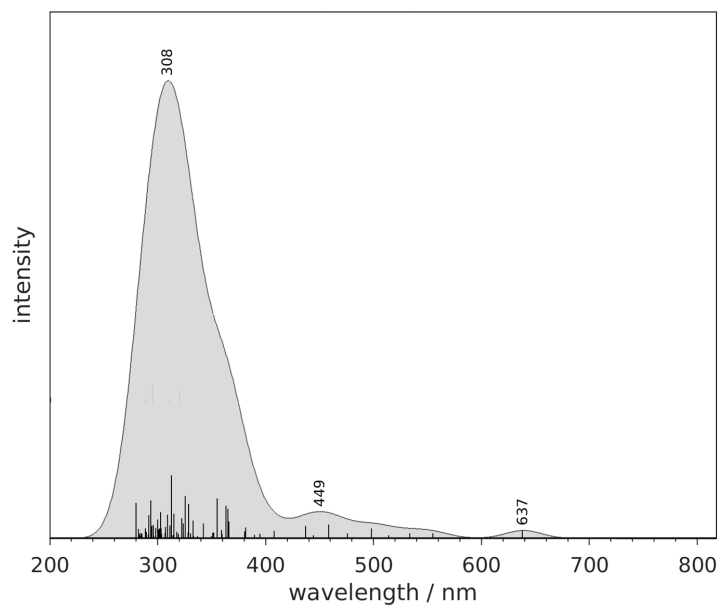


Figure B.15: Calculated absorption spectrum of $\text{K}[\text{LNi}_2(\text{PC(O)PPh}_2)]$ in THF. The spectrum was convoluted using a GAUSSIAN line shape function with a half-width of 20 nm.

B.3.2 ESI-MS spectra of Phosphaketene Derivatives

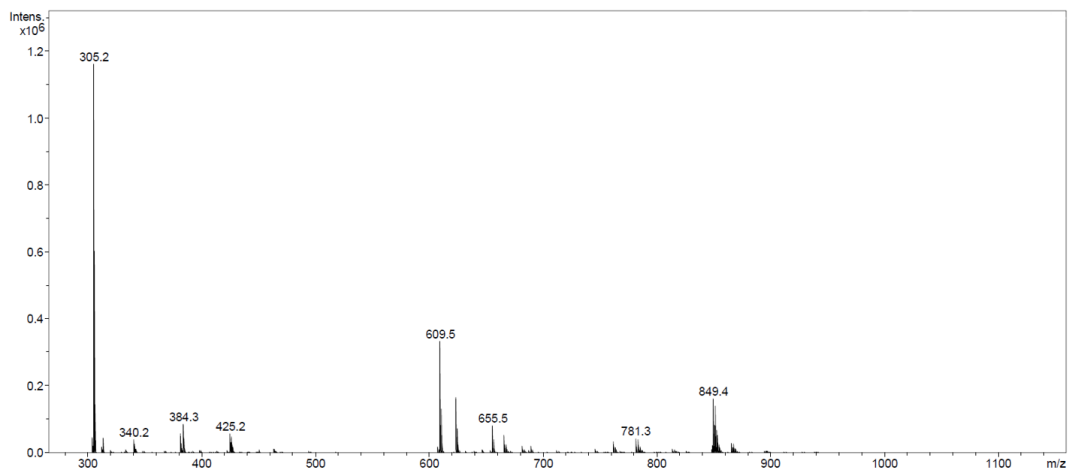


Figure B.16: ESI(+)-MS-spectrum of **9** in THF. The molecular ion peak is found at $m/z=849.4$ [M+H].

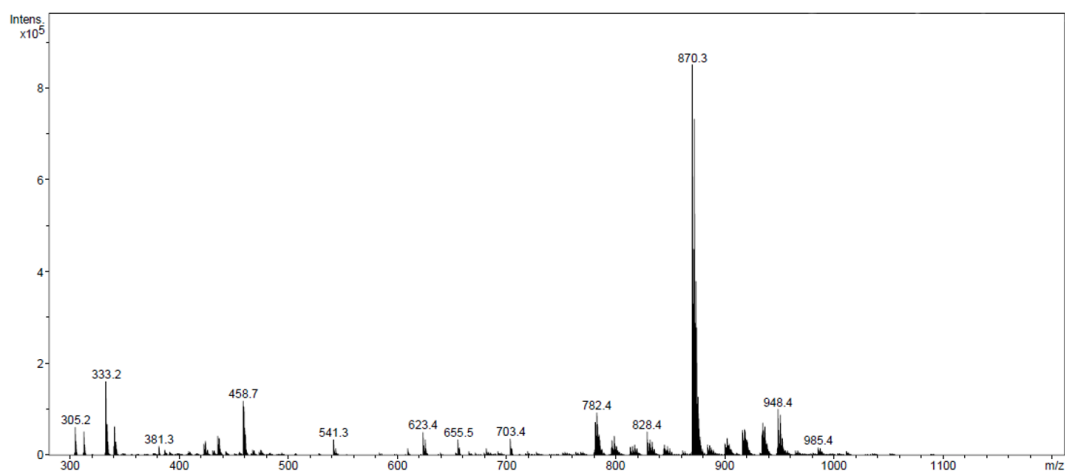


Figure B.17: ESI(+)-MS-spectrum of **10** in THF. The molecular ion peak is found at $m/z=870.3$ [M+H].

B.4 NMR spectroscopy

B.4.1 NMR spectra of 6

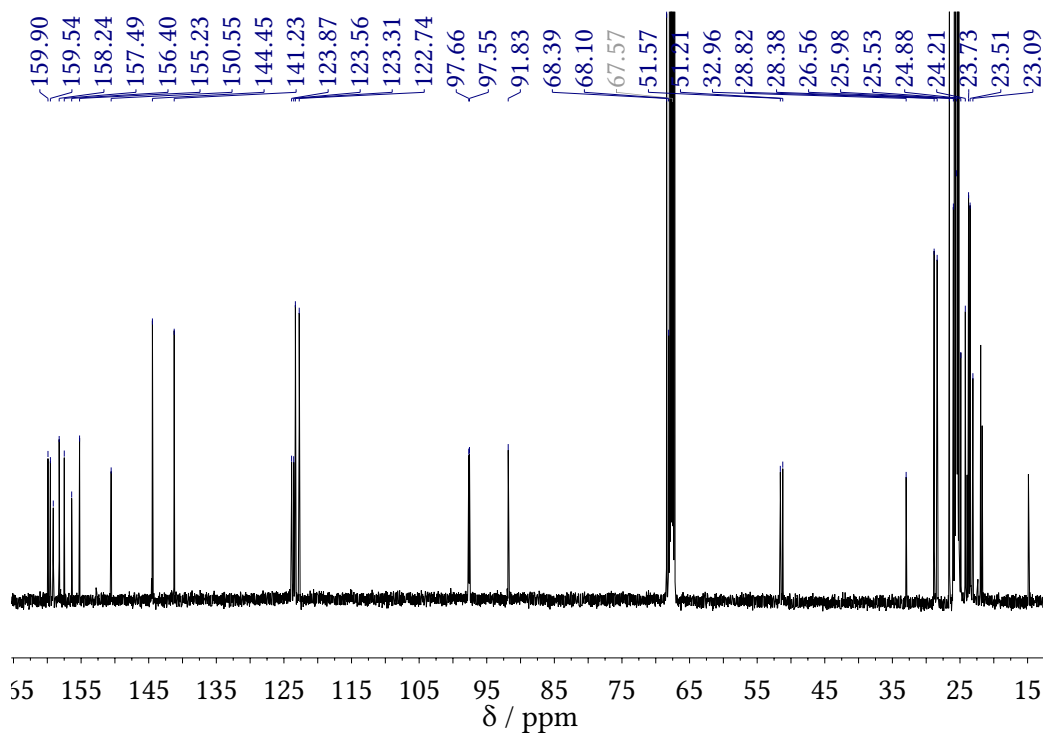


Figure B.18: $^{13}\text{C}\{^1\text{H}\}$ NMR spectrum of 6 at -35°C in $\text{THF-}d_8$.

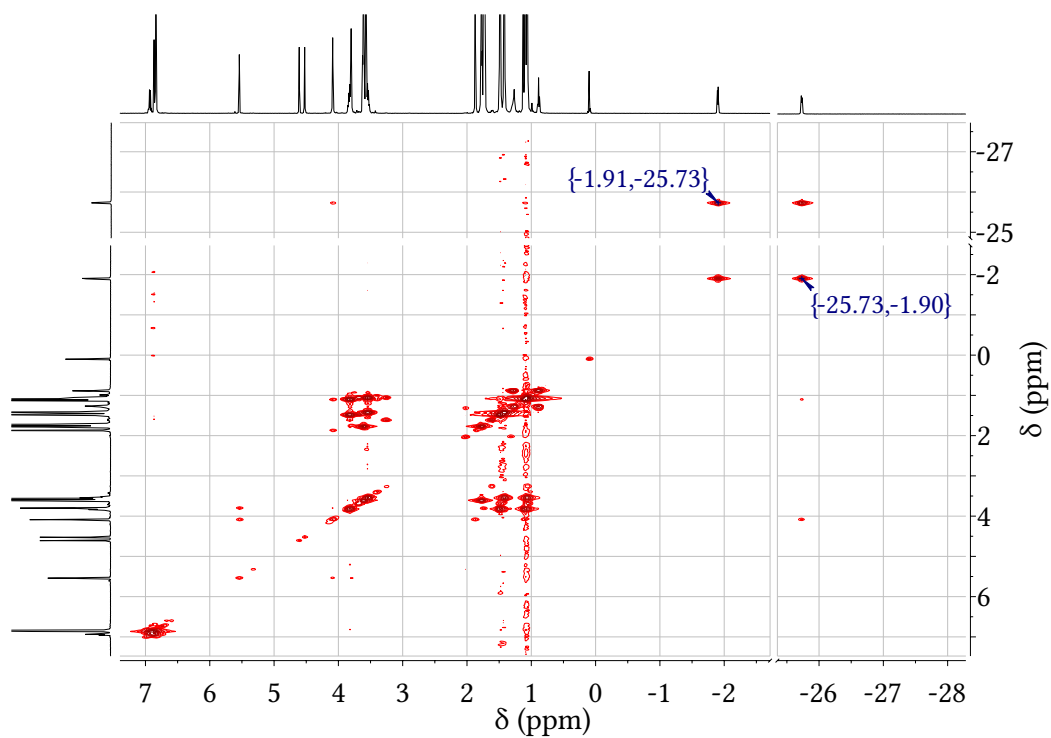


Figure B.19: $^1\text{H},^1\text{H}$ -COSY NMR spectrum of 6 at -35°C in $\text{THF-}d_8$.

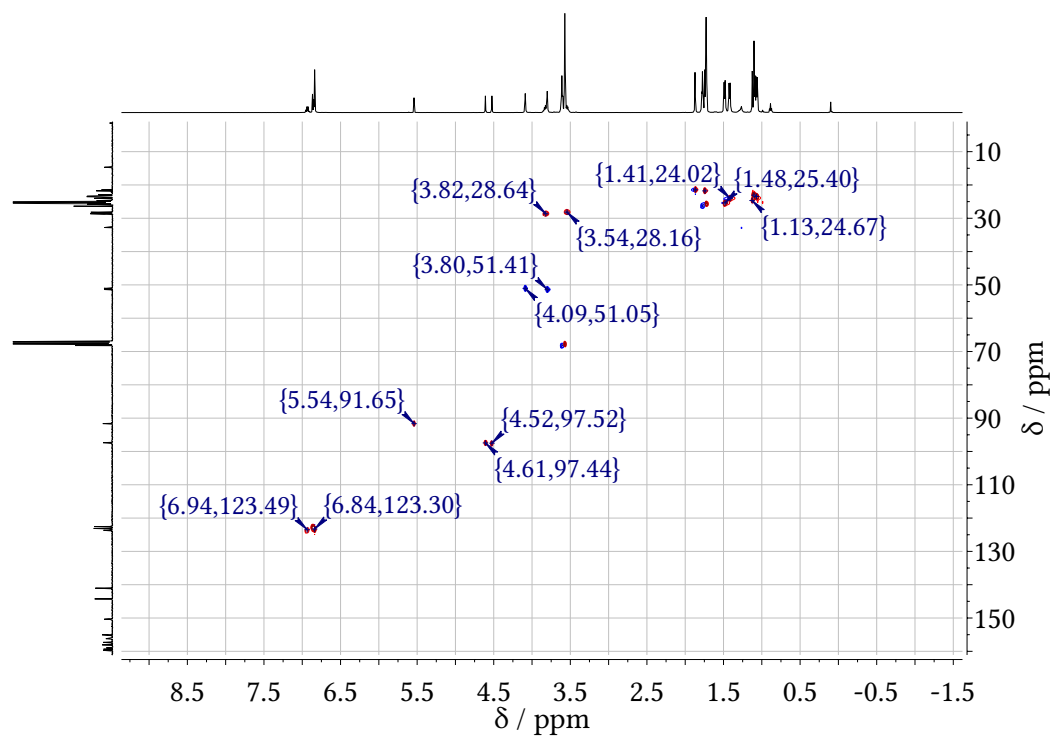


Figure B.20: $^1\text{H},^{13}\text{C}$ -HSQC NMR spectrum of **6** at -35°C in $\text{THF-}d_8$.

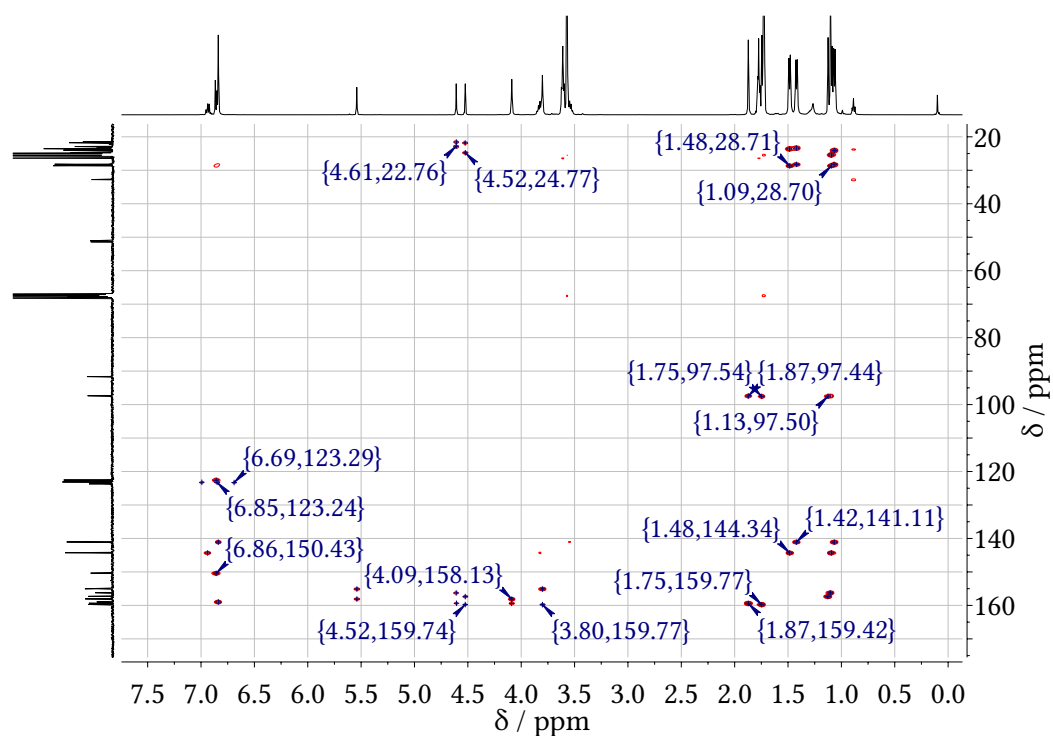


Figure B.21: $^1\text{H},^{13}\text{C}$ -HMBC NMR spectrum of **6** at -35°C in $\text{THF-}d_8$.

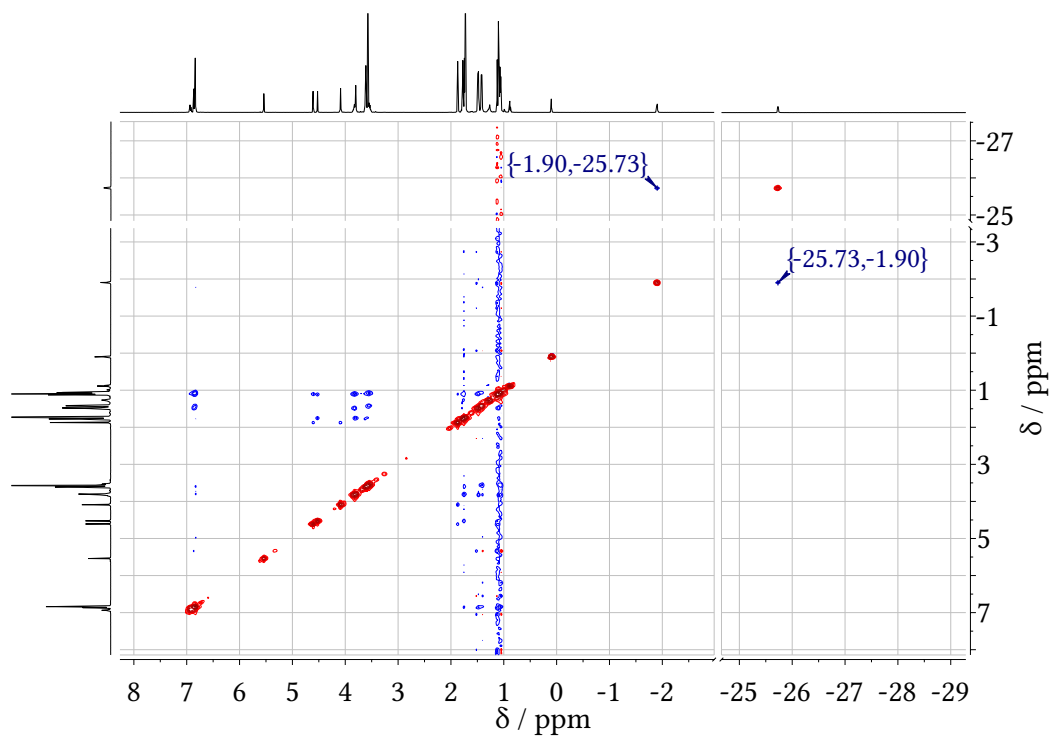


Figure B.22: ^1H , ^1H -NOESY NMR spectrum of **6** at -35°C in $\text{THF-}d_8$.

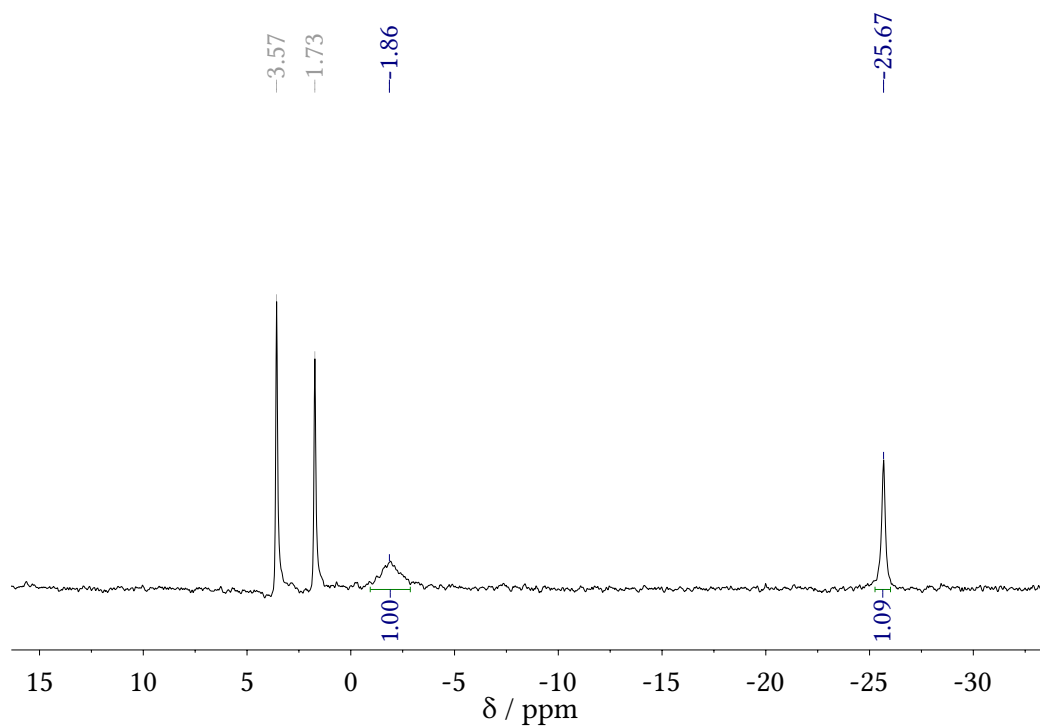
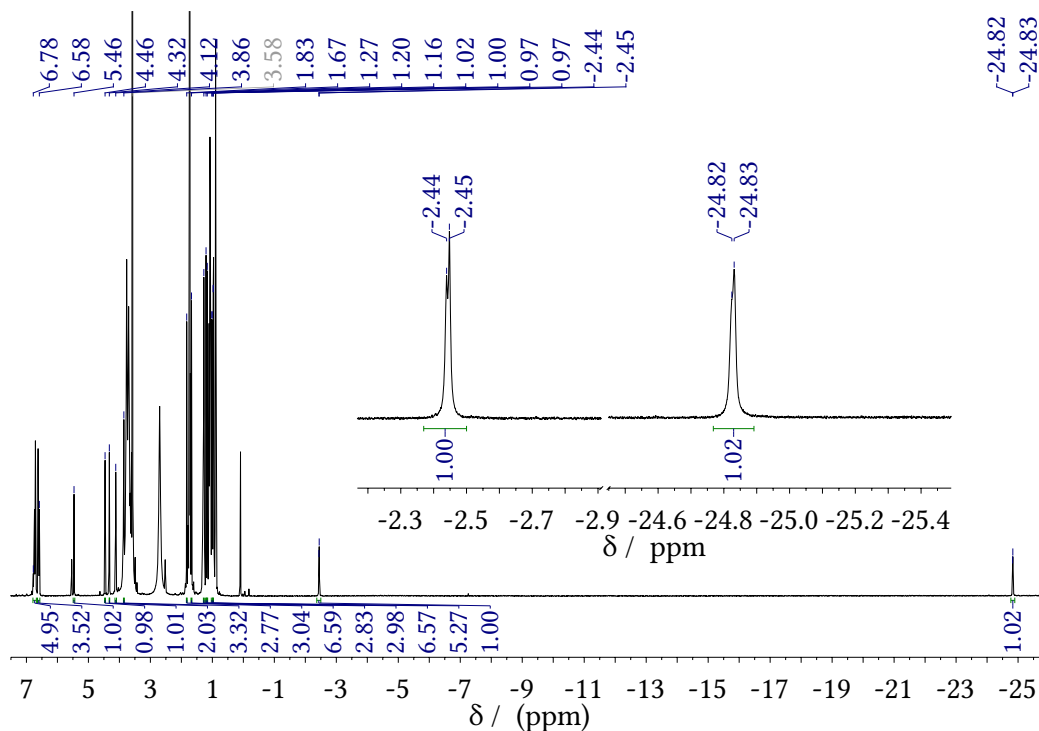
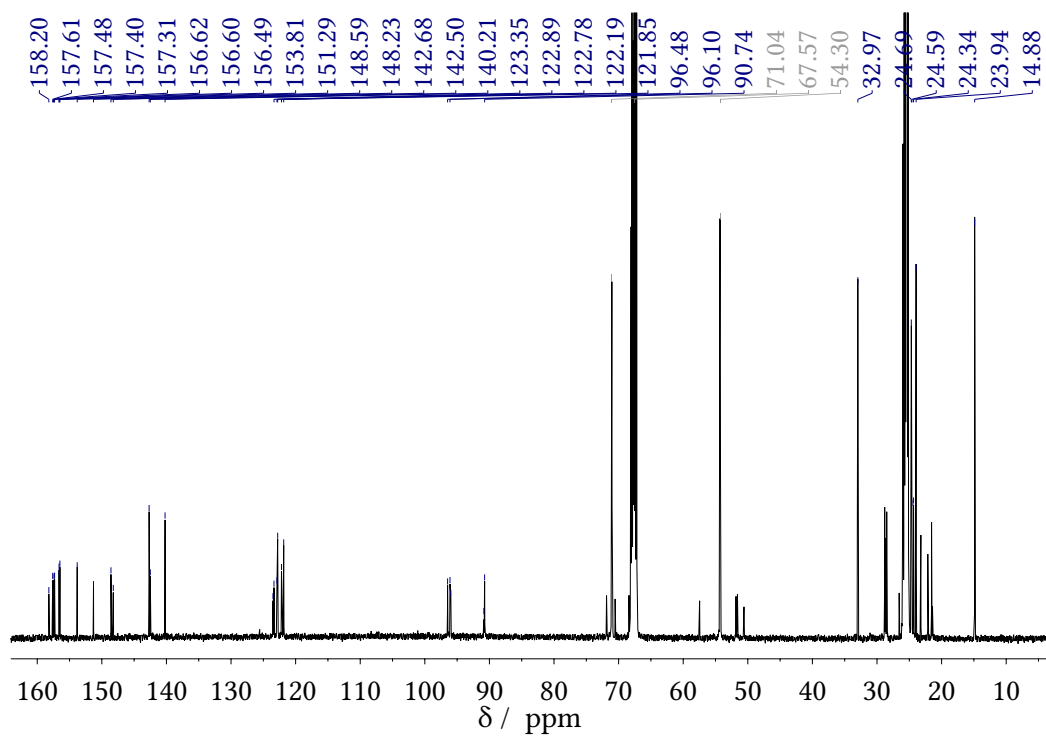


Figure B.23: ^2H NMR spectrum of **6-DOD** at -35°C in $\text{THF-}d_8$.

B.4.2 NMR spectra of 6-K(crypt)

Figure B.24: ^1H NMR spectrum of 6-K(crypt) at -35°C in $\text{THF-}d_8$.Figure B.25: $^{13}\text{C}\{^1\text{H}\}$ NMR spectrum of 6-K(crypt) at -35°C in $\text{THF-}d_8$.

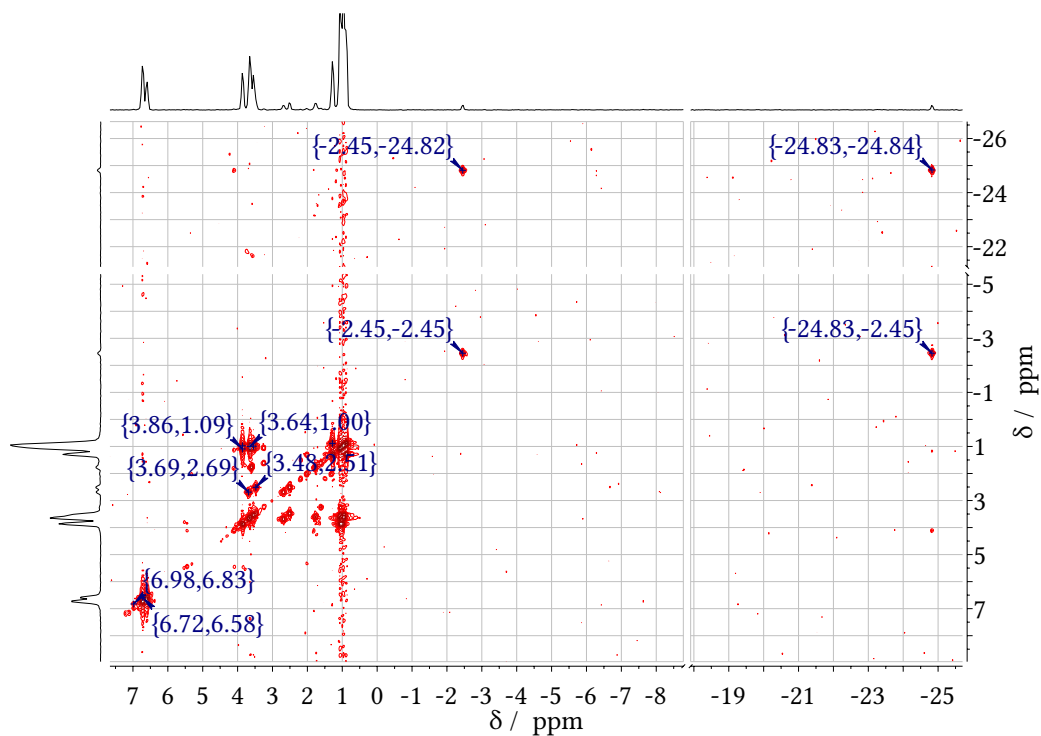


Figure B.26: ^1H , ^1H -COSY NMR spectrum of **6-K(crypt)** at -35°C in $\text{THF-}d_8$.

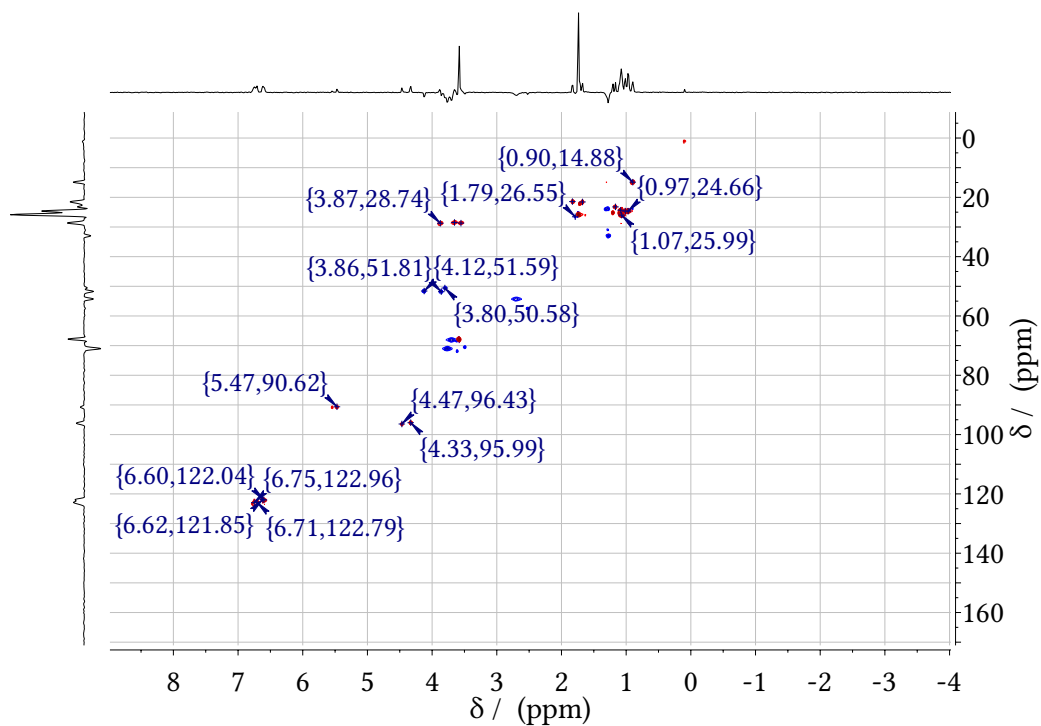


Figure B.27: ^1H , ^{13}C -HSQC NMR spectrum of **6-K(crypt)** at -35°C in $\text{THF-}d_8$.

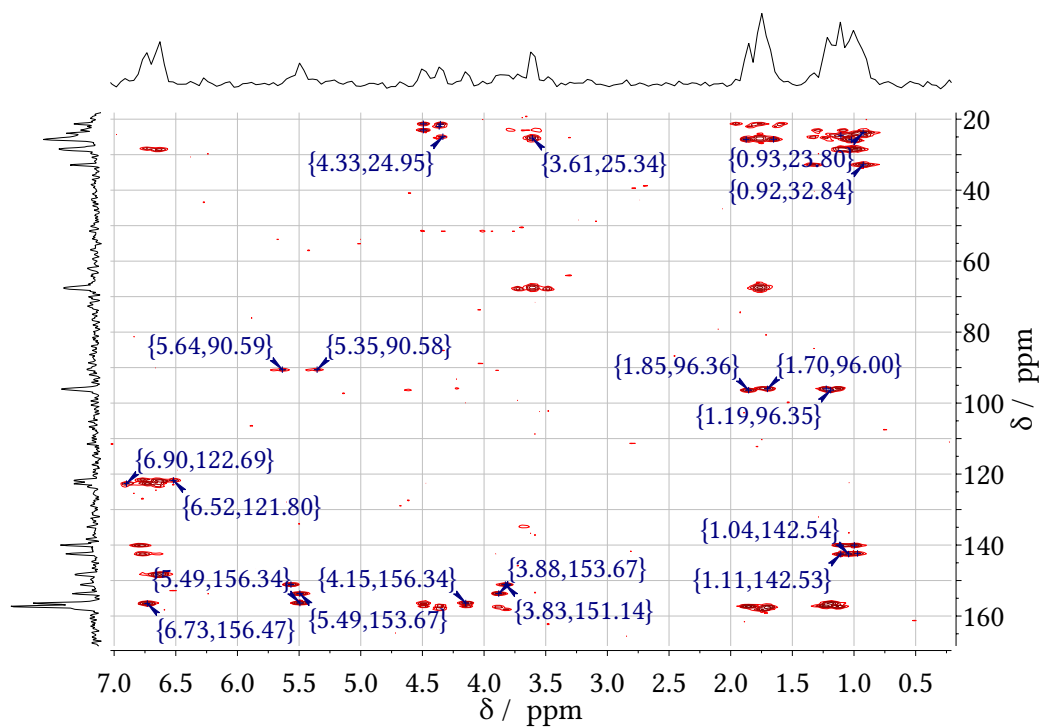


Figure B.28: $^1\text{H},^{13}\text{C}$ -HMBC NMR spectrum of 6-K(crypt) at -35°C in $\text{THF-}d_8$.

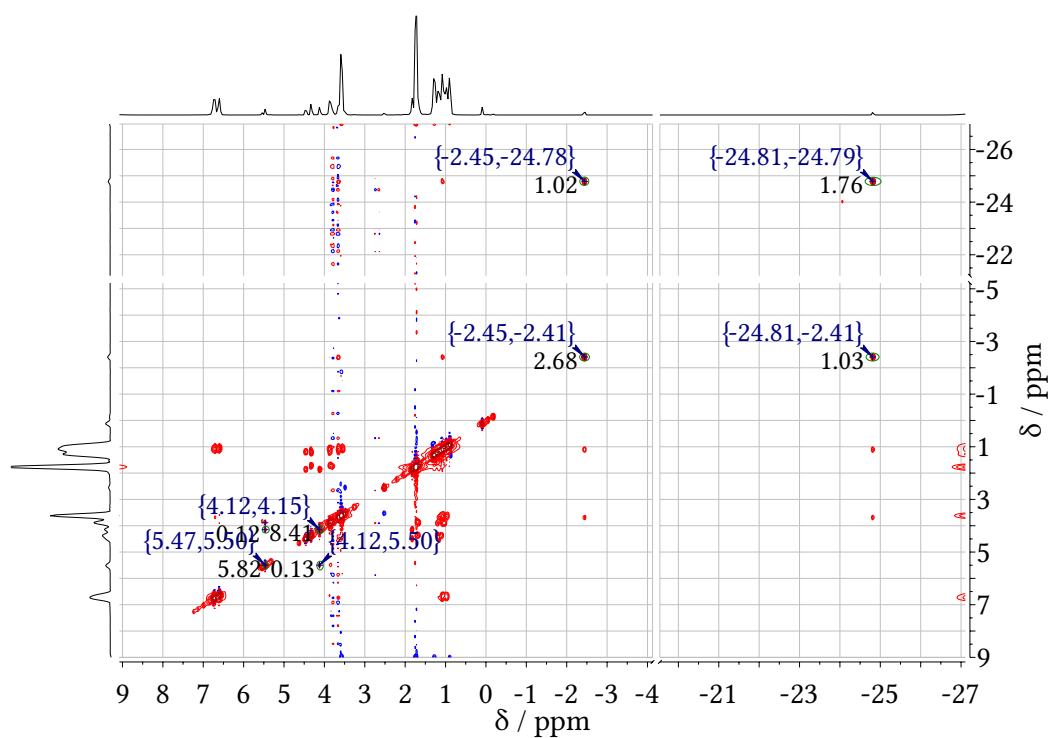
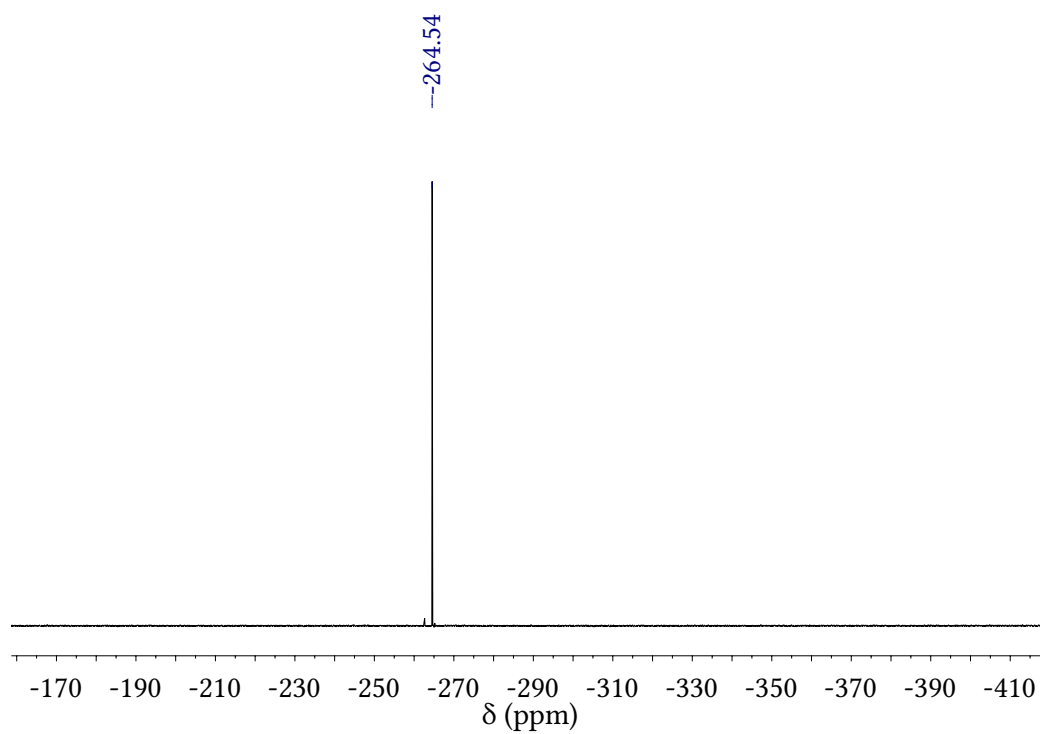
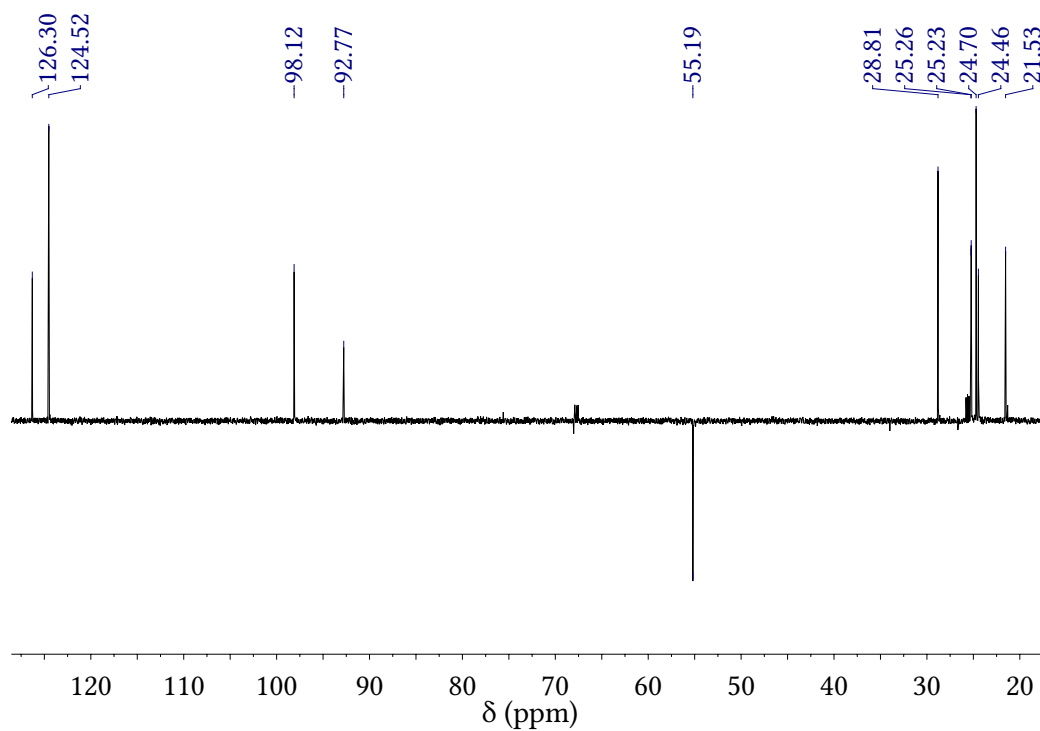


Figure B.29: $^1\text{H},^1\text{H}$ -NOESY NMR spectrum of 6-K(crypt) at -35°C in $\text{THF-}d_8$.

B.4.3 NMR spectra of $[\text{LNi}_2(\mu\text{-PCO})]$ **Figure B.30:** ^{31}P NMR spectrum of **7** at -35°C in $\text{THF-}d_8$.**Figure B.31:** DEPT-135 NMR spectrum of **7** at -35°C in $\text{THF-}d_8$.

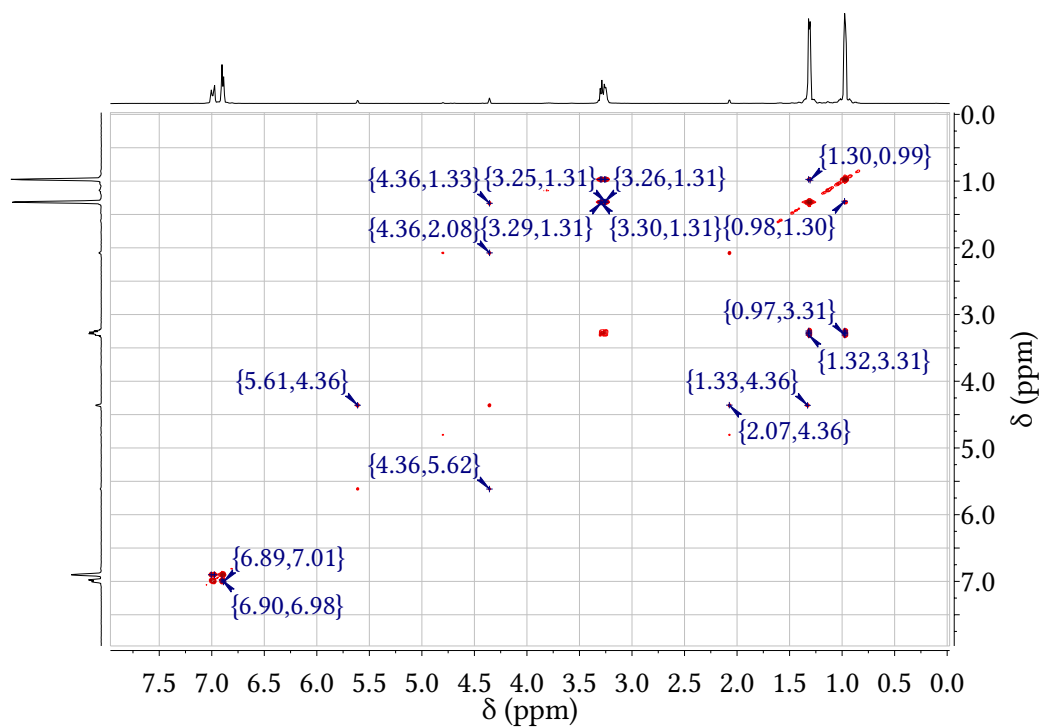


Figure B.32: $^1\text{H}, ^1\text{H}$ -COSY NMR spectrum of 7 at -35°C in $\text{THF-}d_8$.

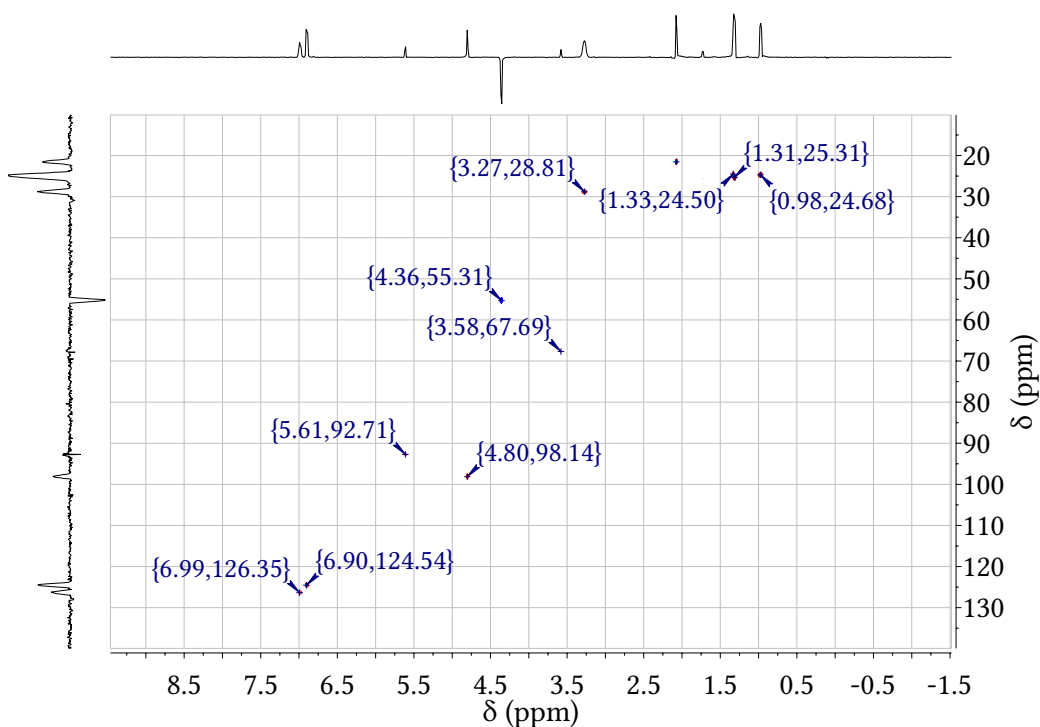


Figure B.33: $^1\text{H}, ^{13}\text{C}$ -HSQC NMR spectrum of 7 at -35°C in $\text{THF-}d_8$.

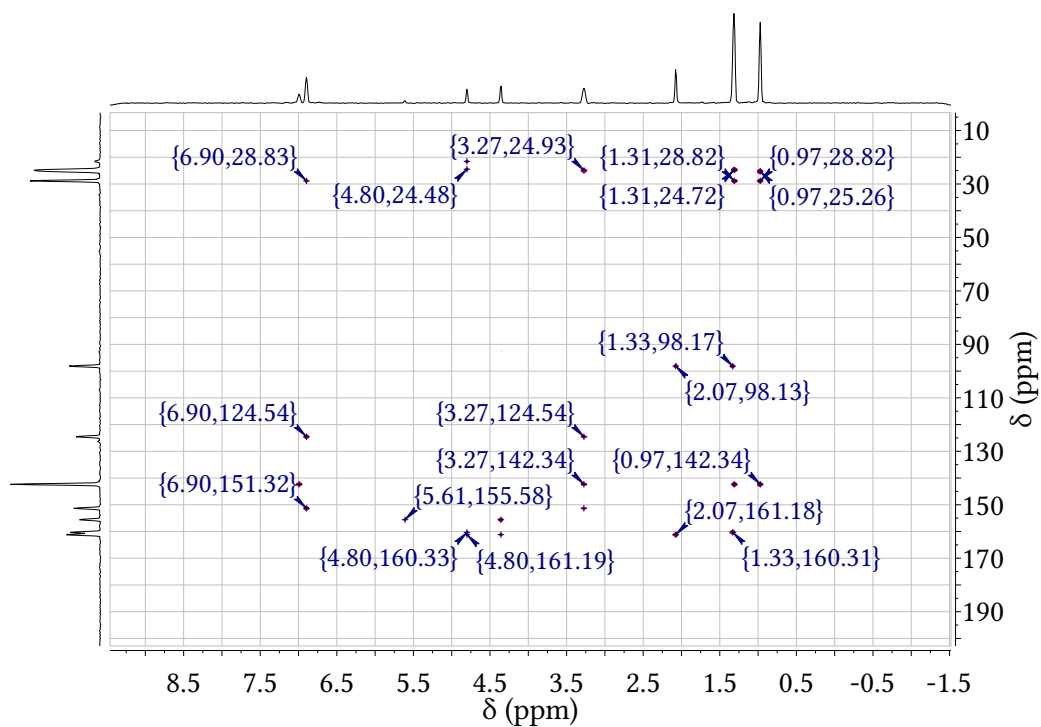


Figure B.34: ^1H , ^{13}C -HMBC NMR spectrum of 7 at -35°C in $\text{THF-}d_8$.

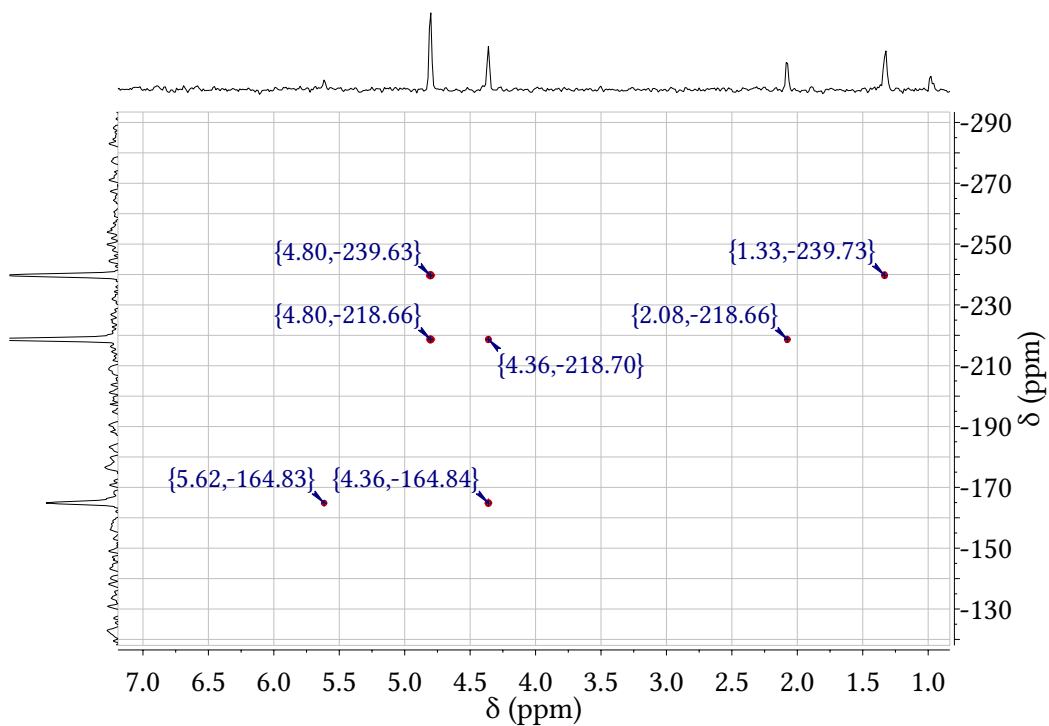
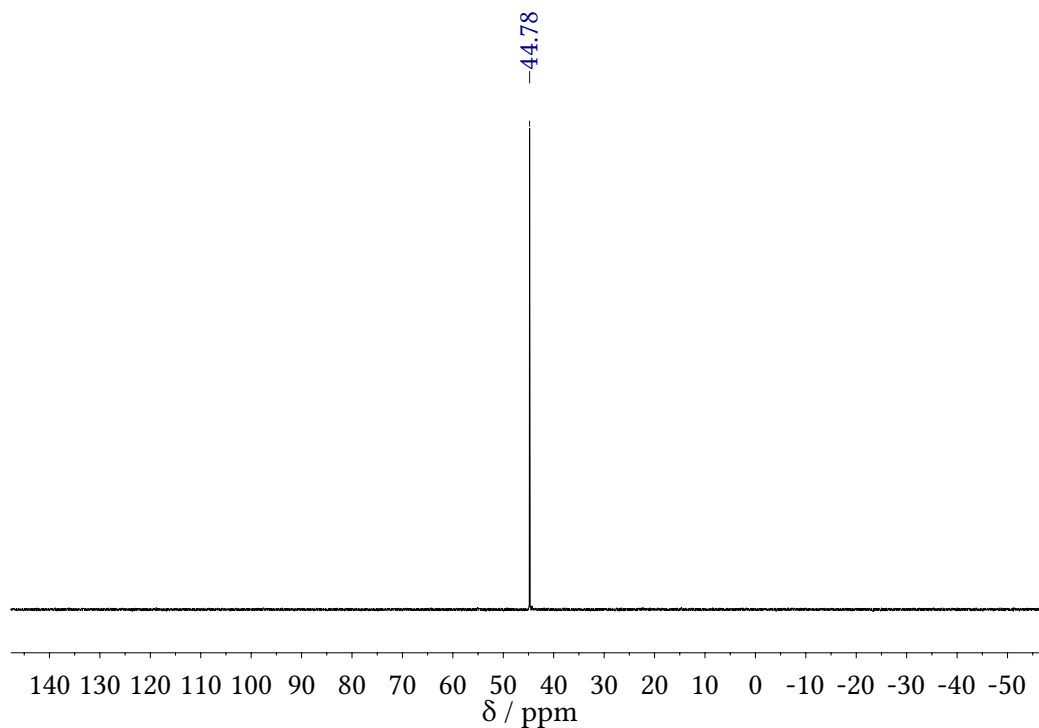
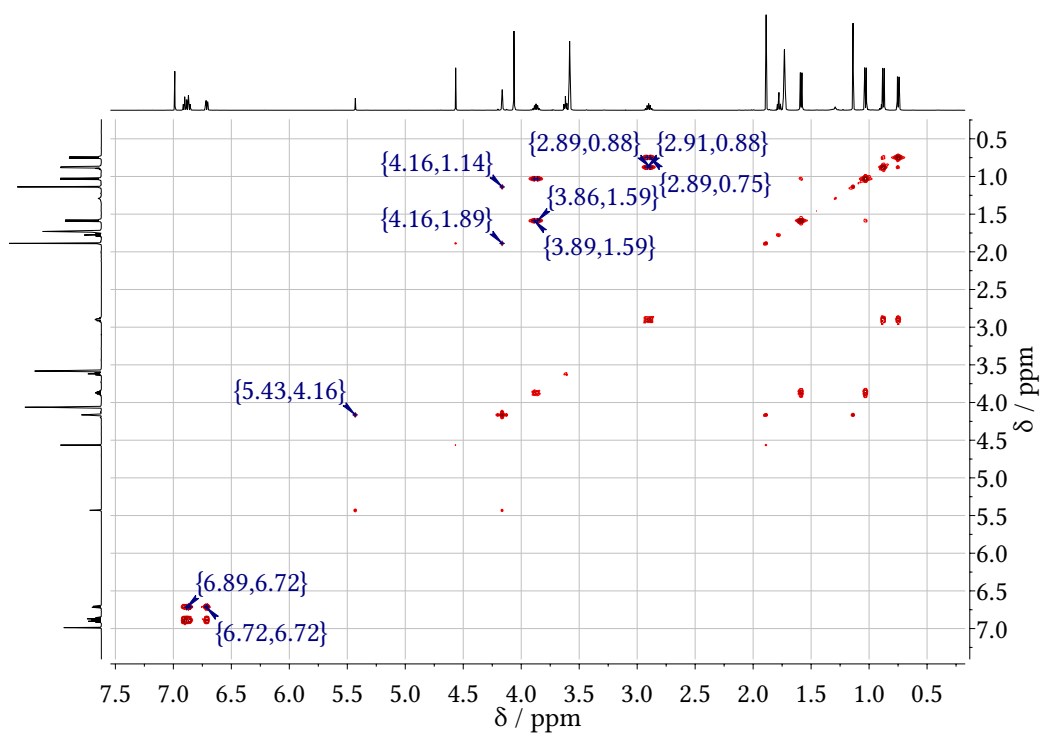


Figure B.35: ^1H , ^{15}N -HMBC NMR spectrum of 7 at -35°C in $\text{THF-}d_8$.

B.4.4 NMR spectra of $[\text{LNi}_2(\mu\text{-P}(\text{NHC}))]$ Figure B.36: ^{31}P NMR spectrum of **9** at -35°C in $\text{THF-}d_8$.Figure B.37: $^1\text{H}, ^1\text{H}$ -COSY NMR spectrum of **9** at -35°C in $\text{THF-}d_8$.

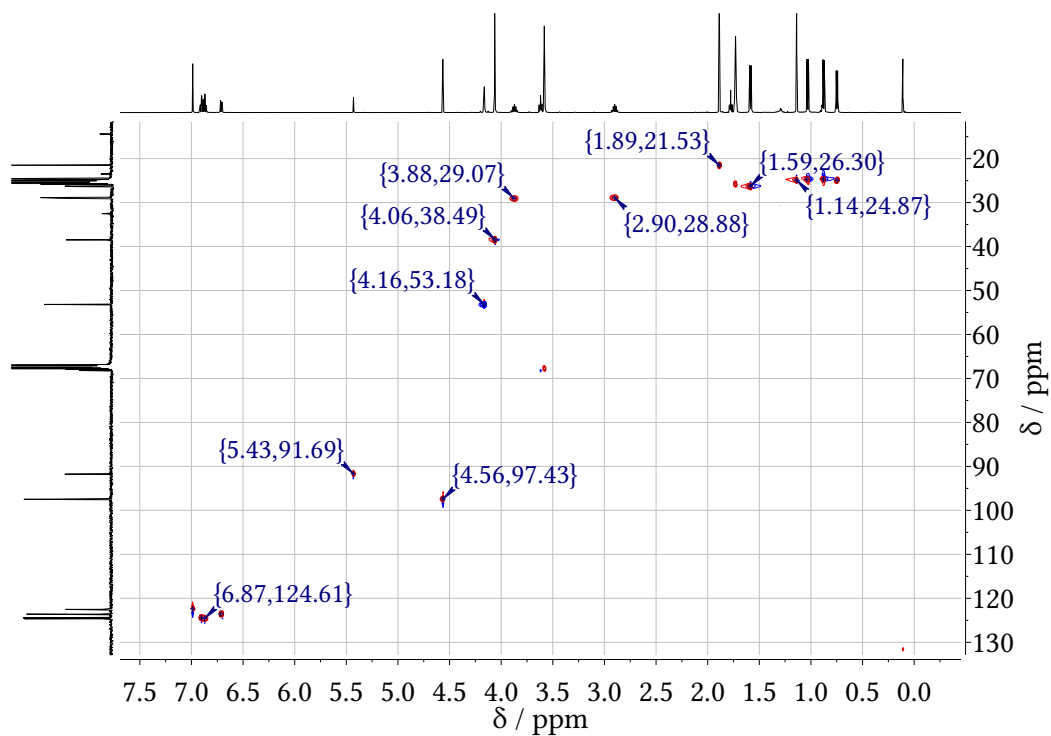


Figure B.38: ^1H , ^{13}C -HSQC NMR spectrum of **9** at -35°C in $\text{THF-}d_8$.

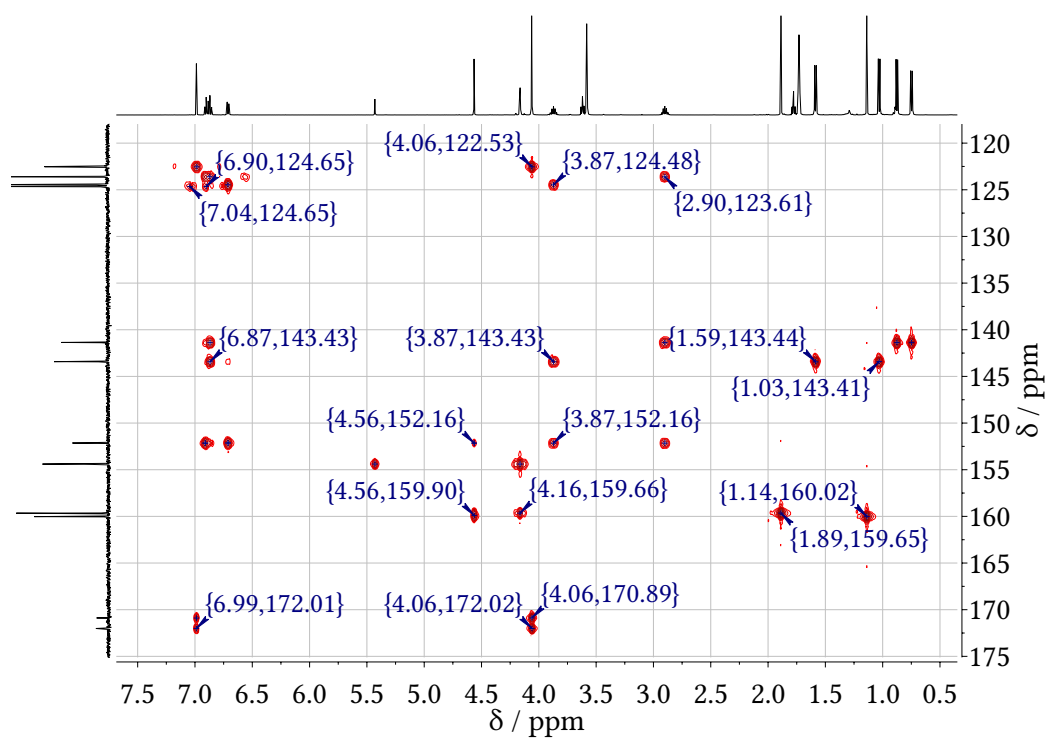


Figure B.39: ^1H , ^{13}C -HSQC NMR spectrum of **9** at -35°C in $\text{THF-}d_8$.

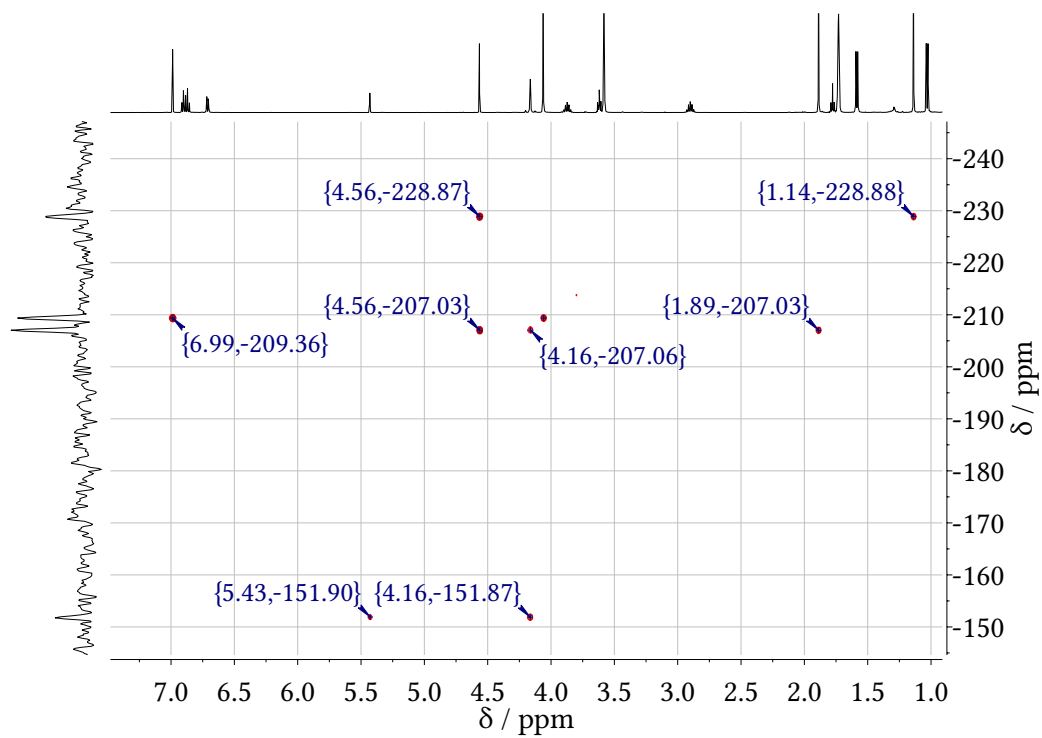


Figure B.40: $^1\text{H},^{15}\text{N}$ -HMBC NMR spectrum of **9** at -35°C in $\text{THF-}d_8$.

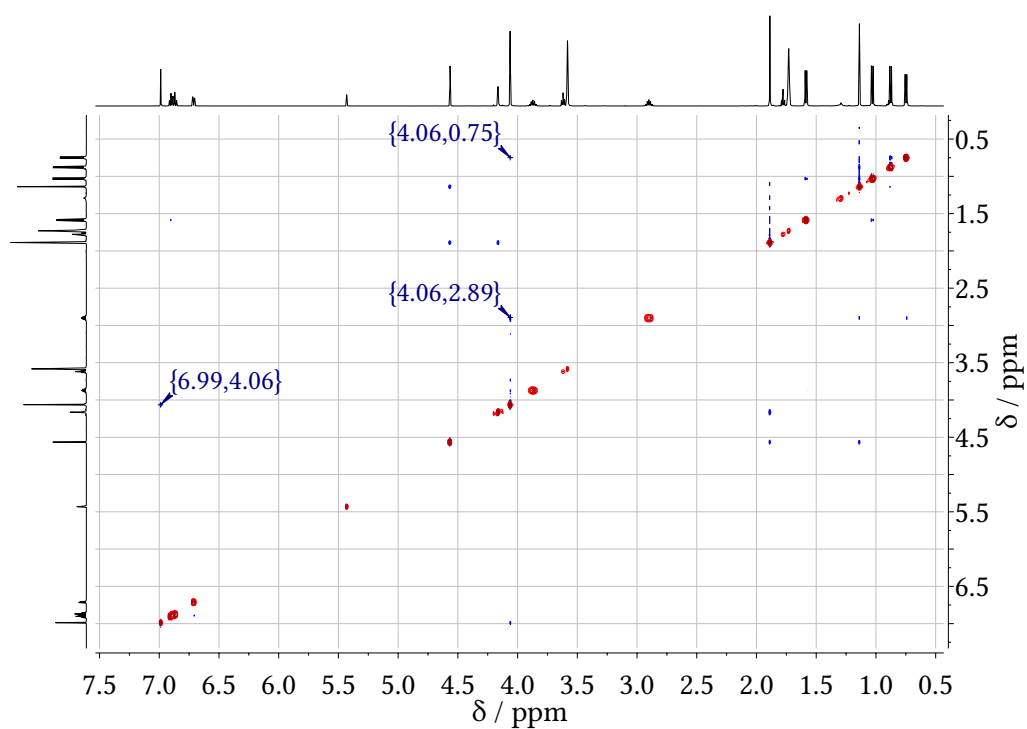
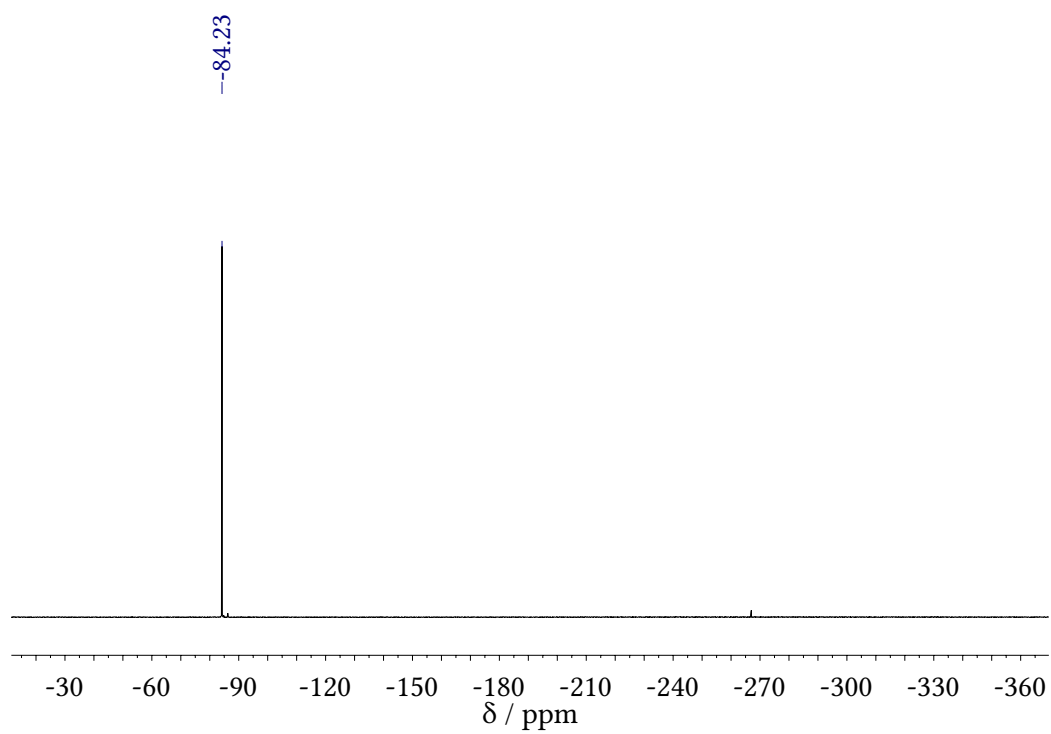
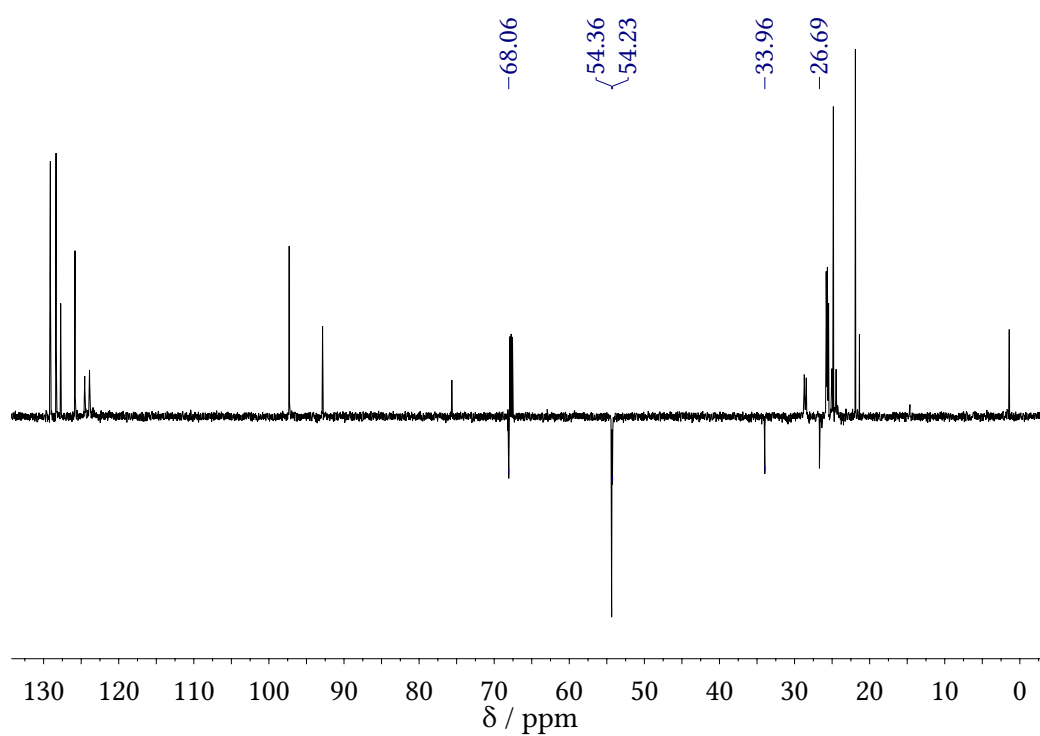


Figure B.41: $^1\text{H},^1\text{H}$ -NOESY NMR spectrum of **9** at -35°C in $\text{THF-}d_8$.

B.4.5 NMR spectra of 10

Figure B.42: ^{31}P NMR spectrum of 9 at -35°C in $\text{THF-}d_8$.Figure B.43: DEPT-135 NMR spectrum of 9 at -35°C in $\text{THF-}d_8$.

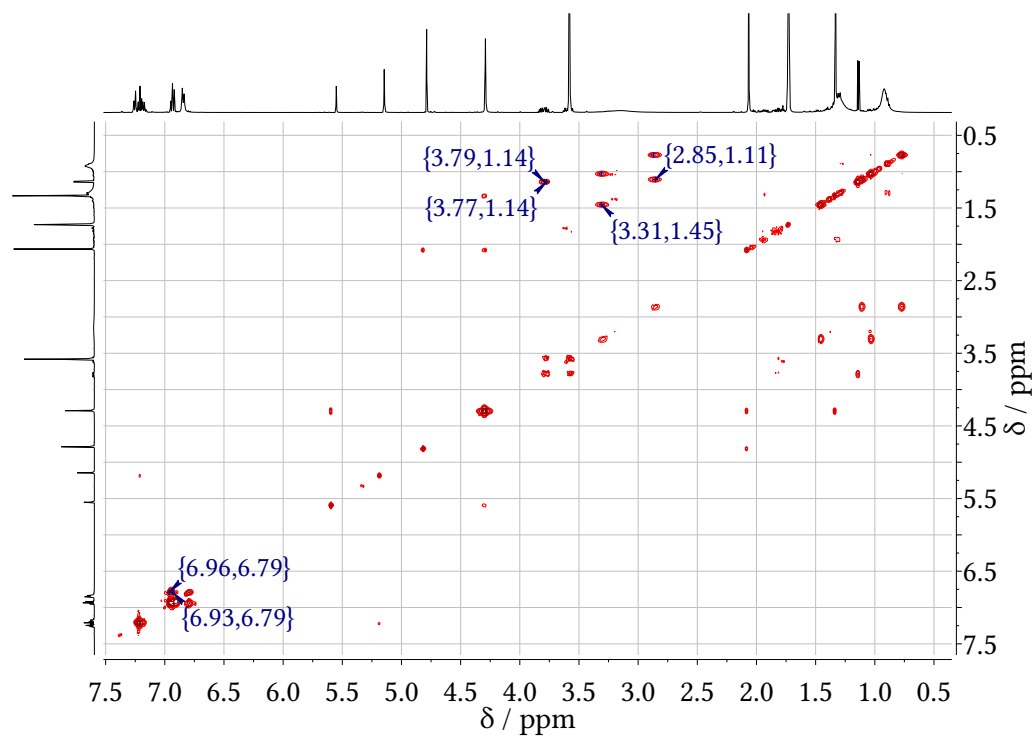


Figure B.44: $^1\text{H},^1\text{H}$ -COSY NMR spectrum of **10** at -35°C in $\text{THF-}d_8$.

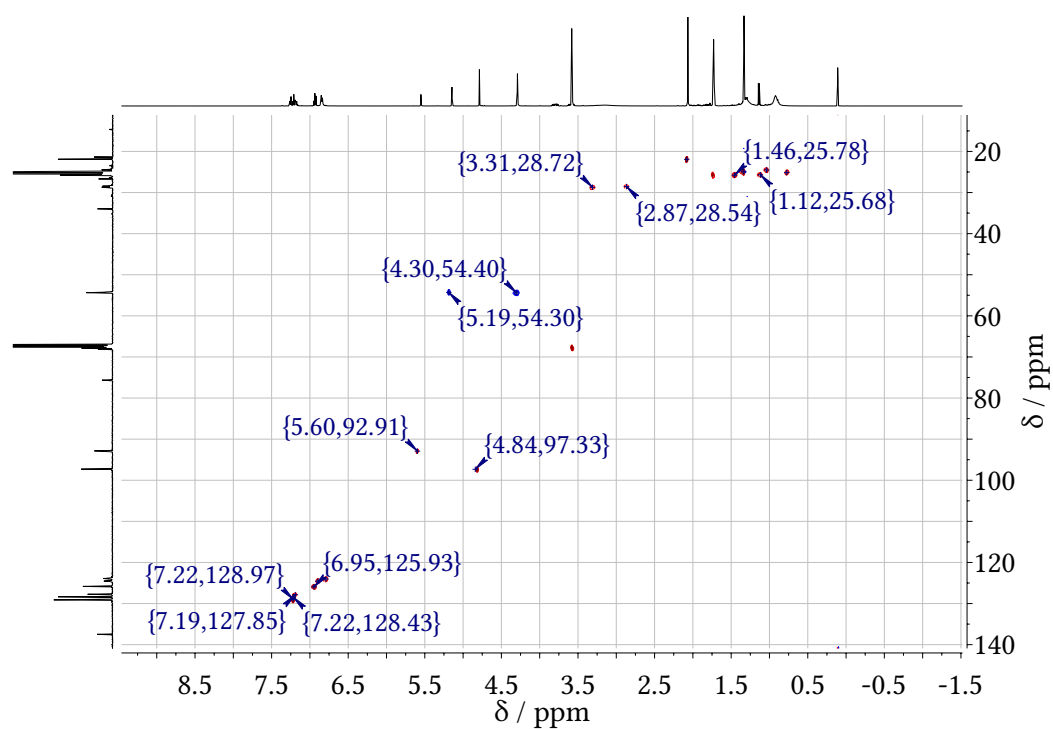


Figure B.45: $^1\text{H},^{13}\text{C}$ -HSQC NMR spectrum of **10** at -35°C in $\text{THF-}d_8$.

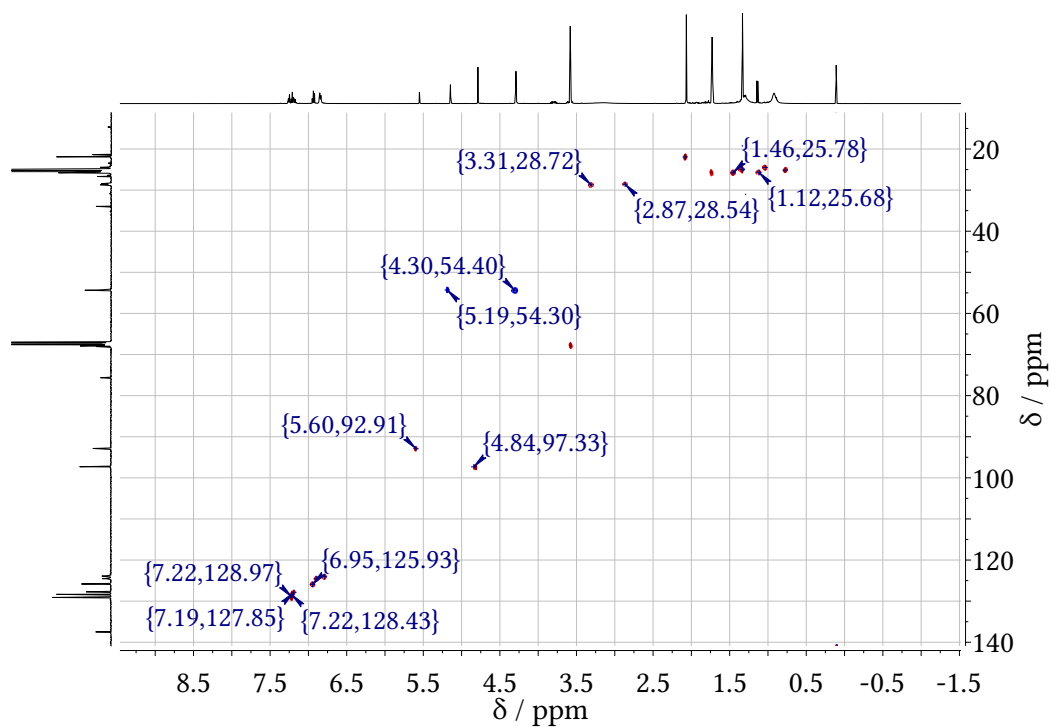


Figure B.46: $^1\text{H},^{13}\text{C}$ -HSQC NMR spectrum of **10** at -35°C in $\text{THF-}d_8$.

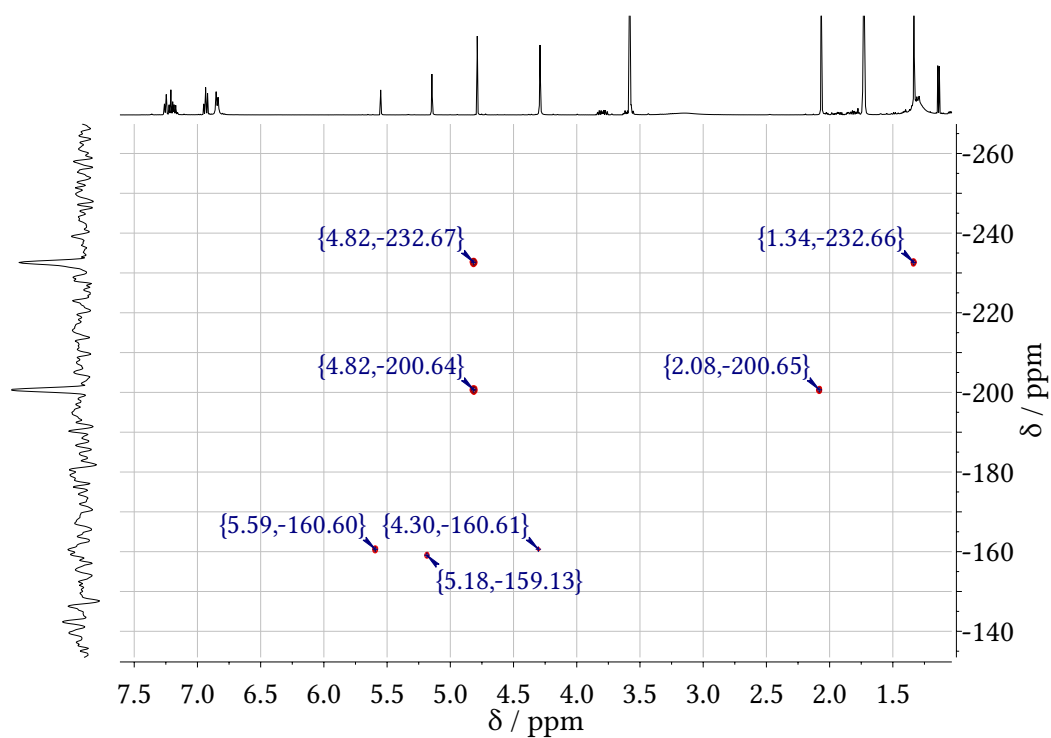
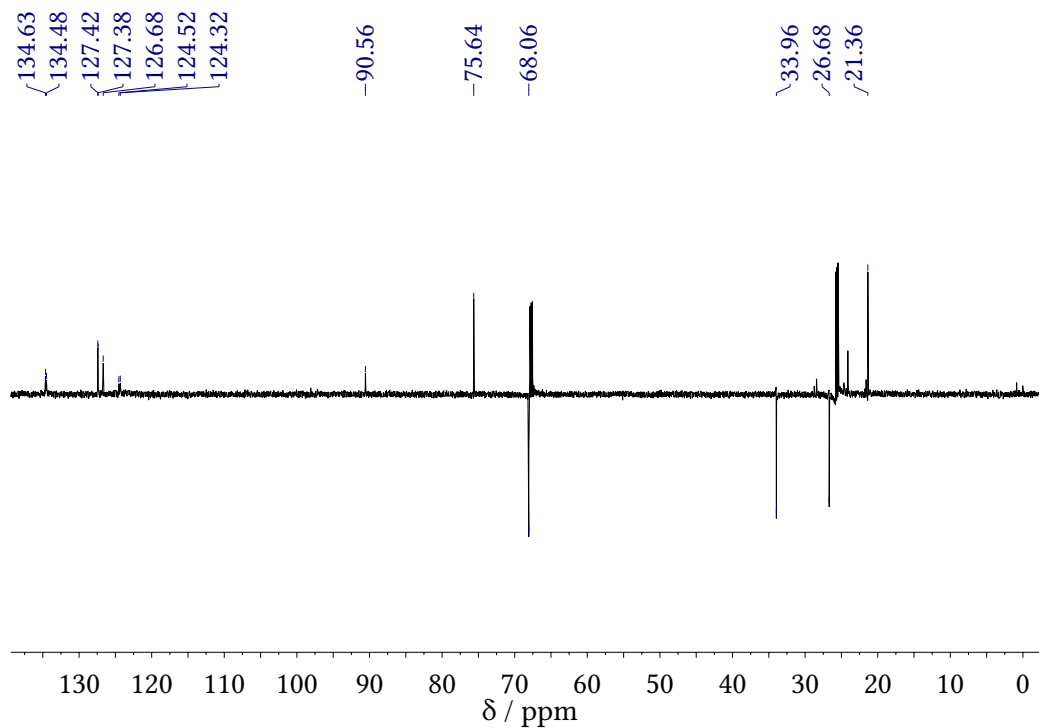
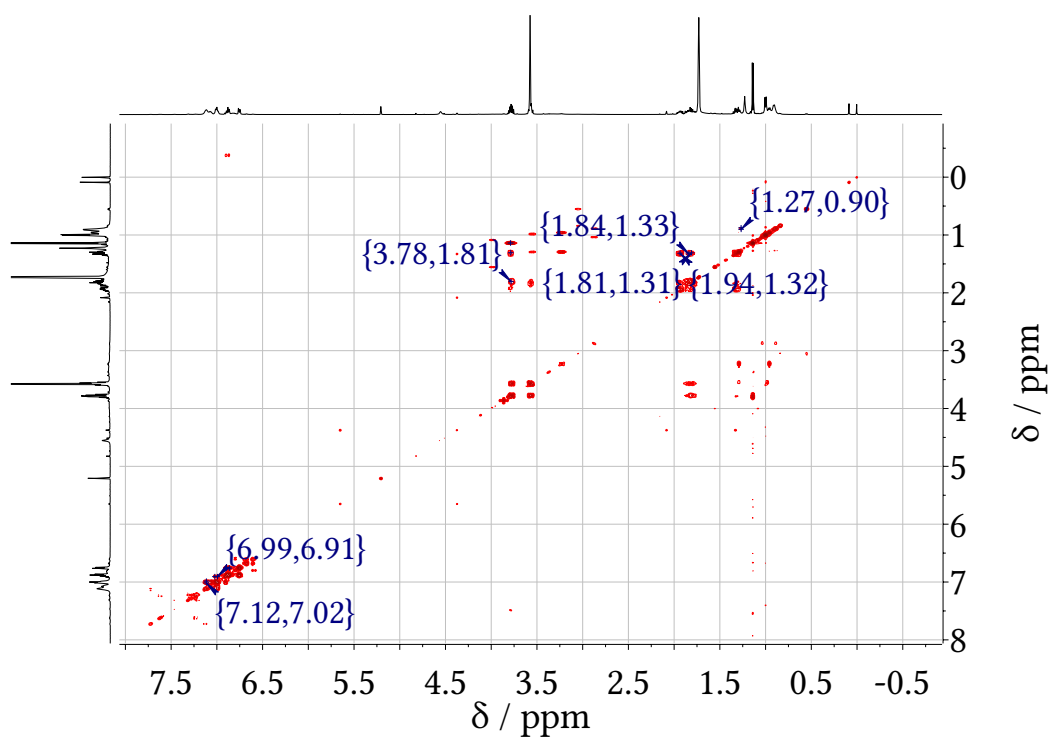


Figure B.47: $^1\text{H},^{15}\text{N}$ -HMBC NMR spectrum of **10** at -35°C in $\text{THF-}d_8$.

B.4.6 NMR spectra of $\text{K}[\text{LNi}_2(\text{PC}(\text{O})\text{PPh}_2)]$ Figure B.48: DEPT-135 NMR spectrum of **11** at -35°C in $\text{THF-}d_8$.Figure B.49: $^1\text{H}, ^1\text{H}$ -COSY NMR spectrum of **11** at -35°C in $\text{THF-}d_8$.

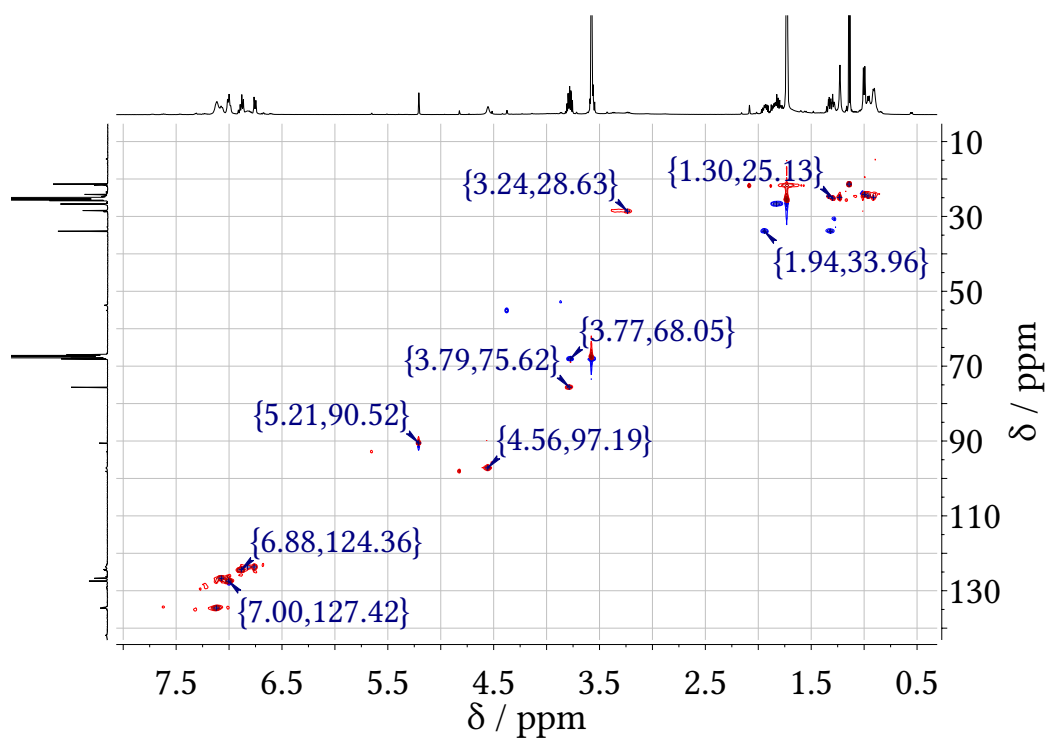


Figure B.50: ^1H , ^{13}C -HSQC NMR spectrum of **11** at -35°C in $\text{THF-}d_8$.

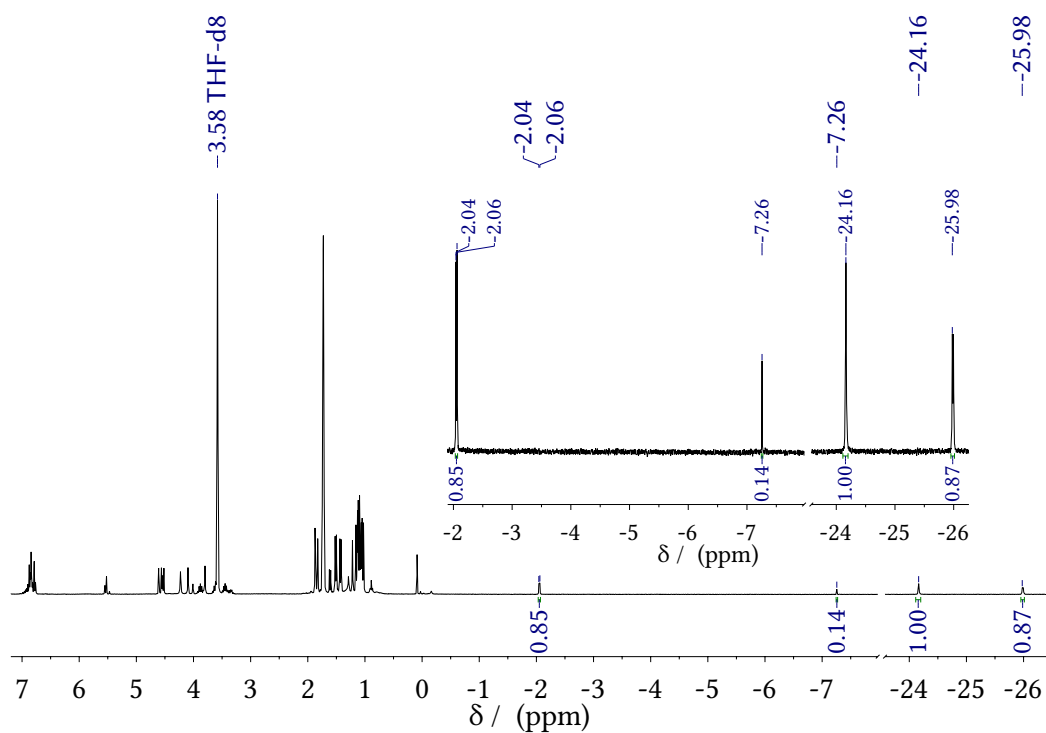
B.4.7 Reaction of 3^{K} with H_2 

Figure B.51: ^1H NMR spectrum of the reaction of 3^{K} with H_2 yielding 2^{K} $\delta_{\text{H}} = \text{ppm}$ at -40°C , recorded in THF- d_8 at r.t. The inset shows the concomitant formation of 1^{OH} ($\delta_{\text{OH}} = 7.27\text{ppm}$) and 6 ($\delta_{\text{OH}} = \text{ppm}$ and $\delta_{\text{H}} = \text{ppm}$), which were identified by their characteristic peaks.

Appendix C

DFT calculations

The ORCA 4.2.1 program package was employed for all calculations.^[276]

C.1 DFT calculations for the dinickel(I) complexes 3^{K} , 3^{Na} and **4**

Geometry optimization and frequency calculation were performed on the basis of the crystallographic data of 3^{K} and **4**; however, to reduce computation time, the simplified complexes were taken used. For 3^{K} the $[\text{K}(\text{THF})_4]^+$ was removed, and for **4** only the cation was taken. The DFT optimized structures were obtained by using the BP86 functional with def2-TZVP basis set,^[277] RI approximation using the auxiliary def2/J basis set, Grimme's D3 dispersion correction with Becke-Johnson damping,^[213,214] tight convergence, and optimization criteria. All other calculations were performed on the optimized coordinates or coordinates from crystallographic data with the B3LYP functional and the RIJCOSX approximation with the same basis sets and dispersion correction. TD-DFT calculations were carried out at the B3LYP/def2-TZVP level of theory under the consideration of 80 electronic states. Molecular structures have been optimized using the conductor-like polarizable continuum mode (CPCM) with default settings for the used solvent THF.^[278]

C.1.1 LöWDIN Spin Population

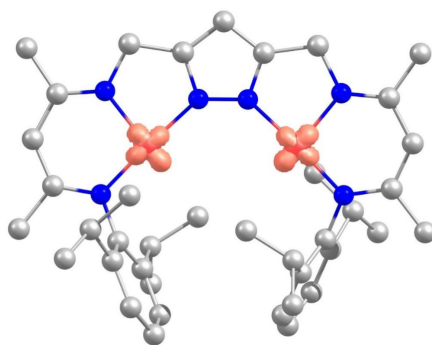


Figure C.1: Spin density plot of $[\text{LNi}_2]^-$ ($S = 1$). Löwdin spin population: Ni1 = 0.87, Ni2 = 0.87. (isosurface value: 0.04).

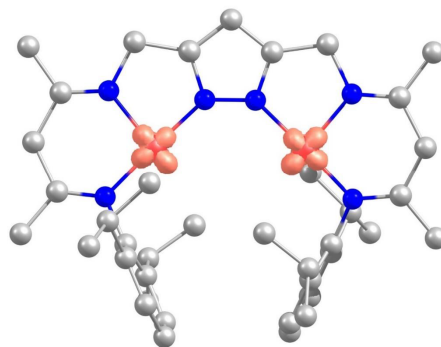


Figure C.2: Spin density plot of $[\text{LNi}_2]^-$ ($S = 1$). Löwdin spin population: Ni1 = 0.87, Ni2 = 0.87. (isosurface value: 0.04).

C.1.2 Magnetic Orbitals

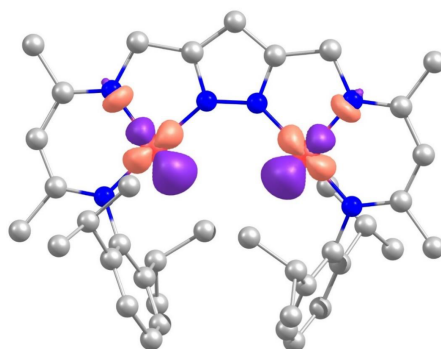


Figure C.3: Combined corresponding orbitals representing the magnetic orbitals for the broken symmetry state of $[\text{LNi}_2]^+$. (isosurface value: 0.08).

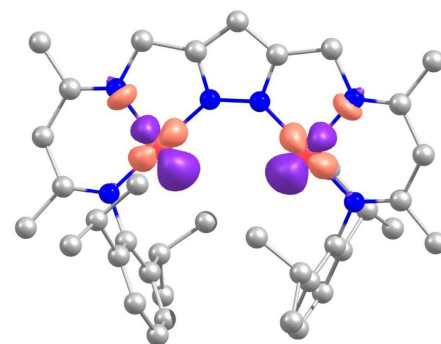


Figure C.4: Combined corresponding orbitals representing the magnetic orbitals for the broken symmetry state of $[\text{LNi}_2]^-$. (isosurface value: 0.08).

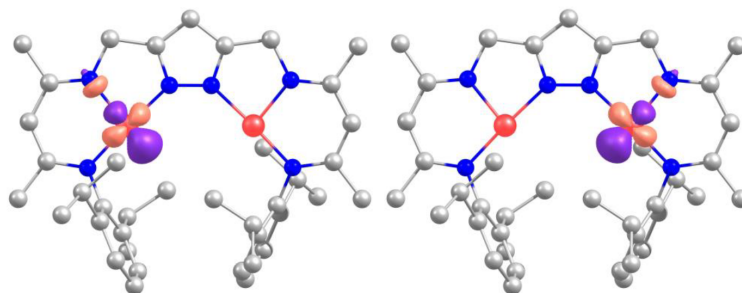


Figure C.5: Corresponding orbitals (left: α , right: β) representing the magnetic orbitals for the broken symmetry state of $[\text{LNi}_2]^-$. (isosurface value: 0.08).

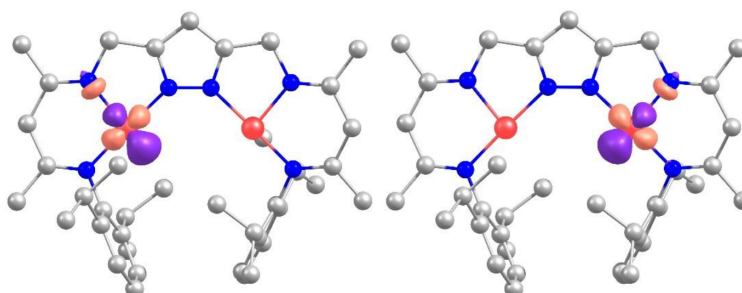


Figure C.6: Corresponding orbitals (left: α , right: β) representing the magnetic orbitals for the broken symmetry state of $[\text{LNi}_2]^+$. (isosurface value: 0.08).

C.1.3 DFT Calculation for the UV-vis spectra of 3^{K} and 4

Table C.1: Selected states (s.), energies (cm^{-1}), λ (wavelengths) (nm), oscillator strengths, and compositions (according to Löwdin reduced orbital populations per MO) of electronic transitions of $[\text{LNi}_2]^-$ ($S = 0$) from TD-DFT calculation (H = HOMO, L = LUMO).

s.	energy	λ	osc. strength	selected large contributions
3	10420.0	959.7	0.000612546	H-2(a)(91% Ni) \rightarrow L+2(a)(16% Ni)(d-d), H-2(a)(91% Ni) \rightarrow L+6(a)(33% Ni)(d-d)
6	11826.8	845.5	0.000907443	H-4(b)(61% Ni) \rightarrow L+2(b)(16% Ni)(d-d), H-3(b)(61% Ni) \rightarrow L+6(b)(33% Ni)(d-d)
7	13747.4	727.4	0.001711298	H-7(a)(67% Ni) \rightarrow L+2(a)(16% Ni)(d-d), H-7(a)(67% Ni) \rightarrow L+6(a)(33% Ni)(d-d)
12	19060.9	524.6	0.006385497	H-1(a)(56% Ni) \rightarrow L+1(a)(7% Ni)(MLCT), H-1(a)(56% Ni) \rightarrow L(a) (8% Ni)(MLCT)
15	21572.8	463.5	0.017377888	H-6(a)(70% Ni) \rightarrow L+1(a)(7% Ni)(MLCT), H-4(a)(63% Ni) \rightarrow L(a) (8% Ni)(MLCT)
18	23010.8	434.6	0.026032864	H-3(a)(60% Ni) \rightarrow L+1(a)(7% Ni)(MLCT), H(a)(63% Ni) \rightarrow L+1(a)(7% Ni)(MLCT)
26	23010.8	405.3	0.029405567	H-1(b)(56% Ni) \rightarrow L+6(b)(3% Ni)(MLCT), H-1(a)(56% Ni) \rightarrow L+6(a)(3% Ni)(MLCT)
57	24673.9	357.8	0.014884541	H-2(b)(91% Ni) \rightarrow L+4(b)(2% Ni)(MLCT)
64	27951.4	339.4	0.014417610	H-2(b)(91% Ni) \rightarrow L+4(b)(2% Ni)(MLCT)
71	29992.8	333.4	0.048750075	H-2(a)(91% Ni) \rightarrow L+5(a)(3% Ni)(MLCT)

Table C.2: Selected states (s), energies (cm^{-1}), λ (wavelengths) (nm), oscillator strengths, and compositions (according to Löwdin reduced orbital populations per MO) of electronic transitions of $[\text{LNi}_2]^+$ ($S = 0$) from TD-DFT calculation (H = HOMO, L = LUMO).

s.	energy	λ	osc. strength	selected large contributions
2	10467.2	955.4	0.001019499	H-2(a)(91% Ni) \rightarrow L+2(a)(33% Ni)(d-d),
6	12033.4	831.0	0.000648272	H-4(b)(87% Ni) \rightarrow L+2(b)(33% Ni)(d-d),
7	14045.3	712.0	0.001166516	H-7(a)(87% Ni) \rightarrow L+2(a)(34% Ni)(d-d),
13	20155.9	496.1	0.012365618	H-1(a)(55% Ni) \rightarrow L+1(a)(6% Ni)(MLCT), H-1(a)(55% Ni) \rightarrow L(a) (6% Ni)(MLCT)
24	24605.7	406.4	0.016499617	H-6(a)(87% Ni) \rightarrow L+1(a)(10% Ni)(MLCT),
32	25303.1	395.2	0.011178716	H-3(a)(55% Ni) \rightarrow L+1(a)(33% Ni)(MLCT),
36	27239.6	367.1	0.034795307	H-1(b)(64% Ni) \rightarrow L+6(b)(6% Ni)(MLCT),
45	28376.4	352.4	0.031564584	H-2(b)(64% Ni) \rightarrow L+4(b)(6% Ni)(MLCT)
56	29578.0	338.1	0.040157944	H-2(b)(64% Ni) \rightarrow L+4(b)(6% Ni)(MLCT)

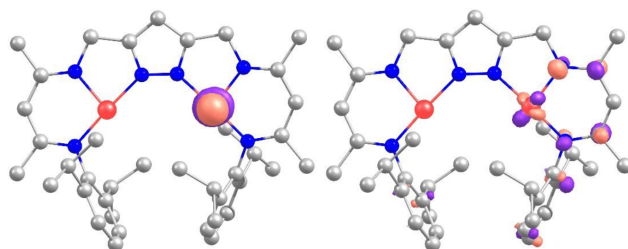


Figure C.7: Orbitals with large contributions to state 3 in $[\text{LNi}_2]^-$. ($S = 0$); H-2(a)(91% Ni) \rightarrow L+2(a)(16% Ni). (isosurface value: 0.08).

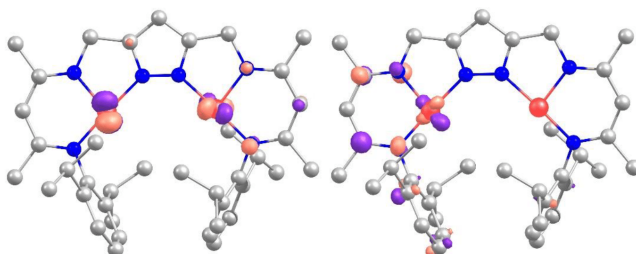


Figure C.8: Orbitals with large contributions to state 6 in $[\text{LNi}_2]^-$. ($S = 0$); H-4(b)(61% Ni) \rightarrow L+2(b)(16% Ni). (isosurface value: 0.08).

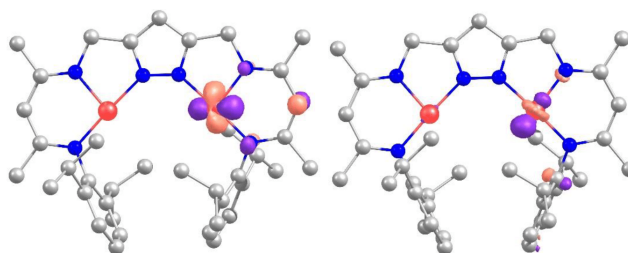


Figure C.9: Orbitals with large contributions to state 7 in $[\text{LNi}_2]^-$. ($S = 0$); H-7(a)(67% Ni) \rightarrow L+6(a)(33% Ni). (isosurface value: 0.08).

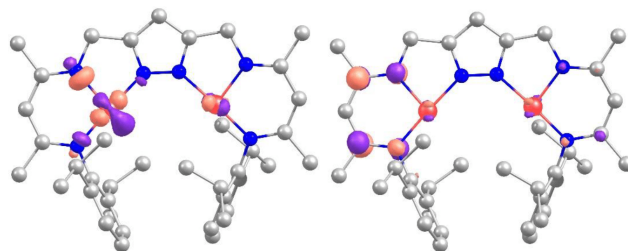


Figure C.10: Orbitals with large contributions to state 12 in $[\text{LNi}_2]^-$. ($S = 0$); H-1(a)(56% Ni) \rightarrow L+1(a)(7% Ni). (isosurface value: 0.08).

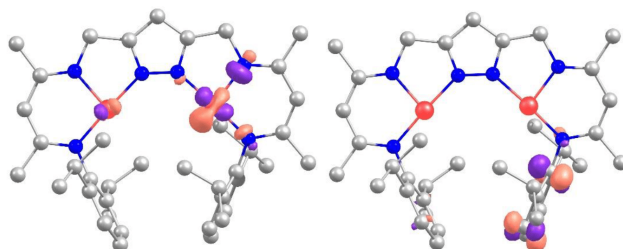


Figure C.11: Orbitals with large contributions to state 26 in $[\text{LNi}_2]^-$. ($S = 0$); H-1(b)(91% Ni) \rightarrow L+6(b)(3% Ni). (isosurface value: 0.08).

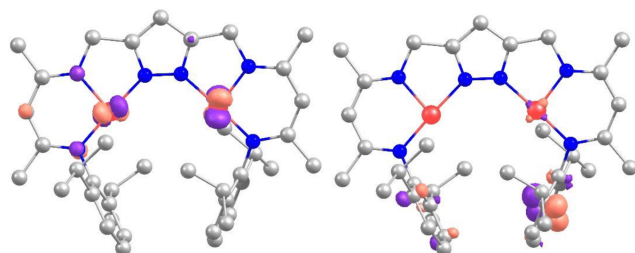


Figure C.12: Orbitals with large contributions to state 64 in $[\text{LNi}_2]^-$. ($S = 0$); H-2(a)(87% Ni) \rightarrow L+4(a)(33% Ni). (isosurface value: 0.08).

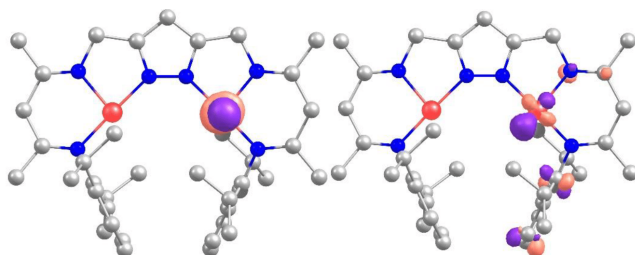


Figure C.13: Orbitals with large contributions to state 2 in $[\text{LNi}_2]^+$. ($S = 0$); H-3(a)(91% Ni) \rightarrow L+4(a)(33% Ni). (isosurface value: 0.08).

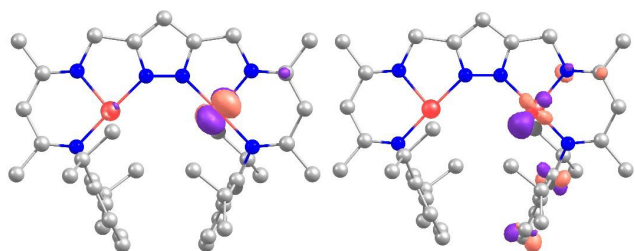


Figure C.14: Orbitals with large contributions to state 6 in $[\text{LNi}_2]^+$. ($S = 0$); H-7(b)(87% Ni) \rightarrow L+4(a)(33% Ni). (isosurface value: 0.08).

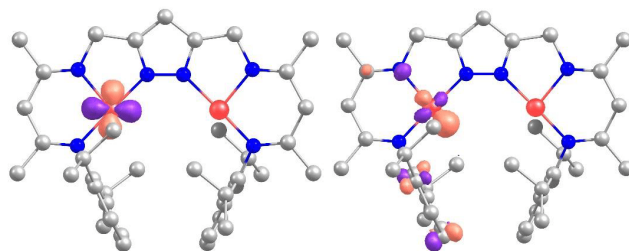


Figure C.15: Orbitals with large contributions to state 7 in $[\text{LNi}_2]^+$. ($S = 0$); H-7(b)(87% Ni) \rightarrow L+4(b)(34% Ni). (isosurface value: 0.08).

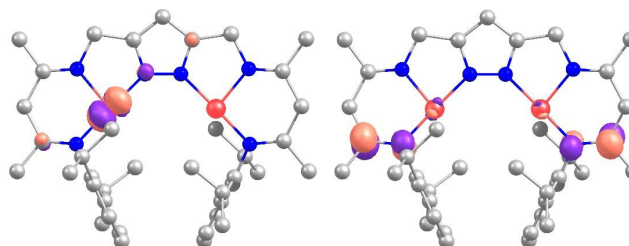


Figure C.16: Orbitals with large contributions to state 13 in $[\text{LNi}_2]^+$. ($S = 0$); H-2(b)(55% Ni) \rightarrow L+1(a)(6% Ni). (isosurface value: 0.08).

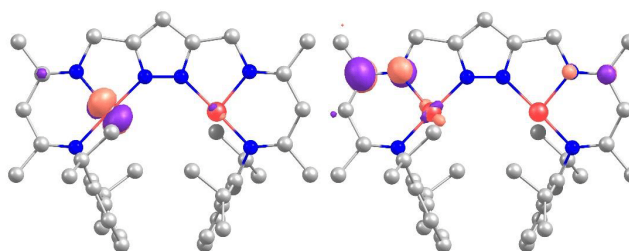


Figure C.17: Orbitals with large contributions to state 24 in $[\text{LNi}_2]^+$. ($S = 0$); H-3(b)(91% Ni) \rightarrow L+3(b)(10% Ni). (isosurface value: 0.08).

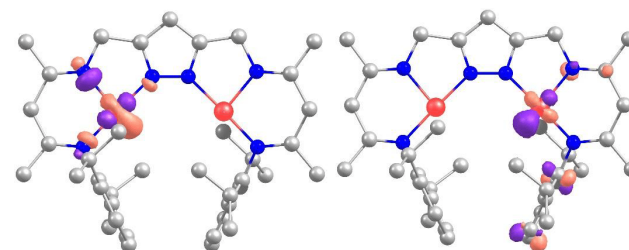


Figure C.18: Orbitals with large contributions to state 32 in $[\text{LNi}_2]^+$. ($S = 0$); H-2(a)(87% Ni) \rightarrow L+3(b)(10% Ni). (isosurface value: 0.08).

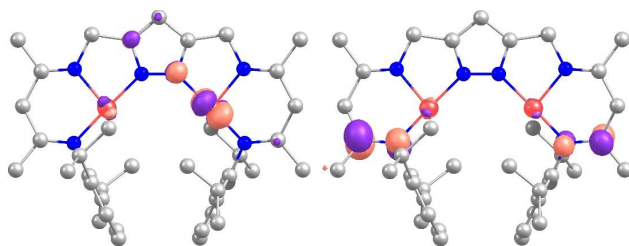


Figure C.19: Orbitals with large contributions to state 36 in $[\text{LNi}_2]^+$. ($S = 0$); H-4(b)(64% Ni) \rightarrow L+2(b)(6% Ni). (isosurface value: 0.08).

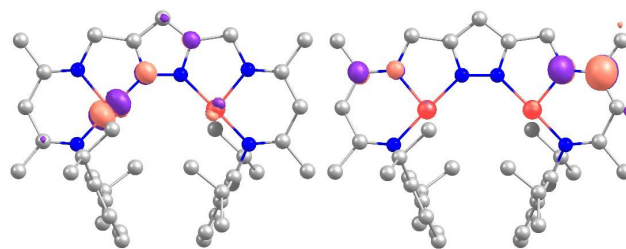


Figure C.20: Orbitals with large contributions to state 45 in $[\text{LNi}_2]^+$. ($S = 0$); H-2(a)(64% Ni) \rightarrow L+2(b)(6% Ni). (isosurface value: 0.08).

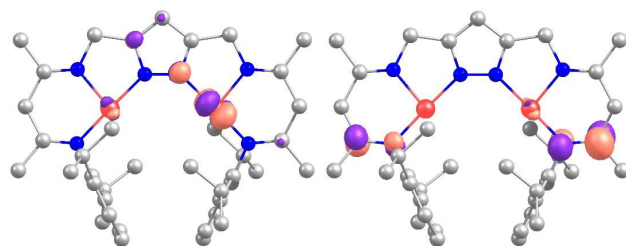


Figure C.21: Orbitals with large contributions to state 56 in $[\text{LNi}_2]^+$. ($S = 0$); H-4(a)(64% Ni) \rightarrow L+2(a)(6% Ni). (isosurface value: 0.08).

Table C.3: XYZ-coordinates of $[\text{LNi}_2]^-$ ($S = 1$).

Atom	x	y	z	Atom	x	y	z
Ni	-2.0483	1.0552	-0.2334	H	-2.9834	4.4563	0.3780
Ni	2.0542	1.0235	0.2174	H	-2.6594	4.4571	-1.3632
N	-0.6594	2.3394	-0.1040	H	0.4966	-0.2340	1.2959
N	-3.1872	2.5577	-0.5540	H	0.0292	-0.7535	2.9266
N	-3.3282	-0.2834	-0.3844	H	-0.4691	-1.7212	1.5138
N	0.6837	2.3288	0.0990	H	0.0365	5.5694	0.0039
N	3.2153	2.5074	0.5450	H	-6.2992	3.4614	-1.4590
N	3.3155	-0.3336	0.3574	H	-4.8210	4.2937	-2.0081
C	-1.0728	3.6303	-0.1765	H	-5.2939	4.3763	-0.3054
C	-2.5312	3.8585	-0.4396	H	-6.4834	-0.9500	-1.3407
C	-4.4637	2.4602	-0.8991	H	-5.7251	-1.7416	0.0634
C	-4.6010	-0.0675	-0.7545	H	-5.0718	-2.0281	-1.5483
C	-2.9219	-1.5526	0.0948	H	-2.4563	-1.2293	-2.4537
C	-0.3747	-1.0977	-1.9677	H	3.0383	4.4153	-0.3733
C	1.1164	3.6131	0.1767	H	2.7155	4.4085	1.3680
C	0.0283	4.4826	0.0019	H	-3.1122	-3.5163	2.8852
C	-5.1228	1.2113	-1.0178	H	-4.7014	-0.3843	1.6724
C	-5.2671	3.7115	-1.1845	H	-1.0866	-4.2759	-0.8238
C	-5.5245	-1.2576	-0.9056	H	-1.3130	-2.6279	-4.1036
C	-3.2815	-1.9514	1.4111	H	-2.3976	-3.6839	-3.1600
C	-2.1175	-2.3907	-0.7171	H	-0.6404	-3.6851	-2.8527
C	-1.6735	-1.9125	-2.0874	H	-1.7481	-5.0084	1.4536
C	2.5780	3.8183	0.4402	H	-3.5980	0.7384	3.5807
C	-2.8500	-3.1975	1.8753	H	-2.4770	0.5367	2.2070
C	-4.0390	-0.9870	2.3113	H	-2.3540	-0.5458	3.6254
C	-1.7091	-3.6273	-0.2080	H	-5.5226	-0.9381	3.8959
C	-1.5011	-3.0471	-3.1038	H	-4.3138	-2.2146	4.1114

C	4.4912	2.3898	0.8860	H	-5.5971	-2.4116	2.8947
C	4.5920	-0.1385	0.7265	H	6.3424	3.3616	1.4458
C	2.8897	-1.5936	-0.1292	H	4.8778	4.2129	2.0026
C	0.3450	-1.1213	1.9401	H	5.3474	4.2963	0.2991
C	-2.0750	-4.0388	1.0741	H	6.4613	-1.0523	1.3067
C	-3.0582	-0.0055	2.9739	H	5.6929	-1.8210	-0.1046
C	-4.9153	-1.6822	3.3584	H	5.0346	-2.1121	1.5044
C	5.1327	1.1311	0.9961	H	2.4272	-1.2726	2.4181
C	5.3133	3.6280	1.1753	H	1.0109	-4.2924	0.7731
C	5.4985	-1.3427	0.8684	H	3.0467	-3.5423	-2.9322
C	2.0723	-2.4237	0.6778	H	4.6894	-0.4464	-1.6988
C	3.2423	-1.9900	-1.4481	H	1.2776	-2.6688	4.0660
C	1.6373	-1.9475	2.0515	H	2.3526	-3.7277	3.1146
C	1.6437	-3.6502	0.1611	H	0.5947	-3.7170	2.8132
C	2.7903	-3.2258	-1.9201	H	1.6593	-5.0213	-1.5092
C	4.0165	-1.0326	-2.3421	H	3.6053	0.7086	-3.5999
C	1.4600	-3.0850	3.0639	H	2.4803	0.5165	-2.2278
C	2.0020	-4.0594	-1.1238	H	2.3401	-0.5544	-3.6534
C	3.0527	-0.0300	-2.9980	H	5.5032	-0.9992	-3.9242
C	4.8804	-1.7358	-3.3942	H	4.2693	-2.2489	-4.1528
H	-6.1601	1.2452	-1.3492	H	5.5468	-2.4828	-2.9362
H	6.1712	1.1487	1.3252	H	2.3401	-0.5544	-3.6534
H	-0.5239	-0.2081	-1.3258	H	5.5032	-0.9992	-3.9242
H	-0.0489	-0.7337	-2.9524	H	4.2693	-2.2489	-4.1528
H	0.4312	-1.7035	-1.5344	H	5.5468	-2.4828	-2.9362

Table C.4: XYZ-coordinates of $[\text{LNi}_2]^-$ ($S = 0$).

Atom	x	y	z	Atom	x	y	z
Ni	-2.0202	1.0519	-0.28664	H	-0.1021	-0.8764	-3.04565
Ni	2.0260	1.0207	0.26701	H	0.4033	-1.7490	-1.57414
N	-0.6524	2.3451	-0.13461	H	-2.99379	4.46156	0.26054
N	-3.1628	2.5458	-0.64327	H	-2.62082	4.4344	-1.47066
N	-3.2961	-0.2928	-0.41629	H	0.55536	-0.27468	1.41707
N	0.6772	2.3347	0.12171	H	0.08539	-0.89166	3.01517
N	3.1904	2.4960	0.63157	H	-0.43714	-1.75495	1.54419
N	3.2825	-0.3428	0.39001	H	0.03629	5.57404	0.00133
C	-1.0654	3.6350	-0.223	H	-6.27503	3.4214	-1.57557
C	-2.5165	3.8524	-0.53319	H	-4.7984	4.24362	-2.14333
C	-4.4371	2.4371	-0.99268	H	-5.27209	4.36511	-0.44386
C	-4.5701	-0.0866	-0.78703	H	-6.4533	-0.99036	-1.33915
N	3.1904	2.4960	0.63157	H	-0.43714	-1.75495	1.54419
N	3.2825	-0.3428	0.39001	H	0.03629	5.57404	0.00133
C	-1.0654	3.6350	-0.223	H	-6.27503	3.4214	-1.57557
C	-2.5165	3.8524	-0.53319	H	-4.7984	4.24362	-2.14333
C	-4.4371	2.4371	-0.99268	H	-5.27209	4.36511	-0.44386
C	-4.5701	-0.0866	-0.78703	H	-6.4533	-0.99036	-1.33915
C	-2.8938	-1.5475	0.10435	H	-5.69153	-1.72709	0.09478
C	-0.4143	-1.1802	-2.03562	H	-5.03999	-2.07435	-1.50604
C	1.1092	3.6179	0.21629	H	-2.50243	-1.36404	-2.48031
C	0.0283	4.4879	-0.00129	H	3.04973	4.4184	-0.26291

C	-5.0923	1.1841	-1.08645	H	2.67596	4.38821	1.46807
C	-5.2432	3.6798	-1.30691	H	-3.06258	-3.39731	2.97246
C	-5.4941	-1.2810	-0.89289	H	-4.62781	-0.29341	1.65864
C	-3.2356	-1.8900	1.44056	H	-1.1274	-4.33804	-0.74377
C	-2.1198	-2.4296	-0.69006	H	-1.35729	-2.82904	-4.07189
C	-1.7040	-2.0159	-2.09055	H	-2.41698	-3.85009	-3.06189
C	2.5633	3.8124	0.52772	H	-0.65607	-3.80928	-2.77552
C	-2.8149	-3.1237	1.94556	H	-1.75068	-4.96816	1.57344
C	-3.9668	-0.8813	2.31332	H	-3.47952	0.89158	3.49815
C	-1.7224	-3.6527	-0.14084	H	-2.37428	0.6016	2.12704
C	-1.5296	-3.1990	-3.05008	H	-2.26199	-0.41436	3.59568
C	4.4628	2.3671	0.98071	H	-5.42572	-0.74718	3.91488
C	4.5591	-0.1572	0.76244	H	-4.22997	-2.02999	4.16427
C	2.8629	-1.5888	-0.13813	H	-5.53524	-2.25992	2.97668
C	0.3900	-1.1987	2.00382	H	6.31491	3.32145	1.56825
C	-2.0691	-4.0078	1.16329	H	4.85055	4.16256	2.14009
C	-2.9593	0.1090	2.92423	H	5.32595	4.28526	0.44119
C	-4.8375	-1.5214	3.39972	H	6.42821	-1.09153	1.31199
C	5.0997	1.1042	1.06862	H	5.65855	-1.80801	-0.12792
C	5.2870	3.5963	1.30092	H	4.99914	-2.1561	1.46943
C	5.4657	-1.3654	0.86223	H	2.47508	-1.41632	2.44792
C	2.0772	-2.4651	0.65115	H	1.05966	-4.36059	0.69352
C	3.2000	-1.9276	-1.47644	H	3.00615	-3.42289	-3.01758
C	1.6671	-2.0538	2.05403	H	4.6138	-0.34891	-1.68452
C	1.6634	-3.6794	0.09459	H	1.30565	-2.87326	4.03002
C	2.7624	-3.1523	-1.98897	H	2.35191	-3.90395	3.01581
C	3.9451	-0.9237	-2.34299	H	0.59221	-3.8355	2.72692
C	1.4742	-3.2398	3.00636	H	1.67349	-4.98448	-1.62784
C	2.0049	-4.0310	-1.21188	H	3.48379	0.86332	-3.51665
C	2.9521	0.0844	-2.94832	H	2.37331	0.58005	-2.14843
C	4.8074	-1.5692	-3.43288	H	2.24796	-0.42443	-3.62384
H	-6.1322	1.2092	-1.41218	H	5.40602	-0.80009	-3.94362
H	6.1396	1.1125	1.39496	H	4.19324	-2.0654	-4.20031
H	-0.5677	-0.2546	-1.44802	H	5.49519	-2.31941	-3.01397

Table C.5: XYZ-coordinates of $[\text{LNi}_2]^+$ ($S = 1$).

Atom	x	y	z	Atom	x	y	z
Ni	-2.0300	0.97408	-0.1985	H	-6.11013	1.1866	-0.9065
Ni	2.0044	0.95014	0.4091	H	-3.05365	4.29603	0.5402
N	-0.6805	2.26595	0.03656	H	-2.65803	4.45541	-1.17831
N	-3.1881	2.49093	-0.55264	H	-0.0173	5.49173	0.30505
N	-3.3155	-0.35079	-0.38545	H	-6.20013	3.406	-1.70079
N	0.6488	2.25507	0.3006	H	-4.70468	4.33132	-1.98178
N	3.1566	2.43264	0.90302	H	-5.39057	4.24223	-0.35444
N	3.3062	-0.37565	0.44752	H	-6.08661	-1.2796	-1.85356
C	-1.0989	3.55549	0.00101	H	-6.21804	-1.31615	-0.09061
C	-2.5452	3.79443	-0.30212	H	-4.99137	-2.32155	-0.89231
C	-4.3994	2.43664	-0.9902	H	3.01832	4.32312	-0.03585
C	-4.5286	-0.21177	-0.82772	H	2.62771	4.33694	1.69121
C	-2.8682	-1.62865	0.10242	H	-2.9911	-3.57395	2.88505

C	1.0659	3.53778	0.4443	H	-4.63701	-0.46241	1.74507
C	-0.0168	4.40743	0.25902	H	-1.11615	-4.35772	-0.89641
C	-5.0728	1.11797	-1.27988	H	-2.50863	-1.34021	-2.52028
C	-5.2232	3.66352	-1.27666	H	-1.71093	-5.07844	1.39871
C	-5.4991	-1.35176	-0.92677	H	-3.43025	0.73222	3.55101
C	-3.1893	-1.99837	1.42837	H	-2.37831	0.51665	2.12552
C	-2.0968	-2.44827	-0.74808	H	-2.1678	-0.52803	3.5553
C	2.5124	3.75231	0.76276	H	-5.30128	-0.97956	4.01812
C	-2.7510	-3.25059	1.87314	H	-4.04223	-2.20647	4.19843
C	-3.9159	-1.03254	2.35182	H	-5.39102	-2.48508	3.07321
C	-1.6907	-3.69295	-0.25391	H	-0.13191	-0.6976	-3.00361
C	-1.6885	-1.96333	-2.12896	H	0.39831	-1.63325	-1.58181
C	4.3717	2.34352	1.32367	H	-0.62139	-0.18711	-1.37548
C	4.5148	-0.27454	0.91111	H	-1.28119	-2.68026	-4.13287
C	2.8849	-1.58595	-0.20678	H	-2.30712	-3.78177	-3.18383
C	-2.0217	-4.09737	1.0385	H	-0.55545	-3.68372	-2.87067
C	-2.9155	-0.01662	2.93172	H	6.16866	3.25253	2.11804
C	-4.7058	-1.72153	3.46806	H	4.67784	4.18042	2.41989
C	-0.4384	-1.07319	-2.01803	H	5.394	4.16695	0.80342
C	-1.4484	-3.09738	-3.13039	H	6.21173	-1.28192	0.05877
C	5.0407	1.00356	1.51125	H	4.99698	-2.37471	0.7575
C	5.2023	3.54345	1.69152	H	6.08688	-1.42633	1.81647
C	5.4962	-1.40877	0.88893	H	1.15816	-4.44446	0.38745
C	2.1233	-2.52756	0.51658	H	2.54301	-1.72185	2.44391
C	3.2190	-1.765	-1.56844	H	3.04131	-3.11749	-3.23538
C	1.7305	-3.69223	-0.15171	H	4.64959	-0.18591	-1.64376
C	1.7122	-2.25617	1.95451	H	1.76182	-4.82698	-1.98532
C	2.7938	-2.94473	-2.18888	H	0.16104	-1.1404	3.01699
C	3.9551	-0.68123	-2.34091	H	-0.35296	-1.7674	1.42715
C	2.0659	-3.90536	-1.48774	H	0.71301	-0.33992	1.53374
C	0.4847	-1.32853	1.98466	H	1.26001	-3.27164	3.81514
C	1.7305	-3.69223	-0.15171	H	4.64959	-0.18591	-1.64376
C	1.7122	-2.25617	1.95451	H	1.76182	-4.82698	-1.98532
C	2.7938	-2.94473	-2.18888	H	0.16104	-1.1404	3.01699
C	1.7305	-3.69223	-0.15171	H	4.64959	-0.18591	-1.64376
C	1.7122	-2.25617	1.95451	H	1.76182	-4.82698	-1.98532
C	2.7938	-2.94473	-2.18888	H	0.16104	-1.1404	3.01699
C	3.9551	-0.68123	-2.34091	H	-0.35296	-1.7674	1.42715
C	2.0659	-3.90536	-1.48774	H	0.71301	-0.33992	1.53374
C	0.4847	-1.32853	1.98466	H	1.26001	-3.27164	3.81514
C	1.4333	-3.52808	2.76096	H	2.27333	-4.23569	2.71279
C	2.9584	0.38984	-2.81937	H	0.52987	-4.03794	2.39754
C	4.7890	-1.2168	-3.50871	H	3.48142	1.21139	-3.32965
H	5.1372	0.84522	2.60522	H	2.39701	0.81705	-1.96873
H	6.0897	1.10587	1.18201	H	2.23131	-0.04578	-3.52023
H	-5.2099	1.06365	-2.3794	H	5.38987	-0.40557	-3.94237

Table C.6: XYZ-coordinates of $[\text{LNi}_2]^+$ ($S = 0$).

Atom	x	y	z	Atom	x	y	z
Ni	-2.01032	0.9790	-0.22109	H	-3.05496	4.30866	0.4906
Ni	1.9906	0.9544	0.41753	H	-2.64293	4.44991	-1.22586
N	-0.6736	2.2775	0.01753	H	-0.01654	5.50207	0.30325
N	-3.17404	2.4914	-0.58539	H	-6.18755	3.3907	-1.74194
N	-3.29549	-0.35032	-0.3965	H	-4.69498	4.32238	-2.01866
N	0.64831	2.26612	0.30032	H	-5.38694	4.23265	-0.39396
N	3.14506	2.43165	0.9287	H	-6.07249	-1.29295	-1.84602
N	3.28985	-0.375	0.45325	H	-6.19589	-1.31147	-0.08219
C	-1.09364	3.56622	-0.02082	H	-4.97372	-2.32595	-0.8792
C	-2.53713	3.79925	-0.34114	H	3.02589	4.32915	0.00136
C	-4.3852	2.43074	-1.02266	H	2.61504	4.3328	1.72395
C	-4.50926	-0.21574	-0.83805	H	-2.95703	-3.53543	2.90989
C	-2.84996	-1.62479	0.10261	H	-4.59088	-0.42348	1.74568
C	1.06518	3.54775	0.4527	H	-1.12975	-4.37873	-0.88188
C	-0.0152	4.41792	0.25433	H	-2.54898	-1.39635	-2.53561
C	-5.05359	1.10834	-1.3062	H	-1.69951	-5.06471	1.42977
C	-5.21335	3.65329	-1.31469	H	-3.36331	0.77785	3.53174
C	-5.48078	-1.35612	-0.92125	H	-2.31793	0.53212	2.10599
C	-3.16012	-1.97627	1.43595	H	-2.11587	-0.49736	3.54777
C	-2.09708	-2.46171	-0.74764	H	-5.25007	-0.91488	4.02612
C	2.50843	3.75524	0.79013	H	-4.00184	-2.15211	4.21136
C	-2.72535	-3.2258	1.89171	H	-5.35819	-2.42762	3.0947
C	-3.87269	-0.99529	2.35431	H	-0.19254	-0.74225	-3.07995
C	-1.69137	-3.70142	-0.24119	H	0.3792	-1.64304	-1.65254
C	-1.71616	-2.00375	-2.14577	H	-0.65231	-0.20441	-1.45113
C	4.35332	2.33405	1.36666	H	-1.34172	-2.76135	-4.14112
C	4.49646	-0.27864	0.92304	H	-2.34148	-3.84909	-3.149
C	2.86769	-1.57943	-0.21162	H	-0.58513	-3.7326	-2.87203
C	-2.00917	-4.0867	1.06038	H	6.14098	3.22737	2.19822
C	-2.85926	0.01546	2.92026	H	4.6495	4.15854	2.48607
C	-4.66407	-1.66711	3.47988	H	5.39145	4.15857	0.88123
C	-0.47309	-1.10017	-2.08015	H	6.26104	-1.21578	0.13316
C	-1.487	-3.1576	-3.1268	H	5.00286	-2.36262	0.65322
C	5.01353	0.98939	1.55242	H	6.0008	-1.49176	1.85797
C	5.1827	3.52676	1.75952	H	1.16233	-4.45324	0.36968
C	5.48305	-1.40793	0.89071	H	2.57354	-1.76168	2.44287
C	2.11903	-2.53295	0.50977	H	3.00913	-3.08194	-3.25531
C	3.19255	-1.74405	-1.5771	H	4.61272	-0.1557	-1.64294
C	1.72474	-3.69195	-0.16719	H	1.74474	-4.80777	-2.01254
C	1.73197	-2.2841	1.95871	H	0.20616	-1.18209	3.06934
C	2.76803	-2.91981	-2.20557	H	-0.34063	-1.78161	1.48023
C	3.92195	-0.65167	-2.34331	H	0.73123	-0.35857	1.58798
C	2.04921	-3.88989	-1.5083	H	1.3076	-3.32871	3.80937
C	0.50896	-1.353	2.02768	H	2.29979	-4.27773	2.67493
C	1.46292	-3.56851	2.74845	H	0.55208	-4.06964	2.39162
C	2.91821	0.41492	-2.8168	H	3.43568	1.24346	-3.32138
C	4.76031	-1.17626	-3.51302	H	2.35306	0.83292	-1.96397
H	5.08068	0.81631	2.64648	H	2.19486	-0.02174	-3.52082

H	6.0705	1.09279	1.25145	H	5.35566	-0.35892	-3.94282
H	-5.18133	1.04386	-2.40638	H	4.12983	-1.5746	-4.32071
H	-6.09386	1.17773	-0.94163	H	5.44912	-1.97217	-3.1958

C.1.4 Reaction Pathway Calculations for the Release of Hydrogen

The starting structures for optimization were derived from extensive constrained scans (on the singlet, broken-symmetry, and triplet PES) of the complexes **2'** and **3'** using the BP86 functional with the basis set def2-SVP.^[277] The reaction pathway was simulated along the decreasing distance of the two leaving hydrogen atoms, serving as an approximated reaction coordinate. The final energies and corresponding structures for the minima **MIN1** and **MIN2** were obtained *via* optimizations at the BP86-D3/def2-SVP level of theory and the CPCM solvation model with default settings for THF.^[278] These two minima served as reference points for the nudged elastic band method^[279] (keyword: NEB-TS in Orca) to obtain the final energies and structures of the first transition state (**TS1**). A different method was applied to derive the second transition state (**TS2**). This was done by fixing the distance between the hydrido ligands within the bimetallic cleft to the equilibrium distance of free hydrogen, which is 0.767 Å at this level of theory. By reducing the H···H distances, an earlier crossover to the broken-symmetry state of **3'** in contrast to **1'** ($r(\text{H}\cdots\text{H}) > 1.2 \text{ \AA}$) was calculated.

C.2 DFT calculations for the Oxidative Addition of Water at Dinickel Complexes

C.2.1 Structure Optimizations of **6** and **6-K(crypt)**

Starting from the crystallographic structure data of **2^K**, geometry optimizations were performed using the BP86 functional with the def2-SVP-basis set,^[277] the def2/J auxiliary basis set^[280] and Grimme's D3 dispersion correction with Becke-Johnson dampening.^[213,214] The resulting DFT optimized molecular structure of **6** and the anion of **6-K(crypt)**, including the XYZ coordinates are displayed in the following:

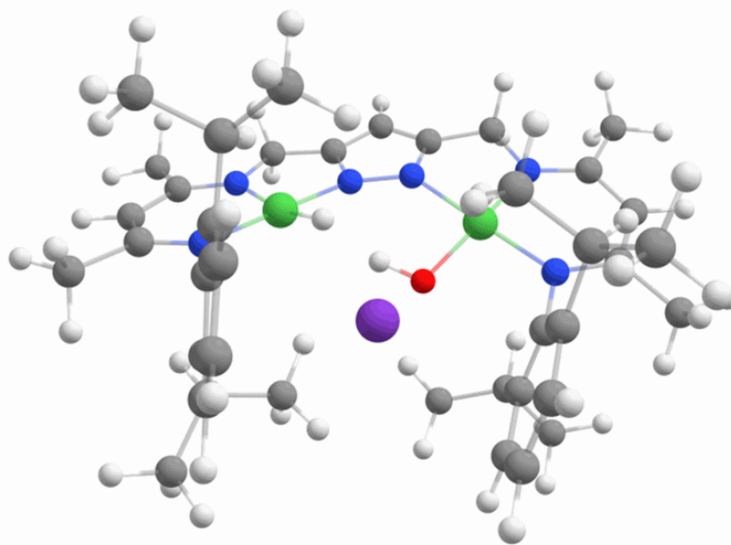


Figure C.22: DFT optimized molecular structure of **6** (Ni green, C grey, H white, K purple, N blue, O red).

Table C.7: XYZ-coordinates of **6**.

Atom	x	y	z	Atom	x	y	z
C	-0.37519	20.99977	22.51073	H	-8.10352	26.61527	28.57868
C	-1.46058	20.21623	23.00104	H	-8.65384	25.03742	27.92093
C	-1.36216	19.5245	24.2382	H	-5.89267	26.93374	28.78652
C	-0.16007	19.6196	24.9701	H	-2.63358	26.41516	29.11779
C	0.92644	20.36987	24.49192	H	-3.86496	27.71707	29.13299
C	0.81479	21.05454	23.26715	H	-2.62388	27.63615	27.8346
N	-2.65926	20.14418	22.23556	H	0.02516	26.84903	24.40894
C	-2.67516	19.26132	21.21494	H	1.54754	25.70489	26.03404
C	-1.47486	18.36118	20.98926	H	0.58535	24.32166	27.87882
C	-2.52639	18.69375	24.76026	H	-3.04837	24.23659	28.72848
C	-2.16949	17.19619	24.80412	H	-1.74415	23.02067	30.41628
C	-0.53959	21.79746	21.21867	H	-0.92548	24.58756	30.10619
C	0.77682	22.07133	20.48109	H	-0.26611	23.06728	29.42154
Ni	-4.08893	21.27498	22.75599	H	-1.50874	21.90932	27.41762
N	-5.2415	20.71069	21.38489	H	-3.09866	22.58866	26.88267
C	-4.98846	19.81579	20.42501	H	-2.94712	21.77414	28.4641
C	-3.76308	19.11747	20.33988	H	-3.68779	26.29189	24.4527
C	-6.56636	21.33887	21.39711	H	-3.0186	27.25826	22.27403

C	-6.66661	22.20366	22.60289	H	-2.05867	25.79459	22.62452
N	-5.49725	22.4561	23.24546	H	-1.32043	27.4251	22.79858
N	-5.76173	23.26171	24.31206	H	-3.56109	28.31764	25.85303
C	-7.10424	23.49818	24.34087	H	-3.77866	28.79552	24.14497
C	-7.72738	22.84694	23.26258	H	-2.16219	28.94381	24.91705
C	-7.60867	24.33343	25.46826	H	-7.37623	20.57359	21.40354
N	-6.45905	24.85001	26.2092	H	-6.72926	21.94932	20.47596
C	-6.6768	25.65649	27.24743	H	-6.96315	19.07974	19.85789
C	-5.61524	26.27398	27.95369	H	-5.67367	18.76512	18.65338
C	-4.24722	26.18415	27.64937	H	-6.3652	20.41031	18.83809
C	-3.29688	27.03261	28.47664	H	-3.66234	18.37674	19.53604
Ni	-4.76549	24.34643	25.48916	H	-0.55802	18.93997	20.75259
N	-3.75051	25.40447	26.6572	H	-1.6673	17.65968	20.15728
C	-2.34307	25.4403	26.46438	H	-1.23928	17.77506	21.90079
C	-1.80299	26.19189	25.3786	H	1.67337	21.63172	22.89175
C	-0.40254	26.26353	25.23726	H	1.86499	20.41675	25.06652
C	0.45533	25.61462	26.14266	H	-0.07372	19.08878	25.93108
C	-0.08968	24.8457	27.18553	H	-3.35613	18.8335	24.03813
C	-1.48531	24.7332	27.3586	H	-2.23858	19.13625	26.90615
C	-2.74494	26.88123	24.40374	H	-3.89681	18.61748	26.46736
C	-3.07602	28.31522	24.85748	H	-3.32556	20.26757	26.00674
C	-2.08233	23.79841	28.40736	H	-1.84338	16.82337	23.8115
C	-2.42412	22.44499	27.75319	H	-3.04778	16.59461	25.11736
C	-8.09332	25.96651	27.68409	H	-1.34875	16.9929	25.52462
C	-1.20444	23.61515	29.65144	H	-1.1834	21.19336	20.54737
C	-2.2497	26.83729	22.953	H	-2.23953	22.89901	22.06911
C	-6.04787	19.49978	19.38933	H	-1.61339	23.59639	20.53922
C	-3.02381	19.20907	26.12224	H	-0.68077	23.83589	22.03657
C	-1.3151	23.10411	21.4863	H	0.57542	22.54202	19.49758
K	-1.08561	23.13445	24.72995	H	1.34811	21.13752	20.30312
H	-8.79088	22.8391	23.00149	H	1.43288	22.76806	21.04487
H	-8.24359	25.16502	25.08161	O	-3.1341	21.76715	24.25818
H	-8.27602	23.72103	26.12177	H	-3.56565	24.08996	24.69287
H	-8.66054	26.47987	26.87785	H	-3.68609	22.46631	24.68244

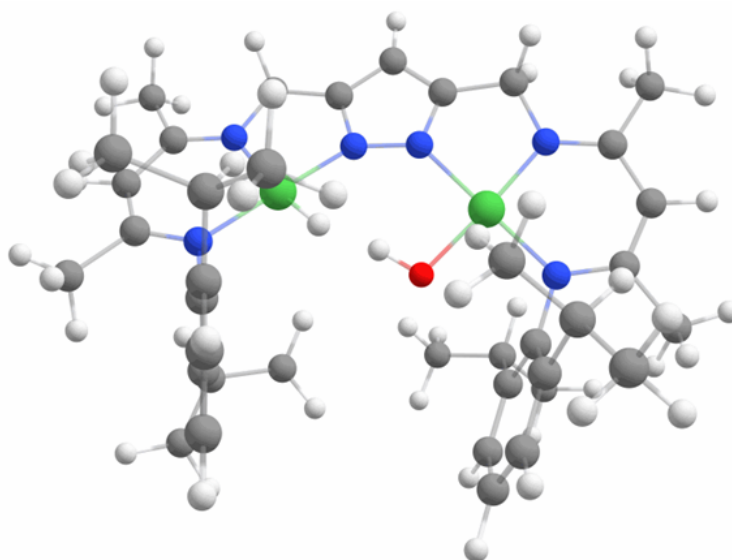


Figure C.23: DFT optimized molecular structure of the anion **6-K(crypt)** (Ni green, C grey, H white, K purple, N blue, O red).

Table C.8: XYZ-coordinates of **6-K(crypt)**.

Atom	x	y	z	Atom	x	y	z
C	-0.37519	20.99977	22.51073	H	-8.65384	25.03742	27.92093
C	-1.46058	20.21623	23.00104	H	-5.89267	26.93374	28.78652
C	-1.36216	19.5245	24.2382	H	-2.63358	26.41516	29.11779
C	-0.16007	19.6196	24.9701	H	-3.86496	27.71707	29.13299
C	0.92644	20.36987	24.49192	H	-2.62388	27.63615	27.8346
C	0.81479	21.05454	23.26715	H	0.02516	26.84903	24.40894
N	-2.65926	20.14418	22.23556	H	1.54754	25.70489	26.03404
C	-2.67516	19.26132	21.21494	H	0.58535	24.32166	27.87882
C	-1.47486	18.36118	20.98926	H	-3.04837	24.23659	28.72848
C	-2.52639	18.69375	24.76026	H	-1.74415	23.02067	30.41628
C	-2.16949	17.19619	24.80412	H	-0.92548	24.58756	30.10619
C	-0.53959	21.79746	21.21867	H	-0.26611	23.06728	29.42154
C	0.77682	22.07133	20.48109	H	-1.50874	21.90932	27.41762
Ni	-4.08893	21.27498	22.75599	H	-3.09866	22.58866	26.88267
N	-5.2415	20.71069	21.38489	H	-2.94712	21.77414	28.4641
C	-4.98846	19.81579	20.42501	H	-3.68779	26.29189	24.4527
C	-3.76308	19.11747	20.33988	H	-3.0186	27.25826	22.27403
C	-6.56636	21.33887	21.39711	H	-2.05867	25.79459	22.62452
C	-6.66661	22.20366	22.60289	H	-1.32043	27.4251	22.79858
N	-5.49725	22.4561	23.24546	H	-3.56109	28.31764	25.85303
N	-5.76173	23.26171	24.31206	H	-3.77866	28.79552	24.14497
C	-7.10424	23.49818	24.34087	H	-2.16219	28.94381	24.91705
C	-7.72738	22.84694	23.26258	H	-7.37623	20.57359	21.40354
C	-7.60867	24.33343	25.46826	H	-6.72926	21.94932	20.47596
N	-6.45905	24.85001	26.2092	H	-6.96315	19.07974	19.85789
C	-6.6768	25.65649	27.24743	H	-5.67367	18.76512	18.65338
C	-5.61524	26.27398	27.95369	H	-6.3652	20.41031	18.83809
C	-4.24722	26.18415	27.64937	H	-3.66234	18.37674	19.53604
C	-3.29688	27.03261	28.47664	H	-0.55802	18.93997	20.75259

C	-7.60867	24.33343	25.46826	H	-6.72926	21.94932	20.47596
N	-6.45905	24.85001	26.2092	H	-6.96315	19.07974	19.85789
C	-6.6768	25.65649	27.24743	H	-5.67367	18.76512	18.65338
C	-5.61524	26.27398	27.95369	H	-6.3652	20.41031	18.83809
C	-4.24722	26.18415	27.64937	H	-3.66234	18.37674	19.53604
C	-3.29688	27.03261	28.47664	H	-0.55802	18.93997	20.75259
Ni	-4.76549	24.34643	25.48916	H	-1.6673	17.65968	20.15728
N	-3.75051	25.40447	26.6572	H	-1.23928	17.77506	21.90079
C	-2.34307	25.4403	26.46438	H	1.67337	21.63172	22.89175
C	-1.80299	26.19189	25.3786	H	1.86499	20.41675	25.06652
C	-0.40254	26.26353	25.23726	H	-0.07372	19.08878	25.93108
C	0.45533	25.61462	26.14266	H	-3.35613	18.8335	24.03813
C	-0.08968	24.8457	27.18553	H	-2.23858	19.13625	26.90615
C	-1.48531	24.7332	27.3586	H	-3.89681	18.61748	26.46736
C	-2.74494	26.88123	24.40374	H	-3.32556	20.26757	26.00674
C	-3.07602	28.31522	24.85748	H	-1.84338	16.82337	23.8115
C	-2.08233	23.79841	28.40736	H	-3.04778	16.59461	25.11736
C	-2.42412	22.44499	27.75319	H	-1.34875	16.9929	25.52462
C	-8.09332	25.96651	27.68409	H	-1.1834	21.19336	20.54737
C	-1.20444	23.61515	29.65144	H	-2.23953	22.89901	22.06911
C	-2.2497	26.83729	22.953	H	-1.61339	23.59639	20.53922
C	-6.04787	19.49978	19.38933	H	-0.68077	23.83589	22.03657
C	-3.02381	19.20907	26.12224	H	0.57542	22.54202	19.49758
C	-1.3151	23.10411	21.4863	H	1.34811	21.13752	20.30312
H	-8.79088	22.8391	23.00149	H	1.43288	22.76806	21.04487
H	-8.24359	25.16502	25.08161	O	-3.1341	21.76715	24.25818
H	-8.27602	23.72103	26.12177	H	-3.56565	24.08996	24.69287
H	-8.66054	26.47987	26.87785	H	-3.68609	22.46631	24.68244
H	-8.10352	26.61527	28.57868				

C.3 Reaction Pathway Calculations for the Oxidative Addition of Water

To elucidate the mechanism of the oxidative addition of water at **6**, DFT calculations were performed in the group of Prof. MATA by ANTON RÖMER. The initial structures for optimization were derived from extensive constrained scans (on the singlet, broken-symmetry, and triplet PES) of the dinickel(I) complex **2^K** with the located potassium ion between the aryl rings and the water molecule placed in multiple different positions, using the BP86 functional with the basis set def2-SVP.^[277] The scans followed the increase of the distance between the hydrogen and oxygen atom of the incoming H₂O molecule, as an approximation to the reaction coordinate. The final energies and structures for the minima (**MIN1**, **MIN2**) were obtained via optimizations at the def2-TZVP basis set^[277] and the CPCM solvation model with default settings for THF.^[278] The final energies and structures for the first transition state (**TS1**) were obtained by employing the nudged elastic band method^[279] integrated in ORCA (using the keyword NEB-TS). The XYZ-coordinates of **MIN1**, **TS**, and **MIN2** are listed below:

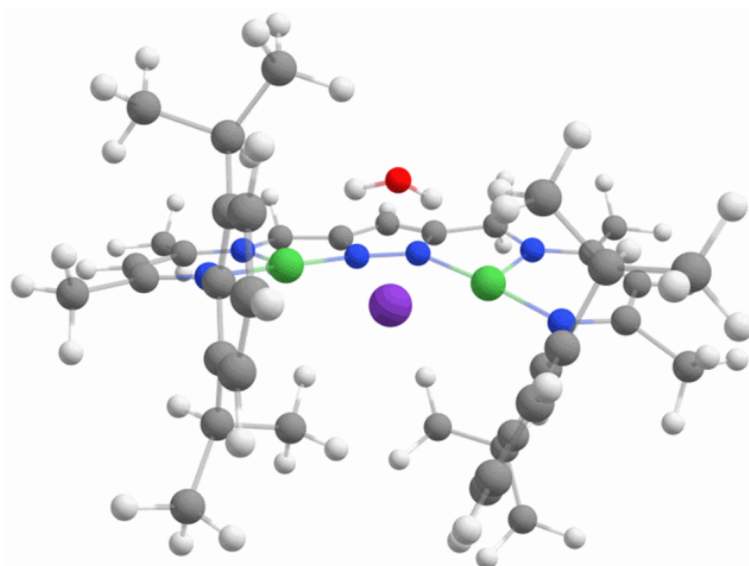


Figure C.24: DFT optimized molecular structure of **MIN1** with a H₂O molecule placed above the bimetallic cleft (Ni green, C grey, H white, K purple, N blue, O red).

Table C.9: XYZ-coordinates of **MIN1**.

Atom	x	y	z	Atom	x	y	z
C	-0.3077	21.1137	22.6485	C	-7.0879	23.3337	24.4879
C	-1.4528	20.3481	23.0368	C	-7.7253	22.6506	23.4362
C	-1.4934	19.7057	24.3176	C	-7.5967	24.2145	25.5881
C	-0.4362	19.9268	25.2205	N	-6.4542	24.7983	26.2828
C	0.6668	20.7286	24.8707	C	-6.6390	25.6076	27.3260
C	0.7283	21.2998	23.5874	C	-5.5560	26.2119	28.0192
N	-2.5724	20.2331	22.1772	C	-4.1869	26.1111	27.7110
C	-2.5826	19.3229	21.1739	C	-3.2010	26.8821	28.5674
C	-1.3736	18.4283	20.9939	Ni	-4.7608	24.2634	25.5969
C	-2.6990	18.8518	24.6902	N	-3.7151	25.3567	26.6902
C	-2.3129	17.5434	25.3972	C	-2.3422	25.4108	26.3540

C	-0.2252	21.7580	21.2655	C	-1.9148	26.2590	25.2820
C	1.1325	21.4995	20.5898	C	-0.5503	26.2606	24.9312
Ni	-4.0369	21.2577	22.6925	C	0.3832	25.4662	25.6198
N	-5.2642	20.6253	21.3890	C	-0.0468	24.6379	26.6724
C	-4.9739	19.7366	20.4373	C	-1.4016	24.5912	27.0540
C	-3.6906	19.1338	20.3275	C	-2.9378	27.1037	24.5333
C	-6.6214	21.1448	21.5309	C	-3.2690	28.4077	25.2865
C	-6.6753	22.0127	22.7530	C	-1.9048	23.6075	28.1050
N	-5.4903	22.2956	23.3682	C	-2.5020	22.3721	27.4050
N	-5.7421	23.1146	24.4325	C	-8.0458	25.9136	27.7981
C	-0.8500	23.2051	29.1418	H	-2.3600	29.0318	25.4178
C	-2.5465	27.4000	23.0801	H	-7.3704	20.3217	21.6154
C	-6.0459	19.3102	19.4551	H	-6.9250	21.7377	20.6333
C	-3.7120	19.6652	25.5187	H	-6.9036	18.8335	19.9769
C	-0.5397	23.2671	21.3127	H	-5.6535	18.5898	18.7136
H	-8.7951	22.6259	23.2013	H	-6.4582	20.1830	18.9057
H	-8.2631	25.0040	25.1656	H	-3.5692	18.3886	19.5293
H	-8.2358	23.6206	26.2856	H	-0.4464	19.0069	20.8066
H	-8.6457	26.3876	26.9916	H	-1.5215	17.7281	20.1515
H	-8.0397	26.5932	28.6698	H	-1.1853	17.8334	21.9130
H	-8.5828	24.9843	28.0860	H	1.6068	21.9032	23.3092
H	-5.8177	26.8511	28.8733	H	1.4838	20.8940	25.5892
H	-2.5549	26.1972	29.1571	H	-0.4656	19.4531	26.2140
H	-3.7298	27.5466	29.2753	H	-3.2018	18.5931	23.7359
H	-2.5149	27.4971	27.9504	H	-3.3111	19.9070	26.5226
H	-0.2105	26.8948	24.0992	H	-4.6589	19.1037	25.6490
H	1.4463	25.4901	25.3350	H	-3.9676	20.6173	24.9990
H	0.6875	24.0109	27.1998	H	-1.5784	16.9609	24.8046
H	-2.7445	24.0976	28.6369	H	-3.2121	16.9123	25.5500
H	-1.3083	22.5793	29.9344	H	-1.8714	17.7246	26.4000
H	-0.3948	24.0927	29.6260	H	-1.0149	21.2895	20.6452
H	-0.0311	22.6053	28.6906	H	-1.5798	23.4681	21.6369
H	-1.7158	21.7855	26.8822	H	-0.4344	23.7234	20.3071
H	-3.2870	22.6829	26.6717	H	0.1597	23.8109	21.9869
H	-2.9930	21.6926	28.1296	H	1.1210	21.8683	19.5444
H	-3.8713	26.4923	24.5340	H	1.3796	20.4186	20.5710
H	-3.3831	27.9161	22.5663	H	1.9613	22.0217	21.1124
H	-2.3363	26.4693	22.5193	O	-3.4698	24.3473	22.7422
H	-1.6647	28.0725	23.0160	H	-4.0892	24.6383	23.4659
H	-3.7059	28.2090	26.2822	H	-3.9137	23.4990	22.4611
H	-4.0108	29.0004	24.7120				

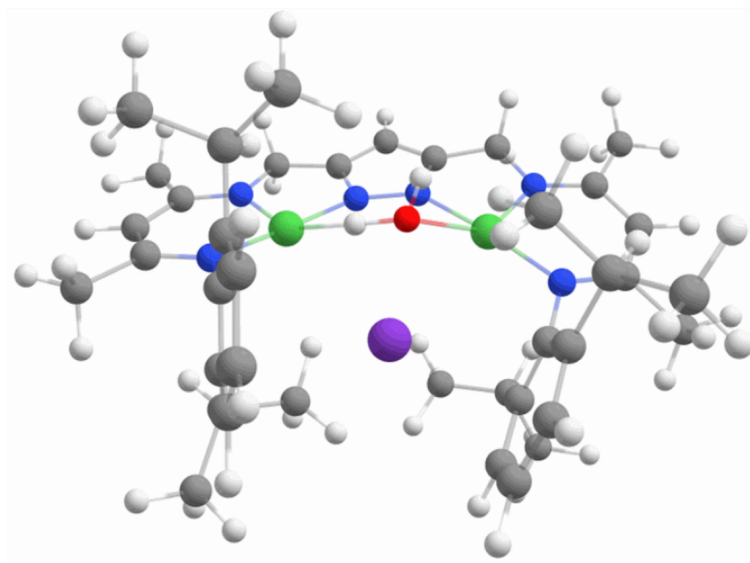


Figure C.25: DFT optimized molecular structure of TS (Ni green, C grey, H white, K purple, N blue, O red).

Table C.10: XYZ-coordinates of TS.

Atom	x	y	z	Atom	x	y	z
C	2.8325	-1.6981	-1.8781	C	4.3441	-1.2534	-3.8927
C	1.5520	-2.2794	-1.6317	Ni	-0.9945	-1.1753	-2.0489
C	1.3049	-2.9805	-0.4093	N	-2.2595	-2.0954	-3.1108
C	2.3604	-3.1379	0.5110	C	-1.9616	-2.8972	-4.1356
C	3.6344	-2.5984	0.2601	C	-0.6440	-3.3595	-4.3832
C	3.8530	-1.8689	-0.9212	C	-3.6667	-1.8231	-2.7892
N	0.5079	-2.1982	-2.5931	C	-3.7067	-1.0352	-1.5194
C	0.4807	-3.1363	-3.5692	N	-2.5248	-0.4758	-1.1445
C	1.6748	-4.0501	-3.7590	N	-2.6981	0.1865	0.0248
C	-0.0889	-3.4974	-0.0716	C	-4.0056	0.0499	0.3918
C	-0.0960	-5.0013	0.2394	C	-4.6912	-0.7256	-0.5654
C	3.0804	-0.8466	-3.1163	C	-4.4192	0.7177	1.6651
N	-3.3083	1.5371	2.1295	H	1.1944	-0.8347	3.4432
C	-3.4976	2.3959	3.1284	H	-0.3001	0.0341	2.8482
C	-2.4643	3.2660	3.5742	H	-0.1675	-0.5222	4.5442
C	-1.1467	3.3410	3.0927	H	-0.5526	2.9028	-0.3323
C	-0.2417	4.4053	3.6903	H	0.0496	3.9513	-2.5017
Ni	-1.6559	1.3126	1.1215	H	1.3272	2.7627	-2.0818
N	-0.6578	2.5409	2.1084	H	1.6286	4.5094	-1.8829
C	0.7313	2.5378	1.8796	H	-0.9019	4.9112	0.9941
C	1.2622	3.1151	0.6780	H	-1.0522	5.3374	-0.7334
C	2.6542	3.1031	0.4792	H	0.4382	5.7839	0.1665
C	3.5284	2.5693	1.4482	H	-4.2453	-2.7687	-2.6759
C	3.0016	2.0167	2.6320	H	-4.1589	-1.2602	-3.6191
C	1.6129	1.9776	2.8678	H	-3.7889	-4.0387	-4.4730
C	0.2862	3.6514	-0.3553	H	-2.6649	-4.0034	-5.8703
C	-0.3390	4.9998	0.0474	H	-3.6560	-2.5625	-5.4614
C	1.0208	1.2728	4.0914	H	-0.5172	-4.0599	-5.2195
C	0.4079	-0.0890	3.7009	H	2.6212	-3.4914	-3.8962

C	-4.8465	2.4895	3.8138	H	1.5257	-4.7099	-4.6331
C	2.0023	1.1259	5.2586	H	1.8212	-4.6894	-2.8627
C	0.8551	3.7187	-1.7757	H	4.8454	-1.4290	-1.1065
C	-3.0702	-3.4036	-5.0348	H	4.4525	-2.7444	0.9823
C	-0.7115	-2.6671	1.0690	H	2.1822	-3.6972	1.4438
C	3.1311	0.6408	-2.7191	H	-0.7204	-3.3272	-0.9678
H	-5.7468	-1.0179	-0.5622	H	-0.1349	-2.7704	2.0132
H	-5.3447	1.3158	1.4926	H	-1.7502	-2.9967	1.2711
H	-4.6967	-0.0492	2.4293	H	-0.7864	-1.5881	0.8075
H	-5.6439	2.7874	3.0990	H	0.3423	-5.5863	-0.5945
H	-4.8310	3.2267	4.6380	H	-1.1340	-5.3587	0.3976
H	-5.1530	1.5075	4.2337	H	0.4788	-5.2392	1.1595
H	-2.7347	3.9812	4.3635	H	2.2019	-0.9829	-3.7784
H	0.6018	3.9749	4.2690	H	2.2020	0.9239	-2.1882
H	-0.8158	5.0692	4.3626	H	3.2316	1.2953	-3.6082

C.3.1 Molecular Dynamics (MD) for **6** and **6-K(crypt)**

Molecular dynamics (MD) simulations were carried out to determine the NiH \cdots HO distance. These MD simulations consists of 5000 timesteps with 1.0 fs intervals at a virtual temperature of 250 K. To complete these simulations in a reasonable time-frame, the PBEh-3c functional was used. Figure C.26 and Figure C.28 show the evolution of the NiH \cdots HO distance for **6** and **6-K(crypt)**. Moreover, it was tried to simulate the solvation of **6** by THF by carrying out the same MD simulation of **6** with one explicit THF molecule, see Figure C.27.

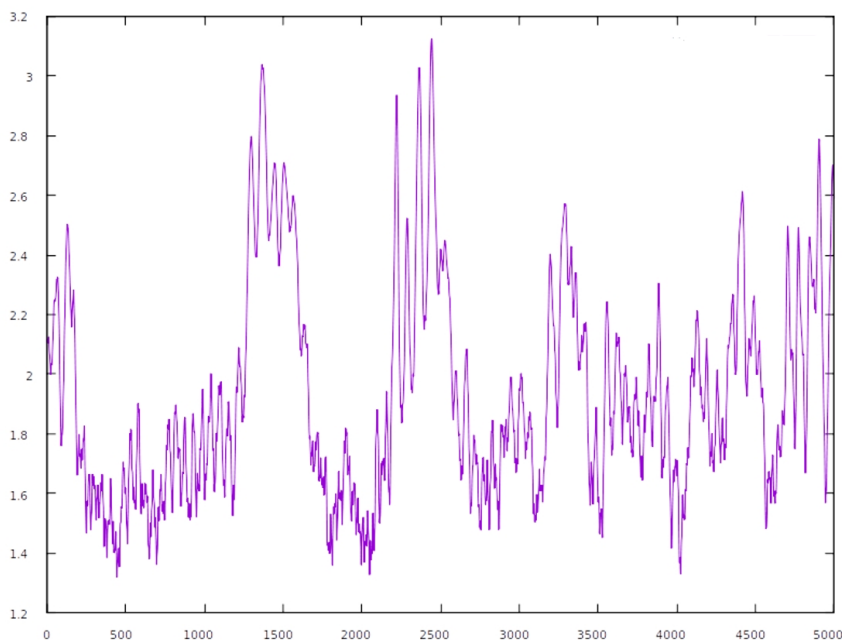


Figure C.26: Simulated evolution of the H \cdots H distance for **6**.

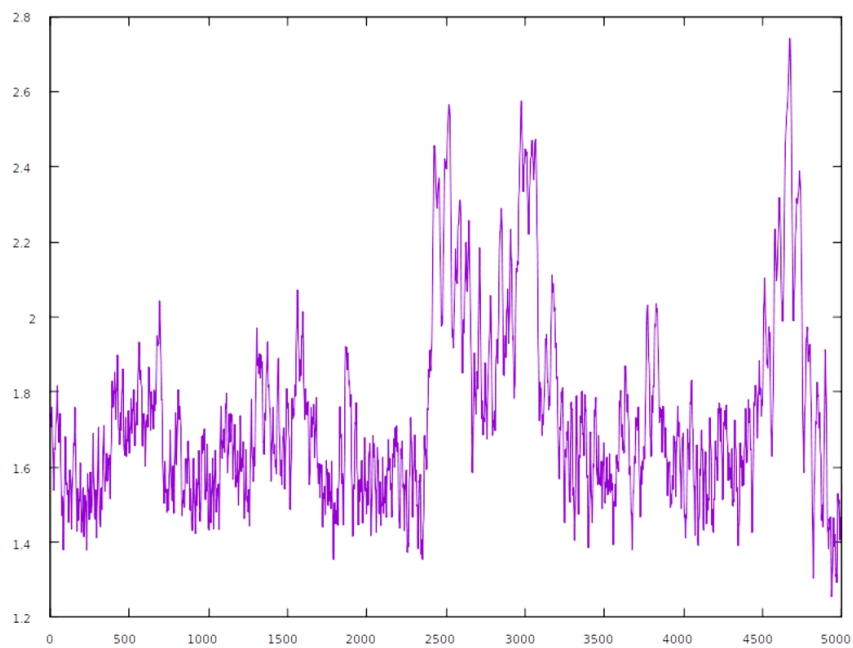


Figure C.27: Simulated evolution of the H...H distance for **6** and one THF molecule.

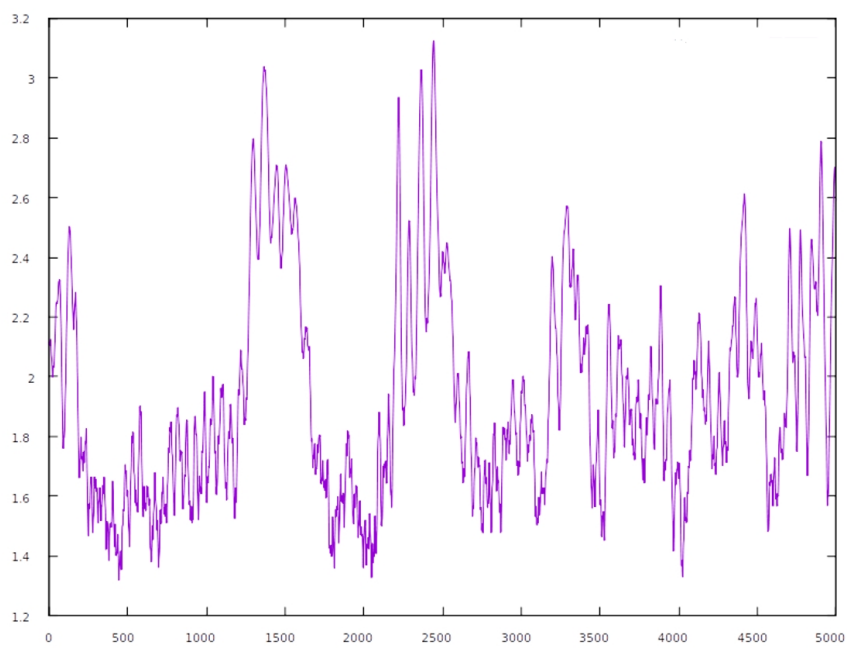


Figure C.28: Simulated evolution of the H...H distance for **6-K(crypt)**.

C.4 DFT Optimized Molecular Structures of 7 and 9

C.4.1 DFT Optimized Molecular Structures of 7

Topological analysis of the electron densities and energy decomposition analyses computed from PBE0-D3(BJ)/ 6-311++G(2d,2p)^[213,214] wavefunctions obtained at the PBEh-3c molecular structures of 7 and 9 were done to obtain further insight into the bonding and electronic structure of the complexes 7 and 9 listed in the following:

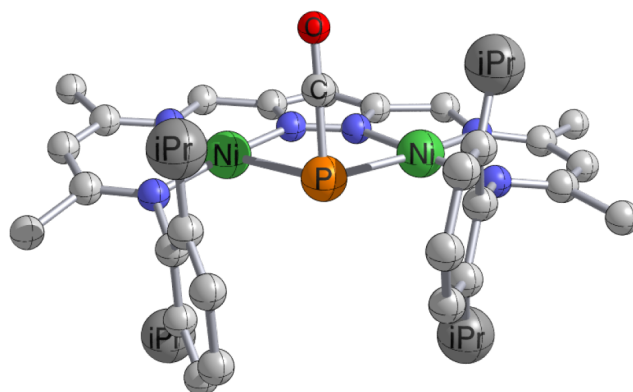


Figure C.29: DFT optimized molecular structures of 7 at the PBEh-3c level of theory.

Table C.11: Selected structural parameters for 7 computed at the PBEh-3c level of theory; XRD parameters are given for comparison.

		Bond length / Å		
Method	Ni1–P1	Ni2–P1	P1–C40	
PBEh-3c	2.403	2.390	1.665	
XRD	2.3354(11)	2.3366(11)	1.671(5)	
		Angle / °		
Method	Ni1–P1–Ni2	Ni1–P1–C40	Ni2–P1–C40	
PBEh-3c	104.4	81.6	86.4	
XRD	106.82(4)	80.85(14)	81.50(14)	

C.4.2 DFT Optimized Molecular Structures of 9

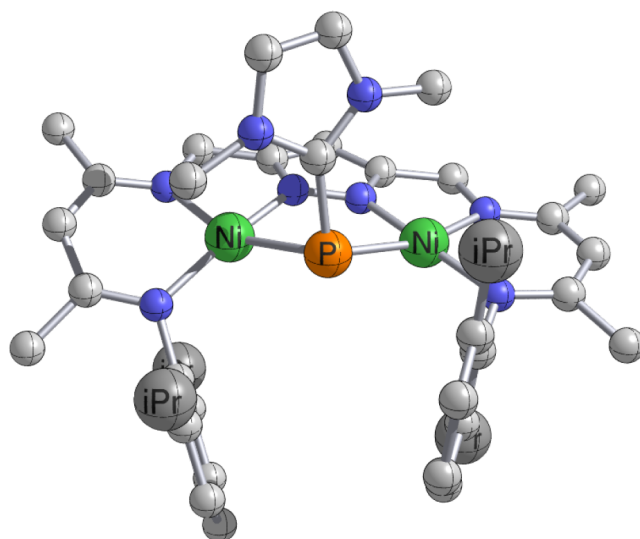


Figure C.30: DFT optimized molecular structures of **9** at the PBEh-3c level of theory.

Table C.12: Selected structural parameters for **9** computed at the PBEh-3c level of theory; XRD parameters are given for comparison.

		Bond length / Å		
Method	Ni1–P1	Ni2–P1	P1–C41	
PBEh-3c	2.403	2.390	1.665	
XRD	2.2949(6)	2.2714(5)	1.841(2)	
		Angle / °		
Method	Ni1–P1–Ni2	Ni1–P1–C41	Ni2–P–C41	
PBEh-3c	104.4	81.6	86.4	
XRD	105.87(3)	93.84(9)	98.58(8)	

Bibliography

- [1] M. Henckens, E. Worrell, *J. Clean. Prod.* **2020**, *264*, 121460.
- [2] M. J. Maroney, S. Ciurli, *Chem. Rev.* **2014**, *114*, 4206–4228.
- [3] Y. Li, D. B. Zamble, *Chem. Rev.* **2009**, *109*, 4617–4643.
- [4] B. T. Muysen, K. V. Brix, D. K. DeForest, C. R. Janssen, *Environ. Rev.* **2004**, *12*, 113–131.
- [5] S. B. Mulrooney, R. P. Hausinger, *FEMS Microbiol. Rev.* **2003**, *27*, 239–261.
- [6] H. Chen, N. C. Giri, R. Zhang, K. Yamane, Y. Zhang, M. Maroney, M. Costa, *J. Biol. Chem.* **2010**, *285*, 7374–7383.
- [7] N. C. Giri, L. Passantino, H. Sun, M. A. Zoroddu, M. Costa, M. J. Maroney, *Biochemistry* **2013**, *52*, 4168–4183.
- [8] N. C. Giri, H. Sun, H. Chen, M. Costa, M. J. Maroney, *Biochemistry* **2011**, *50*, 5067–5076.
- [9] F. Torres, M. das Graças, M. Melo, A. Tosti, *Clin. Cosmet. Investig. Dermatology* **2009**, *2*, 39–48.
- [10] R. K. Thauer, G. Diekert, P. Schönheit, *Trends Biochem. Sci.* **1980**, *5*, 304–306.
- [11] W. Mertz, *Science* **1981**, *213*, 1332–1338.
- [12] C. T. Walsh, W. H. Orme-Johnson, *Biochemistry* **1987**, *26*, 4901–4906.
- [13] H. S. Shafaat, O. Rüdiger, H. Ogata, W. Lubitz, *Biochim. Biophys. Acta* **2013**, *1827*, 986–1002.
- [14] M. Can, F. A. Armstrong, S. W. Ragsdale, *Chem. Rev.* **2014**, *114*, 4149–4174.
- [15] R. Sarangi, M. Dey, S. W. Ragsdale, *Biochemistry* **2009**, *48*, 3146–3156.
- [16] N. E. Dixon, T. C. Gazzola, R. L. Blakeley, B. Zermer, *J. Am. Chem. Soc.* **1975**, *97*, 4131–4133.
- [17] P. E. M. Siegbahn, S.-L. Chen, R.-Z. Liao, *Inorganics* **2019**, *7*, 95.
- [18] J. C. Fontecilla-Camps, P. Amara, C. Cavazza, Y. Nicolet, A. Volbeda, *Nature* **2009**, *460*, 814–822.
- [19] K. O. Konhauser, L. J. Robbins, E. Pecoits, C. Peacock, A. Kappler, S. V. Lalonde, *Astrobiology* **2015**, *15*, 804–815.
- [20] U. Ermler, W. Grabarse, S. Shima, M. Goubeaud, R. K. Thauer, *Science* **1997**, *278*, 1457–1462.
- [21] A. Volbeda, M. H. Charon, C. Piras, E. C. Hatchikian, M. Frey, J. C. Fontecilla-Camps, *Nature* **1995**, *373*, 580–587.
- [22] T. I. Doukov, T. M. Iverson, J. Seravalli, S. W. Ragsdale, C. L. Drennan, *Science* **2002**, *298*, 567–572.
- [23] J.-H. Jeoung, H. Dobbek, *Science* **2007**, *318*, 1461–1464.

- [24] B. Desguin, T. Zhang, P. Soumillion, P. Hols, J. Hu, R. P. Hausinger, *Science* **2015**, *349*, 66–69.
- [25] M. M. He, S. L. Clugston, J. F. Honek, B. W. Matthews, *Biochemistry* **2000**, *39*, 8719–8727.
- [26] J.-H. Jeoung, D. Nianios, S. Fetzner, H. Dobbek, *Angew. Chem. Int. Ed.* **2016**, *55*, 3281–3284.
- [27] T. C. Pochapsky, S. S. Pochapsky, T. Ju, C. Hoefler, J. Liang, *J. Biomol. NMR* **2006**, *34*, 117–127.
- [28] M. Alfano, C. Cavazza, *Protein Sci.* **2020**, *29*, 1071–1089.
- [29] S. W. Ragsdale, *J. Biol. Chem.* **2009**, *284*, 18571–18575.
- [30] S. Yao, M. Driess, *Acc. Chem. Res.* **2012**, *45*, 276–287.
- [31] P. Zimmermann, C. Limberg, *J. Am. Chem. Soc.* **2017**, *139*, 4233–4242.
- [32] C. A. Laskowski, D. J. Bungum, S. M. Baldwin, S. A. Del Ciello, V. M. Iluc, G. L. Hillhouse, *J. Am. Chem. Soc.* **2013**, *135*, 18272–18275.
- [33] K. Zhang, M. Conda-Sheridan, S. Cooke, J. Louie, *Organometallics* **2011**, *30*, 2546–2552.
- [34] M. M. Schwab, D. Himmel, S. Kacprzak, D. Kratzert, V. Radtke, P. Weis, K. Ray, E.-W. Scheidt, W. Scherer, B. de Bruin, S. Weber, I. Krossing, *Angew. Chem. Int. Ed.* **2015**, *127*, 14919–14922.
- [35] C. A. Rettenmeier, H. Wadepohl, L. H. Gade, *Chem. Sci.* **2016**, *7*, 3533–3542.
- [36] M. J. Ingleson, B. C. Fullmer, D. T. Buschhorn, H. Fan, M. Pink, J. C. Huffman, K. G. Caulton, *Inorg. Chem.* **2008**, *47*, 407–409.
- [37] F. Schneck, J. Ahrens, M. Finger, A. C. Stückl, C. Würtele, D. Schwarzer, S. Schneider, *Nat. Commun.* **2018**, *9*, 1161.
- [38] C. Yoo, Y. Lee, *Angew. Chem. Int. Ed.* **2017**, *56*, 9502–9506.
- [39] P. S. Adam, G. Borrel, S. Gribaldo, *Proc. Natl. Acad. Sci. U.S.A.* **2018**, *115*, E1166–E1173.
- [40] A. C. Manesis, M. J. O'Connor, C. R. Schneider, H. S. Shafaat, *J. Am. Chem. Soc.* **2017**, *139*, 10328–10338.
- [41] D. Forster, *Adv. Organomet. Chem.*, *17*, 255–267.
- [42] T. I. Doukov, L. C. Blasiak, J. Seravalli, S. W. Ragsdale, C. L. Drennan, *Biochemistry* **2008**, *47*, 3474–3483.
- [43] S. W. Ragsdale, *Chem. Rev.* **2006**, *106*, 3317–3337.
- [44] G. Bender, S. W. Ragsdale, *Biochemistry* **2011**, *50*, 276–286.
- [45] B. Horn, C. Limberg, C. Herwig, S. Mebs, *Angew. Chem. Int. Ed.* **2011**, *50*, 12621–12625.
- [46] X. Tan, I. V. Surovtsev, P. A. Lindahl, *J. Am. Chem. Soc.* **2006**, *128*, 12331–12338.
- [47] C. D. James, S. Wiley, S. W. Ragsdale, B. M. Hoffman, *J. Am. Chem. Soc.* **2020**, *142*, 15362–15370.
- [48] X. Tan, C. Sewell, Q. Yang, P. A. Lindahl, *J. Am. Chem. Soc.* **2003**, *125*, 318–319.
- [49] A. C. Manesis, H. S. Shafaat, *Inorg. Chem.* **2015**, *54*, 7959–7967.
- [50] A. C. Manesis, B. W. Musselman, B. C. Keegan, J. Shearer, N. Lehnert, H. S. Shafaat, *Inorg. Chem.* **2019**, *58*, 8969–8982.

- [51] M. I. Lipschutz, X. Yang, R. Chatterjee, T. D. Tilley, *J. Am. Chem. Soc.* **2013**, *135*, 15298–15301.
- [52] E. L. Hegg, *Acc. Chem. Res.* **2004**, *37*, 775–783.
- [53] P. A. Lindahl, *Biochemistry* **2002**, *41*, 2097–2105.
- [54] P. A. Lindahl, *J. Biol. Inorg. Chem.* **2004**, *9*, 516–524.
- [55] S. E. Cohen, M. Can, E. C. Wittenborn, R. A. Hendrickson, S. W. Ragsdale, C. L. Drennan, *ACS Catal.* **2020**, *10*, 9741–9746.
- [56] S. Scheller, M. Goenrich, R. Boecher, R. K. Thauer, B. Jaun, *Nature* **2010**, *465*, 606–608.
- [57] M. Krüger, A. Meyerdierks, F. O. Glöckner, R. Amann, F. Widdel, M. Kube, R. Reinhardt, J. Kahnt, R. Böcher, R. K. Thauer, S. Shima, *Nature* **2003**, *426*, 878–881.
- [58] R. K. Thauer, *Biochemistry* **2019**, *58*, 5198–5220.
- [59] B. C. McBride, R. S. Wolfe, *Biochemistry* **1971**, *10*, 2317–2324.
- [60] M. Goubeaud, G. Schreiner, R. K. Thauer, *FEBS J.* **1997**, *243*, 110–114.
- [61] S. Rospert, R. Böcher, S. Albracht, R. K. Thauer, *FEBS Lett.* **1991**, *291*, 371–375.
- [62] M. Goenrich, E. C. Duin, F. Mahlert, R. K. Thauer, *J. Biol. Inorg. Chem.* **2005**, *10*, 333–342.
- [63] S. Scheller, M. Goenrich, R. K. Thauer, B. Jaun, *J. Am. Chem. Soc.* **2013**, *135*, 14975–14984.
- [64] S. G. McGeachin, *Can. J. Chem.* **1968**, *46*, 1903–1912.
- [65] J. E. Parks, R. H. Holm, *Inorg. Chem.* **1968**, *7*, 1408–1416.
- [66] D. J. Mindiola, *Angew. Chem. Int. Ed.* **2009**, *48*, 6198–6200.
- [67] Y.-C. Tsai, *Coord. Chem. Rev.* **2012**, *256*, 722–758.
- [68] L. Bourget-Merle, M. F. Lappert, J. R. Severn, *Chem. Rev.* **2002**, *102*, 3031–3066.
- [69] J. Spielmann, S. Harder, *Dalton Trans.* **2011**, *40*, 8314–8319.
- [70] S. P. Sarish, S. Nembenna, S. Nagendran, H. W. Roesky, *Acc. Chem. Res.* **2011**, *44*, 157–170.
- [71] S. E. Baillie, V. L. Blair, T. D. Bradley, W. Clegg, J. Cowan, R. W. Harrington, A. Hernán-Gómez, A. R. Kennedy, Z. Livingstone, E. Hevia, *Chem. Sci* **2013**, *4*, 1895.
- [72] D. J. Liptrot, M. S. Hill, M. F. Mahon, D. J. MacDougall, *Chem. Eur. J.* **2010**, *16*, 8508–8515.
- [73] J. Huang, X. Zheng, I. Del Rosal, B. Zhao, L. Maron, X. Xu, *Inorg. Chem.* **2020**, *59*, 13473–13480.
- [74] A. Koner, B. M. Gabidullin, Z. Kelemen, L. Nyulászi, G. I. Nikonov, R. Streubel, *Dalton Trans.* **2019**, *48*, 8248–8253.
- [75] W. D. Woodul, E. Carter, R. Müller, A. F. Richards, A. Stasch, M. Kaupp, D. M. Murphy, M. Driess, C. Jones, *J. Am. Chem. Soc.* **2011**, *133*, 10074–10077.
- [76] S. M. Bellows, T. R. Cundari, P. L. Holland, *Organometallics* **2013**, *32*, 4741–4751.
- [77] C. Chen, T. R. Dugan, W. W. Brennessel, D. J. Weix, P. L. Holland, *J. Am. Chem. Soc.* **2014**, *136*, 945–955.

- [78] K. P. Chiang, S. M. Bellows, W. W. Brennessel, P. L. Holland, *Chem. Sci.* **2014**, *5*, 267–274.
- [79] C. Panda, A. Chandra, T. Corona, E. Andris, B. Pandey, S. Garai, N. Lindenmaier, S. Künstner, E. R. Farquhar, J. Roithová, G. Rajaraman, M. Driess, K. Ray, *Angew. Chem. Int. Ed.* **2018**, *57*, 14883–14887.
- [80] W. R. Buratto, R. B. Ferreira, V. J. Catalano, R. García-Serres, L. J. Murray, *Dalton Trans.* **2021**, *50*, 816–821.
- [81] K. R. D. Johnson, P. G. Hayes, *Chem. Soc. Rev.* **2013**, *42*, 1947–1960.
- [82] O. A. Mironova, A. A. Ryadun, T. S. Sukhikh, S. N. Konchenko, N. A. Pushkarevsky, *New J. Chem.* **2020**, *44*, 19769–19779.
- [83] M. B. Jones, A. J. Gaunt, *Chem. Rev.* **2013**, *113*, 1137–1198.
- [84] R. J. Wright, P. P. Power, B. L. Scott, J. L. Kiplinger, *Organometallics* **2004**, *23*, 4801–4803.
- [85] M. J. Monreal, R. J. Wright, D. E. Morris, B. L. Scott, J. T. Golden, P. P. Power, J. L. Kiplinger, *Organometallics* **2013**, *32*, 1423–1434.
- [86] C. Camp, J. Arnold, *Dalton Trans.* **2016**, *45*, 14462–14498.
- [87] D. W. Randall, S. D. George, P. L. Holland, B. Hedman, K. O. Hodgson, W. B. Tolman, E. I. Solomon, *J. Am. Chem. Soc.* **2000**, *122*, 11632–11648.
- [88] J. R. Khusnutdinova, D. Milstein, *Angew. Chem. Int. Ed.* **2015**, *54*, 12236–12273.
- [89] D. G. A. Verhoeven, M.-E. Moret, *Dalton Trans.* **2016**, *45*, 15762–15778.
- [90] P. A. Dub, J. C. Gordon, *ACS Catal.* **2017**, *7*, 6635–6655.
- [91] S. W. Kohl, L. Weiner, L. Schwartsburd, L. Konstantinovski, L. J. W. Shimon, Y. Ben-David, M. A. Iron, D. Milstein, *Science* **2009**, *324*, 74–77.
- [92] J. Li, Y. Shiota, K. Yoshizawa, *J. Am. Chem. Soc.* **2009**, *131*, 13584–13585.
- [93] G. Bai, P. Wei, A. Das, D. W. Stephan, *Organometallics* **2006**, *25*, 5870–5878.
- [94] C. Camp, L. Maron, R. G. Bergman, J. Arnold, *J. Am. Chem. Soc.* **2014**, *136*, 17652–17661.
- [95] S. Pfirrmann, S. Yao, B. Ziemer, R. Stösser, M. Driess, C. Limberg, *Organometallics* **2009**, *28*, 6855–6860.
- [96] T. R. Dugan, P. L. Holland, *J. Organomet. Chem.* **2009**, *694*, 2825–2830.
- [97] S. Yao, Y. Xiong, M. Vogt, H. Grützmacher, C. Herwig, C. Limberg, M. Driess, *Angew. Chem. Int. Ed.* **2009**, *48*, 8107–8110.
- [98] P. Holze, T. Corona, N. Frank, B. Braun-Cula, C. Herwig, A. Company, C. Limberg, *Angew. Chem. Int. Ed.* **2017**, *56*, 2307–2311.
- [99] D. E. DeRosha, B. Q. Mercado, G. Lukat-Rodgers, K. R. Rodgers, P. L. Holland, *Angew. Chem. Int. Ed.* **2017**, *56*, 3211–3215.
- [100] S. Yao, E. Bill, C. Milsman, K. Wieghardt, M. Driess, *Angew. Chem. Int. Ed.* **2008**, *120*, 7110–7113.
- [101] S. Pfirrmann, C. Limberg, C. Herwig, R. Stösser, B. Ziemer, *Angew. Chem. Int. Ed.* **2009**, *48*, 3357–3361.
- [102] K. C. MacLeod, D. J. Vinyard, P. L. Holland, *J. Am. Chem. Soc.* **2014**, *136*, 10226–10229.

- [103] Q. Wang, S. H. Brooks, T. Liu, N. C. Tomson, *Chem. Commun.* **2021**, 57, 2839–2853.
- [104] B. E. Barton, C. M. Whaley, T. B. Rauchfuss, D. L. Gray, *J. Am. Chem. Soc.* **2009**, 131, 6942–6943.
- [105] S. Canaguier, V. Fourmond, C. U. Perotto, J. Fize, J. Pécaut, M. Fontecave, M. J. Field, V. Artero, *Chem. Commun.* **2013**, 49, 5004–5006.
- [106] A. K. Jones, E. Sillery, S. P. J. Albracht, F. A. Armstrong, *Chem. Rev.* **2002**, 866–867.
- [107] D. Brazzolotto, L. Wang, H. Tang, M. Gennari, N. Queyriaux, C. Philouze, S. Demeshko, F. Meyer, M. Orio, V. Artero, M. B. Hall, C. Duboc, *ACS Catal.* **2018**, 8, 10658–10667.
- [108] J. T. Kleinhaus, F. Wittkamp, S. Yadav, D. Siegmund, U.-P. Apfel, *Chem. Soc. Rev.* **2021**, 50, 1668–1784.
- [109] K. Weber, T. Krämer, H. S. Shafaat, T. Weyhermüller, E. Bill, M. van Gastel, F. Neese, W. Lubitz, *J. Am. Chem. Soc.* **2012**, 134, 20745–20755.
- [110] H. Gehring, R. Metzinger, C. Herwig, J. Intemann, S. Harder, C. Limberg, *Chem. Eur. J.* **2013**, 19, 1629–1636.
- [111] D. F.-J. Piesik, R. Stadler, S. Range, S. Harder, *Eur. J. Inorg. Chem.* **2009**, 2009, 3569–3576.
- [112] D. V. Vitanova, F. Hampel, K. C. Hultsch, *Dalton Trans.* **2005**, 1565–1566.
- [113] D.-H. Manz, P.-C. Duan, S. Dechert, S. Demeshko, R. Oswald, M. John, R. A. Mata, F. Meyer, *J. Am. Chem. Soc.* **2017**, 139, 16720–16731.
- [114] P.-C. Duan, D.-H. Manz, S. Dechert, S. Demeshko, F. Meyer, *J. Am. Chem. Soc.* **2018**, 140, 4929–4939.
- [115] T. Kothe, U.-H. Kim, S. Dechert, F. Meyer, *Inorg. Chem.* **2020**, 59, 14207–14217.
- [116] T. R. Dugan, E. Bill, K. C. MacLeod, W. W. Brennessel, P. L. Holland, *Inorg. Chem.* **2014**, 53, 2370–2380.
- [117] S. Pfirrmann, C. Limberg, B. Ziemer, *Dalton Trans.* **2008**, 6689–6691.
- [118] D. H. Manz, *Preorganized Bimetallic Nickel Complexes of Pyrazolate-Bridged Ligands for Cooperative Substrate Transformation*, Dissertation, Göttingen, **2016**.
- [119] E. Ferretti, S. Dechert, F. Meyer, *Inorg. Chem.* **2019**, 58, 5154–5162.
- [120] E. Ferretti, S. Dechert, S. Demeshko, M. C. Holthausen, F. Meyer, *Angew. Chem. Int. Ed.* **2019**, 58, 1705–1709.
- [121] Thomas Kothe, *Reductive Binding of C-O and Nitro Substrates at a Pyrazolate-Bridged Preorganized Dinickel Scaffold*, Dissertation, Göttingen, **2020**.
- [122] S. Dillinger, J. Mohrbach, J. Hewer, M. Gaffga, G. Niedner-Schatteburg, *Phys. Chem. Chem. Phys.* **2015**, 17, 10358–10362.
- [123] M. Ghosh, H. H. Cramer, S. Dechert, S. Demeshko, M. John, M. M. Hansmann, S. Ye, F. Meyer, *Angew. Chem. Int. Ed.* **2019**, 131, 14487–14494.
- [124] D. Ajo, A. Bencini, F. Mani, *Inorg. Chem.* **1988**, 27, 2437–2444.
- [125] F. Neese, *J. Phys. Chem. Solids* **2004**, 65, 781–785.
- [126] P. C. Duan, *A Dinuclear Dihydride Complex for Bimetallic Reductive Activation and Transformation of a Range of Inert Substrates*, Dissertation, Göttingen, **2017**.

- [127] R. R. Fraser, T. S. Mansour, S. Savard, *J. Org. Chem.* **1985**, *50*, 3232–3234.
- [128] R. Tyburski, T. Liu, S. D. Glover, L. Hammarström, *J. Am. Chem. Soc.* **2021**, *143*, 560–576.
- [129] J. Stubbe, D. G. Nocera, C. S. Yee, M. C. Y. Chang, *Chem. Rev.* **2003**, *103*, 2167–2201.
- [130] H. Land, M. Senger, G. Berggren, S. T. Stripp, *ACS Catal.* **2020**, *10*, 7069–7086.
- [131] H. E. Bryndza, W. Tam, *Chem. Rev.* **1988**, *88*, 1163–1188.
- [132] V. Balzani, L. Moggi, M. F. Manfrin, F. Bolletta, M. Gleria, *Science* **1975**, *189*, 852–856.
- [133] A. K. Chandra, T. Uchimaru, *J. Phys. Chem. A* **2000**, *104*, 9244–9249.
- [134] W. E. Piers, *Organometallics* **2011**, *30*, 13–16.
- [135] N. S. Lewis, D. G. Nocera, *Proc. Natl. Acad. Sci. U.S.A.* **2006**, *103*, 15729–15735.
- [136] L. Watson, O. Eisenstein, *J. Chem. Educ.* **2002**, *79*, 1269.
- [137] G. L. Hillhouse, J. E. Bercaw, *J. Am. Chem. Soc.* **1984**, *106*, 5472–5478.
- [138] O. V. Ozerov, *Chem. Soc. Rev.* **2009**, *38*, 83–88.
- [139] D. V. Gutsulyak, W. E. Piers, J. Borau-Garcia, M. Parvez, *J. Am. Chem. Soc.* **2013**, *135*, 11776–11779.
- [140] M.-C. Chang, K. A. Jesse, A. S. Filatov, J. S. Anderson, *Chem. Sci.* **2019**, *10*, 1360–1367.
- [141] E. G. Bryan, B. F. G. Johnson, J. Lewis, *Dalton Trans.* **1977**, 1328–1330.
- [142] C. M. Fafard, D. Adhikari, B. M. Foxman, D. J. Mindiola, O. V. Ozerov, *J. Am. Chem. Soc.* **2007**, *129*, 10318–10319.
- [143] T. Yoshida, T. Matsuda, T. Okano, T. Kitani, S. Otsuka, *J. Am. Chem. Soc.* **1979**, *101*, 2027–2038.
- [144] M. J. Burn, M. G. Fickes, J. F. Hartwig, F. J. Hollander, R. G. Bergman, *J. Am. Chem. Soc.* **1993**, *115*, 5875–5876.
- [145] T. Yoshida, T. Okano, Y. Ueda, S. Otsuka, *J. Am. Chem. Soc.* **1981**, *103*, 3411–3422.
- [146] D. Morales-Morales, D. W. Lee, Z. Wang, C. M. Jensen, *Organometallics* **2001**, *20*, 1144–1147.
- [147] D. Milstein, J. C. Calabrese, I. D. Williams, *J. Am. Chem. Soc.* **1986**, *108*, 6387–6389.
- [148] A. V. Protchenko, J. I. Bates, L. M. A. Saleh, M. P. Blake, A. D. Schwarz, E. L. Kolychev, A. L. Thompson, C. Jones, P. Mountford, S. Aldridge, *J. Am. Chem. Soc.* **2016**, *138*, 4555–4564.
- [149] A. Seifert, D. Scheid, G. Linti, T. Zessin, *Chem. Eur. J.* **2009**, *15*, 12114–12120.
- [150] E. Arunan, G. R. Desiraju, R. A. Klein, J. Sadlej, S. Scheiner, I. Alkorta, D. C. Clary, R. H. Crabtree, J. J. Dannenberg, P. Hobza, H. G. Kjaergaard, A. C. Legon, B. Mennucci, D. J. Nesbitt, *Pure Appl. Chem.* **2011**, *83*, 1637–1641.
- [151] J. A. Gerlt, M. M. Kreevoy, W. W. Cleland, P. A. Frey, *Chem. Biol.* **1997**, *4*, 259–267.
- [152] P. Yakovchuk, E. Protozanova, M. D. Frank-Kamenetskii, *Nucleic Acids Res. Spec. Publ.* **2006**, *34*, 564–574.

- [153] N. V. Belkova, L. M. Epstein, O. A. Filippov, E. S. Shubina, *Chem. Rev.* **2016**, *116*, 8545–8587.
- [154] M. P. Brown, R. W. Heseltine, P. A. Smith, P. J. Walker, *J. Chem. Soc. A* **1970**, 410.
- [155] M. P. Brown, R. W. Heseltine, *Chem. Commun.* **1968**, 1551.
- [156] N. V. Belkova, E. S. Shubina, L. M. Epstein, *Acc. Chem. Res.* **2005**, *38*, 624–631.
- [157] J. Echeverría, *Cryst. Growth Des.* **2017**, *17*, 2097–2103.
- [158] Y. Feng, S.-W. Zhao, L. Liu, J.-T. Wang, X.-S. Li, Q.-X. Guo, *J. Phys. Org. Chem.* **2004**, *17*, 1099–1106.
- [159] Y. Yang, W. Zhang, *J. Mol. Struct. THEOCHEM* **2007**, *814*, 113–117.
- [160] P. Hobza, Z. Havlas, *Chem. Rev.* **2000**, *100*, 4253–4264.
- [161] M. Solimannejad, S. Scheiner, *J. Phys. Chem. A* **2005**, *109*, 11933–11935.
- [162] M. Solimannejad, A. Boutalib, *Chem. Phys.* **2006**, *320*, 275–280.
- [163] S. A. McDowell, T. S. Forde, *J. Mol. Struct.* **2003**, *624*, 109–114.
- [164] L. M. Epstein, E. S. Shubina, *Coord. Chem. Rev.* **2002**, *231*, 165–181.
- [165] G. A. Jeffrey, *An introduction to hydrogen bonding*, Oxford Univ. Press, New York, **1997**.
- [166] E. S. Shubina, N. V. Belkova, A. N. Krylov, E. V. Vorontsov, L. M. Epstein, D. G. Gusev, M. Niedermann, H. Berke, *J. Am. Chem. Soc.* **1996**, *118*, 1105–1112.
- [167] V. I. Bakhmutov, *Dihydrogen bonds: Principles, experiments, and applications*, Wiley-Interscience, Hoboken, N.J., **2008**.
- [168] S. Gründemann, S. Ulrich, H.-H. Limbach, N. S. Golubev, G. S. Denisov, L. M. Epstein, S. Sabo-Etienne, B. Chaudret, *Inorg. Chem.* **1999**, *38*, 2550–2551.
- [169] J. Ayllon, S. Sabo-Etienne, B. Chaudret, S. Ulrich, H.-H. Limbach, *Inorg. Chim. Acta* **1997**, *259*, 1–4.
- [170] E. I. Gutsul, N. V. Belkova, M. S. Sverdlov, L. M. Epstein, E. S. Shubina, V. I. Bakhmutov, T. N. Gribova, R. M. Minyaev, C. Bianchini, M. Peruzzini, F. Zanobini, *Chem. Eur. J.* **2003**, *9*, 2219–2228.
- [171] N. V. Belkova, A. V. Ionidis, L. M. Epstein, E. S. Shubina, S. Gruendemann, N. S. Golubev, H.-H. Limbach, *Eur. J. Inorg. Chem.* **2001**, *2001*, 1753–1761.
- [172] A. J. Lough, S. Park, R. Ramachandran, R. H. Morris, *J. Am. Chem. Soc.* **1994**, *116*, 8356–8357.
- [173] J. C. Lee, A. L. Rheingold, B. Muller, P. S. Pregosin, R. H. Crabtree, *Chem. Commun.* **1994**, 1021–1022.
- [174] A. Bondi, *J. Phys. Chem.* **1964**, *68*, 441–451.
- [175] H. Cybulski, M. Pecul, J. Sadlej, T. Helgaker, *J. Chem. Phys.* **2003**, *119*, 5094–5104.
- [176] I. Alkorta, J. Elguero, S. J. Grabowski, *J. Phys. Chem. A* **2008**, *112*, 2721–2727.
- [177] I. Majerz, I. Olovsson, *Phys. Chem. Chem. Phys.* **2010**, *12*, 5462–5467.
- [178] R. Parthasarathi, V. Subramanian, N. Sathyamurthy, *J. Phys. Chem. A* **2006**, *110*, 3349–3351.
- [179] J. Ireta, J. Neugebauer, M. Scheffler, *J. Phys. Chem. A* **2004**, *108*, 5692–5698.

- [180] D. Donghi, T. Beringhelli, G. D'Alfonso, M. Mondini, *Chemistry - A European Journal* **2006**, *12*, 1016–1025.
- [181] G. A. Morris, *Magn. Reson. Chem.* **1986**, *24*, 371–403.
- [182] P. J. Desrosiers, L. Cai, Z. Lin, R. Richards, J. Halpern, *J. Am. Chem. Soc.* **1991**, *113*, 4173–4184.
- [183] V. I. Bakhmutov, E. V. Vorontsov, G. I. Nikonov, D. A. Lemenovskii, *Inorg. Chem.* **1998**, *37*, 279–282.
- [184] V. I. Bakhmutov, *Practical NMR relaxation for chemists*, Wiley, Chichester, **2004**.
- [185] K. Akasaka, T. Imoto, H. Hatano, *Chem. Phys. Lett.* **1973**, *21*, 398–400.
- [186] C. P. Butts, C. R. Jones, E. C. Towers, J. L. Flynn, L. Appleby, N. J. Barron, *Org. Biomol. Chem.* **2011**, *9*, 177–184.
- [187] C. R. Jones, C. P. Butts, J. N. Harvey, *Beilstein J. Org. Chem.* **2011**, *7*, 145–150.
- [188] O. A. Filippov, N. V. 1, L. M. Epstein, A. Lledos, E. S. Shubina, *Chem-PhysChem* **2012**, *13*, 2677–2687.
- [189] G. R. Fulmer, A. J. M. Miller, N. H. Sherden, H. E. Gottlieb, A. Nudelman, B. M. Stoltz, J. E. Bercaw, K. I. Goldberg, *Organometallics* **2010**, *29*, 2176–2179.
- [190] Y. Wang, T. Szilvási, S. Yao, M. Driess, *Nat. Chem.* **2020**, *12*, 801–807.
- [191] D. Heift, Z. Benkő, H. Grützmacher, *Dalton Trans.* **2014**, *43*, 831–840.
- [192] A. R. Jupp, J. M. Goicoechea, *Angew. Chem. Int. Ed.* **2013**, *52*, 10064–10067.
- [193] J. M. Goicoechea, H. Grützmacher, *Angew. Chem. Int. Ed.* **2018**, *57*, 16968–16994.
- [194] G. Becker, W. Schwarz, N. Seidler, M. Westerhausen, *Z. anorg. allg. Chem.* **1992**, *612*, 72–82.
- [195] M. Westerhausen, S. Schneiderbauer, H. Piotrowski, M. Suter, H. Nöth, *J. Organomet. Chem.* **2002**, *643-644*, 189–193.
- [196] F. F. Puschmann, D. Stein, D. Heift, C. Hendriksen, Z. A. Gal, H.-F. Grützmacher, H. Grützmacher, *Angew. Chem. Int. Ed.* **2011**, *123*, 8420–8423.
- [197] I. Krummenacher, C. C. Cummins, *Polyhedron* **2012**, *32*, 10–13.
- [198] Z.-J. Quan, X.-C. Wang, *Org. Chem. Front.* **2014**, *1*, 1128–1131.
- [199] D. Heift, Z. Benkő, H. Grützmacher, *Dalton Trans.* **2014**, *43*, 5920–5928.
- [200] L. N. Grant, B. Pinter, B. C. Manor, H. Grützmacher, D. J. Mindiola, *Angew. Chem. Int. Ed.* **2018**, *57*, 1049–1052.
- [201] L. Liu, D. A. Ruiz, F. Dahcheh, G. Bertrand, R. Suter, A. M. Tondreau, H. Grützmacher, *Chem. Sci.* **2016**, *7*, 2335–2341.
- [202] G. Hierlmeier, A. Hinz, R. Wolf, J. M. Goicoechea, *Angew. Chem. Int. Ed.* **2018**, *130*, 439–444.
- [203] S. Alidori, D. Heift, G. Santiso-Quinones, Z. Benkő, H. Grützmacher, M. Caporali, L. Gonsalvi, A. Rossin, M. Peruzzini, *Chem. Eur. J.* **2012**, *18*, 14805–14811.
- [204] S. Bestgen, M. Mehta, T. C. Johnstone, P. W. Roesky, J. M. Goicoechea, *Chem. Eur. J.* **2020**, *26*, 9024–9031.
- [205] L. Weber, B. Torwiehe, G. Bassmann, H.-G. Stammer, B. Neumann, *Organometallics* **1996**, *15*, 128–132.

- [206] G. Becker, G. Heckmann, K. Hbler, W. Schwarz, *Z. anorg. allg. Chem.* **1995**, *621*, 34–46.
- [207] O. Back, M. Henry-Ellinger, C. D. Martin, D. Martin, G. Bertrand, *Angew. Chem. Int. Ed.* **2013**, *52*, 2939–2943.
- [208] M. M. Hansmann, R. Jazzar, G. Bertrand, *J. Am. Chem. Soc.* **2016**, *138*, 8356–8359.
- [209] A. M. Tondreau, Z. Benkő, J. R. Harmer, H. Grützmacher, *Chem. Sci.* **2014**, *5*, 1545–1554.
- [210] C. A. Tsipis, P. A. Karipidis, *J. Am. Chem. Soc.* **2003**, *125*, 2307–2318.
- [211] K. M. Szkop, A. R. Jupp, D. W. Stephan, *J. Am. Chem. Soc.* **2018**, *140*, 12751–12755.
- [212] Z. Li, J. E. Borger, F. Müller, J. R. Harmer, C.-Y. Su, H. Grützmacher, *Angew. Chem. Int. Ed.* **2019**, *58*, 11429–11433.
- [213] S. Grimme, J. Antony, S. Ehrlich, H. Krieg, *J. Chem. Phys.* **2010**, *132*, 154104.
- [214] S. Grimme, S. Ehrlich, L. Goerigk, *J. Comput. Chem.* **2011**, *32*, 1456–1465.
- [215] F. F. Puschmann, D. Stein, D. Heift, C. Hendriksen, Z. A. Gal, H.-F. Grützmacher, H. Grützmacher, *Angew. Chem. Int. Ed.* **2011**, *50*, 8420–8423.
- [216] Y. Xiong, S. Yao, T. Szilvási, E. Ballester-Martínez, H. Grützmacher, M. Driess, *Angew. Chem. Int. Ed.* **2017**, *56*, 4333–4336.
- [217] Y. Wu, L. L. Liu, J. Su, J. Zhu, Z. Ji, Y. Zhao, *Organometallics* **2016**, *35*, 1593–1596.
- [218] L. Liu, D. A. Ruiz, D. Munz, G. Bertrand, *Chem* **2016**, *1*, 147–153.
- [219] B. A. Surgenor, M. Bühl, A. M. Z. Slawin, J. D. Woollins, P. Kilian, *Angew. Chem. Int. Ed.* **2012**, *124*, 10297–10300.
- [220] Z. Li, X. Chen, M. Bergeler, M. Reiher, C.-Y. Su, H. Grützmacher, *Dalton Trans.* **2015**, *44*, 6431–6438.
- [221] N. Del Rio, A. Baceiredo, N. Saffon-Merceron, D. Hashizume, D. Lutters, T. Müller, T. Kato, *Angew. Chem. Int. Ed.* **2016**, *55*, 4753–4758.
- [222] S. Shah, J. D. Protasiewicz, *Chem. Commun.* **1998**, 1585–1586.
- [223] D. V. Partyka, M. P. Washington, J. B. Updegraff, R. A. Woloszynek, J. D. Protasiewicz, *Angew. Chem. Int. Ed.* **2008**, *47*, 7489–7492.
- [224] B. Deschamps, X. Le Goff, L. Ricard, P. Le Floch, *Heteroat. Chem.* **2007**, *18*, 363–371.
- [225] E. Deschamps, B. Deschamps, J. Laure Dormieux, L. Ricard, N. Mézailles, P. Le Floch, *Dalton Trans.* **2006**, 594–602.
- [226] *Multiple bonds and low coordination in phosphorus chemistry*, (Eds.: M. Regitz, O. J. Scherer, R. Appel), Thieme, Stuttgart, **1990**.
- [227] A. J. Arduengo, J. C. Calabrese, A. H. Cowley, H. V. R. Dias, J. R. Goerlich, W. J. Marshall, B. Riegel, *Inorg. Chem.* **1997**, *36*, 2151–2158.
- [228] A. B. Burg, W. Mahler, *J. Am. Chem. Soc.* **1961**, *83*, 2388–2389.
- [229] D. C. Pestana, P. P. Power, *J. Am. Chem. Soc.* **1989**, *111*, 6887–6888.
- [230] A. J. Arduengo III, C. J. Carmalt, J. A. C. Clyburne, A. H. Cowley, R. Pyati, *Chem. Commun.* **1997**, 981–982.

- [231] I. A. J. Arduengo, H. V. R. Dias, J. C. Calabrese, *Chem. Lett.* **1997**, *26*, 143–144.
- [232] R. R. Rodrigues, C. L. Dorsey, C. A. Arceneaux, T. W. Hudnall, *Chem. Commun.* **2014**, *50*, 162–164.
- [233] O. Lemp, M. Balmer, K. Reiter, F. Weigend, C. von Hänisch, *Chem. Commun.* **2017**, *53*, 7620–7623.
- [234] A. Beil, R. J. Gilliard, H. Grützmacher, *Dalton Trans.* **2016**, *45*, 2044–2052.
- [235] M. Yam, J. H. Chong, C.-W. Tsang, B. O. Patrick, A. E. Lam, D. P. Gates, *Inorg. Chem.* **2006**, *45*, 5225–5234.
- [236] J. Dugal-Tessier, G. R. Dake, D. P. Gates, *Angew. Chem. Int. Ed.* **2008**, *120*, 8184–8187.
- [237] P. FLOCH, *Coord. Chem. Rev.* **2006**, *250*, 627–681.
- [238] T. Krachko, J. C. Slootweg, *Eur. J. Inorg. Chem.* **2018**, *2018*, 2734–2754.
- [239] A. Schmidpeter, W. Gebler, F. Zwaschka, W. S. Sheldrick, *Angew. Chem. Int. Ed.* **1980**, *19*, 722–723.
- [240] L. Weber, *Eur. J. Inorg. Chem.* **2000**, *2000*, 2425–2441.
- [241] T. G. Larocque, G. G. Lavoie, *New J. Chem.* **2014**, *38*, 499–502.
- [242] A. Doddi, D. Bockfeld, T. Bannenberg, P. G. Jones, M. Tamm, *Angew. Chem. Int. Ed.* **2014**, *53*, 13568–13572.
- [243] Z. Li, X. Chen, Y. Li, C.-Y. Su, H. Grützmacher, *Chem. Commun.* **2016**, *52*, 11343–11346.
- [244] M. Cicač-Hudi, J. Bender, S. H. Schlindwein, M. Bispinghoff, M. Nieger, H. Grützmacher, D. Gudat, *Eur. J. Inorg. Chem.* **2016**, *2016*, 649–658.
- [245] T. Krachko, M. Bispinghoff, A. M. Tondreau, D. Stein, M. Baker, A. W. Ehlers, J. C. Slootweg, H. Grützmacher, *Angew. Chem. Int. Ed.* **2017**, *129*, 8056–8059.
- [246] W. W. Schoeller, J. Niemann, R. Thiele, W. Haug, *Eur. J. Inorg. Chem.* **1991**, *124*, 417–421.
- [247] R. Kinjo, B. Donnadiou, G. Bertrand, *Angew. Chem. Int. Ed.* **2010**, *49*, 5930–5933.
- [248] D. W. N. Wilson, M. P. Franco, W. K. Myers, J. E. McGrady, J. M. Goicoechea, *Chem. Sci.* **2019**, *11*, 862–869.
- [249] G. Becker, H. Brombach, S. T. Horner, E. Niecke, W. Schwarz, R. Streubel, E.-U. Würthwein, *Inorg. Chem.* **2005**, *44*, 3080–3086.
- [250] A. S. Ionkin, W. J. Marshall, B. M. Fish, L. A. Howe, *Organometallics* **2010**, *29*, 4154–4158.
- [251] H. Tian, J. Hong, K. Wang, I. Del Rosal, L. Maron, X. Zhou, L. Zhang, *J. Am. Chem. Soc.* **2018**, *140*, 102–105.
- [252] C. Zhang, G. Hou, G. Zi, W. Ding, M. D. Walter, *J. Am. Chem. Soc.* **2018**, *140*, 14511–14525.
- [253] H. Aktas, J. Mulder, F. J. J. de Kanter, J. C. Slootweg, M. Schakel, A. W. Ehlers, M. Lutz, A. L. Spek, K. Lammertsma, *J. Am. Chem. Soc.* **2009**, *131*, 13531–13537.
- [254] A. Grundmann, M. B. Sárosi, P. Lönnecke, E. Hey-Hawkins, *Eur. J. Inorg. Chem.* **2014**, *2014*, 2997–3001.
- [255] A. C. Behrle, J. R. Walensky, *Dalton Trans.* **2016**, *45*, 10042–10049.

- [256] P. Pyykkö, M. Atsumi, *Chem. Eur. J.* **2009**, *15*, 186–197.
- [257] P. Pyykkö, M. Atsumi, *Chem. Eur. J.* **2009**, *15*, 12770–12779.
- [258] M. Fischer, C. Hering-Junghans, *Chem. Sci.* **2021**, 10279–10289.
- [259] J. Escudié, H. Ranaivonjatovo, L. Rigon, *Chem. Rev.* **2000**, *100*, 3639–3696.
- [260] K. M. Szkop, A. R. Jupp, H. Razumkov, M. Xu, D. W. Stephan, *Chem. Eur. J.* **2019**, *25*, 10084–10087.
- [261] E. Kraka, D. Cremer, *ChemPhysChem* **2009**, *10*, 686–698.
- [262] E. J. Thompson, L. A. Berben, *Angew. Chem. Int. Ed.* **2015**, *54*, 11642–11646.
- [263] Eckhard Bill, *julX: Program for Simulation of Molecular Magnetic Data*, Max-Planck Institute for Chemical Energy Conversion: Mülheim/Ruhr, **2008**.
- [264] MATLAB, *version 9.1 R2019b*, The MathWorks Inc., Natick, Massachusetts, **2019**.
- [265] S. Stoll, A. Schweiger, *Journal of magnetic resonance (San Diego Calif. : 1997)* **2006**, *178*, 42–55.
- [266] N. G. Connelly, W. E. Geiger, *Chemical reviews* **1996**, *96*, 877–910.
- [267] G. M. Sheldrick, *Acta Crystallogr. A* **2015**, *71*, 3–8.
- [268] G. M. Sheldrick, *Acta Crystallogr. C Struct. Chem.* **2015**, *71*, 3–8.
- [269] STOE & CIE GmbH, Ed., *X-RED*, Darmstadt, Germany, **2002**.
- [270] BRUKER AXS GmbH, Ed., *SADABS*, Karlsruhe, Germany, **2016**.
- [271] J. H. Noggle, R. E. Schirmer, *The nuclear Overhauser effect: Chemical applications*, Academic Pr, New York, **1971**.
- [272] S. Aime, W. Dastrù, R. Gobetto, A. Viale, *Inorg. Chem.* **2000**, *39*, 2422–2425.
- [273] D. Neuhaus, M. P. Williamson, *The nuclear Overhauser effect in structural and conformational analysis*, 2. ed., Wiley-VCH, New York, NY, **2000**.
- [274] A. L. Spek, *Acta Crystallogr. Sect. C: Struct. Chem.* **2015**, *71*, 9–18.
- [275] M. K. Kesharwani, B. Brauer, J. M. L. Martin, *J. Phys. Chem. A* **2015**, *119*, 1701–1714.
- [276] F. Neese, *WIREs Comput. Mol. Sci.* **2012**, *2*, 73–78.
- [277] F. Weigend, R. Ahlrichs, *Phys. Chem. Chem. Phys.* **2005**, *7*, 3297–3305.
- [278] V. Barone, M. Cossi, *J. Phys. Chem. A* **1998**, *102*, 1995–2001.
- [279] *Classical and quantum dynamics in condensed phase simulations*, World Scientific, Singapore, **1998**.
- [280] F. Weigend, *Phys. Chem. Chem. Phys.* **2006**, *8*, 1057–1065.

Curriculum Vitae

Personal Details

Name: Roland Alexander Schulz

Date of Birth: 16.07.1992

Place of Birth: Bremen

Nationality: German

Academic Education

- 10/17 - current** PhD candidate, Advisor: PROF. DR. FRANC MEYER
Thesis: *Bioinspired small molecule activation at pyrazolate-based dinuclear complexes*
- 10/2015 - 10/2017** M. Sc. in Chemistry, Advisor: PROF. DR. FRANC MEYER
Thesis: *Bimetallic nickel complexes for oxygen activation*
- Stay Abroad: 09/2016-02/2017
Disiloxane-based organometallics as single-molecule magnets
PROF. DR. RICHARD LAYFIELD, The University of Manchester
- 10/2012 - 10/2015** B. Sc. in Chemistry, Advisor: PROF. DR. FRANC MEYER
Thesis: *Bioinspired bimetallic copper complexes for oxygen activation*

Publications

- A. Brinkmeier, R. A. Schulz, M. Buchhorn, C-J.Spyra, S. Dechert, S. Demeshko, V. Krewald, and F. Meyer *J. Am. Chem. Soc.* **2021**, *27*, 10361-10366. *Structurally Characterized μ -1,2-Peroxo/Superoxo Dicopper(II) Pair*
- P.-C. Duan, R. A. Schulz, A. Römer, B. E. Van Kuiken, S. Dechert, S. Demeshko, G. E. Cutsail III, S. DeBeer, R. A. Mata, F. Meyer *Angew. Chem. Int. Ed.*, **2021**, *60*, 1891-1896. *Ligand Protonation Triggers H₂ Release from a Dinickel Dihydride Complex to Give a Doubly "T"-Shaped Dinickel(I) Metallodiradical*
- J. Altnöder, K. Krüger, D. Borodin, L. Reuter, D. Rohleder, F. Hecker, R. A. Schulz, X. T. Nguyen, H. Preiß, M. Eckhoff, M. Levien, M. A. Suhm, *The Chemical Record* **2014**, *14*, 1116-1133. *The Guinness Molecules for the Carbohydrate Formula*

Poster Presentations at Conferences

23. JCF-Frühjahrssymposium, online conference, **29/03 – 1/4/2021** "*A Dinickel Complex Hosting an end-on Bridging Phosphaketene and its Versatile PCO-Centered Reactivity*" (Poster)

3. Oldenburg Symposium on Chemical Bond Activation, online conference, **08/03/2021** "*Bimetallic Oxidative Addition of Water Supported by Intramolecular Dihydrogen Bonding*" (Poster)